ISSN 1949-8470 (online)

World Journal of *Radiology*

World J Radiol 2014 August 28; 6(8): 519-635

Published by Baishideng Publishing Group Inc

WJR World Journal of Radiology

A peer-reviewed, online, open-access journal of Radiology

Editorial Board

2014-2017

The *World Journal of Radiology* Editorial Board consists of 365 members, representing a team of worldwide experts in radiology. They are from 36 countries, including Afghanistan (1), Argentina (2), Australia (5), Austria (7), Belgium (2), Brazil (8), Canada (6), Chile (1), China (43), Croatia (1), Denmark (4), Egypt (6), France (5), Germany (22), Greece (10), India (12), Iran (6), Ireland (2), Israel (3), Italy (47), Japan (13), Netherlands (1), New Zealand (1), Pakistan (1), Poland (2), Portugal (1), Serbia (1), Singapore (3), Slovakia (1), South Korea (18), Spain (4), Sweden (2), Switzerland (4), Thailand (1), Turkey (26), United Kingdom (11), and United States (82).

Yue-Qi Zhu, *Shanghai*

Croatia

Goran Kusec, Osijek

Denmark

Poul E Andersen, *Odense*
Lars J Petersen, *Aalborg*
Thomas Z Ramsoy, *Frederiksberg*
Morten Ziebell, *Copenhagen*

Egypt

Mohamed F Bazeed, *Mansoura*
Mohamed Abou El-Ghar, *Mansoura*
Reem HA Mohamed, *Cairo*
Mohamed R Nouh, *Alexandria*
Ahmed AKA Razek, *Mansoura*
Ashraf A Zytoon, *Shebin El-Koom*

France

Sabine F Bensamoun, *Compiègne*
Romaric Loffroy, *Dijon*
Stephanie Nougaret, *Montpellier*
Hassane Oudadesse, *Rennes*
Vincent Vinh-Hung, *Fort-de-France*

Germany

Henryk Barthel, *Leipzig*
Peter Bannas, *Hamburg*
Martin Beeres, *Frankfurt*
Ilja F Ciernik, *Dessau*
A Dimitrakopoulou-Strauss, *Heidelberg*
Peter A Fasching, *Erlanegn*
Andreas G Schreyer, *Regensburg*
Philipp Heusch, *Duesseldorf*
Sonja M Kirchhoff, *Munich*
Sebastian Ley, *Munich*
Adel Maataoui, *Frankfurt am Main*
Stephan M Meckel, *Freiburg*
Hans W Muller, *Duesseldorf*
Kay Raum, *Berlin*
Dirk Rades, *Luebeck*
Marc-Ulrich Regier, *Hamburg*
Alexey Surov, *Halle*
Martin Walter, *Magdeburg*
Axel Wetter, *Essen*
Christoph Zilkens, *Düsseldorf*

Greece

Panagiotis Antoniou, *Thessaloniki*
Nikos Efthimiou, *Athens*
Dimitris Karnabatidis, *Patras*
George Latsios, *Athens*
Stylianos Megremis, *Iraklion*
Alexander D Rapidis, *Athens*
Kiki Theodorou, *Larissa*
Ioannis A Tsalafoutas, *Athens*
Evanthia E Tripoliti, *Ioannina*
Athina C Tsili, *Ioannina*

India

Ritesh Agarwal, *Chandigarh*
Chandan J Das, *New Delhi*
Prathamesh V Joshi, *Mumbai*
Naveen Kalra, *Chandigarh*
Chandrasekharan Kesavadas, *Trivandrum*
Jyoti Kumar, *New Delhi*
Atin Kumar, *New Delhi*
Kaushala P Mishra, *Allahabad*
Daya N Sharma, *New Delhi*
Binit Sureka, *New Delhi*
Sanjay Sharma, *New Delhi*
Raja R Yadav, *Allahabad*

Iran

Majid Assadi, *Bushehr*
SeyedReza Najafizadeh, *Tehran*
Mohammad Ali Oghabian, *Tehran*
Amir Reza Radmard, *Tehran*
Ramin Sadeghi, *Mashhad*
Hadi Rokni Yazdi, *Tehran*

Ireland

Tadhg Gleeson, *Wexford*
Frederik JAI Vernimmen, *Cork*

Israel

Dafna Ben Bashat, *Tel Aviv*
Amit Gefen, *Tel Aviv*
Tamar Sella, *Jerusalem*

Italy

Adriano Alippi, *Rome*
Dante Amelio, *Trento*
Michele Anzidei, *Rome*
Filippo F Angileri, *Messinas*
Stefano Arcangeli, *Rome*
Roberto Azzoni, *San Donato milanese*
Tommaso V Bartolotta, *Palermo*
Tommaso Bartalena, *Imola*
Livia Bernardin, *San Bonifacio*
Federico Boschi, *Verona*
Sergio Casciaro, *Lecce*
Emanuele Casciani, *Rome*
Musa M Can, *Napoli*
Alberto Cuocolo, *Napoli*
Michele Ferrara, *Coppito*
Mauro Feola, *Fossano*
Giampiero Francica, *Castel Volturno*
Luigi De Gennaro, *Rome*
Giulio Giovannetti, *Pisa*
Francesca Iacobellis, *Napoli*
Formato Invernizzi, *Monza Brianza*
Francesco Lassandro, *Naples*
Lorenzo Livi, *Florence*
Pier P Mainenti, *Napoli*
Laura Marzetti, *Chieti*
Giuseppe Malinverni, *Crescentino*
Enrica Milanesi, *Turin*
Giovanni Morana, *Treviso*
Lorenzo Monti, *Milan*
Silvia D Morbelli, *Genoa*
Barbara Palumbo, *Perugia*
Cecilia Parazzini, *Milan*
Stefano Pergolizzi, *Messina*
Antonio Pinto, *Naples*
Camillo Porcaro, *Rome*
Carlo C Quattrocchi, *Rome*
Alberto Rebonato, *Perugia*
Giuseppe Rizzo, *Rome*
Roberto De Rosa, *Naples*
Domenico Rubello, *Rovigo*
Andrea Salvati, *Bari*
Sergio Sartori, *Ferrara*
Luca M Sconfienza, *Milano*
Giovanni Storto, *Rionero*
Nicola Sverzellati, *Parma*
Alberto S Tagliafico, *Genova*
Nicola Troisi, *Florence*

Japan

Yasuhiko Hori, *Chiba*
Hidetoshi Ikeda, *Koriyama*
Masahito Kawabori, *Sapporo*
Tamotsu Kamishima, *Sapporo*
Hiro Kiyosue, *Yufu*
Yasunori Minami, *Osaka-sayama*
Yasuhiro Morimoto, *Kitakyushu*
Satoru Murata, *Tokyo*
Shigeki Nagamachi, *Miyazaki*
Hiroshi Onishi, *Yamanashi*
Morio Sato, *Wakayama Shi*
Yoshito Tsushima, *Maebashi*
Masahiro Yanagawa, *Suita*

Netherlands

Willem Jan van Rooij, *Tilburg*

New Zealand

W Howell Round, *Hamilton*

Pakistan

Wazir Muhammad, *Abbottabad*

Poland

Maciej S Baglaj, *Wroclaw*

Piotr Czauderna, *Gdansk*

Portugal

Joao Manuel RS Tavares, *Porto*

Serbia

Olivera Ciraj-Bjelac, *Belgrade*

Singapore

Gopinathan Anil, *Singapore*
Terence KB Teo, *Singapore*
Cher Heng Tan, *Singapore*

Slovakia

Stefan Sivak, *Martin*

South Korea

Ki Seok Choo, *Busan*
Seung Hong Choi, *Seoul*
Dae-Seob Choi, *Jinju*
Hong-Seok Jang, *Seoul*
Yong Jeong, *Daejeon*
Chan Kyo Kim, *Seoul*
Se Hyung Kim, *Seoul*
Joong-Seok Kim, *Seoul*
Sang Eun Kim, *Seongnam*
Sung Joon Kwon, *Seoul*
Jeong Min Lee, *Seoul*
In Sook Lee, *Busan*
Noh Park, *Goyang*
Chang Min Park, *Seoul*
Sung Bin Park, *Seoul*
Deuk Jae Sung, *Seoul*
Choongsoo Shin, *Seoul*
Kwon-Ha Yoon, *Iksan*

Spain

Miguel A De Gregorio, *Zaragoza*
Antonio Luna, *Jaén*
Enrique Marco de Lucas, *Santander*
Fernando Ruiz Santiago, *Granada*

Sweden

Dmitry Grishenkov, *Stockholm*
Tie-Qiang Li, *Stockholm*

Switzerland

Nicolau Beckmann, *Basel*
Christian Boy, *Bern*
Giorgio Treglia, *Bellinzona*

Stephan Ulmer, *Kiel*

Thailand

Sirianong Namwongprom, *Chiang Mai*

Turkey

Kubilay Aydin, *Istanbul*
Ramazan Akdemir, *Sakarya*
Serhat Avcu, *Ankara*
Ayse Aralasmak, *Istanbul*
Oktay Algin, *Ankara*
Nevbahar Akcar, *Meselik*
Bilal Battal, *Ankara*
Zulkif Bozgeyik, *Elazig*
Nazan Ciledag, Aakara
Fuldem Y Donmez, *Ankara*
Gulgun Engin, *Istanbul*
Ahmet Y Goktay, *Izmir*
Oguzhan G Gumustas, *Bursa*
Kaan Gunduz, *Ankara*
Pelin Ozcan Kara, *Mersin*
Kivanc Kamburoglu, *Ankara*
Ozgur Kilickesmez, *Istanbul*
Furuzan Numan, *Istanbul*
Cem Onal, *Adana*
Ozgur Oztekin, *Izmir*
Seda Ozbek (Boruban), *Konya*
Selda Sarikaya, *Zonguldak*
Figen Taser, *Kutahya*
Baran Tokar, *Eskisehir*
Ender Uysal, *Istanbul*
Ensar Yekeler, *Istanbul*

United Kingdom

Indran Davagnanam, *London*
M DC Valdés Hernández, *Edinburgh*
Alan Jackson, *Manchester*
Suneil Jain, *Belfast*
Long R Jiao, *London*
Miltiadis Krokidis, *Cambridge*
Pradesh Kumar, *Liverpool*
Peter D Kuzmich, *Derby*
Georgios Plataniotis, *Brighton*
Vanessa Sluming, *Liverpool*

United States

Garima Agrawal, *Saint Louis*
James R Brasic, *Baltimore*
Rajendra D Badgaiyan, *Buffalo*
Ulas Bagci, *Bethesda*
Anat Biegon, *Stony Brook*
Ramon Casanova, *Winston Salem*
Wenli Cai, *Boston*
Zheng Chang, *Durham*
Corey J Chakarun, *Long Beach*
Kai Chen, *Los Angeles*
Hyun-Soon Chong, *Chicago*
Marco Cura, *Dallas*
Ravi R Desai, *Bensalem*
Delia DeBuc, *Miami*
Carlo N De Cecco, *Charleston*
Timm-Michael L Dickfeld, *Baltimore*
Subba R Digumarthy, *Boston*
Huy M Do, *Stanford*
Todd A Faasse, *Grand Rapids*
Salomao Faintuch, *Boston*
Girish M Fatterpekar, *New York*
Dhakshinamoorthy Ganeshan, *Houston*
Robert J Griffin, *Little Rock*
Andrew J Gunn, *Boston*
Sandeep S Hedgire, *Boston*
Timothy J Hoffman, *Columbia*
Mai-Lan Ho, *San Francisco*
Juebin Huang, *Jackson*
Abid Irshad, *Charleston*
Matilde Inglese, *New York*
El-Sayed H Ibrahim, *Jacksonville*
Paul R Julsrud, *Rochester*
Pamela T Johnson, *Baltimore*
Ming-Hung Kao, *Tempe*
Sunil Krishnan, *Houston*
Richard A Komoroski, *Cincinnati*
Sandi A Kwee, *Honolulu*
King Kim, *Ft. Lauderdale*
Guozheng Liu, *Worcester*
Yiyan Liu, *Newark*
Venkatesh Mani, *New York*
Lian-Sheng Ma, *Pleasanton*
Rachna Madan, *Boston*
Zeyad A Metwalli, *Houston*
Yilong Ma, *Manhasset*
Hui Mao, *Atlanta*
Feroze B Mohamed, *Philadelphia*
Gul Moonis, *Boston*
John L Nosher, *New Brunswick*
Rahmi Oklu, *Boston*
Aytekin Oto, *Chicago*
Bishnuhari Paudyal, *Philadelphia*
Rajul Pandya, *Youngstown*
Chong-Xian Pan, *Sacramento*
Jay J Pillai, *Baltimore*
Neal Prakash, *Duarte*
Reza Rahbar, *Boston*
Ali S Raja, *Boston*
Gustavo J Rodriguez, *El Paso*
David J Sahn, *Portlsand*
Steven Schild, *Scottsdale*
Ali R Sepahdari, *Los Angeles*
Li Shen, *Indianapolis*
JP Sheehan, *Charlottesville*
Atul B Shinagare, *Boston*
Sarabjeet Singh, *Boston*
Charles J Smith, *Columbia*
Kenji Suzuki, *Chicago*
Monvadi Srichai-Parsia, *Washington*
Sree H Tirumani, *Boston*
Hebert A Vargas, *New York*
Sachit Verma, *Philadelphia*
Yoichi Watanabe, *Minneapolis*
Li Wang, *Chapel Hill*
Carol C Wu, *Boston*
Shoujun Xu, *Houston*
Min Yao, *Cleveland*
Xiaofeng Yang, *Atlanta*
Qingbao Yu, *Albuquerque*
Aifeng Zhang, *Chicago*
Chao Zhou, *Bethlehem*
Hongming Zhuang, *Philadelphia*

WJR World Journal of Radiology

Contents

Monthly Volume 6 Number 8 August 28, 2014

Contents

World Journal of Radiology
Volume 6 Number 8 August 28, 2014

NAME OF JOURNAL
World Journal of Radiology

ISSN
ISSN 1949-8470 (online)

LAUNCH DATE
December 31, 2009

FREQUENCY
Monthly

EDITORIAL OFFICE
Jin-Lei Wang, Director
Xiu-Xia Song, Vice Director
World Journal of Radiology
Room 903, Building D, Ocean International Center,
No. 62 Dongsihuan Zhonglu, Chaoyang District,
Beijing 100025, China
Telephone: +86-10-59080039
Fax: +86-10-85381893
E-mail: editorialoffice@wjgnet.com
Help Desk: http://www.wjgnet.com/esps/helpdesk.aspx
http://www.wjgnet.com

PUBLISHER
Baishideng Publishing Group Inc
8226 Regency Drive,
Pleasanton, CA 94588, USA
Telephone: +1-925-223-8242
Fax: +1-925-223-8243
E-mail: bpgoffice@wjgnet.com
Help Desk: http://www.wjgnet.com/esps/helpdesk.aspx
http://www.wjgnet.com

PUBLICATION DATE
August 28, 2014

INSTRUCTIONS TO AUTHORS
Full instructions are available online at http://www.wjgnet.com/1949-8470/g_info_20100316162358.htm.

ONLINE SUBMISSION
http://www.wjgnet.com/esps/

World Journal of Radiology

Submit a Manuscript: http://www.wjgnet.com/esps/
Help Desk: http://www.wjgnet.com/esps/helpdesk.aspx
DOI: 10.4329/wjr.v6.i8.519

World J Radiol 2014 August 28; 6(8): 519-522
ISSN 1949-8470 (online)

TOPIC HIGHLIGHT

WJR 6th Anniversary Special Issues (5): Molecular imaging

Radiogenomic imaging-linking diagnostic imaging and molecular diagnostics

Mathias Goyen

Mathias Goyen, UKE Consult und Management GmbH, University Medical Center Hamburg-Eppendorf, 20251 Hamburg, Germany
Author contributions: Goyen M wrote and edited the entire manuscript.
Correspondence to: Mathias Goyen, MD, UKE Consult und Management GmbH, University Medical Center Hamburg-Eppendorf, Martinistrasse 52, 20251 Hamburg, Germany. mathias@goyen.de
Telephone: +49-40-741056810 Fax: +49-40-7410575
Received: December 30, 2013 Revised: June 5, 2014
Accepted: June 10, 2014
Published online: August 28, 2014

Abstract

Radiogenomic imaging refers to the correlation between cancer imaging features and gene expression and is one of the most promising areas within science and medicine. High-throughput biological techniques have reshaped the perspective of biomedical research allowing for fast and efficient assessment of the entire molecular topography of a cell's physiology providing new insights into human cancers. The use of non-invasive imaging tools for gene expression profiling of solid tumors could serve as a means for linking specific imaging features with specific gene expression patterns thereby allowing for more accurate diagnosis and prognosis and obviating the need for high-risk invasive biopsy procedures. This review focuses on the medical imaging part as one of the main drivers for the development of radiogenomic imaging.

Key words: Radiogenomic imaging; Personalized medicine; Diagnostic imaging

Core tip: Radiogenomic imaging has the potential to catalyze the health system by creating imaging biomarkers that identify the genomics of a disease. The use of noninvasive imaging for gene expression profiling is a fast and reliable technique which has the potential to replace high-risk invasive biopsy procedures.

Goyen M. Radiogenomic imaging-linking diagnostic imaging and molecular diagnostics. *World J Radiol* 2014; 6(8): 519-522 Available from: URL: http://www.wjgnet.com/1949-8470/full/v6/i8/519.htm DOI: http://dx.doi.org/10.4329/wjr.v6.i8.519

INTRODUCTION

Recent developments in high-throughput molecular techniques promise to generate biomarkers driving the future of personalized medicine[1-3]. Gene expression profiling has the potential to gather key information regarding biology and its relationship to diagnosis, prognosis and therapy. However, a main limitation of these techniques is the need to acquire tissue for gene expression profiling through invasive biopsy thereby limiting the clinical application of this method in an everyday patient care setting. In addition, in these biopsies samples are frequently obtained from only a part of the lesion and therefore do not entirely represent the lesion's unique anatomic, functional, and physiologic properties, such as size, location, and morphology. Many of these features are obtained in routine clinical imaging exams and are very useful for diagnosis, staging, and treatment planning. Although these image features provide anatomical and morphological information, only few studies[4-6] have generated a "radiogenomics map" integrating the genomic and image data thereby introducing the field of "radiogenomics" or "radiogenomic imaging"[3]. Specific radiological tumor phenotypes can be used as surrogates for signatures of gene expression. If imaging can be linked to these treat-

ment-response gene-expression patterns routine clinical imaging is able to predict the likely response to specific chemotherapeutics and helps to choose the best form and duration of treatment.

DIAGNOSTIC IMAGING AS A PLATFORM FOR GENE EXPRESSION PROFILING

Radiologic imaging plays an important part in every stage of cancer treatment. Besides screening, detection and staging of disease, imaging is used to predict and evaluate individual patient's responsiveness to therapies in every stage of cancer treatment. Diagnostic imaging is a safe and accurate tool to noninvasively assess location, morphology and physiology of tissues[3]. This crucial role for imaging biomarkers in cancer treatment is reflected by the fact that more than 90 percent of cancer patients are evaluated by imaging. However, much of the data generated by radiologic imaging remains largely unspecific at a molecular level. The integration of these noninvasive imaging tools with functional genomic assays has the power for a quick clinical translation of high-throughput technology.

IMAGING FOR MOLECULAR ASSESSMENT OF TUMOR STAGING AND DIAGNOSIS

A study by Kuo *et al*[6] in patients with liver cancer demonstrated the relationship between imaging traits, histopathologic markers, and several predefined gene-expression programs. The study found that a liver-specific gene expression program was highly correlated with the imaging trait "tumor margin score, arterial phase". The data suggest that this radiophenotype could potentially form the basis to categorize hepatocellular carcinomas (HCCs).

Segal *et al*[4] also demonstrated that dynamic imaging traits in computed tomography (CT) strongly correlated with the global gene expression programs of primary HCC. The authors managed to reconstruct 78% of the gene expression profiles by combining twenty-eight imaging traits, thereby showing cell proliferation, liver synthetic function, and patient outcome. Therefore, noninvasive imaging could decode genomic activity of human liver cancers, allowing for a noninvasive, frequent and quick molecular work-up on an individual level.

In patients with glioblastoma multiforme (GBM) Zinn *et al*[7] introduced a new diagnostic imaging technique to assess molecular cancer subtypes and genomic correlates of cellular invasion using quantitative magnetic resonance imaging (MRI) volumetrics and large-scale gene- and microRNA expression profiling in GBM. Based on The Cancer Genome Atlas, discovery and validation sets with gene, microRNA, and quantitative

MRI data were created. Zinn *et al*[7] showed that in patients with GBM the used fluid-attenuated inversion recovery sequence reliably detected main cancer genomic components responsible for cellular migration and invasion. In addition it revealed genes and microRNAs highly associated with mesenchymal transformation and invasion. As cellular invasion is one of the main causes of treatment failure, the surgical extent of resection and adjuvant treatment planning are highly important. Thus, the authors conclude that the used method has potential therapeutic significance since successful molecular inhibition of invasion will improve therapy and patient survival in GBM.

In a recently published study in patients with GBM Jamshidi *et al*[8] could show that MRI, messenger RNA expression and DNA copy number variation can identify MR traits which are associated with some known high-grade glioma biomarkers and associated with genomic biomarkers that have been identified for other malignancies but not GBM. Further work is needed to determine the clinical value of these findings.

IMAGING FOR MOLECULAR ASSESSMENT OF TUMOR PROGNOSIS

Radiogenomic imaging is a useful tool for molecular assessment of tumor staging and diagnosis; however, for its success in a clinical setting it is crucial that radiogenomics has the potential to also impact clinical management. Despite much recent activity in developing imaging biomarkers of disease, it is challenging to link these biomarkers to clinical outcomes as it takes years to obtain these outcomes in cohort studies[9].

The above mentioned study by Kuo *et al*[6] in patients with HCC showed that the tumor margin score highly correlated with a venous invasion gene expression program as well as histologically-confirmed venous invasion.

A study by Diehn *et al*[5] sought to correlate imaging surrogates for gene-expression profiles with prognostic implications in patients with GBM. The radiogenomic maps showed a statistically significant overlap between a survival-associated gene signature and an infiltrative pattern of the edema on T2-weighted images. The hyperintense signal on the T2-weighted images allowed for a clear differentiation between edematous and infiltrative patterns reflecting the interface between a tumor and the adjacent normal brain. In a second part of the study another 110 GBMs were included; the results revealed a correlation between the infiltrative radiophenotype and a poor prognosis: a median survival of 390 d was found for those without infiltrative pattern compared to 216 for those with infiltrative pattern. The study shows a quick, easy-to-use technique to discover prognostic imaging biomarkers associated with underlying gene-expression signatures.

A study by Gevaert *et al*[9] explored the clinical prognostic value of Radiogenomic imaging by looking at features from non-small cell lung cancer (NSCLC) CT- and positron emission tomography (PET)-cases[10]. Gevaert *et al*[9] study comprised 26 patients with NSCLC whose imaging features were comprehensively extracted and statistically analyzed. To obtain survival data which were

not available the authors derived prognostic conclusions by using a genomically matched NSCLC case set with known clinical outcomes from public databases[11]. Gevaert *et al*[9] demonstrated an imaging approach able to quickly identify prognostically relevant image biomarkers requiring only the paired acquisition of image and gene expression data as well as the existence of a large public gene expression data set where survival outcomes are available. The authors conclude that by mapping image features to gene expression data, it is possible to leverage public gene expression microarray data to determine prognosis and therapeutic response as a function of image features.

In a follow-up study Nair *et al*[12] analyzed Nuclear factor-κB (NF-κB) protein expression in a group of 355 patients with NSCLC (365 tumor samples) with long-term follow-up by means of immunohistochemistry (IHC) using a Tissue Microarray.

NF-κBp65 as well as a positive uptake of fluorodeoxyglucose (FDG) was significantly associated with more advanced stage, tumor histology and invasion. Higher NF-κBp65 expression was associated with death by Kaplan Meier analysis ($P = 0.06$) while LDHA was strongly associated with recurrence ($P = 0.04$). Increased levels of combined NF-κBp65 and lactate dehydrogenase A (LDHA) expression were synergistic and associated with both recurrence ($P = 0.04$) and death ($P = 0.03$). The authors conclude that NF-κB IHC was a modest biomarker of prognosis that associated with tumor glucose metabolism on FDG PET when compared to existing molecular correlates like LDHA, which was synergistic with NF-κB for outcome.

IMAGING FOR MOLECULAR ASSESSMENT OF OPTIMAL THERAPY

By using an integrated imaging-genomic approach Kuo *et al*[6] determined whether contrast-enhanced CT was capable to assess imaging phenotypes which are associated with a doxorubicin drug response gene expression program in patients with HCC. The authors included 30 HCCs into the study and scored them individually across six predefined imaging phenotypes. An imaging phenotype related to tumor margins on arterial phase images showed a significant correlation with the doxorubicin-response transcriptional program ($P < 0.05$, $q < 0.1$). In addition it was significantly associated with HCC venous invasion and tumor stage ($P < 0.05$, $q < 0.1$). Tumors with higher tumor margin scores were more strongly associated with the doxorubicin resistance transcriptional program and had a greater prevalence of venous invasion and worse stage. Tumors with lower tumor margin scores, however, showed a converse relationship. The authors conclude that CT has the potential to identify HCC imaging phenotypes correlating with a doxorubicin drug response gene expression program. As doxorubicin is a standard treatment in regional therapies for patients with HCC, the used imaging strategy could be used to guide HCC therapy on a tumor-by-tumor basis on the basis of underlying tumor gene expression patterns.

The previously mentioned study by Diehn *et al*[5] also evaluated whether in patients with GBM the expression of a therapeutic target could be predicted based on its imaging-gene-expression association. Activation of specific gene-expression programs can be inferred from imaging traits, thereby giving insights into tumor biology on a tumor-by-tumor basis. The authors could reveal potential imaging biomarkers for several classes of anti-GBM therapeutic agents, including antiangiogenesis and epidermal growth factor receptor-based therapies. In addition, the results show that intratumoral heterogeneity of several gene-expression programs can be spatially resolved by means of imaging. Furthermore, the authors identified an imaging phenotype characterized by an infiltrative appearance that was associated with aggressive clinical behavior and expression of genes involved in central nervous system development and gliogenesis. As this imaging approach is noninvasive and widely available in clinical practice it can be applied to a broad range of human disease processes.

CONCLUSION

Radiogenomic imaging has the potential to catalyze the health system by creating imaging biomarkers that identify the genomics of a disease. The use of noninvasive imaging as a surrogate for gene expression profiling is a quick and reliable tool which has the potential to replace high-risk invasive biopsy procedures. Additional studies with larger numbers of patients are necessary to confirm links between gene expression patterns and imaging features permitting fast and reliable clinical diagnosis of tumors as well as estimation of prognosis and decision for optimal therapy.

REFERENCES

1 **Pao W**, Kris MG, Iafrate AJ, Ladanyi M, Jänne PA, Wistuba II, Miake-Lye R, Herbst RS, Carbone DP, Johnson BE, Lynch TJ. Integration of molecular profiling into the lung cancer clinic. *Clin Cancer Res* 2009; **15**: 5317-5322 [PMID: 19706816 DOI: 10.1158/1078-0432.CCR-09-0913]

2 **Gevaert O**, De Moor B. Prediction of cancer outcome using DNA microarray technology: past, present and future. *Expert Opin Med Diagn* 2009; **3**: 157-165 [PMID: 23485162 DOI: 10.1517/17530050802680172]

3 **Rutman AM**, Kuo MD. Radiogenomics: creating a link between molecular diagnostics and diagnostic imaging. *Eur J Radiol* 2009; **70**: 232-241 [PMID: 19303233 DOI: 10.1016/j.ejrad.2009.01.050]

4 **Segal E**, Sirlin CB, Ooi C, Adler AS, Gollub J, Chen X, Chan BK, Matcuk GR, Barry CT, Chang HY, Kuo MD. Decoding global gene expression programs in liver cancer by noninvasive imaging. *Nat Biotechnol* 2007; **25**: 675-680 [PMID: 17515910]

5 **Diehn M**, Nardini C, Wang DS, McGovern S, Jayaraman M, Liang Y, Aldape K, Cha S, Kuo MD. Identification of noninvasive imaging surrogates for brain tumor gene-expression modules. *Proc Natl Acad Sci USA* 2008; **105**: 5213-5218 [PMID: 18362333 DOI: 10.1073/pnas.0801279105]

6 **Kuo MD**, Gollub J, Sirlin CB, Ooi C, Chen X. Radiogenomic

analysis to identify imaging phenotypes associated with drug response gene expression programs in hepatocellular carcinoma. *J Vasc Interv Radiol* 2007; **18**: 821-831 [PMID: 17609439]

7 **Zinn PO**, Mahajan B, Sathyan P, Singh SK, Majumder S, Jolesz FA, Colen RR. Radiogenomic mapping of edema/cellular invasion MRI-phenotypes in glioblastoma multiforme. *PLoS One* 2011; **6**: e25451 [PMID: 21998659 DOI: 10.1371/journal.pone.0025451]

8 **Jamshidi N**, Diehn M, Bredel M, Kuo MD. Illuminating radiogenomic characteristics of glioblastoma multiforme through integration of MR imaging, messenger RNA expression, and DNA copy number variation. *Radiology* 2014; **270**: 1-2 [PMID: 24056404 DOI: 10.1148/radiol.13130078]

9 **Gevaert O**, Xu J, Hoang CD, Leung AN, Xu Y, Quon A, Rubin DL, Napel S, Plevritis SK. Non-small cell lung cancer: identifying prognostic imaging biomarkers by leveraging public gene expression microarray data--methods and preliminary results. *Radiology* 2012; **264**: 387-396 [PMID: 22723499 DOI: 10.1148/radiol.12111607]

10 **Jaffe CC**. Imaging and genomics: is there a synergy? *Radiology* 2012; **264**: 329-331 [PMID: 22821693 DOI: 10.1148/radiol.12120871]

11 **Parkinson H**, Sarkans U, Kolesnikov N, Abeygunawardena N, Burdett T, Dylag M, Emam I, Farne A, Hastings E, Holloway E, Kurbatova N, Lukk M, Malone J, Mani R, Pilicheva E, Rustici G, Sharma A, Williams E, Adamusiak T, Brandizi M, Sklyar N, Brazma A. ArrayExpress update--an archive of microarray and high-throughput sequencing-based functional genomics experiments. *Nucleic Acids Res* 2011; **39**: D1002-D1004 [PMID: 21071405 DOI: 10.1093/nar/gkq1040]

12 **Nair VS**, Gevaert O, Davidzon G, Plevritis SK, West R. NF-κB protein expression associates with (18)F-FDG PET tumor uptake in non-small cell lung cancer: a radiogenomics validation study to understand tumor metabolism. *Lung Cancer* 2014; **83**: 189-196 [PMID: 24355259 DOI: 10.1016/j.lungcan.2013.11.001]

P- Reviewer: Tang GH **S- Editor**: Qi Y
L- Editor: A **E- Editor**: Liu SQ

World Journal of Radiology

Submit a Manuscript: http://www.wjgnet.com/esps/
Help Desk: http://www.wjgnet.com/esps/helpdesk.aspx
DOI: 10.4329/wjr.v6.i8.523

World J Radiol 2014 August 28; 6(8): 523-529
ISSN 1949-8470 (online)

TOPIC HIGHLIGHT

WJR 6th Anniversary Special Issues (8): fMRI

Quantitative magnetic resonance imaging of the fetal brain in utero: Methods and applications

Anat Biegon, Chen Hoffmann

Anat Biegon, Department of Neurology and Radiology, School of Medicine, Stony Brook University, Stony Brook, NY 11794-2565, United States
Chen Hoffmann, Department of Diagnostic Imaging, Sheba Health Center, Ramat Gan 52622, Israel
Author contributions: Biegon A and Hoffmann C solely contributed to this paper.
Correspondence to: Anat Biegon, PhD, Professor of Neurology and Radiology, School of Medicine, Stony Brook University, 100 Nicols Rd, Stony Brook, NY 11794-2565, United States. anat.biegon@stonybrook.edu
Telephone: +1-631-6326228 Fax: +1-631-6326294
Received: February 9, 2014 Revised: April 24, 2014
Accepted: June 10, 2014
Published online: August 28, 2014

Abstract

Application of modern magnetic resonance imaging (MRI) techniques to the live fetus in utero is a relatively recent endeavor. The relative advantages and disadvantages of clinical MRI relative to the widely used and accepted ultrasonographic approach are the subject of a continuing debate; however the focus of this review is on the even younger field of quantitative MRI as applied to non-invasive studies of fetal brain development. The techniques covered under this header include structural MRI when followed by quantitative (*e.g.*, volumetric) analysis, as well as quantitative analyses of diffusion weighted imaging, diffusion tensor imaging, magnetic resonance spectroscopy and functional MRI. The majority of the published work reviewed here reflects information gathered from normal fetuses scanned during the 3rd trimester, with relatively smaller number of studies of pathological samples including common congenital pathologies such as ventriculomegaly and viral infection.

Key words: Fetal brain; Fetal magnetic resonance imaging; Fetal magnetic resonance spectroscopy; Fetal apparent diffusion coefficients; Fetal functional magnetic resonance imaging; Cortical development

Core tip: This review focuses on the budding field of quantitative magnetic resonance imaging and studies of the fetal brain designed to establish normative databases relevant to regional brain growth, connectivity and function and their application to a deeper understanding of the etiology, diagnosis and prognosis of fetal brain pathologies.

Biegon A, Hoffmann C. Quantitative magnetic resonance imaging of the fetal brain in utero: Methods and applications. *World J Radiol* 2014; 6(8): 523-529 Available from: URL: http://www.wjgnet.com/1949-8470/full/v6/i8/523.htm DOI: http://dx.doi.org/10.4329/wjr.v6.i8.523

INTRODUCTION

The history of fetal magnetic resonance imaging (MRI) in utero spans more than 3 decades, beginning with clinically driven T1 and T2 weighted studies at relatively low magnetic field published in the 1980's[1-4]. This was followed by early echo planar imaging of fetal brains attempted in the early 1990s[5,6]. Throughout this period, the mainstay of fetal imaging for all organ systems has been ultrasound, but the better contrast resolution of MRI relative to ultrasound made it especially attractive for studies of the central nervous system (CNS), which is relatively vulnerable to congenital anomalies. Progressive improvements in imaging hardware and software, resulting in shortened scan times and increasingly wider choice of imaging sequences, have made fetal brain MRI an increasingly valuable imaging tool in cases with uncertain

diagnosis of CNS abnormalities[7,8].

The biggest problem in acquiring reliable, reproducible and comprehensive MRI images of the fetal brain has been motion. Early studies attempted to overcome this problem by sedation of mother and/or fetus[9] although this approach has obviously limited the widespread use of the technique in clinical and research settings. The breakthrough came with the development of faster imaging techniques and sophisticated methods for motion correction[10-16]. The Ultrafast sequences which have been developed, including single shot fast spin echo, fast spin echo and the half fourier single shot turbo spin echo require a second or less per slice acquisition. In these studies multiple stacks of slices are acquired at different orthogonal orientations, providing a comprehensive view of the anatomy while allowing for manual adjustment to fetal motion or gating to maternal breathing. The most recent and ongoing developments in image reconstruction and motion correction methods[17-20] have enabled the adoption of all major MR approaches currently used in adults to in utero studies; including diffusion weighted imaging, tractography and MR spectroscopy[21-26] consequently enabling the gathering of unprecedented amounts of information on fetal brain development in utero.

This review focuses on the budding filed of quantitative MRI and studies of the fetal brain aiming at the establishment of normative databases relevant to normal regional brain growth, connectivity and function and their application to a deeper understanding of the etiology, diagnosis and prognosis of fetal brain pathologies.

QUANTIATIVE MRI IN THE STUDY OF NORMAL FETAL BRAIN DEVELOPMENT

Mapping regional and local patterns of normal fetal brain growth

An early study using the Cavalieri method to estimate whole brain volumes in a small cohort (n = 18) of third trimester fetuses[27] described a linear relationship between gestational age and whole brain volume, with a growth rate averaging 2.3 mL/d. The first study to measure volume changes in brain hemispheric parenchyma, cerebellum and ventricles of 27 normal, third trimester fetal brains[28] revealed different, non-linear growth trajectories for the three compartments, with a faster growth of cerebral hemispheres relative to cerebellum and a steady decrease in the ventricular/parenchymal volume with increasing gestational age. Subsequent work by Gholipour *et al*[29] using supervised automated segmentation of brain volumes in fetuses aged 19 to 37 wk compared linear and non linear models and concluded that a quadratic model provided the best fit to the data describing the changes of fetal brain volume with gestational age. Hu *et al*[30] also confirmed that the growth rates of the cerebral volumes are region-dependent, with the frontal and parieto-temporal regions growing significantly faster than other regions. More recent studies have added substantial amount of detail on normal fetal brain growth, with the publication of a spatiotemporal atlas of MR intensity, tissue probability and shape of the fetal brain[31] and detailed descriptions of the growth of the fetal subplate and other regions[32,33]. Corbett-Detig *et al*[32] examined subplate growth in relatively young (18-24 wk old) fetuses and found that the occipital pole, ventral occipitotemporal region, and planum temporale underwent the most statistically significant increases in subplate thickness, while the thickest region during this period was the developing somatosensory/motor cortex.

A more detailed study of volumetric changes in the growing fetal brain was published by Scott *et al*[33] examining volumes of cortical plate, subplate and intermediate zone, germinal matrix, deep gray nuclei, and ventricles from automatic segmentation of motion-corrected, 3D reconstructed MRI scans from 39 normally developing fetuses at gestational age (GA) ranging from 21 to 31. The findings again show region-specific growth trajectories, with the cortical plate having the highest growth rate (18%/wk).

The supratentorial volume, subplate and intermediate zone, germinal matrix and deep gray nuclei exhibited similar growth rates of approximately 15%/wk while the slowest growth rate was found for ventricles (9.2%/wk). Interestingly, the authors did not find sex differences or asymmetries in hemispheric volumes. This could be a group size/power issue but may also indicate that such difference only emerge later in brain development.

Quantitative studies of cortical folding

Hu *et al*[34] provided a regional quantification of cortical shape development from a group of normal fetuses in the gestational age range of 22-33 wk. They report faster shape changes in the occipital lobe than in other regions and conserved patterns of shape changes in gyri and sulci, whereby the gyral surface smoothens, while the sulcal surface becomes more angular, with gestational age. In addition, the authors report that smoothing of gyri is related mainly to the changes in shape of gyral crowns.

Clouchoux *et al*[35] examined *in vivo* fetal cortical folding patterns in healthy fetuses between 25 and 35 wk gestation, providing an explicit delineation of the sulcal pattern as well as surface area and gyrification index. The findings suggest an exuberant third trimester gyrification process and a non-linear evolution of sulcal development.

Employing a younger group (GA 20-28 wk) of fetuses, Habas *et al*[36] and Rajagopalan *et al*[37] have been able to detect early folding patterns and asymmetries in fetal brain development. Their Tensor based morphometry results show that fetal brain development exhibits a distinct spatial pattern of anisotropic growth, with the most significant changes in the directionality of growth occurring in the cortical plate at major sulci. The authors also report significant directional growth asymmetry in the peri-sylvian region and the medial frontal lobe of the

fetal brain.

Studies of water diffusion in the normal developing brain

Regional differences and developmental changes in apparent diffusion coefficients (ADC) have been the subject of several studies conducted and published during the last decade[23,38-47]. All of the published studies report absolute values for ADC in a similar range and detect a trend towards a reduction in ADC with increased GA, which could be explained by progressive myelination. However, the relationship between ADC and GA appears to be region-dependent and non-linear. Thus, whether a specific study reports on significant changes of ADC with GA appears to depend on the range of developmental ages and regions included in the analysis. To illustrate, Righini *et al*[38] reported a mean ADC value of 1.96 ± 0.1 microm^2/ms (SD) in frontal white matter, 1.95 ± 0.1 microm^2/ms in occipital white matter, and 1.56 ± 0.1 microm^2/ms in basal ganglia of fetuses aged 22-35 wk, with a significant negative correlation between ADC and gestational age for basal ganglia, and only a trend for frontal white matter. A subsequent study by another group involving fetuses between 31 and 37 wk gestation[39] reported mean ADC values of 1.8 microm^2/ms in the centrum semiovale, 1.2 microm^2/ms in the splenium of the corpus callosum and 1.1 microm^2/ms in the pyramidal tract, with mean fractional anisotropy (FA) values of 1.1%, 3.8% and 4.7%, respectively. The authors report a significant age-related decrease in ADC and an increase in FA in the pyramidal tract and corpus callosum. Manganaro *et al*[40] measured ADC in the grey matter, reporting mean ADC values from 1.76 × 10^{-3} mm^2/s (at week 19) to 0.89 × 10^{-3} mm^2/s (at week 37), whereas in the white matter, the values varied from 2.03 × 10^{-3} mm^2/s (at week 19) to 1.25 × 10^{-3} mm^2/s (at week 37). Cartry *et al*[42] reported a linear inverse correlation existed between ADC values and gestational age only in the occipital lobes of 22 normal fetuses scanned between 30 and 34 wk gestation. This theme of region-dependent developmental changes in ADC is reiterated in the largest and most recent study of this kind, where Boyer *et al*[43] described a study of 50 normal fetuses between 19 and 37 wk gestation. The authors report that ADC values remained constant in the basal ganglia, frontal, parietal, temporal and occipital white matter and in the centrum semiovale while significant decreases were observed in the cerebellum, pons and thalamus with advancing menstrual age.

Development of regional connectivity

Tractography presents a bigger challenge for in utero fetal imaging relative to other techniques since acquisition times are longer and therefore studies are more susceptible to motion artifacts[21-23]. Consequently, only a few recent studies provide quantitative data from in utero studies of neuronal pathways. Kasprian *et al*[23] examined a group of fetuses ranging in age from 18 to 37 wk and reported that only in 40% of examined fetuses, diffusion tensor imaging measurements were robust enough to successfully calculate and visualize bilateral, craniocaudally oriented (mainly sensorimotor), and callosal trajectories in utero. However, the successful studies resulted in a wealth of quantitative information on fiber lengths, ADC, FA, and eigenvalues at different anatomically defined areas. FA values and the axial eigenvalue [lambda(1)] showed a characteristic distribution, with the highest values for the splenium, followed by the genu, the right and the left posterior limb of the internal capsule. Intriguing evidence for early asymmetry was also obtained, showing that the right-sided sensorimotor trajectories were significantly longer than on the left side, reflecting higher right-sided lambda(1) values.

A more recent publications from the same group[44] reports on successful visualization and delineation of sensorimotor tracts and the corpus callosum as well as smaller fiber bundles, separating the internal capsule fibers into thalamocortical fibers, corticopontine and corticospinal tracts and segregating the thalamocortical fiber system to anterior, superior and posterior radiations. Association fiber tracts connecting ipsilateral cortical areas were also successfully visualized.

Development of brain chemistry using MR spectroscopy

Development of the normal fetal brain in utero using MR spectroscopy (MRS) has been studied by a number of groups. The size of the voxel necessary to acquire reliable information limits the possibility of regional measurements, so these studies mostly reflect whole brain maturation. With this caveat, levels of choline (Cho), creatine (Cr), myo-inositol (Myo-ins) and N-acetyl aspartate (NAA) have been measured in utero in fetuses in the age range of 22 to 41 wk[26,45-48]. Kok *et al*[45] found no change in the absolute level of Cr using an echo time of 135 ms with 35 fetuses between 30 and 41 wk. In a later study[46], the group reported absolute tissue levels of these metabolites resemble values measured in preterm and term babies, especially of relatively more mature brain regions, from which most of the MR spectra have been obtained. Brain maturation between 30 and 41 wk of gestation was most clearly reflected by increasing levels of the neuronal marker NAA. Subsequent studies by Girard *et al*[47,48] confirmed that by 34 wk the fetal brain spectrum is comparable to that of a term born neonate, with dominant resonances of Cho, Cr and NAA at a long echo time and Myo-ins, Cho, Cr and NAA dominant resonances at a short echo time. The authors further report that creatine and phosphocreatine, compounds involved in energy metabolism, both contribute to the Cr peak. In a study of 58 fetuses with a gestational age range of 22-39 wk, the authors reported that Cr levels increased in the fetal brain with increasing gestational age. However, this was only found at a short echo time (30 ms) and not at a longer echo time (135 ms).

Imaging developing brain function: Functional MRI

The feasibility of studying fetal brain activity with functional MRI was demonstrated by Hykin *et al*[49] just be-

fore the turn of the century, reporting on responses to maternal speech. This was followed by additional studies reporting the detection of responses to visual[50] and various auditory[51-54] stimuli, which were detected between 33 and 34 wk of gestation. Functional connectivity (FC) at rest was subsequently investigated by Schöpf *et al*[55] in fetuses from 20 to 36 gestational weeks of age. The authors report a bilateral occipital network and medial and lateral prefrontal activity pattern that involved the future Brodmann areas 9-11 and a hemispheric lateralized network that involved the superior temporal cortical regions (Brodmann areas 22 and 39). Frequency oscillations were in the range of 0.01-0.06 Hz for all networks. Thomason *et al*[56] studied 25 healthy human fetuses in the second and third trimesters of pregnancy (24 to 38 wk of gestation) and reported the presence of bilateral fetal brain FC as well as regional and age-related variation in the strength of FC between homologous cortical brain regions, which increased with advancing gestational age. The authors also observed medial to lateral gradients in fetal functional brain connectivity. Sørensen *et al*[57] examined the fetal blood oxygen level dependent response to maternal hyperoxia, demonstrating an increased oxygenation in a number of human fetal organs while oxygenation of the fetal brain remained constant. These studies, together with findings from other modalities like fetal electroencephalography and magnetoencencephalography[58] are truly revolutionary since unlike information on maturation of brain morphology and microstructure/chemistry which can be obtained postmortem, the development of function can only be studied *in vivo*.

QUANTIATIVE MRI IN THE STUDY OF FETAL BRAIN PATHOLOGY

Fetal ventriculomegaly/hydrocephalus

The first quantitative MRI studies in ventriculomegaly (VM) employed magentic resonance spectroscopy[59,60]. Kok *et al*[59] performed ^{1}HMRS of the brain in 10 fetuses with ventricular dilatation and 36 normal fetuses between 28 and 37 wk and found that the inositol: Cr ratio was significantly lower in fetuses with hydrocephalus. Roelants-van Rijn *et al*[60] examined the brain of six fetuses with ventricular dilation and were able to detect the presence of Lactate (Lac) in two of the six fetuses, two had no Lac and two spectra were un-interpretable due to contaminating lipid peaks.

The first study applying quantitative MRI to the comparison of ventricular and parenchymal volumes in cases referred because of VM and normal controls revealed that fetal VM is not associated with decreases in parenchymal volume[28]. Using conventional T1- and T2-weighted imaging, Erdem *et al*[61] also found that hydrocephalic fetuses had a normal signal pattern in cerebral parenchyma, but their ADC values, derived from diffusion weighted imaging, were significantly lower than those reported for fetuses with normal brain. The largest volumetric study of VM published to date[62], which included postnatal outcomes in more than 300 fetuses, revealed that ventricular, but not parenchymal, volume was a significant predictor of live birth. The association was stronger in isolated VM relative to VM with other anomalies present. Most recently, the absence of changes in parenchymal volume was confirmed in a cohort of mild isolated VM using motion-corrected 3D reconstruction and automatic segmentation[63].

Congenital cytomegalo virus infection

A recently published study[64] examined the maturation of hemispheric and temporal lobe volumes in 27 congenital cytomegalo virus (CMV) infected fetuses relative to GA-matched normal controls, all scanned during the third trimester. Temporal lobe volumes, normalized to whole brain and co-varied with gestational age; were significantly smaller in fetuses infected with CMV compared to uninfected fetuses. Furthermore, Infection during the 1st and 2nd trimester had a more pronounced effect than infection during the 3rd trimester. While Infected fetuses with no MRI findings had significantly lower temporal lobe/whole brain ratios than controls, the lowest temporal lobe/forebrain ratios were observed in fetuses with CMV as well as overt findings such as cysts or gray matter heterotopy. These findings suggest a regional vulnerability to maternal immune activation in the fetal brain, although the relationship between the results and neurological outcome still needs to be established.

Congenital heart disease

Limperopoulos *et al*[65] compared brain volume and metabolism in 55 fetuses with Congenital heart disease (CHD) and 50 normal fetuses (gestational age range 25-37 wk) with the use of 3-dimensional volumetric MRI and proton MRS. they found progressive and significant declines in gestational age-adjusted total brain volume and intracranial cavity volume in CHD fetuses relative to controls, as well as a significantly slower increase in the NAA:Cho ratio. Predictors of lower NAA:Cho included diagnosis, absence of anterograde aortic arch flow, and evidence of cerebral lactate. In a subsequent study[66] of 18 fetuses with hypoplastic left heart syndrome (HLHS, a severe form of congenital heart disease) and 30 control fetuses in the same age range, the authors found a progressive fall-off in cortical gray and white matter volumes as well as subcortical gray matter in fetuses with HLHS. These fetuses also showed significant delays in cortical gyrification, whereby local cortical folding delays were detected as early as 25 wk in the frontal, parietal, calcarine, temporal, and collateral regions and appeared to precede volumetric brain growth disturbances.

Intrauterine growth restriction

Quantitative studies of fetal organ growth in intrauterine growth restriction (IUGR) confirmed the expected relative sparing of the brain. Damodaram *et al*[67] measured peripheral organs and brain volumes in 20 growth restricted and 19 normal fetuses scanned at gestational age

21-37 wk and found a significant reduction in fetal whole body volume and volume of all internal organs except the brain. A brain:liver ratio above 3.0 was associated with a 3.3 fold increase in risk of perinatal mortality. Interestingly, an MRS study[68] detected a lactate peak in the brain of the most severely affected IUGR fetus which was consistent with low oxygen content and high lactic acid concentration in umbilical blood obtained at delivery.

Ischemic stroke

The likelihood of detecting acute hypoxic-ischemic brain lesions by prenatal magnetic resonance imaging is small. However, a published case study[69] reports on a fetus with a vein of Galen arteriovenous malformation in whom prenatal diffusion-weighted magnetic resonance imaging at 33 wk of gestation clearly detected cerebral acute ischemic lesions, associated with remarkable decrease of the average apparent diffusion coefficient.

Environmental toxicity

Quantitative MRI is uniquely suitable for the study of the effects of exposure of pregnant women to environmental toxins and drugs on fetal brain development. A recent study by Anblagan *et al*[70] reported on the effects of maternal smoking during pregnancy on fetal organ growth in 13 smokers and 13 non-smokers examined at 22-27 wk and again at 33-38 wk of gestation. Exposed fetuses showed lower brain volumes at both time points, and the effect size was larger in the 2nd visit, closer to the end of gestation.

CONCLUSION

The adaptation of quantitative MRI techniques to fetal brain imaging in utero is truly revolutionary, embodying the potential to transform this area of basic and clinical research and practice from the subjective, qualitative and arbitrarily dichotomous identification of "lesions" and "abnormalities" to the much richer and promising domain of objective, continuous measurements of salient parameters reflecting different morphological, microstructural and biochemical aspects of brain maturation. It is fair to say that if fetal MRI is in its infancy, quantitative fetal MRI is in its embryonic developmental stage, undergoing an explosive phase of methods development, fine-tuning and validation. Consequently, the majority of the published work reviewed here reflects information gathered from relatively small cohorts of normal fetuses scanned during the 3rd trimester, and the relatively smaller number of studies of pathological samples to date offer very limited or no postnatal follow-up. Further improvements in methodology and safety are needed before these studies can be extended to earlier fetal ages, affording a comprehensive view of fetal brain development in utero. The progressive accumulation of normative data bases and extended postnatal follow-up are essential prerequisite for the future use of quantitative MRI in the diagnosis, prognosis and prenatal treatment[71] of congenital brain disorders.

REFERENCES

1 **Smith FW**, Adam AH, Phillips WD. NMR imaging in pregnancy. *Lancet* 1983; **1**: 61-62 [PMID: 6129387]
2 **Thickman D**, Mintz M, Mennuti M, Kressel HY. MR imaging of cerebral abnormalities in utero. *J Comput Assist Tomogr* 1984; **8**: 1058-1061 [PMID: 6389620]
3 **McCarthy SM**, Filly RA, Stark DD, Hricak H, Brant-Zawadzki MN, Callen PW, Higgins CB. Obstetrical magnetic resonance imaging: fetal anatomy. *Radiology* 1985; **154**: 427-432 [PMID: 3966129]
4 **Williamson RA**, Weiner CP, Yuh WT, Abu-Yousef MM. Magnetic resonance imaging of anomalous fetuses. *Obstet Gynecol* 1989; **73**: 952-956 [PMID: 2657526]
5 **Mansfield P**, Stehling MK, Ordidge RJ, Coxon R, Chapman B, Blamire A, Gibbs P, Johnson IR, Symonds EM, Worthington BS. Echo planar imaging of the human fetus in utero at 0.5 T. *Br J Radiol* 1990; **63**: 833-841 [PMID: 2252974 DOI: 10.1259/0007-1285-63-755-833]
6 **Johnson IR**, Stehling MK, Blamire AM, Coxon RJ, Howseman AM, Chapman B, Ordidge RJ, Mansfield P, Symonds EM, Worthington BS. Study of internal structure of the human fetus in utero by echo-planar magnetic resonance imaging. *Am J Obstet Gynecol* 1990; **163**: 601-607 [PMID: 2386150]
7 **De Wilde JP**, Rivers AW, Price DL. A review of the current use of magnetic resonance imaging in pregnancy and safety implications for the fetus. *Prog Biophys Mol Biol* 2005; **87**: 335-353 [PMID: 15556670]
8 **Paladini D**, Quarantelli M, Sglavo G, Pastore G, Cavallaro A, D'Armiento, Salvatore M, Nappi C. The role of MRI in the clinical management of foetuses with central nervous system abnormalities in a tertiary referral center. *Ultrasound Obstet Gynecol* 2014; **44**: 188-196 [DOI: 10.1002/uog.13243]
9 **Daffos F**, Forestier F, Mac Aleese J, Aufrant C, Mandelbrot L, Cabanis EA, Iba-Zizen MT, Alfonso JM, Tamraz J. Fetal curarization for prenatal magnetic resonance imaging. *Prenat Diagn* 1988; **8**: 312-314 [PMID: 2969509]
10 **Haase A**, Frahm J, Matthaei D, Hänicke W, Merboldt KD. FLASH imaging: rapid NMR imaging using low flip-angle pulses. 1986. *J Magn Reson* 2011; **213**: 533-541 [PMID: 22152368 DOI: 10.1016/0022-2364(86)90433-6]
11 **Kubik-Huch RA**, Huisman TA, Wisser J, Gottstein-Aalame N, Debatin JF, Seifert B, Ladd ME, Stallmach T, Marincek B. Ultrafast MR imaging of the fetus. *AJR Am J Roentgenol* 2000; **174**: 1599-1606 [PMID: 10845491]
12 **Busse RF**, Riederer SJ, Fletcher JG, Bharucha AE, Brandt KR. Interactive fast spin-echo imaging. *Magn Reson Med* 2000; **44**: 339-348 [PMID: 10975883 DOI: 10.1002/1522-2594(200009)44:3<339::AID-MRM1>3.0.CO;2-N]
13 **Rousseau F**, Glenn OA, Iordanova B, Rodriguez-Carranza C, Vigneron DB, Barkovich JA, Studholme C. Registration-based approach for reconstruction of high-resolution in utero fetal MR brain images. *Acad Radiol* 2006; **13**: 1072-1081 [PMID: 16935719]
14 **Bonel H**, Frei KA, Raio L, Meyer-Wittkopf M, Remonda L, Wiest R. Prospective navigator-echo-based real-time triggering of fetal head movement for the reduction of artifacts. *Eur Radiol* 2008; **18**: 822-829 [PMID: 18075742]
15 **Kim K**, Hansen MF, Habas PA, Rousseau F, Glenn OA, Barkovich AJ, Studholme C. Intersection-based registration of slice stacks to form 3D images of the human fetal brain. IEEE International Symposium on Biomedical Imaging: From Nano to Macro, 2008: 1167-1170
16 **Jiang S**, Xue H, Counsell S, Anjari M, Allsop J, Rutherford M, Rueckert D, Hajnal JV. Diffusion tensor imaging (DTI) of the brain in moving subjects: application to in-utero fetal and ex-utero studies. *Magn Reson Med* 2009; **62**: 645-655 [PMID: 19526505 DOI: 10.1002/mrm.22032]
17 **Kim K**, Habas PA, Rousseau F, Glenn OA, Barkovich AJ, Studholme C. Intersection based motion correction of multislice MRI for 3-D in utero fetal brain image formation. *IEEE*

Trans Med Imaging 2010; **29**: 146-158 [PMID: 19744911 DOI: 10.1109/TMI.2009.2030679]
18 **Kim K**, Habas PA, Rousseau F, Glenn OA, Barkovich AJ, Studholme C. Reconstruction of a geometrically correct diffusion tensor image of a moving human fetal brain. Proceedings Medical Imaging 2010: Image Processing, 2010: 7623 [DOI: 10.1117/12.844542]
19 **Malamateniou C**, Malik SJ, Counsell SJ, Allsop JM, McGuinness AK, Hayat T, Broadhouse K, Nunes RG, Ederies AM, Hajnal JV, Rutherford MA. Motion-compensation techniques in neonatal and fetal MR imaging. *AJNR Am J Neuroradiol* 2013; **34**: 1124-1136 [PMID: 22576885]
20 **Griffiths PD**, Jarvis D, McQuillan H, Williams F, Paley M, Armitage P. MRI of the foetal brain using a rapid 3D steady-state sequence. *Br J Radiol* 2013; **86**: 20130168 [PMID: 24043616 DOI: 10.1259/bjr.20130168]
21 **Studholme C**. Mapping fetal brain development in utero using magnetic resonance imaging: the Big Bang of brain mapping. *Annu Rev Biomed Eng* 2011; **13**: 345-368 [PMID: 21568716 DOI: 10.1146/annurev-bioeng-071910-124654]
22 **Hüppi PS**, Dubois J. Diffusion tensor imaging of brain development. *Semin Fetal Neonatal Med* 2006; **11**: 489-497 [PMID: 16962837 DOI: 10.1016/j.siny.2006.07.006]
23 **Kasprian G**, Brugger PC, Weber M, Krssák M, Krampl E, Herold C, Prayer D. In utero tractography of fetal white matter development. *Neuroimage* 2008; **43**: 213-224 [PMID: 18694838 DOI: 10.1016/j.neuroimage.2008.07.026]
24 **Saleem SN**. Fetal magnetic resonance imaging (MRI): a tool for a better understanding of normal and abnormal brain development. *J Child Neurol* 2013; **28**: 890-908 [PMID: 23644716 DOI: 10.1177/0883073813486296]
25 **Hüppi PS.** Cortical development in the fetus and the newborn: advanced MR techniques. *Top Magn Reson Imaging* 2011; **22:** 33-38 [DOI: 10.1097/RMR.0b013e3182416f78]
26 **Story L**, Damodaram MS, Allsop JM, McGuinness A, Wylezinska M, Kumar S, Rutherford MA. Proton magnetic resonance spectroscopy in the fetus. *Eur J Obstet Gynecol Reprod Biol* 2011; **158**: 3-8 [PMID: 20413207 DOI: 10.1016/j.ejogrb.2010.03.003]
27 **Gong QY**, Roberts N, Garden AS, Whitehouse GH. Fetal and fetal brain volume estimation in the third trimester of human pregnancy using gradient echo MR imaging. *Magn Reson Imaging* 1998; **16**: 235-240 [PMID: 9621964]
28 **Grossman R**, Hoffman C, Mardor Y, Biegon A. Quantitative MRI measurements of human fetal brain development in utero. *Neuroimage* 2006; **33**: 463-470 [PMID: 16938471]
29 **Gholipour A**, Estroff JA, Barnewolt CE, Connolly SA, Warfield SK. Fetal brain volumetry through MRI volumetric reconstruction and segmentation. *Int J Comput Assist Radiol Surg* 2011; **6**: 329-339 [PMID: 20625848 DOI: 10.1007/s11548-010-0512-x]
30 **Hu HH**, Guo WY, Chen HY, Wang PS, Hung CI, Hsieh JC, Wu YT. Morphological regionalization using fetal magnetic resonance images of normal developing brains. *Eur J Neurosci* 2009; **29**: 1560-1567 [PMID: 19419421 DOI: 10.1111/j.1460-9568.2009.06707.x]
31 **Habas PA**, Kim K, Corbett-Detig JM, Rousseau F, Glenn OA, Barkovich AJ, Studholme C. A spatiotemporal atlas of MR intensity, tissue probability and shape of the fetal brain with application to segmentation. *Neuroimage* 2010; **53**: 460-470 [PMID: 20600970 DOI: 10.1016/j.neuroimage.2010.06.054]
32 **Corbett-Detig J**, Habas PA, Scott JA, Kim K, Rajagopalan V, McQuillen PS, Barkovich AJ, Glenn OA, Studholme C. 3D global and regional patterns of human fetal subplate growth determined in utero. *Brain Struct Funct* 2011; **215**: 255-263 [PMID: 21046152 DOI: 10.1007/s00429-010-0286-5]
33 **Scott JA**, Habas PA, Kim K, Rajagopalan V, Hamzelou KS, Corbett-Detig JM, Barkovich AJ, Glenn OA, Studholme C. Growth trajectories of the human fetal brain tissues estimated from 3D reconstructed in utero MRI. *Int J Dev Neurosci* 2011; **29**: 529-536 [PMID: 21530634 DOI: 10.1016/j.ijdevneu.2011.04.001]
34 **Hu HH**, Hung CI, Wu YT, Chen HY, Hsieh JC, Guo WY. Regional quantification of developing human cortical shape with a three-dimensional surface-based magnetic resonance imaging analysis in utero. *Eur J Neurosci* 2011; **34**: 1310-1319 [PMID: 21995768 DOI: 10.1111/j.1460-9568.2011.07855.x]
35 **Clouchoux C**, Kudelski D, Gholipour A, Warfield SK, Viseur S, Bouyssi-Kobar M, Mari JL, Evans AC, du Plessis AJ, Limperopoulos C. Quantitative in vivo MRI measurement of cortical development in the fetus. *Brain Struct Funct* 2012; **217**: 127-139 [PMID: 21562906 DOI: 10.1007/s00429-011-0325-x]
36 **Habas PA**, Scott JA, Roosta A, Rajagopalan V, Kim K, Rousseau F, Barkovich AJ, Glenn OA, Studholme C. Early folding patterns and asymmetries of the normal human brain detected from in utero MRI. *Cereb Cortex* 2012; **22**: 13-25 [PMID: 21571694 DOI: 10.1093/cercor/bhr053]
37 **Rajagopalan V**, Scott J, Habas PA, Kim K, Rousseau F, Glenn OA, Barkovich AJ, Studholme C. Mapping directionality specific volume changes using tensor based morphometry: an application to the study of gyrogenesis and lateralization of the human fetal brain. *Neuroimage* 2012; **63**: 947-958 [PMID: 22503938 DOI: 10.1016/j.neuroimage.2012.03.092]
38 **Righini A**, Bianchini E, Parazzini C, Gementi P, Ramenghi L, Baldoli C, Nicolini U, Mosca F, Triulzi F. Apparent diffusion coefficient determination in normal fetal brain: a prenatal MR imaging study. *AJNR Am J Neuroradiol* 2003; **24**: 799-804 [PMID: 12748074]
39 **Bui T**, Daire JL, Chalard F, Zaccaria I, Alberti C, Elmaleh M, Garel C, Luton D, Blanc N, Sebag G. Microstructural development of human brain assessed in utero by diffusion tensor imaging. *Pediatr Radiol* 2006; **36**: 1133-1140 [PMID: 16960686]
40 **Manganaro L**, Perrone A, Savelli S, Di Maurizio M, Maggi C, Ballesio L, Porfiri LM, De Felice C, Marinoni E, Marini M. Evaluation of normal brain development by prenatal MR imaging. *Radiol Med* 2007; **112**: 444-455 [PMID: 17440691]
41 **Schneider JF**, Confort-Gouny S, Le Fur Y, Viout P, Bennathan M, Chapon F, Fogliarini C, Cozzone P, Girard N. Diffusion-weighted imaging in normal fetal brain maturation. *Eur Radiol* 2007; **17**: 2422-2429 [PMID: 17404738]
42 **Cartry C**, Viallon V, Hornoy P, Adamsbaum C. [Diffusion-weighted MR imaging of the normal fetal brain: marker of fetal brain maturation]. *J Radiol* 2010; **91**: 561-566 [PMID: 20657355]
43 **Boyer AC**, Gonçalves LF, Lee W, Shetty A, Holman A, Yeo L, Romero R. Magnetic resonance diffusion-weighted imaging: reproducibility of regional apparent diffusion coefficients for the normal fetal brain. *Ultrasound Obstet Gynecol* 2013; **41**: 190-197 [PMID: 22744761 DOI: 10.1002/uog.11219]
44 **Mitter C**, Kasprian G, Brugger PC, Prayer D. Three-dimensional visualization of fetal white-matter pathways in utero. *Ultrasound Obstet Gynecol* 2011; **37**: 252-253 [PMID: 21264986 DOI: 10.1002/uog.8899]
45 **Kok RD**, van den Berg PP, van den Bergh AJ, Nijland R, Heerschap A. Maturation of the human fetal brain as observed by 1H MR spectroscopy. *Magn Reson Med* 2002; **48**: 611-616 [PMID: 12353277 DOI: 10.1002/mrm.10264]
46 **Heerschap A**, Kok RD, van den Berg PP. Antenatal proton MR spectroscopy of the human brain in vivo. *Childs Nerv Syst* 2003; **19**: 418-421 [PMID: 12811484]
47 **Girard N**, Gouny SC, Viola A, Le Fur Y, Viout P, Chaumoitre K, D'Ercole C, Gire C, Figarella-Branger D, Cozzone PJ. Assessment of normal fetal brain maturation in utero by proton magnetic resonance spectroscopy. *Magn Reson Med* 2006; **56**: 768-775 [PMID: 16964617 DOI: 10.1002/mrm.21017]
48 **Girard N**, Fogliarini C, Viola A, Confort-Gouny S, Fur YL, Viout P, Chapon F, Levrier O, Cozzone P. MRS of normal and impaired fetal brain development. *Eur J Radiol* 2006; **57**: 217-225 [PMID: 16387464]
49 **Hykin J**, Moore R, Duncan K, Clare S, Baker P, Johnson I, Bowtell R, Mansfield P, Gowland P. Fetal brain activity dem-

onstrated by functional magnetic resonance imaging. *Lancet* 1999; **354**: 645-646 [PMID: 10466668]
50 **Fulford J**, Vadeyar SH, Dodampahala SH, Moore RJ, Young P, Baker PN, James DK, Gowland PA. Fetal brain activity in response to a visual stimulus. *Hum Brain Mapp* 2003; **20**: 239-245 [PMID: 14673807 DOI: 10.1002/hbm.10139]
51 **Fulford J**, Vadeyar SH, Dodampahala SH, Ong S, Moore RJ, Baker PN, James DK, Gowland P. Fetal brain activity and hemodynamic response to a vibroacoustic stimulus. *Hum Brain Mapp* 2004; **22**: 116-121 [PMID: 15108299 DOI: 10.1002/hbm.20019]
52 **Moore RJ**, Vadeyar S, Fulford J, Tyler DJ, Gribben C, Baker PN, James D, Gowland PA. Antenatal determination of fetal brain activity in response to an acoustic stimulus using functional magnetic resonance imaging. *Hum Brain Mapp* 2001; **12**: 94-99 [PMID: 11169873 DOI: 10.1002/1097-0193(200102)12:2<94::AID-HBM1006>3.0.CO;2-E]
53 **Jardri R**, Pins D, Houfflin-Debarge V, Chaffiotte C, Rocourt N, Pruvo JP, Steinling M, Delion P, Thomas P. Fetal cortical activation to sound at 33 weeks of gestation: a functional MRI study. *Neuroimage* 2008; **42**: 10-18 [PMID: 18539048 DOI: 10.1016/j.neuroimage.2008.04.247]
54 **Jardri R**, Houfflin-Debarge V, Delion P, Pruvo JP, Thomas P, Pins D. Assessing fetal response to maternal speech using a noninvasive functional brain imaging technique. *Int J Dev Neurosci* 2012; **30**: 159-161 [PMID: 22123457 DOI: 10.1016/j.ijdevneu.2011.11.002]
55 **Schöpf V**, Kasprian G, Brugger PC, Prayer D. Watching the fetal brain at 'rest'. *Int J Dev Neurosci* 2012; **30**: 11-17 [PMID: 22044604 DOI: 10.1016/j.ijdevneu.2011.10.006]
56 **Thomason ME**, Dassanayake MT, Shen S, Katkuri Y, Alexis M, Anderson AL, Yeo L, Mody S, Hernandez-Andrade E, Hassan SS, Studholme C, Jeong JW, Romero R. Cross-hemispheric functional connectivity in the human fetal brain. *Sci Transl Med* 2013; **5**: 173ra24 [PMID: 23427244 DOI: 10.1126/scitranslmed.3004978]
57 **Sørensen A**, Peters D, Simonsen C, Pedersen M, Stausbøl-Grøn B, Christiansen OB, Lingman G, Uldbjerg N. Changes in human fetal oxygenation during maternal hyperoxia as estimated by BOLD MRI. *Prenat Diagn* 2013; **33**: 141-145 [PMID: 23233459 DOI: 10.1002/pd.4025]
58 **Anderson AL**, Thomason ME. Functional plasticity before the cradle: a review of neural functional imaging in the human fetus. *Neurosci Biobehav Rev* 2013; **37**: 2220-2232 [PMID: 23542738 DOI: 10.1016/j.neubiorev.2013.03.013]
59 **Kok RD**, Steegers-Theunissen RP, Eskes TK, Heerschap A, van den Berg PP. Decreased relative brain tissue levels of inositol in fetal hydrocephalus. *Am J Obstet Gynecol* 2003; **188**: 978-980 [PMID: 12712096]
60 **Roelants-van Rijn AM**, Groenendaal F, Stoutenbeek P, van der Grond J. Lactate in the foetal brain: detection and implications. *Acta Paediatr* 2004; **93**: 937-940 [PMID: 15303809 DOI: 10.1111/j.1651-2227.2004.tb02692.x]
61 **Erdem G**, Celik O, Hascalik S, Karakas HM, Alkan A, Firat AK. Diffusion-weighted imaging evaluation of subtle cerebral microstructural changes in intrauterine fetal hydrocephalus. *Magn Reson Imaging* 2007; **25**: 1417-1422 [PMID: 17513078]
62 **Pier DB**, Levine D, Kataoka ML, Estroff JA, Werdich XQ, Ware J, Beeghly M, Poussaint TY, Duplessis A, Li Y, Feldman HA. Magnetic resonance volumetric assessments of brains in fetuses with ventriculomegaly correlated to outcomes. *J Ultrasound Med* 2011; **30**: 595-603 [PMID: 21527607]
63 **Scott JA**, Habas PA, Rajagopalan V, Kim K, Barkovich AJ, Glenn OA, Studholme C. Volumetric and surface-based 3D MRI analyses of fetal isolated mild ventriculomegaly: brain morphometry in ventriculomegaly. *Brain Struct Funct* 2013; **218**: 645-655 [PMID: 22547094 DOI: 10.1007/s00429-012-0418-1]
64 **Hoffmann C**, Grossman R, Bokov I, Lipitz S, Biegon A. Effect of cytomegalovirus infection on temporal lobe development in utero: quantitative MRI studies. *Eur Neuropsychopharmacol* 2010; **20**: 848-854 [PMID: 20833515 DOI: 10.1016/j.euroneuro.2010.08.006]
65 **Limperopoulos C**, Tworetzky W, McElhinney DB, Newburger JW, Brown DW, Robertson RL, Guizard N, McGrath E, Geva J, Annese D, Dunbar-Masterson C, Trainor B, Laussen PC, du Plessis AJ. Brain volume and metabolism in fetuses with congenital heart disease: evaluation with quantitative magnetic resonance imaging and spectroscopy. *Circulation* 2010; **121**: 26-33 [PMID: 20026783 DOI: 10.1161/CIRCULATIONAHA.109.865568]
66 **Clouchoux C**, du Plessis AJ, Bouyssi-Kobar M, Tworetzky W, McElhinney DB, Brown DW, Gholipour A, Kudelski D, Warfield SK, McCarter RJ, Robertson RL, Evans AC, Newburger JW, Limperopoulos C. Delayed cortical development in fetuses with complex congenital heart disease. *Cereb Cortex* 2013; **23**: 2932-2943 [PMID: 22977063 DOI: 10.1093/cercor/bhs281]
67 **Damodaram MS**, Story L, Eixarch E, Patkee P, Patel A, Kumar S, Rutherford M. Foetal volumetry using magnetic resonance imaging in intrauterine growth restriction. *Early Hum Dev* 2012; **88** Suppl 1: S35-S40 [PMID: 22285415 DOI: 10.1016/j.earlhumdev.2011.12.026]
68 **Cetin I**, Barberis B, Brusati V, Brighina E, Mandia L, Arighi A, Radaelli T, Biondetti P, Bresolin N, Pardi G, Rango M. Lactate detection in the brain of growth-restricted fetuses with magnetic resonance spectroscopy. *Am J Obstet Gynecol* 2011; **205**: 350.e1-350.e7 [PMID: 21861968 DOI: 10.1016/j.ajog.2011.06.020]
69 **Baldoli C**, Righini A, Parazzini C, Scotti G, Triulzi F. Demonstration of acute ischemic lesions in the fetal brain by diffusion magnetic resonance imaging. *Ann Neurol* 2002; **52**: 243-246 [PMID: 12210800 DOI: 10.1002/ana.10255]
70 **Anblagan D**, Jones NW, Costigan C, Parker AJ, Allcock K, Aleong R, Coyne LH, Deshpande R, Raine-Fenning N, Bugg G, Roberts N, Pausova Z, Paus T, Gowland PA. Maternal smoking during pregnancy and fetal organ growth: a magnetic resonance imaging study. *PLoS One* 2013; **8**: e67223 [PMID: 23843995 DOI: 10.1371/journal.pone.0067223]
71 **Guedj F**, Bianchi DW. Noninvasive prenatal testing creates an opportunity for antenatal treatment of Down syndrome. *Prenat Diagn* 2013; **33**: 614-618 [PMID: 23595836 DOI: 10.1002/pd.4134]

P- Reviewer: Li S, Ni Y, Schopf V **S- Editor**: Song XX
L- Editor: A **E- Editor**: Liu SQ

World Journal of Radiology

Submit a Manuscript: http://www.wjgnet.com/esps/
Help Desk: http://www.wjgnet.com/esps/helpdesk.aspx
DOI: 10.4329/wjr.v6.i8.530

World J Radiol 2014 August 28; 6(8): 530-537
ISSN 1949-8470 (online)

TOPIC HIGHLIGHT

WJR 6th Anniversary Special Issues (8): fMRI

Role of MRI in the diagnosis and treatment of osteomyelitis in pediatric patients

Brian S Pugmire, Randheer Shailam, Michael S Gee

Brian S Pugmire, Randheer Shailam, Michael S Gee, Department of Radiology, Massachusetts General Hospital, Boston, MA 01890, United States
Author contributions: Pugmire BS and Shailam R contributed equally to the writing and editing of the manuscript; Gee MS provided editorial input and overall direction.
Correspondence to: Brian S Pugmire, MD, Department of Radiology, Massachusetts General Hospital, 55 Fruit St. FND-216, Boston, MA 01890, United States. bpugmire@partners.org
Telephone: +1-617-7244255 Fax: +1-617-7263077
Received: February 11, 2014 Revised: April 8, 2014
Accepted: July 18, 2014
Published online: August 28, 2014

Abstract

Osteomyelitis is a significant cause of morbidity in children throughout the world. Multiple imaging modalities can be used to evaluate for suspected osteomyelitis, however magnetic resonance imaging (MRI) has distinct advantages over other modalities given its ability to detect early changes related to osteomyelitis, evaluate the true extent of disease, depict extraosseous spread of infection, and help guide surgical management. MRI has assumed a greater role in the evaluation of osteomyelitis with the increase in musculoskeletal infections caused by methicillin-resistant *Staphylococcus aureus* which have unique imaging features that are well-demonstrated with MRI. This review focuses primarily on the use of MRI in the evaluation of osteomyelitis in children and will include a discussion of the clinically important and characteristic findings on MRI of acute bacterial osteomyelitis and related conditions.

Key words: Magnetic resonance imaging; Osteomyelitis; Pediatrics; Infectious diseases

Core tip: Osteomyelitis is a significant cause of morbidity and mortality in children. Plain radiography and radionuclide bone scintigraphy, which have been the traditional imaging modalities for detecting osteomyelitis, both have significant limitations. Magnetic resonance imaging (MRI) is increasingly relied upon for detecting osteomyelitis in children, due to its superior soft tissue contrast for detecting early disease and extraosseous complication, as well as its lack of ionizing radiation exposure to patients. This article focuses on basic and advanced MRI techniques for evaluating osteomyelitis, as well as MRI imaging features of disease and their impact on clinical management.

Pugmire BS, Shailam R, Gee MS. Role of MRI in the diagnosis and treatment of osteomyelitis in pediatric patients. *World J Radiol* 2014; 6(8): 530-537 Available from: URL: http://www.wjgnet.com/1949-8470/full/v6/i8/530.htm DOI: http://dx.doi.org/10.4329/wjr.v6.i8.530

INTRODUCTION

Musculoskeletal infection is a significant cause of morbidity and mortality in children throughout the world. This category of disease encompasses both osteomyelitis and septic arthritis, however this review will be primarily focused on the former. Osteomyelitis is typically categorized as either hematogenous or non-hematogenous. Hematogenous osteomyelitis typically occurs when circulating pathogenic organisms take up residence in the metaphyses of long bones due to sluggish circulation in these regions. Non-hematogenous osteomyelitis, on the other hand, results from direct inoculation of organisms into bone due to penetrating trauma, open fractures, etc. Acute hematogenous osteomyelitis (AHO) is the most common type of musculoskeletal infection in children with an estimated incidence of 1 case per 5000 children per year in the United States[1]. It is primarily a disease

of young children with approximately half of all cases occurring in children 5 years of age or younger[2]. Some recent studies have indicated that the incidence of AHO is increasing with a concurrent increase in the number of cases due to methicillin-resistant *Staphylococcus aureus* (*S. aureus*) (MRSA) infections[3]. The signs and symptoms of AHO in children are nonspecific and as such, imaging frequently plays a significant role in the diagnosis and management of this condition.

EPIDEMIOLOGY

Infection by *S. aureus* is the most common cause of osteomyelitis. Community acquired *S. aureus* is implicated in most cases with 30% of these cases caused by community acquired MRSA (CA-MRSA)[4,5]. Other organisms that cause osteomyelitis include *Streptococcus pneumoniae*, *Streptococcus pyogenes*, *Pseudomonas aeruginosa* and *Bartonella henselae*. *Salmonella* is an important cause of osteomyelitis in patients with Sickle cell disease. Gram-negative bacteria and group B streptococci are common causes in newborns and *Kingella Kingae* in the first two years of age[5].

PATHOPHYSIOLOGY

Hematogenous osteomyelitis is the most common type of osteomyelitis in children[4]. This occurs when an infection elsewhere in the body spreads to the bone *via* the bloodstream. Risk factors for development of hematogenous osteomyelitis include trauma, prematurity, urinary tract infections, vascular catheters and immunodeficiencies. The blood vessels in the metaphyses have sluggish flow and discontinuous endothelium, which predispose to infection[4]. The most common bones to be affected are the fastest growing bones that have highly vascularized long bone metaphyses and metaphyseal equivalents. Common sites include the distal femur, proximal tibia, proximal humerus and distal radius. Most cases start with a focal infection in the metaphyseal marrow which progresses to local decalcification and bony destruction. Occasionally, multiple foci may be infected which eventually coalesce. This infection can spread within the marrow cavity and as the pressure increases within the marrow cavity, the infection can spread through Haversian canals in the cortex into the subperiosteal space, giving rise to a subperiosteal abscess. Similarly, the infection can traverse the periosteum and infect the adjacent soft tissues leading to pyomyositis. Infection may also spread across the physis into the epiphysis and joint space[4].

The first stage of osteomyelitis occurs with vascular congestion, intravascular thrombosis and increased intraosseous pressure. Next is the suppurative stage where pus traverses the Haversian canals and forms a subperiosteal abscess. Subsequently a sequestrum may form when the periosteal and endosteal blood supply is compromised from increased pressure and vascular obstruction. This may lead to formation of an involucrum: new bone growing from the periosteum. Depending on medical or surgical treatment at this point the infection may resolve or progress with complications.

The site of osteomyelitis varies with patient age and is related to the blood supply. In early infancy osteomyelitis occurs in epiphyses and metaphyses and epiphyseal-equivalent regions. Transphyseal vessels are present in infants younger than 18-24 mo of age, which allow easier spread of infection across the physis from the metaphysis to the epiphysis[4,6]. This is the reason that infantile osteomyelitis frequently involves the epiphysis and joint space. It is important to note that this is not the most common cause of septic arthritis, which more often results from direct hematogenous synovial seeding[4]. During early infancy, isolated involvement of the epiphyseal growth plate can occur. Infection of the epiphyseal growth plate during infancy can result in growth disturbance. In the 2-16 years age group, osteomyelitis is most often located in the metaphyses[6].

IMAGING APPROACH TO OSTEOMYELITIS

Osteomyelitis in children demonstrates abnormalities on nearly all imaging modalities, including radiography, ultrasound, computed tomography, radionuclide bone scintigraphy, and magnetic resonance imaging (MRI). The conventional approach to the imaging evaluation of suspected AHO in the past has been radiography followed by bone scintigraphy if the radiographs were negative. In this algorithm, MRI was typically been reserved for cases of poor treatment response or suspected vertebral diskitis-osteomyelitis. However, due to multiple factors, including the rise of rapidly aggressive and invasive musculoskeletal infections with CA-MRSA, this approach may no longer be ideal[7] (Figure 1).

As a first line modality radiography is useful for excluding other differential diagnoses such as trauma or tumor, however radiographs are insensitive for the detection of early osteomyelitis. Radiography may be normal in cases of osteomyelitis up to 14 d after the onset of infection and even then, only 20% of cases demonstrate radiographic abnormalities after this two-week delay[8]. Additionally, the early radiographic findings, including soft tissue swelling, vague bony lucency, and periosteal reaction, may be subtle and may not reflect the true extent of disease.

Triple-phase bone scintigraphy using 99mTc-methylene diphosphonate (99mTc-MDP) can demonstrate evidence of infection as soon as 24 h after onset and also has the advantage of being able to depict multiple sites of infection. Osteomyelitis typically manifests as increased radiotracer uptake on all phases (angiographic, blood pool, and delayed) of the triple-phase examination. However 99mTc-MDP scintigraphy is limited by poor anatomic detail and is insensitive for the detection of abscesses and extraosseous involvement. Furthermore, the sensitivity of 99mTc-MDP scintigraphy for

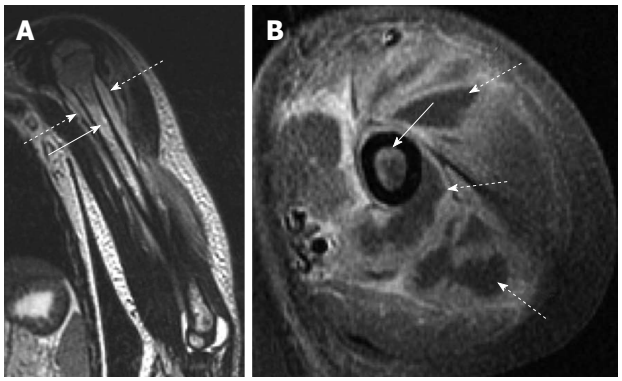

Figure 1 Acute osteomyelitis secondary to methicillin-resistant *Staphylococcus aureus* infection. A: Coronal T2-weighted image of the left humerus shows bone marrow edema (solid arrow) as well as a periosteal fluid collection (dashed arrow) consistent with periosteal abscess; B: Axial T1-weighted post-contrast image shows both enhancement of the bone marrow (solid arrow) as well as extensive periosteal and soft tissue abscess formation (dashed arrows) which is characteristic of methicillin-resistant *Staphylococcus aureus* infection.

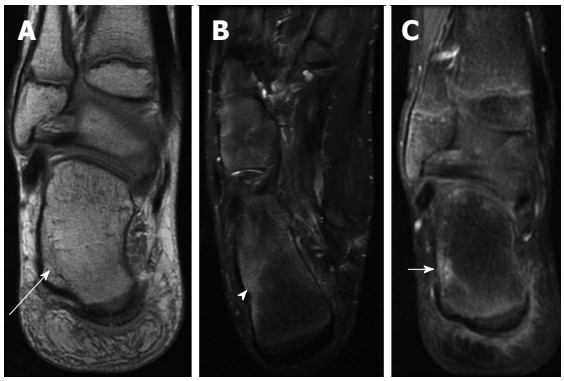

Figure 2 Early acute osteomyelitis. A: Coronal proton-density weighted image of the right ankle of a 12-year-old male shows a subtle area of decreased intramedullary signal along the lateral aspect of the calcaneus (long arrow); B: Axial T2-weighted image with fat suppression demonstrates more conspicuous bone marrow edema (arrowhead); C: Coronal post-contrast T1-weighted image with fat suppression shows an area of enhancement corresponding to the bone marrow edema. Bone biopsy revealed bacterial osteomyelitis.

the diagnosis of osteomyelitis, which in the past has been reported to be as high as 80%[9], may be decreasing with the increasing incidence of MRSA infections that tend to have significant soft-tissue involvement[7]. Positron emission tomography with 18-fluorodeoxyglucose appears to be sensitive (95%) and specific (87%) for the diagnosis of osteomyelitis[9], however it has limited availability and involves a significant amount of radiation exposure. Scintigraphic studies using white blood cells labeled with indium-111 or 99mTc hexamethylpropyleneamine oxime require relatively large volumes of blood and are not used frequently in younger children.

In contrast to the modalities listed above, MRI is both sensitive for the detection of early osteomyelitis (Figure 2) and can also accurately depict the extent of disease as well as any associated abscess or soft-tissue extension without the risks associated with radiation exposure. MRI combines high-resolution anatomic delineation of the medullary space, cortex, and periosteum with high soft tissue contrast for detection of edema and fluid. Preoperative MRI has been shown to reduce operative time and extent of surgical exposure in cases requiring surgical debridement[10]. MRI does have distinct disadvantages in children including long scan times and susceptibility to motion artifacts which necessitate sedation or anesthesia in young children (approximately 6 mo to 8 years of age). Additionally, MRI is contraindicated in some patients with metallic foreign bodies and certain types of implanted hardware. However, the overall superiority of MRI in evaluating osteomyelitis is reflected in recent clinical practice guidelines which indicate that MRI is the imaging modality of choice for the detection of osteomyelitis and associated infection of the extraosseous soft tissues[11]. As such, the current best imaging approach for suspected osteomyelitis is radiography followed by MRI.

MRI TECHNIQUE

Multiple variations of MRI protocols for the evaluation of osteomyelitis exist, however the essential sequences include both multiplanar T1 and T2-weighted fast-spin echo or turbo spin-echo (FSE/TSE) sequences and short-tau inversion recovery (STIR) or T2-weighted FSE/TSE sequences with fat-suppression (T2-FS). STIR and T2-FS sequences are particularly helpful for increasing the conspicuity of bone marrow edema and fluid collections. There is some controversy regarding when to use gadolinium in infants and children with suspected osteomyelitis. Intravenous gadolinium contrast does not appear to improve the sensitivity or specificity for the diagnosis of osteomyelitis overall. Recent studies suggest that if the fluid-sensitive images (*e.g.*, STIR, T2-FS) are normal, gadolinium enhancement provides no additional diagnostic value[12,13]. If the fluid-sensitive images are abnormal, however, gadolinium enhancement is of value in increasing confidence in the diagnosis of an abscess (if present) and planning of the approach to abscess aspiration and drainage[12]. Despite these recent studies that suggests that gadolinium contrast administration may not be needed for all cases, there are some specific indications for which contrast is always indicated. In cases of suspected vertebral osteomyelitis, contrast is necessary to assist in the differentiation of abscess in the epidural space or paravertebral masses from inflammatory masses[4] (Figure 3). Additionally, epiphyseal growth plate involvement by osteomyelitis may sometimes only be seen on gadolinium enhanced T1 sequences and not seen on non-contrast T1 and fluid sensitive sequences or on radiography or bone scintigraphy. Active epiphyseal infection manifests as one or more areas of decreased or no enhancement of the epiphyseal cartilage which otherwise should enhance uniformly[14,15]. As mentioned above, infection of the epiphyseal growth plate during infancy can result in growth disturbance and therefore gadolinium use in this age group is advised.

Because it is frequently difficult to precisely localize sites of involvement by clinical exam, especially in infants, an initial large field-of-view coronal STIR or T2-FS

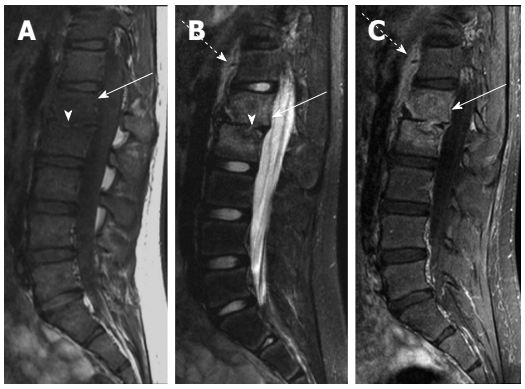

Figure 3 Chronic vertebral diskitis-osteomyelitis secondary to *S. typhi*. A: Sagittal T1-weighted image shows abnormally decreased T1 marrow signal in the L1 and L2 vertebral bodies (arrow) and loss of the L1-2 disk space (arrowhead); B: Sagittal T2-weighted image with fat suppression shows abnormally increased T2 signal in the L1 and L2 vertebral bodies (solid arrow) with loss of normal T2 intervertebral disk signal (arrowhead). T2 hyperintensity anterior to the spine (dashed arrow) likely represents adjacent soft tissue edema; C: Sagittal T1-weighted image after intravenous contrast shows intramedullary enhancement in the L1 and L2 vertebral bodies (solid arrow) with soft tissue enhancement anterior to the spine (dashed arrow).

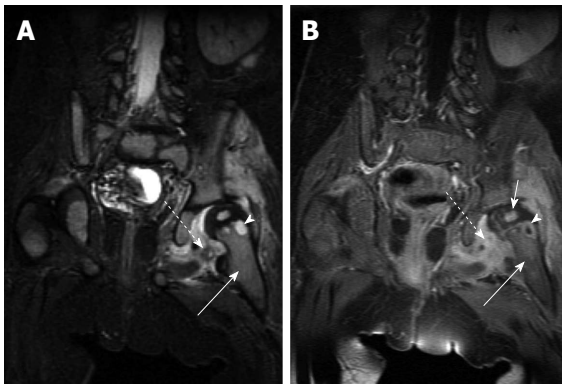

Figure 4 Acute osteomyelitis of the hip. A: Coronal fast spin echo inversion recovery image shows T2-hyperintense marrow edema in the left femoral metaphysis (solid arrow) with a small round very intense focus of T2 signal (arrowhead) which is consistent with an intraosseous abscess. Surrounding soft tissue edema (dashed arrow) is also noted; B: Coronal T1-weighted post-contrast image in the same patient shows enhancement in the metaphyseal bone marrow (solid long arrow), peripheral enhancement of the abscess (arrowhead), and surrounding soft tissue enhancement (dashed arrow). Note enhancement of the left femoral head (solid short arrow) which indicates adequate perfusion.

sequence of the general region of concern can be used to help localize the site(s) of disease followed by a tailored evaluation of the involved areas. In cases of suspected osteomyelitis affecting the lower extremities, imaging of the contralateral extremity may also be considered: abnormalities in the contralateral extremity are common, however they may not affect clinical management[16]. Whole-body MRI (WBMRI) may be indicated in cases of suspected multifocal involvement such as in cases of severe CA-MRSA infections, which frequently involve multiple sites, or in cases of suspected chronic multifocal recurrent osteomyelitis (CRMO). WBMRI is typically performed using a series of coronal STIR acquisitions

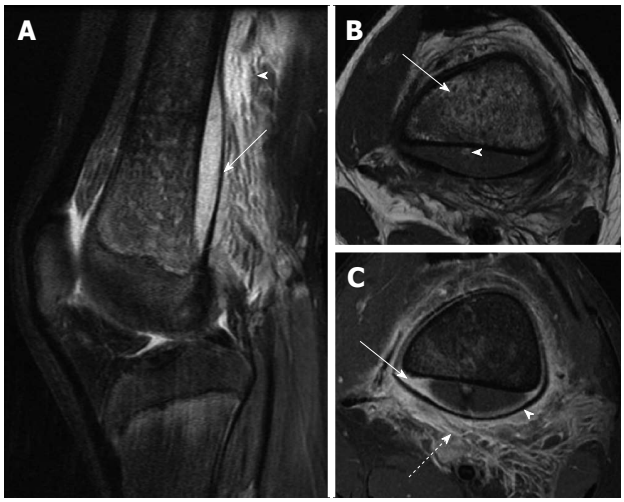

Figure 5 Osteomyelitis with subperiosteal abscess. A: Sagittal T2-weighted image with fat suppression shows a large subperiosteal abscess (solid arrow) with adjacent soft tissue edema (arrowhead); B: Axial T1-weighted image shows heterogeneous T1 hypointense marrow signal (solid arrow). Note small T1 hyperintense focus in the posterior subperiosteal fluid collection (arrowhead) indicative of a fat globule; C: Axial T1-weighted post-contrast image demonstrates peripheral enhancement of the subperiosteal abscess (solid arrow), significant periosteal elevation (arrowhead) and adjacent soft tissue inflammation (dashed arrow).

obtained in multiple anatomic stations using receiver coils spanning the entire body, with the scan table moved through the magnet between stations. The images from each station are then digitally fused at points of overlap to create a single whole body image stack.

MRI FEATURES OF ACUTE OSTEOMYELITIS

Because MRI is able to detect early marrow involvement, it is an important modality for detection of osteomyelitis in early stages. Additionally, MRI is helpful for detection of fluid collections and abscesses that may occur in the marrow, subperiosteal region or in soft tissues. Anatomical information provided by MR can be helpful for drainage and surgical treatment. T1 fat saturation gadolinium-enhanced images will show non-enhancement of fluid and pus with peripheral enhancement.

The earliest finding of osteomyelitis on MRI is bone marrow edema and T2 and STIR sequences are very important for detecting these early changes (Figures 2 and 4). MRI is also sensitive for detection of periosteal elevation and the presence of a subperiosteal fluid collection or abscess (Figure 5). Distinguishing normal hematopoietic marrow from abnormal marrow can be challenging in certain situations because of the normal hematopoietic marrow often seen in the metaphyses in children. Normal hematopoietic marrow T1 signal should be hyperintense relative to muscle. If there is marrow infiltration or edema, the T1 signal is generally isointense or hypointense to muscle (Figure 6). Normal hematopoietic marrow should appear similar in adjacent or contralateral metaphyses.

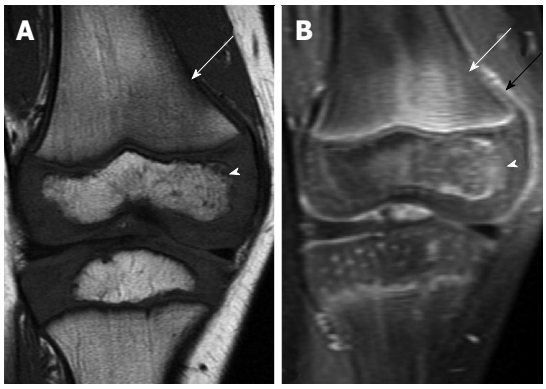

Figure 6 Early acute osteomyelitis. A: Coronal T1-weighted image of the right knee of a 4-year-old male shows ill-defined areas of low T1 signal in the bone marrow in the lateral femoral metaphysis (arrow) and lateral epiphysis (arrowhead); B: Coronal T1-weighted post-contrast image in the same patient shows associated enhancement in these areas (white arrow and arrowhead) as well as some periosteal reaction, indicated by periosteal enhancement (black arrow).

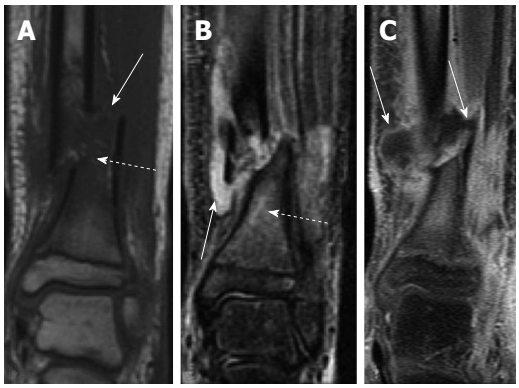

Figure 7 Osteomyelitis secondary to open fracture. A: Coronal T1-weighted image of the left distal tibia shows a displaced fracture of the distal tibial metadiaphysis (solid arrow) with associated bone marrow edema (dashed arrow); B: Coronal T2-weighted image of the same patient shows a fluid collection adjacent to the fracture (solid arrow) with T2 hyperintense marrow edema (dashed arrow); C: Coronal T1-weighted post-contrast image shows peripheral enhancement surrounding the above-mentioned fluid collection, consistent with an abscess (solid arrows).

Imaging of the contralateral body part is often helpful for this and is more easily obtained during imaging of the pelvis and lower extremities. Since detailed small structure anatomical information is less important during evaluation of osteomyelitis (OM), imaging with a body coil should be considered if large field of view imaging would be helpful.

Pelvic osteomyelitis often occurs in metaphyseal equivalents such as the ischiopubic synchondrosis, pubic symphysis, triradiate cartilage, iliac apophyses and adjacent to the sacroiliac joint. Involvement of adjacent soft tissues, muscles and bowel is not uncommon and MRI is helpful in imaging the extent and often the source of infection.

CHRONIC OSTEOMYELITIS

Chronic infections of bone may be indolent and have minor signs, symptoms and serologic abnormalities.

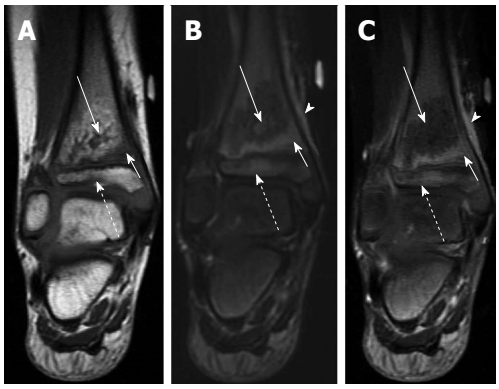

Figure 8 Transphyseal methicillin-resistant *Staphylococcus aureus* osteomyelitis with intraosseous abscess. A: Coronal T1-weighted image of the right ankle shows an area of T1 hyperintensity in the distal tibial metaphysis with central T1 hypointensity (solid long arrow) indicative of abscess formation. T1 hypointensity is seen surrounding this area in metaphysis (solid short arrow) and in the epiphysis (dashed arrow) indicative of transphyseal spread; B: Coronal T2-weighted image with fat suppression shows an area of T2 hypointensity with central T2 hyperintensity (solid long arrow) corresponding to the areas of abnormal T1 signal in A. T2 hyperintensity in the distal metaphysis (solid short arrow) and epiphysis (dashed arrow) are consistent with edema. T2 hyperintensity in periosteum and adjacent soft tissues indicating inflammation (arrowhead); C: Coronal T1-weighted image post contrast shows a lack of enhancement in the central distal metaphysis consistent with necrosis and abscess formation (solid long arrow). Enhancement is seen peripherally in the distal metaphysis and epiphysis (solid short arrow and dashed arrow). Enhancement in periosteum and adjacent soft tissues indicating inflammation (arrowhead).

However, cases of chronic osteomyelitis may be severe, incapacitating and difficult to treat. Chronic osteomyelitis may occur after the following: acute osteomyelitis, trauma (Figure 7), joint replacement, orthopedic hardware (ex. used in fracture reduction), and mycobacterium tuberculosis or syphilis infections. Chronic osteomyelitis is defined if symptoms persist after one month of appropriate antibiotic treatment or if there is persistent infection after one month of inadequate treatment.

Imaging chronic osteomyelitis is helpful to evaluate the extent of infection within bone and surrounding soft tissues, identification of an abscess, sequestrum and sinus tract (Figure 8). Sequestra of cortical bone appear as low signal on T1, T2 and STIR and do not enhance. Imaging findings of chronic osteomyelitis include Brodie abscess, thick periosteum, sequestrum/necrotic bone fragments, and cloaca/draining tract (Figure 9). Sequestra of cancellous bone also do not enhance but are relatively hyperintense to cortical sequestra on T1, T2 and STIR. Granulation tissue, soft tissue inflammation and sinus tracts are all T1 hypointense, T2 and STIR hyperintense and enhance with gadolinium.

Brodie's abscesses are usually metaphyseal and appear as a fluid filled cavity with an enhancing lining, rim of low signal sclerosis and peripheral edema (Figure 10). A "penumbra sign" has been described with Brodie abscess and results from the lining of granulation tissue around the abscess that is T1 hyperintense relative to the abscess cavity. A "double-line sign" has also been described on T2 and STIR images representing hyperintense granulation tissue surrounded by low signal sclerosis.

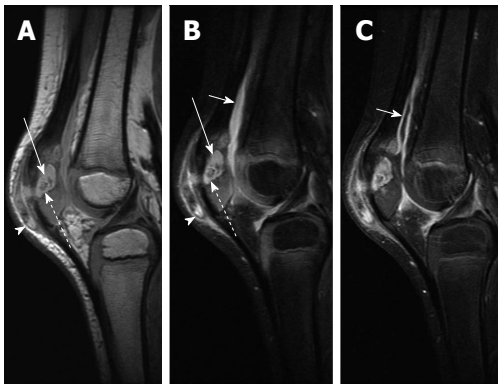

Figure 9 Chronic patellar osteomyelitis with abscess and sequestrum. A: Sagittal proton-density-weighted image of the right knee shows an abscess cavity in the patella (solid arrow) with a central low-density focus consistent with a sequestrum (dashed arrow). There is also disruption of the anterior cortex with spread of infection into the prepatellar bursa (arrowhead); B: Sagittal T2-weighted image with fat suppression again shows the intraosseous abscess (solid long arrow) with central T2 hypointense sequestrum (dashed arrow) and extension of infection into the prepatellar soft tissues (arrowhead). A knee joint effusion is more apparent on this image (solid short arrow); C: Sagittal T1-weighted post-contrast image shows enhancement of the synovium (solid short arrow) indicative synovitis, likely from intra-articular extension of infection.

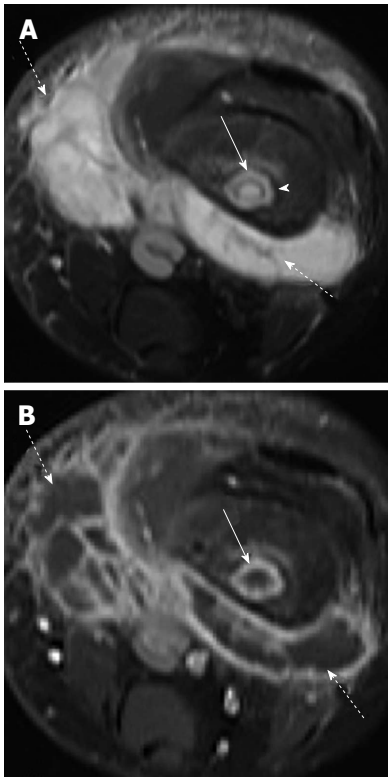

Figure 10 Osteomyelitis with intraosseous and soft tissue abscess secondary to methicillin-resistant *Staphylococcus aureus* infection. A: Axial T2-weighted fat suppressed image shows intraosseous abscess cavity (solid arrow) with rim of surrounding edema and large surrounding soft tissue fluid collection (dashed arrow). Note T2 hypointense rim (arrowhead) forming the "double-line" sign; B: Axial T1-weighted post-contrast image shows peripheral enhancement associated with the intraosseous abscess (solid arrow) and soft tissue abscesses (dashed arrows).

Sclerosing osteomyelitis of Garre is a type of chronic bone infection manifesting primarily with bony sclerosis.

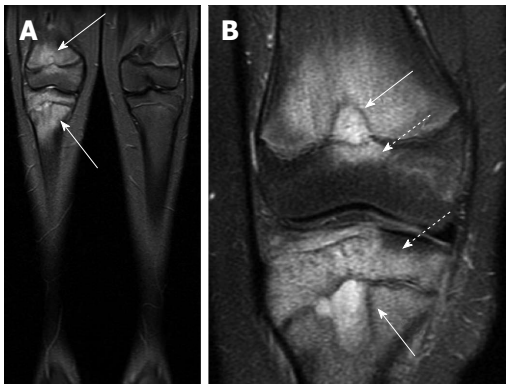

Figure 11 Chronic recurrent multifocal osteomyelitis. A: Coronal short-tau inversion recovery image from whole body magnetic resonance imaging (lower extremity station) shows areas of bone marrow edema in the distal femur and proximal tibia; B: Coronal T2-weighted fat suppressed image with smaller field of view again demonstrates the bone marrow edema as well as two areas of very hyperintense T2 signal in the femur and tibia which may represent intraosseous abscesses (solid arrows), though these are not typically found in chronic multifocal recurrent osteomyelitis. Involvement of the epiphysis is apparent at both sites (dashed arrows).

CHRONIC RECURRENT MULTIFOCAL OSTEOMYELITIS

Chronic recurrent multifocal osteomyelitis is a non-bacterial, noninfectious inflammation of bone that has been characterized as an auto-inflammatory disease. Cultures do not show an infectious source and biopsy shows non-specific inflammation. Antibiotics do not alter the course of the disease and symptoms are better treated with anti-inflammatory medications. Frequent sites of involvement include the metaphyses of the long bones, clavicles, spine and pelvis. Other sites include the mandible, scapula, ribs, sternum, hands and feet. Radiographic findings typically include lysis and sclerosis. Since this disease frequently involves multiple sites, some of which are asymptomatic, WBMRI is recommended both to help aid in the diagnosis with multifocal involvement and document the extent of disease. During the active phase, there is bone marrow edema and often periostitis and soft tissue inflammation. MRI can show transphyseal disease, which can lead to physeal bars affecting growth and angular deformities (Figure 11). Joint effusions, synovitis cartilage and subchondral bone erosions may also be seen. Larger fluid collections, abscess, sinus tracts and sequestra are not typical features of CRMO and are more often seen with bacterial osteomyelitis[17].

DIAGNOSTIC CHALLENGES

Differentiating osteomyelitis from Ewing sarcoma can often be challenging. The fact that children often do not present with the classic signs and symptoms of an infection makes the clinical differentiation between these two diagnoses difficult. Plain film findings of both osteomyelitis and Ewing sarcoma are often similar with an aggressive intramedullary process destroying normal cancellous and cortical bone creating a moth eaten and permeative

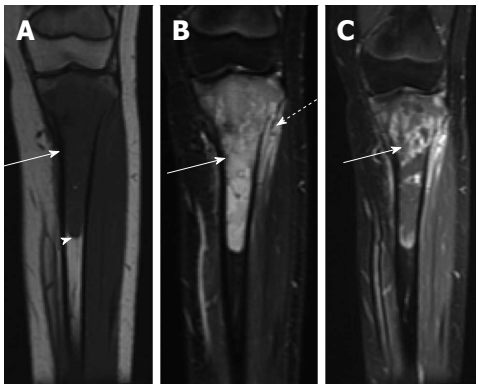

Figure 12 Ewing sarcoma. A: Coronal T1-weighted image of the left tibia shows a long segment of intramedullary T1 hypointensity (solid arrow). Note abrupt transition to normal marrow signal inferiorly (arrowhead); B: Coronal fast multi-planar inversion recovery image of the same patient shows very intense T2 signal in the marrow cavity (solid arrow) with extraosseous extension (dashed arrow); C: T1-weighted post-contrast image shows very heterogeneous intramedullary enhancement associated with this lesion (solid arrow).

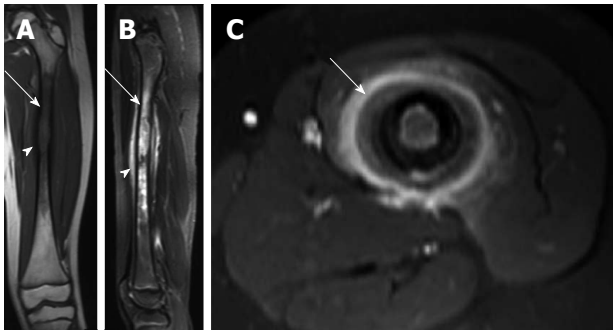

Figure 13 Langerhans cell histiocytosis. A: Coronal T1-weighted image of the left femur shows a long segment of marrow T1 hypointensity (arrow) and cortical erosion/expansion (arrowhead); B: Sagittal short-tau inversion recovery image from the same patient shows very intense T2-signal in the marrow cavity (arrow). T2 hyperintensity in the periosteum (arrowhead) is indicative of periosteal reaction; C: Axial T1-weighted image post contrast shows intense enhancement of the periosteum (arrow).

appearance. MRI can be helpful in differentiating between these two aggressive diseases. Both may produce periostitis, periosteal elevation, adjacent soft tissue mass and effacement of fat planes. Soft tissue enhancement, cystic and necrotic foci and cortical destruction are found in both diseases and are less reliable at differentiation. The presence of fat globules within the infiltrating marrow process or in a subperiosteal location is a feature of osteomyelitis more often than neoplasia[18] (Figure 5). A recent study by Henninger *et al*[19] showed that all cases of Ewing sarcoma had a sharp or defined margin of the bone lesion between normal bone and edematous/affected bone on T1 which was not present in cases of osteomyelitis (Figure 12).

Langerhans cell histiocytosis often has a very similar appearance to osteomyelitis with an aggressive lytic lesion with ill-defined borders and surrounding inflammatory changes (Figure 13). A process centered in the diaphysis favors langerhans cell histiocytosis over OM. However, differentiation from Langerhans cell histiocytosis, lymphoma and leukemia can be challenging and biopsy is necessary for definitive diagnosis. Fractures, bone infarcts and healed osteomyelitis may pose a diagnostic challenge in differentiating between active osteomyelitis due to common features.

ADVANCED MRI TECHNIQUES

As noted above, the current protocols for MRI of suspected osteomyelitis utilize standard T1 and T2-weighted, STIR, and sometimes contrast-enhanced sequences. More advanced imaging techniques such as diffusion-weighted imaging (DWI), dynamic contrast-enhanced (DCE) MRI, and MR spectroscopy can be used as well, however their role is currently not well defined. A potential application for DWI would be characterization of fluid collections associated with osteomyelitis as abscesses characteristically demonstrate restricted diffusion on DWI. Additionally, DCE-MRI could potentially be used to identify areas of soft tissue necrosis, femoral/humeral head avascular necrosis, or possibly increase sensitivity for detection of CA-MRSA infection in non-ossified growth cartilage. Whole body MRI with digital merging of multiple anatomic stations can be helpful for assessment of multiple sites of disease as well as suspected cases of CRMO. Further research is needed to define the utility of these imaging techniques in this setting.

REFERENCES

1 **Steer AC**, Carapetis JR. Acute hematogenous osteomyelitis in children: recognition and management. *Paediatr Drugs* 2004; **6**: 333-346 [PMID: 15612835]
2 **Nelson JD**. Acute osteomyelitis in children. *Infect Dis Clin North Am* 1990; **4**: 513-522 [PMID: 2212603]
3 **Arnold SR**, Elias D, Buckingham SC, Thomas ED, Novais E, Arkader A, Howard C. Changing patterns of acute hematogenous osteomyelitis and septic arthritis: emergence of community-associated methicillin-resistant Staphylococcus aureus. *J Pediatr Orthop* 2006; **26**: 703-708 [PMID: 17065930]
4 **Jaramillo D**. Infection: musculoskeletal. *Pediatr Radiol* 2011; **41** Suppl 1: S127-S134 [PMID: 21523583 DOI: 10.1007/s00247-011-2001-y]
5 **Kalyoussef S**, Tolan RW, Noel GJ. Pediatric Osteomyelitis. 2014. Available from: URL: http: //emedicine.medscape.com/article/967095-overview
6 **DiPoce J**, Jbara ME, Brenner AI. Pediatric osteomyelitis: a scintigraphic case-based review. *Radiographics* 2012; **32**: 865-878 [PMID: 22582364 DOI: 10.1148/rg.323115110]
7 **Browne LP**, Mason EO, Kaplan SL, Cassady CI, Krishnamurthy R, Guillerman RP. Optimal imaging strategy for community-acquired Staphylococcus aureus musculoskeletal infections in children. *Pediatr Radiol* 2008; **38**: 841-847 [PMID: 18560822 DOI: 10.1007/s00247-008-0888-8]
8 **Capitanio MA**, Kirkpatrick JA. Early roentgen observations in acute osteomyelitis. *Am J Roentgenol Radium Ther Nucl Med* 1970; **108**: 488-496 [PMID: 5415924]
9 **Gotthardt M**, Bleeker-Rovers CP, Boerman OC, Oyen WJ. Imaging of inflammation by PET, conventional scintigraphy, and other imaging techniques. *J Nucl Med* 2010; **51**: 1937-1949 [PMID: 21078798 DOI: 10.2967/jnumed.110.076232]
10 **Kan JH**, Hilmes MA, Martus JE, Yu C, Hernanz-Schulman M. Value of MRI after recent diagnostic or surgical intervention in children with suspected osteomyelitis. *AJR Am J Roentgenol* 2008; **191**: 1595-1600 [PMID: 18941107 DOI: 10.2214/

AJR.08.1115]
11 **Liu C**, Bayer A, Cosgrove SE, Daum RS, Fridkin SK, Gorwitz RJ, Kaplan SL, Karchmer AW, Levine DP, Murray BE, J Rybak M, Talan DA, Chambers HF. Clinical practice guidelines by the infectious diseases society of america for the treatment of methicillin-resistant Staphylococcus aureus infections in adults and children: executive summary. *Clin Infect Dis* 2011; **52**: 285-292 [PMID: 21217178 DOI: 10.1093/cid/cir034]
12 **Averill LW**, Hernandez A, Gonzalez L, Peña AH, Jaramillo D. Diagnosis of osteomyelitis in children: utility of fat-suppressed contrast-enhanced MRI. *AJR Am J Roentgenol* 2009; **192**: 1232-1238 [PMID: 19380545 DOI: 10.2214/AJR.07.3400]
13 **Kan JH**, Young RS, Yu C, Hernanz-Schulman M. Clinical impact of gadolinium in the MRI diagnosis of musculoskeletal infection in children. *Pediatr Radiol* 2010; **40**: 1197-1205 [PMID: 20180105 DOI: 10.1007/s00247-010-1557-2]
14 **Browne LP**, Guillerman RP, Orth RC, Patel J, Mason EO, Kaplan SL. Community-acquired staphylococcal musculoskeletal infection in infants and young children: necessity of contrast-enhanced MRI for the diagnosis of growth cartilage involvement. *AJR Am J Roentgenol* 2012; **198**: 194-199 [PMID: 22194497 DOI: 10.2214/AJR.10.5730]
15 **Guillerman RP**. Osteomyelitis and beyond. *Pediatr Radiol* 2013; **43** Suppl 1: S193-S203 [PMID: 23478935 DOI: 10.1007/s00247-012-2594-9]
16 **Metwalli ZA**, Kan JH, Munjal KA, Orth RC, Zhang W, Guillerman RP. MRI of suspected lower extremity musculoskeletal infection in the pediatric patient: how useful is bilateral imaging? *AJR Am J Roentgenol* 2013; **201**: 427-432 [PMID: 23883225 DOI: 10.2214/AJR.12.9644]
17 **Khanna G**, Sato TS, Ferguson P. Imaging of chronic recurrent multifocal osteomyelitis. *Radiographics* 2009; **29**: 1159-1177 [PMID: 19605663 DOI: 10.1148/rg.294085244]
18 **Davies AM**, Hughes DE, Grimer RJ. Intramedullary and extramedullary fat globules on magnetic resonance imaging as a diagnostic sign for osteomyelitis. *Eur Radiol* 2005; **15**: 2194-2199 [PMID: 15864595]
19 **Henninger B**, Glodny B, Rudisch A, Trieb T, Loizides A, Putzer D, Judmaier W, Schocke MF. Ewing sarcoma versus osteomyelitis: differential diagnosis with magnetic resonance imaging. *Skeletal Radiol* 2013; **42**: 1097-1104 [PMID: 23685708 DOI: 10.1007/s00256-013-1632-5]

P- Reviewer: Lichtor T **S- Editor**: Wen LL
L- Editor: A **E- Editor**: Liu SQ

World Journal of Radiology

Submit a Manuscript: http://www.wjgnet.com/esps/
Help Desk: http://www.wjgnet.com/esps/helpdesk.aspx
DOI: 10.4329/wjr.v6.i8.538

World J Radiol 2014 August 28; 6(8): 538-543
ISSN 1949-8470 (online)

TOPIC HIGHLIGHT

WJR 6th Anniversary Special Issues (8): fMRI

Intraoperative perfusion magnetic resonance imaging: Cutting-edge improvement in neurosurgical procedures

Stephan Ulmer

Stephan Ulmer, Neuroradiology, Medical Radiological Institute, 8001 Zurich, Switzerland
Stephan Ulmer, Institute of Neuroradiology, Department of Radiology and Neuroradiology, University Hospital of Schleswig-Holstein, 24105 Kiel, Germany
Author contributions: Ulmer S reviewed the literature, analyzed own data, created all figures, wrote the paper and performed all corrections in the revision.
Correspondence to: Stephan Ulmer, MD, Neuroradiology, Medical Radiological Institute, Bahnhofplatz 3, 8001 Zurich, Switzerland. ulmer@email.com
Telephone: +41-44-2252090 Fax: +41-44-2118754
Received: January 16, 2014 Revised: April 17, 2014
Accepted: June 18, 2014
Published online: August 28, 2014

Abstract

The goal in brain tumor surgery is to remove the maximum achievable amount of the tumor, preventing damage to "eloquent" brain regions as the amount of brain tumor resection is one of the prognostic factors for time to tumor progression and median survival. To achieve this goal, a variety of technical advances have been introduced, including an operating microscope in the late 1950s, computer-assisted devices for surgical navigation and more recently, intraoperative imaging to incorporate and correct for brain shift during the resection of the lesion. However, surgically induced contrast enhancement along the rim of the resection cavity hampers interpretation of these intraoperatively acquired magnetic resonance images. To overcome this uncertainty, perfusion techniques [dynamic contrast enhanced magnetic resonance imaging (DCE-MRI), dynamic susceptibility contrast magnetic resonance imaging (DSC-MRI)] have been introduced that can differentiate residual tumor from surgically induced changes at the rim of the resection cavity and thus overcome this remaining uncertainty of intraoperative MRI in high grade brain tumor resection.

Key words: Intraoperative magnetic resonance imaging; Dynamic susceptibility contrast magnetic resonance imaging; Dynamic contrast enhanced magnetic resonance imaging; Surgically induced contrast enhancement; Neurosurgery

Core tip: The amount of brain tumor resection is one of the prognostic factors for time to tumor progression and median survival. To achieve maximum brain tumor removal, while preventing damage to "eloquent" brain regions, a variety of technical advances have been introduced, including intraoperative magnetic resonance imaging. Brain shift can thus be compensated; however, surgically induced contrast enhancement along the rim of the resection cavity hampers interpretation of these intraoperatively acquired images. Recently, perfusion techniques (dynamic contrast enhanced magnetic resonance imaging, dynamic susceptibility contrast magnetic resonance imaging) have been introduced that can differentiate residual tumor from surgically induced changes and thus overcome this remaining uncertainty in high grade brain tumor resection.

Ulmer S. Intraoperative perfusion magnetic resonance imaging: Cutting-edge improvement in neurosurgical procedures. *World J Radiol* 2014; 6(8): 538-543 Available from: URL: http://www.wjgnet.com/1949-8470/full/v6/i8/538.htm DOI: http://dx.doi.org/10.4329/wjr.v6.i8.538

INTRODUCTION

The goal in brain tumor surgery is to remove the maximum achievable amount of the tumor, preventing damage to "eloquent" brain regions, as the amount of brain tumor resection is one of the prognostic factors for time to tumor progression and median survival[1,2]. Preop-

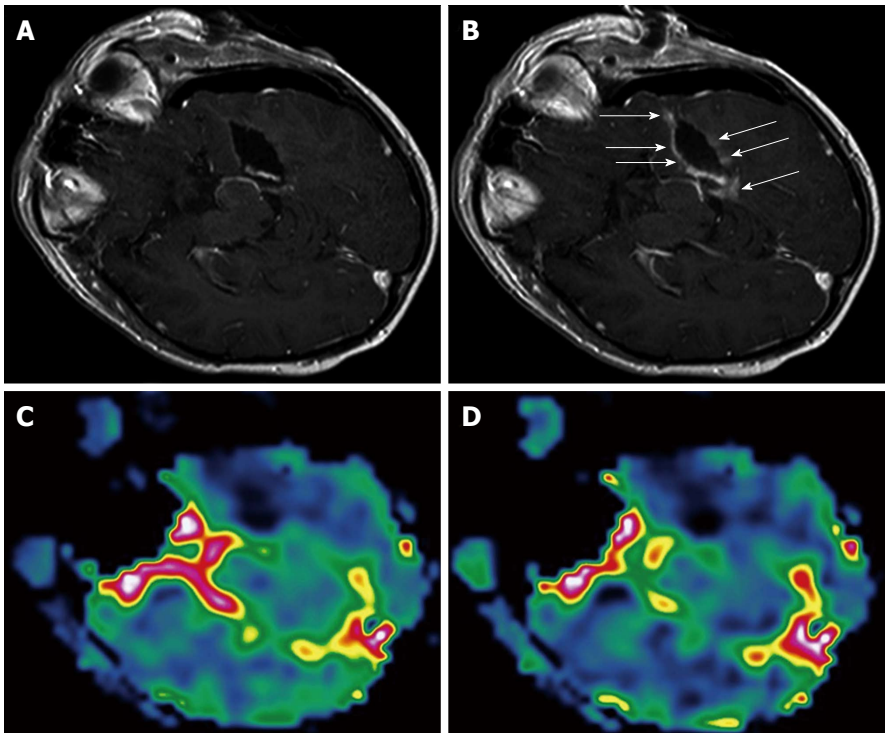

Figure 1 Surgically induced intraoperative contrast leakage. Reprinted from NeuroImage with permission[9]. A: T1-weighted magnetic resonance (MR) image of the initial resection control. Residual tumor was depicted (not shown), neuronavigation was updated and the residual tumor was removed; B: T1-weighted MR image in identical orientation as in (A) of the second intraoperative resection control. At the border of the resection cavity there is contrast enhancement of previously non-enhancing tissue (arrows), which is caused by the neurosurgical resection leading to a leakage phenomenon. Perfusion maps of rCBV (C) and rCBF (D) at the second resection control demonstrate no elevated values in areas of contrast enhancement but complete resection of the tumor. rCBV: Regional cerebral blood volume; rCBF: Regional cerebral blood flow.

eratively acquired magnetic resonance (MR) images can nicely delineate the tumor extent and adjacent anatomical structures. The application of an operating microscope in the late 1950s[3,4] revolutionized neurosurgery. Further advances included computer-assisted devices for surgical navigation[4,5] and, more recently, intraoperative imaging[6] to incorporate and correct for brain shift during the resection of the lesion. However, surgically induced contrast enhancement along the rim of the resection cavity[7] hampers interpretation of these intraoperatively acquired MR images (Figure 1). To overcome this uncertainty, perfusion techniques have been introduced. Dynamic susceptibility contrast magnetic resonance imaging (DSC-MRI) is a T2*-weighted technique that enables calculation of regional cerebral blood flow (rCBF) and regional cerebral blood volume (rCBV) maps. The measurement takes only 1 min, 20 s and does not extend the overall scanning procedure. It can be applied various times as it is independent of T1-effects after saturation, has proven to be as reliable as preoperatively performed DSC-MRI[8,9] and can distinguish residual tumor form surgically induced artefacts. Dynamic contrast-enhanced T1-weighted perfusion (DCE-MRI) has alternatively been used intraoperatively[10]. The beauty of this approach that requires more time than DSC-MRI (also at 3T) is that there is a by-product with the acquired T1-weighted images as the slope of contrast enhancement can easily be analyzed without the need for additional software. A quickly climbing slope depicts residual tumor tissue. However, the following still needs to be proven: can the DCE-MRI be repeatedly applied, is analysis unaffected by the commonly used absorbable hemostats (such as surgical®, Ethicon 360), and can it reliably differentiate other sources of contrast enhancement over time, such as bleedings. Both techniques, however, can differentiate residual tumor from surgically induced changes at the rim of the resection cavity and thus overcome the remaining uncertainty of intraoperative MRI in high grade brain tumor resection.

The extent of tumor resection is one of the prognostic factors for time to tumor progression and median survival for patients with both high and low grade gliomas[1,2]. Various attempts have been undertaken to achieve the maximum resection of a lesion. Most of them are imaging-based. Beginning in 1980, intraoperative ultrasound was the first imaging modality guiding neurosurgical procedures[3]. Preoperatively acquired images were integrated in computer-assisted devices for surgical navigation beginning in 1986[4,5]. Prior to resection of a lesion, an "image-to-patient" registration is necessary to align the MRI coordinates with the patient's head position in the OR. However, due to brain shift during the resection of the lesion, or leakage of CSF, these preoperatively acquired images were progressively imprecise over time. The double-donut was the first intraoperative MRI system at the Brigham and Women's hospital in

Boston in 1997[6]. This enabled an update of the underlying anatomy at any time during the resection of a lesion, including an update of the navigation system. One major drawback, besides the costs of such a system, is that there is a surgically induced contrast enhancement along the resection cavity margin in intraoperatively acquired T1-weighted images after contrast administration[7] that can hamper judgment concerning the differentiation between residual solid tumor or just surgically induced artefact, especially taken together with the well known brain shift that may also preclude the comparison with preoperatively acquired images. Another approach that found wide acceptance was the use of intravenous administration of 5-aminolevulinic acid[11], leading to tumor fluorescence intraoperatively that also resulted in more complete tumor removal. However, lack of visible fluorescence in the adjacent tissue is not as highly predictive of normal tissue as biopsy proven[12]. Thus, some centers (where available) use both complementary methods. However, the contrast enhancement in these intraoperative images remains a challenge with conventional imaging only.

INTRAOPERATIVE SETUP

Instead of using the double-donut setup, which requires that the surgeon is within the magnetic field thus requiring non-magnetic tools[6], "twin operating theatres" have been proposed for both low[13,14] and more recently high field systems, with the need to transfer the patient between the imaging and surgical site. This has become the setup of choice in most institutions[8,15,16], although some move the magnet towards the surgical site[17]. Lower field systems with permanent magnets are also in use[18], which is a compromise but does not allow advanced imaging (see below). To use the conventional neurosurgical setup, including neuronavigation, microscope and conventional ferromagnetic instruments, the patient has to be outside the 0.5 mT or 5-Gauss line of the magnet during the surgical procedures to avoid a pull of ferromagnetic objects into the bore of the scanner, especially when the patient is positioned for scanning. Also, these objects interfere with imaging and can hamper image quality, causing artefacts. Dynamic sequences like DSC-MRI require a high field scanner (1.5 T or more), which come in "closed-bore" designs. Head fixation devices need to be MR-compatible. Whenever the surgeon wants an update, MRI can be performed after removing all ferromagnetic objects and sterile coverage of the craniotomy.

ADVANCED INTRAOPERATIVE MRI

To define residual tumor, various approaches have been performed using advanced imaging techniques. It has been demonstrated that parts of brain tumors do not enhance as biopsy proven[19] which can be depicted by MR spectroscopy (MRS), a technique that is very susceptible to artefacts and also time consuming. However, it helps to delineate typical changes associated with brain tumors and to define the real extent of a lesion more precisely than the use of conventional MR imaging only. Recently, this had been used intraoperatively to identify residual tumor with a sensitivity of 85.7% and specificity of 100%[20]. However, air filled (resection) cavities might preclude MRS, or small residual tumor areas might be missed, and it is impossible to map the complete rim of a resection cavity intraoperatively due to time restraints, thus the area to be monitored has to be defined.

Perfusion imaging in clinical routine is most commonly performed as DSC-MRI-weighted perfusion, which is T2*-weighted or as DCE-MRI. Both techniques are most commonly used for stroke imaging but also in neuro-oncology and intraoperatively.

DSC-MRI

DSC-MRI enables calculation of regional maps for relative blood volume and flow by administering conventional MR contrast agents while T2*-weighted images (*i.e.*, 40 images/slice) are being acquired. In areas of blood-brain barrier breakdown (such as brain tumors), distinct zones with increased cerebral blood flow and volume can be depicted, which correspond to neovascularization and active metabolism within the tumor[21-28]. Prior to the DSC measurement, 2 cc of contrast agent are injected for reduction of the T1 effect (saturation). For perfusion imaging, the contrast agent is administered as a bolus, followed by a saline flush with a flow rate of 5 cc/s during a dynamic susceptibility-dependent T2*-weighted GE EPI sequence (*i.e.*, TR/TE = 17/8 ms; FOV 240 mm; matrix 128 × 128; EPI factor = 17, number of slices 30 with slice thickness of 3.5 mm, duration: 1 min 20 s[8,9]). These data are then transferred to a workstation to create maps of the rCBF and rCBV and to measure the mean transit time of the contrast agent passing through the brain[29] based on the tissue dilution theorem. As absolute quantification is not yet possible, ratios to the unaffected hemisphere or adjacent tissue are created to judge the perfusion data. As T2*-weighted images are susceptible to artefacts caused by air fluid levels (such as resection cavities) or air filled spaces (like sinus), its intraoperative application required a multistage approach. Initially, a phantom study was performed using a model with a rigorous air water level that showed only moderate artefacts. In a second step, a model with continuous laminar flow was used that showed susceptibility artefacts close to the tubes (overestimation of perfusion adjacent to vessels[8]). In patients, residual tumor was depicted intraoperatively by DSC-MRI[8], which is independent of brain shift and surgically induced disruption of the blood brain barrier and was proven by histology. In a third step, the reliability of intraoperatively acquired data was demonstrated in a series of patients with high grade gliomas who had undergone pre- and intraoperative DSC-MRI with some residual tumor in the early intraoperative resection control[8,9]. Ratios of identical areas within the tumor tissue

did not differ significantly between pre- and intraoperatively acquired data. Furthermore, there was a high correlation of the analyzed rCBV and rCBF ratios between pre- and intraoperative MRI exams. Intraoperatively, flexible two-channel surface coils were used, whereby one part was placed below the patient's head at the beginning of the operation and the second part adjusted prior to intraoperative scanning on the craniotomy defect, both draped in a sterile fashion. DSC-MRI was performed in 1 min 20 s, which did not extend overall intraoperative MR imaging. Intraoperative sedation (such as propofol anesthesia) reduces the absolute values of CBF and CBV; however, the ratios between tumor and unaffected contralateral tissue remain constant[30]. DSC-MRI can be repeated various times as previously used contrast agent leads to a desired saturation of T1 effects but does not influence T2*-weighted images.

DCE-MRI

Dynamic contrast-enhanced T1-weighted perfusion MR imaging (DCE-MRI)[31-33] is the other commonly used perfusion technique. In DCE-MRI, k-trans is analyzed, which is the transfer coefficient (endothelial permeability surface product). DCE-MRI requires various sampling points over time and usually takes much longer than DSC-MRI. T1 is reduced by clinically used contrast agents, leading to a signal intensity increase in T1-weighted images. Thus, DCE-MRI measures contrast agent concentration as a function of time. Very recently, DCE-MRI was used intraoperatively at a 3 T MR scanner[10]. The used setup took 3 min and 45 s for the perfusion sequence. In addition to a pharmacokinetic modelling, the authors analyzed the slope of the signal intensity increase in these T1-weighted images. Residual solid tumor could be distinguished from surgically induced contrast enhancement at the rim of the resection border by a quickly climbing slope in tumors, compared to a low-amplitude undulating curve in brain tissue as proven by histology. This may have great potential as it is obviously much easier to apply and analysis of the slope of contrast enhancement does not require any additional software as such programs come with the scanner software. However, it still has to be proven whether or not DCE-MRI can be repeatedly applied in the unlikely event of multiple resection controls, whether analysis is affected by commonly used absorbable hemostats (such as surgical®, Ethicon 360), and also if it can reliably differentiate other sources of contrast enhancement over time, such as bleedings.

CONCLUSION

The goal in brain tumor surgery is to remove the maximum achievable amount of the tumor, preventing damage to "eloquent" brain regions, as the amount of brain tumor resection is one of the prognostic factors for time to tumor progression and median survival[1,2]. Preoperatively acquired MR images can nicely delineate the tumor extent and adjacent anatomical structures. The application of an operating microscope in the late 1950s[34] revolutionized neurosurgery. Further advances included computer-assisted devices for surgical navigation[4,5] and, more recently, intraoperative imaging[6] to incorporate and correct for brain shift during the resection of the lesion. However, surgically induced contrast enhancement along the rim of the resection cavity[7] hampers interpretation of these intraoperatively acquired MR images. To overcome this uncertainty, perfusion techniques have been introduced. DSC-MRI is a T2*-weighted technique that enables calculation of rCBF and rCBV maps. The measurement takes only 1 min 20 s and therefore does not extend the overall scanning procedure. It can be applied various times as it is independent of T1-effects after saturation, has proven to be as reliable as preoperatively performed DSC-MRI[8,9], and can distinguish residual tumor from surgically induced artefacts. DCE-MRI has also been used intraoperatively as an alternative[10]. The beauty of this approach that requires more time than DSC-MRI (also at 3 T) is that there is a by-product with the acquired T1-weighted images as the slope of contrast enhancement can easily be analyzed without the need for additional software. A quickly climbing slope depicts residual tumor tissue. However, it still has to be proven that DCE-MRI can be repeatedly applied, that analysis is unaffected by commonly used absorbable hemostats (such as surgical®, Ethicon 360), and that it can also reliably differentiate other sources of contrast enhancement over time, such as bleedings. Both techniques can differentiate residual tumor from surgically induced chances at the rim of the resection cavity and thus overcome the remaining uncertainty of intraoperative MRI in high grade brain tumor resection.

REFERENCES

1 **Keles GE**, Anderson B, Berger MS. The effect of extent of resection on time to tumor progression and survival in patients with glioblastoma multiforme of the cerebral hemisphere. *Surg Neurol* 1999; **52**: 371-379 [PMID: 10555843 DOI: 10.1016/S0090-3019(99)00103-2]

2 **Sanai N**, Berger MS. Operative techniques for gliomas and the value of extent of resection. *Neurotherapeutics* 2009; **6**: 478-486 [PMID: 19560738 DOI: 10.1016/j.nurt.2009.04.005]

3 **Rubin JM**, Mirfakhraee M, Duda EE, Dohrmann GJ, Brown F. Intraoperative ultrasound examination of the brain. *Radiology* 1980; **137**: 831-832 [PMID: 6255514]

4 **Roberts DW**, Strohbehn JW, Hatch JF, Murray W, Kettenberger H. A frameless stereotaxic integration of computerized tomographic imaging and the operating microscope. *J Neurosurg* 1986; **65**: 545-549 [PMID: 3531430 DOI: 10.3171/jns.1986.65.4.0545]

5 **Watanabe E**, Watanabe T, Manaka S, Mayanagi Y, Takakura K. Three-dimensional digitizer (neuronavigator): new equipment for computed tomography-guided stereotaxic surgery. *Surg Neurol* 1987; **27**: 543-547 [PMID: 3554569 DOI: 10.1016/0090-3019(87)90152-2]

6 **Black PM**, Moriarty T, Alexander E, Stieg P, Woodard EJ, Gleason PL, Martin CH, Kikinis R, Schwartz RB, Jolesz FA. Development and implementation of intraoperative magnetic resonance imaging and its neurosurgical applications.

Neurosurgery 1997; **41**: 831-842; discussion 842-845 [PMID: 9316044 DOI: 10.1097/00006123-199710000-00013]

7 **Knauth M**, Aras N, Wirtz CR, Dörfler A, Engelhorn T, Sartor K. Surgically induced intracranial contrast enhancement: potential source of diagnostic error in intraoperative MR imaging. *AJNR Am J Neuroradiol* 1999; **20**: 1547-1553 [PMID: 10512244]

8 **Ulmer S**, Helle M, Jansen O, Mehdorn HM, Nabavi A. Intraoperative dynamic susceptibility contrast weighted magnetic resonance imaging (iDSC-MRI)-Technical considerations and feasibility. *Neuroimage* 2009; **45**: 38-43 [PMID: 19100843 DOI: 10.1016/j.neuroimage.2008.11.021]

9 **Ulmer S**, Hartwigsen G, Riedel C, Jansen O, Mehdorn HM, Nabavi A. Intraoperative dynamic susceptibility contrast MRI (iDSC-MRI) is as reliable as preoperatively acquired perfusion mapping. *Neuroimage* 2010; **49**: 2158-2162 [PMID: 19900562 DOI: 10.1016/j.neuroimage.2009.10.084]

10 **Özduman K**, Yıldız E, Dinçer A, Sav A, Pamir MN. Using intraoperative dynamic contrast-enhanced T1-weighted MRI to identify residual tumor in glioblastoma surgery. *J Neurosurg* 2014; **120**: 60-66 [PMID: 24138206 DOI: 10.3171/2013.9.JNS121924]

11 **Stummer W**, Pichlmeier U, Meinel T, Wiestler OD, Zanella F, Reulen HJ. Fluorescence-guided surgery with 5-aminolevulinic acid for resection of malignant glioma: a randomised controlled multicentre phase III trial. *Lancet Oncol* 2006; **7**: 392-401 [PMID: 16648043 DOI: 10.1016/S1470-2045(06)70665-9]

12 **Roberts DW**, Valdés PA, Harris BT, Fontaine KM, Hartov A, Fan X, Ji S, Lollis SS, Pogue BW, Leblond F, Tosteson TD, Wilson BC, Paulsen KD. Coregistered fluorescence-enhanced tumor resection of malignant glioma: relationships between δ-aminolevulinic acid-induced protoporphyrin IX fluorescence, magnetic resonance imaging enhancement, and neuropathological parameters. Clinical article. *J Neurosurg* 2011; **114**: 595-603 [PMID: 20380535 DOI: 10.3171/2010.2.JNS091322]

13 **Steinmeier R**, Fahlbusch R, Ganslandt O, Nimsky C, Buchfelder M, Kaus M, Heigl T, Lenz G, Kuth R, Huk W. Intraoperative magnetic resonance imaging with the magnetom open scanner: concepts, neurosurgical indications, and procedures: a preliminary report. *Neurosurgery* 1998; **43**: 739-747; discussion 747-748 [PMID: 9766299 DOI: 10.1097/00006123-199810000-00005]

14 **Tronnier VM**, Wirtz CR, Knauth M, Lenz G, Pastyr O, Bonsanto MM, Albert FK, Kuth R, Staubert A, Schlegel W, Sartor K, Kunze S. Intraoperative diagnostic and interventional magnetic resonance imaging in neurosurgery. *Neurosurgery* 1997; **40**: 891-900; discussion 900-902 [PMID: 9149246 DOI: 10.1097/00006123-199705000-00001]

15 **Hall WA**, Martin AJ, Liu H, Pozza CH, Casey SO, Michel E, Nussbaum ES, Maxwell RE, Truwit CL. High-field strength interventional magnetic resonance imaging for pediatric neurosurgery. *Pediatr Neurosurg* 1998; **29**: 253-259 [PMID: 9917543 DOI: 10.1159/000028732]

16 **Nimsky C**, Ganslandt O, Von Keller B, Romstöck J, Fahlbusch R. Intraoperative high-field-strength MR imaging: implementation and experience in 200 patients. *Radiology* 2004; **233**: 67-78 [PMID: 15317949 DOI: 10.1148/radiol.2331031352]

17 **Sutherland GR**, Kaibara T, Louw D, Hoult DI, Tomanek B, Saunders J. A mobile high-field magnetic resonance system for neurosurgery. *J Neurosurg* 1999; **91**: 804-813 [PMID: 10541238 DOI: 10.3171/jns.1999.91.5.0804]

18 **Hadani M**, Spiegelman R, Feldman Z, Berkenstadt H, Ram Z. Novel, compact, intraoperative magnetic resonance imaging-guided system for conventional neurosurgical operating rooms. *Neurosurgery* 2001; **48**: 799-807; discussion 807-809 [PMID: 11322440]

19 **Stadlbauer A**, Buchfelder M, Doelken MT, Hammen T, Ganslandt O. Magnetic resonance spectroscopic imaging for visualization of the infiltration zone of glioma. *Cent Eur Neurosurg* 2011; **72**: 63-69 [PMID: 20635312 DOI: 10.1055/s-0030-1253410]

20 **Pamir MN**, Özduman K, Yıldız E, Sav A, Dinçer A. Intraoperative magnetic resonance spectroscopy for identification of residual tumor during low-grade glioma surgery: clinical article. *J Neurosurg* 2013; **118**: 1191-1198 [PMID: 23432196 DOI: 10.3171/2013.1.JNS111561]

21 **Belliveau JW**, Rosen BR, Kantor HL, Rzedzian RR, Kennedy DN, McKinstry RC, Vevea JM, Cohen MS, Pykett IL, Brady TJ. Functional cerebral imaging by susceptibility-contrast NMR. *Magn Reson Med* 1990; **14**: 538-546 [PMID: 2355835 DOI: 10.1002/mrm.1910140311]

22 **Rosen BR**, Belliveau JW, Vevea JM, Brady TJ. Perfusion imaging with NMR contrast agents. *Magn Reson Med* 1990; **14**: 249-265 [PMID: 2345506 DOI: 10.1002/mrm.1910140211]

23 **Edelman RR**, Mattle HP, Atkinson DJ, Hill T, Finn JP, Mayman C, Ronthal M, Hoogewoud HM, Kleefield J. Cerebral blood flow: assessment with dynamic contrast-enhanced T2*-weighted MR imaging at 1.5 T. *Radiology* 1990; **176**: 211-220 [PMID: 2353094]

24 **Conturo TE**, Akbudak E, Kotys MS, Chen ML, Chun SJ, Hsu RM, Sweeney CC, Markham J. Arterial input functions for dynamic susceptibility contrast MRI: requirements and signal options. *J Magn Reson Imaging* 2005; **22**: 697-703 [PMID: 16261571 DOI: 10.1002/jmri.20457]

25 **Østergaard L**. Principles of cerebral perfusion imaging by bolus tracking. *J Magn Reson Imaging* 2005; **22**: 710-717 [PMID: 16261573 DOI: 10.1002/jmri.20460]

26 **Provenzale JM**, Wang GR, Brenner T, Petrella JR, Sorensen AG. Comparison of permeability in high-grade and low-grade brain tumors using dynamic susceptibility contrast MR imaging. *AJR Am J Roentgenol* 2002; **178**: 711-716 [PMID: 11856703 DOI: 10.2214/ajr.178.3.1780711]

27 **Sorensen AG**, Copen WA, Ostergaard L, Buonanno FS, Gonzalez RG, Rordorf G, Rosen BR, Schwamm LH, Weisskoff RM, Koroshetz WJ. Hyperacute stroke: simultaneous measurement of relative cerebral blood volume, relative cerebral blood flow, and mean tissue transit time. *Radiology* 1999; **210**: 519-527 [PMID: 10207439 DOI: 10.1148/radiology.210.2.r99fe06519]

28 **Sugahara T**, Korogi Y, Kochi M, Ikushima I, Hirai T, Okuda T, Shigematsu Y, Liang L, Ge Y, Ushio Y, Takahashi M. Correlation of MR imaging-determined cerebral blood volume maps with histologic and angiographic determination of vascularity of gliomas. *AJR Am J Roentgenol* 1998; **171**: 1479-1486 [PMID: 9843274 DOI: 10.2214/ajr.171.6.9843274]

29 **Emblem KE**, Nedregaard B, Nome T, Due-Tonnessen P, Hald JK, Scheie D, Borota OC, Cvancarova M, Bjornerud A. Glioma grading by using histogram analysis of blood volume heterogeneity from MR-derived cerebral blood volume maps. *Radiology* 2008; **247**: 808-817 [PMID: 18487536 DOI: 10.1148/radiol.2473070571]

30 **Rasmussen M**, Juul N, Christensen SM, Jónsdóttir KY, Gyldensted C, Vestergaard-Poulsen P, Cold GE, Østergaard L. Cerebral blood flow, blood volume, and mean transit time responses to propofol and indomethacin in peritumor and contralateral brain regions: perioperative perfusion-weighted magnetic resonance imaging in patients with brain tumors. *Anesthesiology* 2010; **112**: 50-56 [PMID: 19952725 DOI: 10.1097/ALN.0b013e3181c38bd3]

31 **Brix G**, Semmler W, Port R, Schad LR, Layer G, Lorenz WJ. Pharmacokinetic parameters in CNS Gd-DTPA enhanced MR imaging. *J Comput Assist Tomogr* 1991; **15**: 621-628 [PMID: 2061479 DOI: 10.1097/00004728-199107000-00018]

32 **Bullock PR**, Mansfield P, Gowland P, Worthington BS, Firth JL. Dynamic imaging of contrast enhancement in brain tumors. *Magn Reson Med* 1991; **19**: 293-298 [PMID: 1881318 DOI: 10.1002/mrm.1910190217]

33 **Donahue KM**, Weisskoff RM, Parmelee DJ, Callahan RJ,

Wilkinson RA, Mandeville JB, Rosen BR. Dynamic Gd-DTPA enhanced MRI measurement of tissue cell volume fraction. *Magn Reson Med* 1995; **34**: 423-432 [PMID: 7500882 DOI: 10.1002/mrm.1910340320]

34 **Kriss TC**, Kriss VM. History of the operating microscope: from magnifying glass to microneurosurgery. *Neurosurgery* 1998; **42**: 899-907; discussion 907-908 [PMID: 9574655 DOI: 10.1097/00006123-199804000-00116]

P- Reviewer: Sivak S **S- Editor**: Ji FF
L- Editor: Roemmele A **E- Editor**: Liu SQ

World Journal of Radiology

Submit a Manuscript: http://www.wjgnet.com/esps/
Help Desk: http://www.wjgnet.com/esps/helpdesk.aspx
DOI: 10.4329/wjr.v6.i8.544

World J Radiol 2014 August 28; 6(8): 544-566
ISSN 1949-8470 (online)

REVIEW

Gastrointestinal imaging-practical magnetic resonance imaging approach

Baodong Liu, Miguel Ramalho, Mamdoh AlObaidy, Kiran K Busireddy, Ersan Altun, Janaka Kalubowila, Richard C Semelka

Baodong Liu, Miguel Ramalho, Mamdoh AlObaidy, Kiran K Busireddy, Ersan Altun, Janaka Kalubowila, Richard C Semelka, Department of Radiology, University of North Carolina at Chapel Hill, North Carolina, NC 27599-7510, United States
Author contributions: Liu B, Ramalho M, AlObaidy M, Busireddy KK, Altun E, Kalubowila J and Semelka RC equally contributed to this work; including literature review, manuscript writing, manuscript editing, figures collection and writing figures captions.
Correspondence to: Richard C Semelka, MD, Department of Radiology, University of North Carolina at Chapel Hill, 2001 Old Clinic Bldg., CB 7510, Chapel Hill, North Carolina, NC 27599-7510, United States. richsem@med.unc.edu
Telephone: +1-919-9669676 Fax: +1-919-8437147
Received: February 11, 2014 Revised: April 15, 2014
Accepted: May 31, 2014
Published online: August 28, 2014

Abstract

Over the past two decades, advances in cross-sectional imaging such as computed tomography and magnetic resonance imaging (MRI) have dramatically changed the concept of gastrointestinal imaging. MR is playing an increasing role in the evaluation of gastrointestinal disorders. MRI combines the advantages of excellent soft-tissue contrast, noninvasiveness, functional information and lack of ionizing radiation. Furthermore, recent developments of MRI have led to improved spatial and temporal resolution as well as decreased motion artifacts. In this article we describe the technical aspects of gastrointestinal MRI and present a practical approach for a well-known spectrum of gastrointestinal disease processes.

Key words: Magnetic resonance imaging; Crohn's disease; Celiac disease; Appendicitis; Diverticulitis; Rectal cancer; Gastric tumors; Small bowel tumors

Core tip: The implementation of fast and ultra-fast sequences and dedicated advanced imaging protocols render magnetic resonance imaging (MRI) an excellent tool for gastrointestinal (GI) imaging. State of the art MRI/magnetic resonance enterography has rapidly emerged as successful gastrointestinal imaging modality, offering detailed anatomic and morphologic information and also permitting evaluation of extra-luminal manifestation and extension of disease. The lack of ionizing radiation makes MRI the preferred modality in many GI disease processes. In this article we describe the technical aspects of gastrointestinal MRI and present a practical approach for a well-known spectrum of gastrointestinal disease processes.

Liu B, Ramalho M, AlObaidy M, Busireddy KK, Altun E, Kalubowila J, Semelka RC. Gastrointestinal imaging-practical magnetic resonance imaging approach. *World J Radiol* 2014; 6(8): 544-566 Available from: URL: http://www.wjgnet.com/1949-8470/full/v6/i8/544.htm DOI: http://dx.doi.org/10.4329/wjr.v6.i8.544

INTRODUCTION

Medical imaging of the gastrointestinal (GI) tract is crucial for the diagnosis of GI diseases. Historically, barium techniques have been the only available method. Although many diagnoses have been made on the basis of these exams, the diagnostic performance of these exams for certain abnormalities has been disappointing[1].

Over the past two decades, advances in cross-sectional imaging such as computed tomography (CT) and magnetic resonance imaging (MRI) have dramatically changed the concept of GI imaging. Recently, developments in endoscopic techniques, especially the advent of capsule

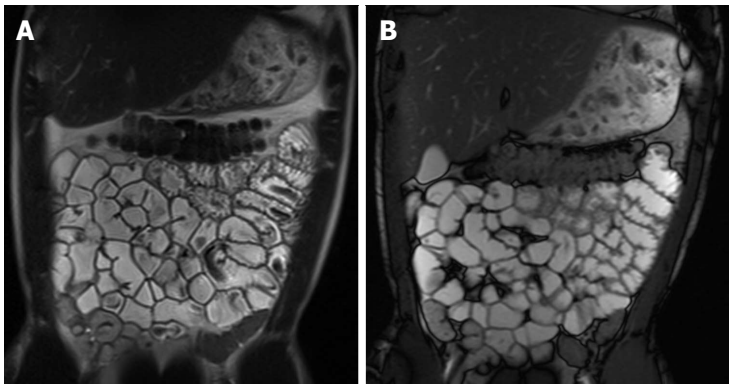

Figure 1 Coronal T2-weighted single shot fast spin echo and coronal balanced steady state free precession images. Good bowel distension is achieved with the administration of peroral fluid (A and B). Balanced steady state free precession sequence (B) is robust to flow voids; in addition to its ability to demonstrate fine anatomical details including bowel thickness, mesenteric vessels and lymph nodes; even without the use of spasmolytic agents.

endoscopy (CE) have made it possible to provide direct mucosal visualization of the GI tract. However, CE also has such limitations in disease localization, and is contraindicated in patients with suspected of bowel stricture or obstruction[1,2].

MR and CT techniques optimized for small bowel imaging are playing an increasing role in the evaluation of gastrointestinal disorders. Several studies have shown the advantage of these techniques over traditional barium fluoroscopic examinations. Cross-sectional techniques have several advantages, including their ability to display the entire thickness of the gastric and bowel wall, visualize the deep pelvis ileal loops without superimposition, and evaluate the mesentery and perienteric fat. Another intrinsic advantage is the possibility to assess solid organs and provide a global overview of the abdominopelvic cavity.

The preference of MR over CT is mainly based on available resources and public policies. However, similar to fluoroscopic procedures, CT is associated with patients' radiation exposure. With the increasing awareness of radiation exposure, there has been a more global interest in implementing techniques that either reduce or eliminate radiation exposure[3]. This may be of particular importance in radiosensitive patient population with chronic inflammatory bowel disease; who may require multiple studies over a lifetime[4]. As a result, MRI has become increasingly important as a method of evaluating various gastrointestinal disease processes[5].

MRI combines the advantages of excellent soft-tissue contrast, noninvasiveness, functional information and lack of ionizing radiation. Furthermore, recent developments of MRI have led to improved spatial and temporal resolution as well as decreased motion artifacts[6]. In this article we describe technical aspects of gastrointestinal MRI and present a practical approach for a well-known spectrum of gastrointestinal disease processes.

PRACTICAL ASPECTS OF GASTROINTESTINAL MRI TECHNIQUE

Similar to other imaging techniques, adequate luminal distension is desirable since poorly distended loops can simulate[7] or hide pathologic processes; especially in less experienced hands. Two different techniques to provide sufficient luminal distension of the small bowel have been proposed: MR enteroclysis and MR enterography. MR enteroclysis is associated with excellent image quality because of superb bowel distension achieved by fluid administration after nasojejunal intubation. However, the placement of the catheter is unpleasant and stressful for the patient. The improved distention achieved with enteroclysis does not necessarily translate into an improvement in diagnostic effectiveness[8,9] and peroral fluid administration results in effective and most often satisfactory means of achieving small bowel distention. One advantage of MR enteroclysis may reside in the detection of mesenteric small bowel tumors[10,11].

Three groups of contrast agents can be utilized to achieve distension and are classified as positive (bright lumen), negative (dark lumen), or biphasic contrast agents. Biphasic contrast agents (water-based) are usually preferred because they are easy to implement and provide excellent signal characteristics, resulting in bright lumen on T2-weighted and dark lumen on T1-weighted sequences. Tap water is frequently used as a biphasic contrast agent, especially when imaging the upper gastrointestinal segment (stomach, duodenum and proximal jejunum); however, it is rapidly reabsorbed in the small intestine, leading to a poor distension of the distal jejunum and ileum. In order to slow intestinal absorption of water, higher-osmolality and viscosity agents are routinely added[12-14]. After a 4 to 6-h fast, patients are asked to drink between 1000 mL and 1500 mL of intraluminal contrast (Figure 1); 45 to 55 min prior to examination. Metoclopramide (20 mg) may be added directly to the oral contrast to promote gastric emptying. Adverse effects are rare, usually mild and transitory, and experienced mainly after the termination of the MR examination[15].

Some patients cannot tolerate the ingestion of high volumes of oral contrast; in our experience, we found that luminal distension is not as critical as on CT and the MR examination can still be performed even if only a

small volume has been ingested.

Patients undergoing magnetic resonance enterography (MRE) should be examined in prone position. This position may facilitate separation of small bowel loops while decreasing the volume of peritoneal cavity to be image and, as a result, the number of coronal sections to be acquired[16]. Hence, acquisition times and consequently the time span for breath holding can be decreased. However, many patients may not tolerate lying prone in the MR scanner, and therefore supine position is almost always adequate.

Gastrointestinal MR evaluation is based on the ultrafast imaging generally applied for body MRI. Body MRI is still based on T1-weighted and T2-weighted sequences plus or minus fat-suppression and postgadolinium T1-weighted sequences. A combination of single-shot fast/turbo spin-echo T2-weighted and gradient recalled echo (GRE) T1-weighted sequences with intravenous gadolinium enhancement and fat-suppression result in consistent image quality of the gastrointestinal tract. Two- or three-dimensional balanced steady-state free precession (bSSFP) sequences are additionally collected as part of the MRE protocol.

Single-Shot turbo spin echo (TSE)/FSE T2-weighted sequences are very robust to motion and usually acquired with and without fat-saturation. These sequences have high sensitivity for fluid and are crucial to depict edema in or adjacent to the bowel wall. This is especially important in Crohn's disease (CD), which can be regarded as a marker for active inflammation. Single-shot sequences are susceptible to flow artifacts, and thus intraluminal flow voids can be seen (Figure 1).

Because bSSFP sequences are relatively robust with regard to motion artifacts and intraluminal flow voids, these sequences are performed in the beginning of the study prior to glucagon or intravenous contrast administration. These sequences can be performed quickly and are complementary to single-shot TSE/FSE sequences and the preferred pulse sequence to evaluate the mesentery. The ratio of T1/T2 contrast provides images that appear primarily T2-weighted, with very high signal for all types of fluid. This feature allows good evaluation of the bowel wall, particularly in the definition of edema and of bowel wall layering appearance. Cine-analysis can also be performed with this technique allowing supplementary functional information. We generally acquire 15-25 frames per section location during free breathing. These images may then be displayed as a cine loop to assess bowel motility to exclude or confirm fixed stenoses, segmental dilatation, and detect adhesions.

T1-weighted GRE MRI represents the core of the body MR protocol. Since these sequences are quite prone to bowel motion artifacts, spasmolytic agents (*e.g.*, Glucagon® or Buscopan®) should be administered intravenously immediately before image acquisition. Buscopan® is less expensive; however, it is not Food and Drug Administration approved and therefore not available in the United States. These sequences are performed as either 2D or 3D techniques, and on newer MR systems, the most commonly used is the 3D-GRE with fat-suppression. Post-contrast coronal and axial images are also acquired. Our protocol includes an arterial and interstitial phase in the coronal plane and an enteric (early hepatic-venous) phase (circa 50 s) in the axial plane. Gadolinium-enhanced T1-weighted images are helpful to detect both intestinal tumors and inflammatory bowel diseases with high sensitivity[17].

Diffusion-weighted imaging (DWI) has been increasingly used for body MRI. Initial studies underline a possible value of DWI also for small bowel imaging, aiding in the assessment of disease activity[18,19]. A set of coronal diffusion-weighted images (b = 0-50 s/mm^2; b = 600-800 s/mm^2) may be added to the protocol, depending on the indication of the examination and preference of the radiologist. This is especially important in pregnant patients those with contraindications to gadolinium administration (Figure 2).

PRACTICAL APPROACH TO INFLAMMATORY CONDITIONS-SMALL BOWEL

CD

CD is a chronic relapsing inflammatory disease of the gastrointestinal tract involving all layers of the bowel wall and may be classified as active inflammatory (without fistulas or strictures), penetrating, or fibrostenotic disease[20]. Although any segment of the gastrointestinal tract may be involved with CD, it most commonly involves the terminal ileum, and frequently in association with disease in the right colon.

Endoscopy and histologic examination have served as the standard approach for the diagnosis of CD; however, diagnosing lesions in the small bowel between the distal duodenum and mid ileum has been a challenge. Furthermore, the major disadvantage of endoscopic methods endoscopic tests and biopsies will evaluate the mucosa but do not evaluate inflammation or fibrosis within the submucosa or deeper tissues. Currently, CT enterography and MRE are the only two imaging modalities that enable the visualization of submucosal tissues throughout the entire small bowel; however, as stated above, MRE does not expose patients to ionizing radiation and it provides additional technical and diagnostic advantages[21].

The following important questions can be addressed on MRE: (1) extent of small and large bowel involvement; (2) distinction between active inflammatory and fibrotic stricturing disease; (3) recognition of penetrating disease ± extramural complications; (4) evaluation of response to medical therapy; and (5) detection of recurrent disease following surgery.

A relatively simple and accurate approach for evaluation of CD activity is based on the association of T2-weighted and post-gadolinium T1-weighted sequences. This combination allows comprehensive evaluation and discrimination between quiescent disease and active inflammation and for evaluation of complications includ-

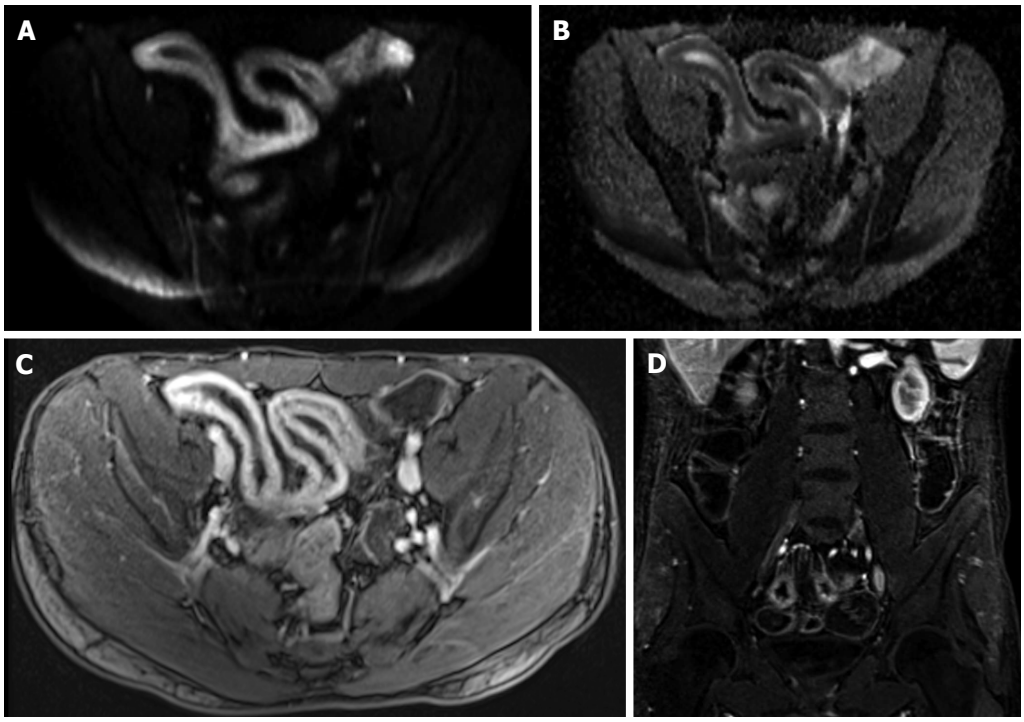

Figure 2 Active distal ileal Crohn's disease. Axial diffusion weighted imaging (A) (*b* = 150) and (B) apparent diffusion coefficient map as well as (C) axial and (D) coronal fat-suppressed post-gadolinium 3D-GRE T1-weighted images. There is a long segment of distal ilial diffuse thickening associated with diffusion restriction (A and B) as well as significant contrast enhancement (C) and vasa recta engorgement (comb sign) (D) in keeping with active Crohn's disease. GRE: Gradient recalled echo.

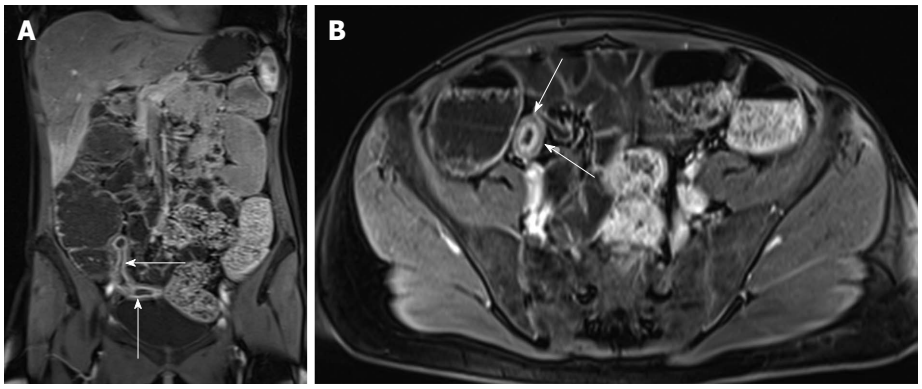

Figure 3 Enhancement of bowel wall layers in active Crohn's disease. Coronal (A) and (B) axial fat-suppressed post-gadolinium 3D-GRE T1-weighted images during the (A) arterial and (B) enteric in a patient with active Crohn's disease. There is extensive mucosal enhancement involving the affected terminal ileum (arrows, A), reflecting active disease. Enteric phase images (B) shows serosal enhancement providing the tri-laminar appearance of active disease (arrows, B). GRE: Gradient recalled echo.

ing abscesses or fistulas[21,22].

Findings perceived on post-gadolinium T1-weighted images

Increased mucosal enhancement has long been one of the most important findings and is the most sensitive finding of disease activity, which may approach 100% sensitivity[23-27]. Imaging findings of mucosal enhancement; bowel wall edematous thickening (> 3 mm); and enhancement of different bowel layers, termed "mural stratification", are classic features of active small bowel disease[28,29] (Figure 3). Quantitative bowel enhancement parameters were found to correlate highly with histologic and endoscopic disease severity[30].

Other findings include stranding extending into the mesenteric border fat and engorgement of the hyperemic vasa recta surrounding the inflamed bowel segment (comb sign) and reactively enlarged and hyper-enhancing mesenteric lymph nodes.

Perceived on T2-weighted images

Bowel wall thickening with increased T2-signal within or adjacent to the abnormal bowel on fat-suppressed images indicates active inflammation[31]. Other sings include fluid accumulation in adjacent intraperitoneal and mesenteric spaces (Figure 4).

Fibrofatty proliferation or creeping of the mesenteric fat along the mesentery and onto the involved bowel seg-

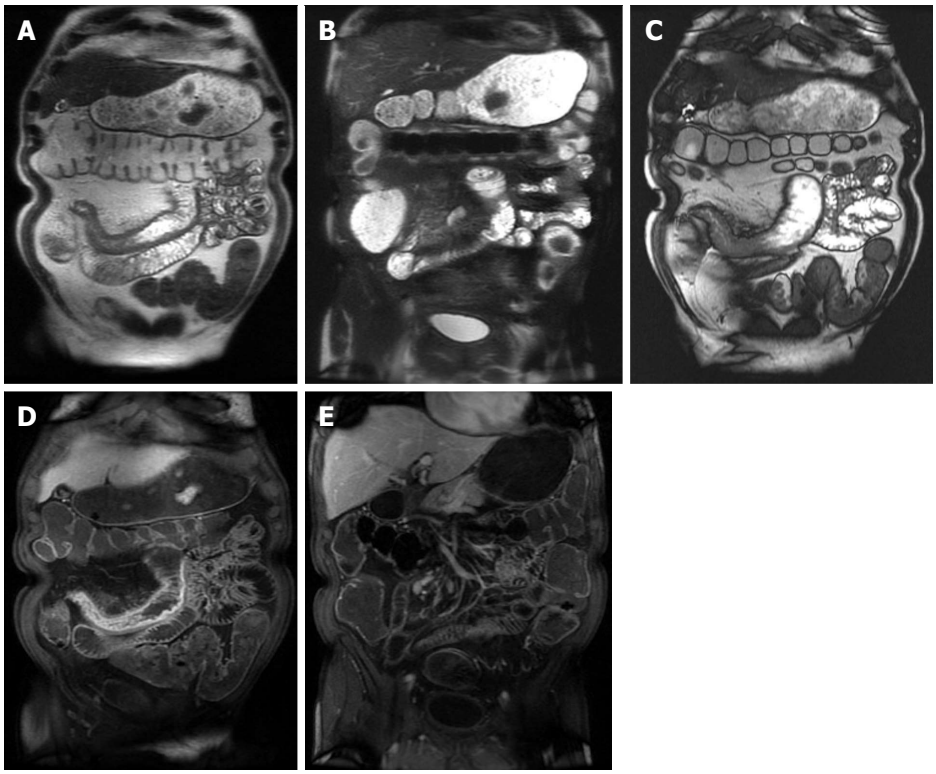

Figure 4 Active Crohn's disease. A and B: Coronal T2-weighted single shot fast spin echo without and with fat suppression and © coronal balanced steady state free precession image as well as coronal fat-suppressed post-gadolinium 3D-GRE T1-weighted images during the (D) arterial and E: interstitial phases. There is abnormal bowel wall thickening and edema involving distal ileal segments, associated with small fluid collection in the adjacent mesentery (A and B), engorgement of the mesenteric vessels (comb sign) (C-E), and extensive mucosal enhancement (D and E), in addition to the presence of enhancing mesenteric lymph nodes, in keeping with active Crohn's disease.

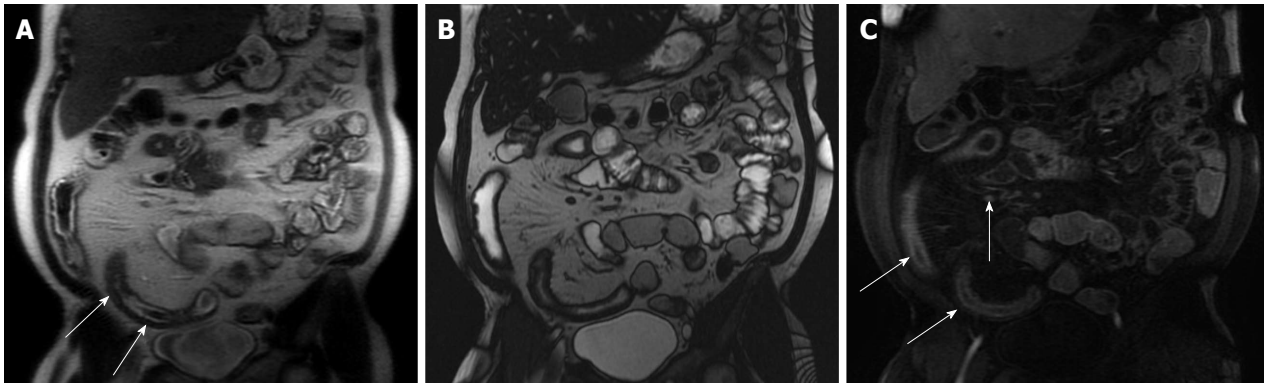

Figure 5 Active Crohn's disease. A: Coronal T2-weighted single shot fast spin echo and (B) coronal balanced steady state free precession (bSSFP) images as well as (C) coronal fat-suppressed post-gadolinium 3D-GRE T1-weighted images during the interstitial phase. There is an abnormal segment of distal ileal thickening with diffuse submucosal increased T2 signal intensity (arrows, A) displaying high signal intensity, consistent with edema. The bSSFP image (B) doesn't demonstrate submucosal edema, but clearly depicts mesenteric lymph nodes and comb sign, associated with extensive mucosal enhancement (arrows, C), reflecting disease activity. Fibrofatty proliferation around the affected ileal segments is also seen. GRE: Gradient recalled echo.

ment (Figure 5) suggests a chronically inflamed bowel loop, a sign mostly seen in chronic disease. However, when it is associated with engorged perpendicular distal mesenteric vessels (comb sign), it is considered surgically pathognomonic for the disease and highly specific for active CD[32]. Comb sign is usually well depicted on bSSFP sequences (Figure 5).

Practical interpretive approach to a thickened bowel wall segment

Active inflammation: Bowel wall thickening and enhancement on post-gadolinium T1-weighted images, plus high signal intensity on T2-weighted fat-suppressed images[21] (Figures 4 and 5).

Chronic disease without active inflammation: Bowel wall thickening and reduced and homogeneous enhancement on post-gadolinium T1-weighted images without a layering enhancement; plus low T2-signal intensity on fat-suppressed images with possible stenosis with obstruction and occasionally sacculations or dilated amorphous bowel loops. In the fibrostenotic disease subtype, MRE

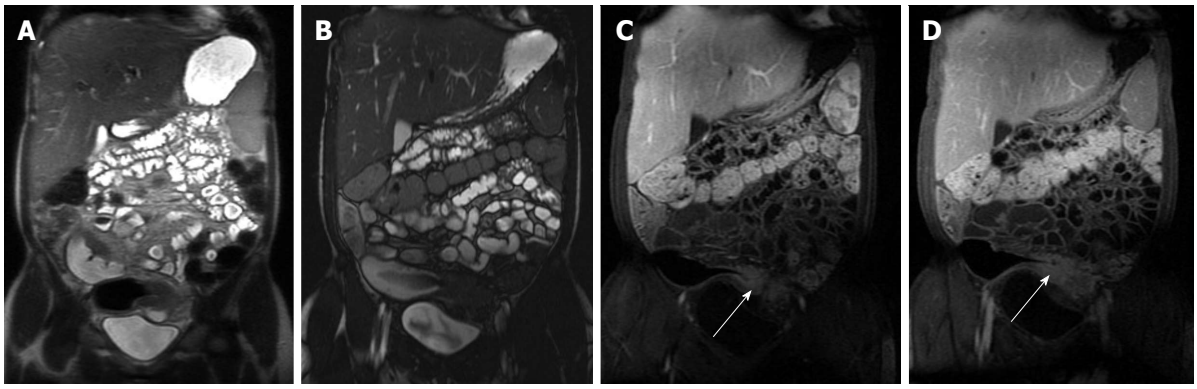

Figure 6 Chronic Crohn's disease. A: Coronal T2-weighted single shot fast spin echo and (B) coronal balanced steady state free precession (bSSFP), images as well as coronal fat-suppressed post-gadolinium 3D-GRE T1-weighted images during the (C) arterial and (D) interstitial phases. There is an intermediately low T2 signal intensity bowel wall thickening involving the distal ileum (A), also well-appreciated on bSSFP image (B), showing negligible enhancement on post-gadolinium images (arrows, C and D), consistent with chronic fibrotic segment without superimposed inflammation. A pre-stenotic dilatation is observed. GRE: Gradient recalled echo.

demonstrates a fixed narrowing of the involved bowel with associated wall thickening and marked pre-stenotic dilatation[21]. On MRE cine imaging, fibrotic strictures appear as aperistaltic bowel segment that often demonstrate fixed mural thickening and luminal narrowing; these sequences help to differentiate a fibrotic stricture from small bowel obstruction secondary to spasm associated with active inflammatory disease[33] (Figure 6).

Chronic disease with active inflammation: These features can overlap with active inflammation and sometimes only distinguished upon further short-term follow-up post-trial medical treatment. Acute on chronic involvement is suggested by marked enhancement of the mucosa with substantial low T2 signal intensity and minimal enhancement of the outer layer; therefore, appreciation of these findings may have a role in the evaluation of acute exacerbations of CD. The presence of sub-mucosal intramural fat deposition, which is also related to prior or ongoing chronic inflammation, can be accurately identified when combining features from steady state free precession as well as T2-weighted images with and without fat-suppression (Figure 7).

Complications of CD

Complications of CD are also well shown in MRE and include: fistulas, phlegmons, abscesses and bowel obstruction. Fistulas and sinus tracts are demonstrated by the high signal intensity of their fluid content on steady-state free-precession and single-shot fast/turbo spin echo T2-weighted images, and enhancement of the linear tract on the post gadolinium T1-weighted sequences. Entero-enteric (Figure 8) and entero-colic fistulas are not uncommon. Fistulous communication with adjacent pelvic organs can also be seen. They should be suspected when crowded retracted and angulated small bowel loops are appreciated; known as star sign. Deep fissuring ulcers are occasionally appreciated, and better see on bSSFP images. Extra-enteric collections and abscesses (Figures 9 and 10) can be recognized by their fluid content and increased wall enhancement on post-gadolinium images. The irregular morphology of an abscess cavity and appreciation of its rounded configuration on multiple planes allows distinction from tubular-shaped bowel.

Identifying active inflammation is rarely an interpretive problem in MRE. However, active inflammation can mask underlying fibrosis related to chronic disease of the bowel wall. In the setting of active inflammation, short-term MRE follow-up may be implemented to confirm improvements of active inflammation and to then evaluate the presence of unmasked chronic fibrotic disease[21]. It is important to identify fibrotic strictures because these are unresponsive to medical therapy and oftentimes require surgical intervention.

Assessment of inflammatory activity of CD is important to identify patients with active inflammation so that appropriate medical therapy may be prescribed. Given the advent of new medications some with serious side effects such as tumor necrosis factors alpha inhibitors, objective measures of activity are needed to justify their use and judge their effectiveness. Currently, there is no gold standard for determination of CD activity. Various authors have proposed MRE-based scoring systems for the assessment of inflammatory activity that includes features such as bowel wall thickening, lumen narrowing and the number of peri-intestinal lymph nodes[34-37]. However, these evaluation algorithms are relatively demanding, which may ultimately limit clinical utilization. Quantitative bowel enhancement parameters were found to correlate highly with histologic and endoscopic disease severity[30,38]. Although the perfusion analysis seems to be an accurate tool and correlates well with clinical parameters, it is relatively time consuming and requires special software and image post-processing. A recent study by Taylor *et al*[30] outlines another difficulty regarding perfusion analyses of the bowel wall. The use of DWI may also help in assessing disease severity and is thought to be a promising tool, especially if the use of a contrast agent is contraindicated[39].

For clinical follow-up of patients with CD, MRE is the preferred examination of choice due to lack of ionizing radiation and allowance of more frequent monitoring, which is important given the costs and side effects asso-

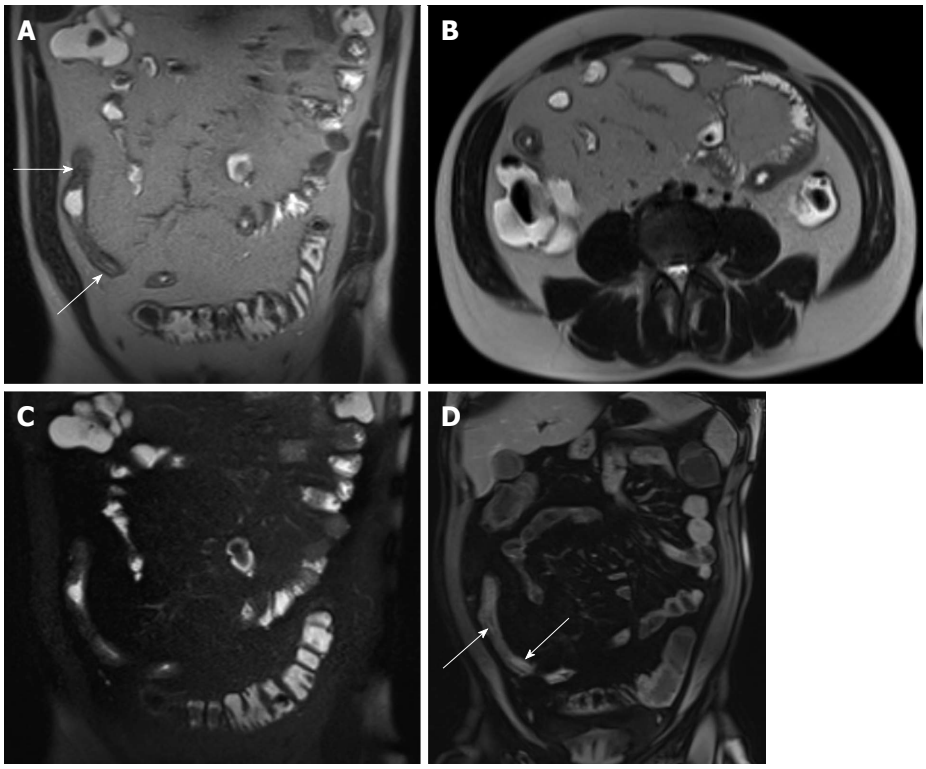

Figure 7 Acute on chronic Crohn's disease. A: Coronal and (B) axial T2-weighted single shot fast spin echo (SSFSE) as well as (C) coronal fat-suppressed T2-weighted SSFSE and (D) coronal fat-suppressed interstitial post-gadolinium 3D-GRE T1-weighted images during the interstitial phase. There is distal small bowel segment which demonstrates diffuse thickening and luminal narrowing (arrows, A), associated with submucosal high signal intensity on T2-weighted images (A and B) and with low-signal intensity on the fat-suppressed T2-weighted images (C), related to submucosal fat deposition, in keeping with chronic Crohn's disease. There is also a superimposed increased mucosal enhancement in affected bowel segments (arrows, D) and comb sign post-gadolinium images (D), reflecting disease activity, in keeping with acute on top of chronic disease. GRE: Gradient recalled echo.

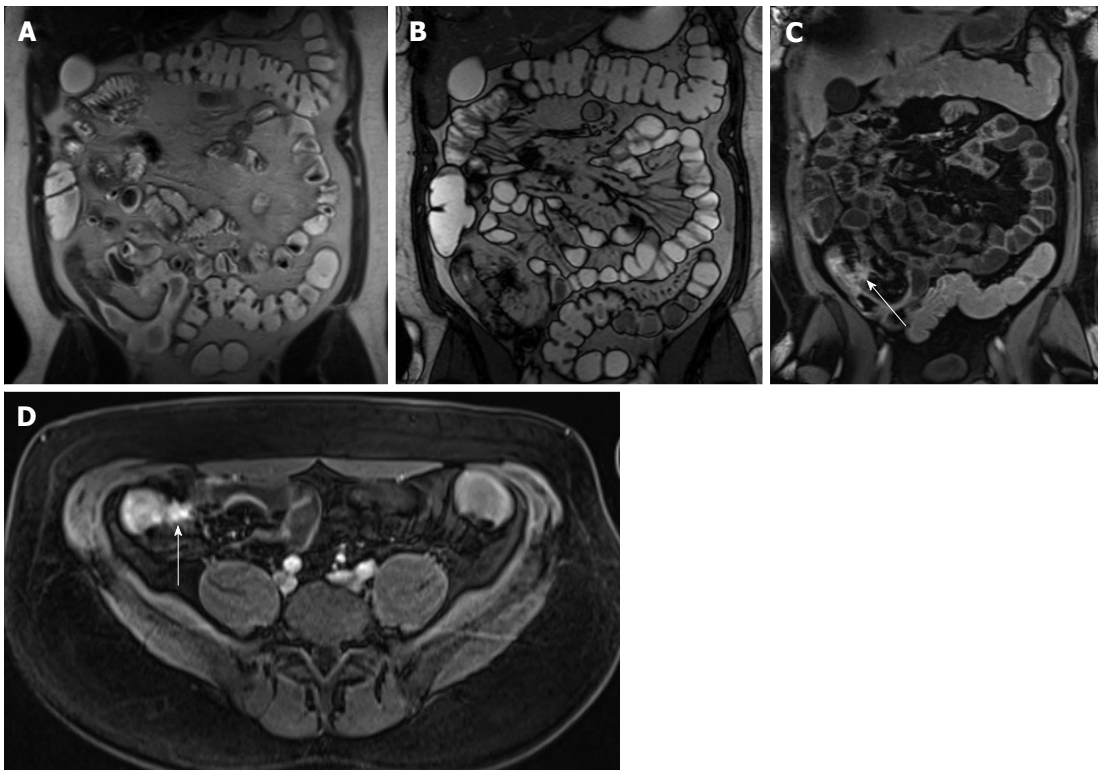

Figure 8 Enteroenteric fistula in active Crohn's disease. A: Coronal T2-weighted single shot fast spin echo and (B) coronal balanced steady state free precession images as well as (C) axial and (D) coronal fat-suppressed post-gadolinium 3D-GRE T1-weighted images during the (C) enteric and (D) interstitial phases. There is short-segment terminal ileal wall thickening (A and B), which shows extensive mucosal enhancement (C and D). There is also a linear tract extending from the involved segment to an adjacent ileal loop, showing increased enhancement, consistent with enteroenteric fistula (arrows, C and D). GRE: Gradient recalled echo.

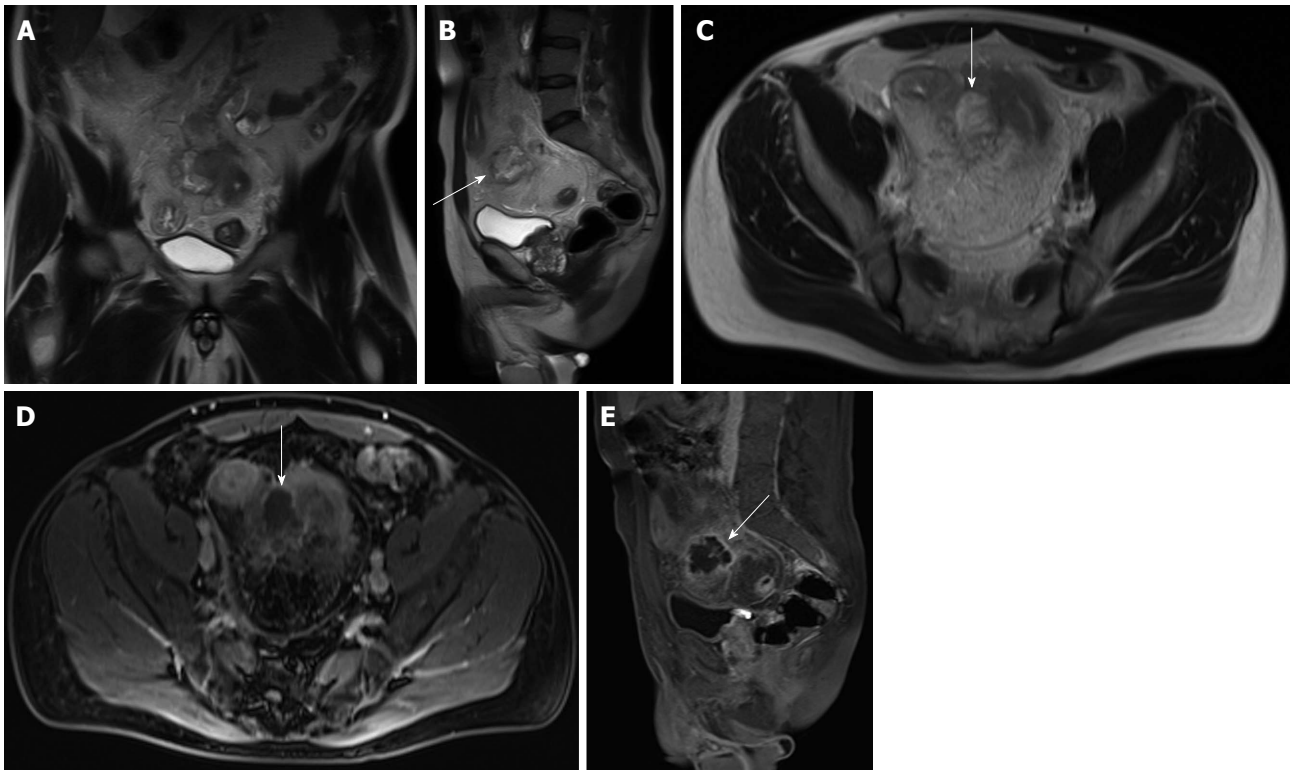

Figure 9 Abscess formation complicating active Crohn's disease. A: Coronal; B: Sagittal; C: Axial T2-weighted TSE images; D: Axial; E: Sagittal fat-suppressed post-gadolinium 3D-GRE T1-weighted images during the interstitial phase. Here is evidence of thickened small bowel loop segment and interloop mesenteric high T2 signal fluid collection (A, arrows, B and C) is noted, associated with rim enhancement (arrows, D and E) in keeping with mesenteric abscess formation complicating active Crohn's disease. GRE: Gradient recalled echo.

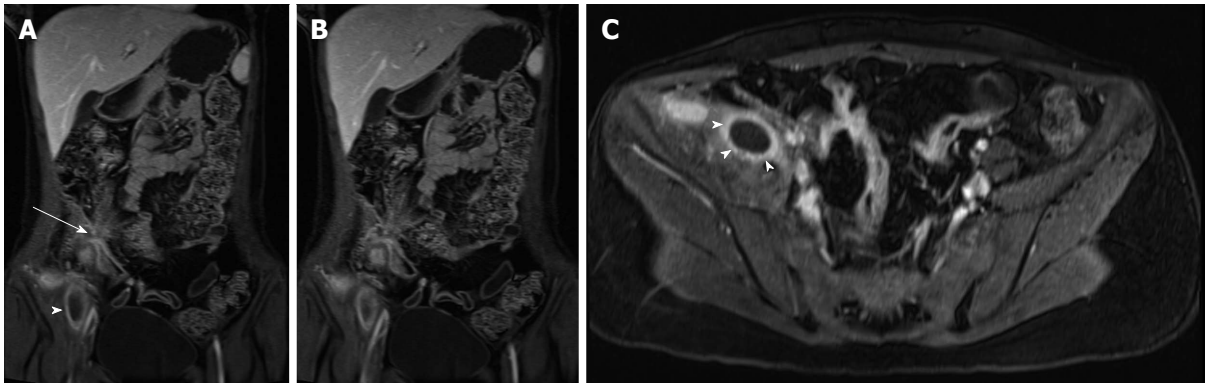

Figure 10 Active distal ileal Crohn's disease with complex fistulization and iliopsoas abscess formation. A and B: Coronal; C: Axial fat-suppressed post-gadolinium 3D-GRE T1-weighted images. There is evidence of terminal ilial thickening and enhancement in keeping with active Crohn's disease, associated with complex ileoileal and ileosigmoidal fistula formation (star sign, arrow, A and B) as well as iliopsoas inflammation and abscess formation (arrowheads, A, B and C). GRE: Gradient recalled echo.

ciated with medical treatment (Figure 11). Furthermore, MRE is also adequate for detection of recurrent disease following surgery (Figure 12).

CELIAC DISEASE

Celiac disease is a permanent gluten-sensitive enteropathy of the gastrointestinal tract that affects the small intestine in genetically susceptible individuals. It is a systemic disease that may entail a variety of autoimmune disorders; the most important finding is an inflamed and flattened small intestinal mucosa with impaired function[40]. The disease may present at any age and may show a wide range of clinical presentations of variable severity. The diagnosis of celiac disease can be challenging due to a wide range of clinical manifestations and the lack of specificity. Although the diagnosis is confirmed by small-intestine biopsy, patients who are referred for MRE with nonspecific gastro-intestinal complaints might have celiac disease as the underlying pathology.

MRE allow the visualization of the entire small bowel, and can demonstrate findings useful to suggest the

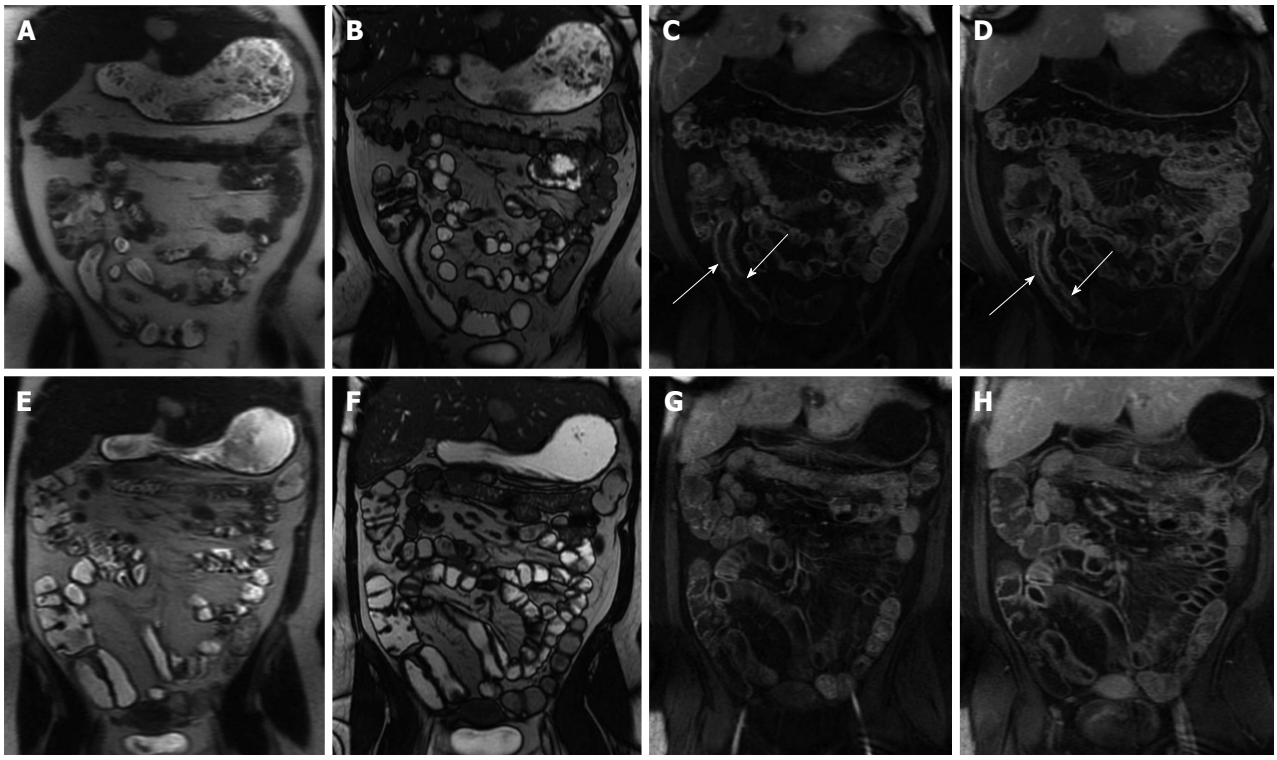

Figure 11 Imaging followup in a patient with Crohn's disease. A and E: Coronal T2-weighted single shot fast spin echo; B and F: Coronal balanced steady state free precession images; C and G: Coronal; D and H: Axial fat-suppressed post-gadolinium 3D-GRE T1-weighted images. There is evidence of active Crohn's disease involving a long segment of the terminal ileum (A, B, C and D) in form of diffuse wall thickening and submucosal mucosal enhancement (arrows, C and D). Four-month re-evaluation shows interval decreased wall thickening and significant decreased mucosal/serosal enhancement, consistent with favourable response to medical therapy. GRE: Gradient recalled echo.

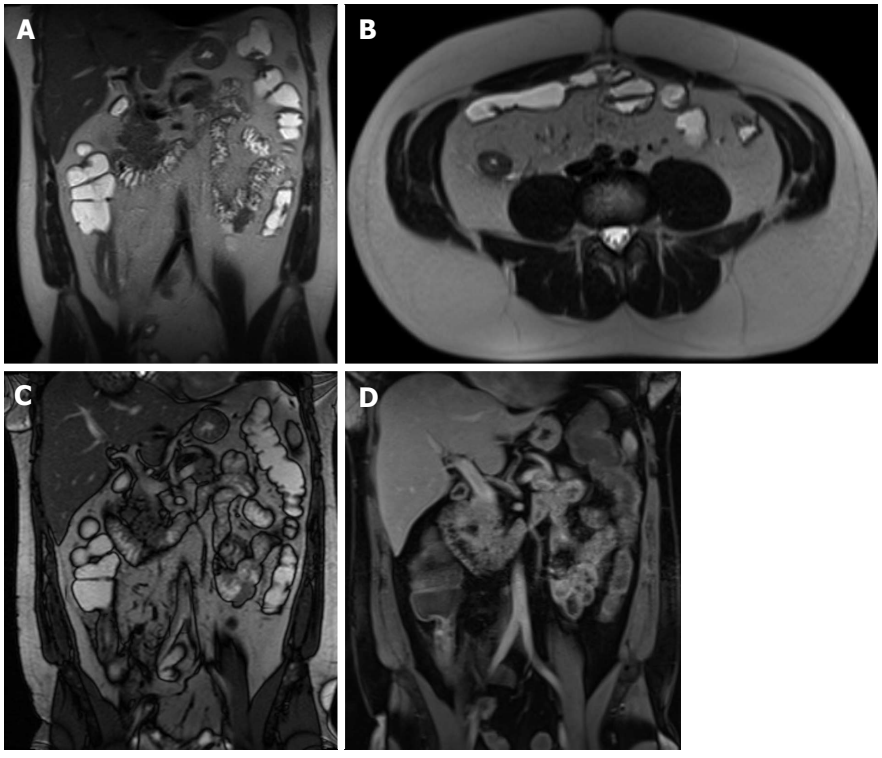

Figure 12 Recurrent Crohn's disease post-surgery. A: Coronal; B: Axial T2-weighted single shot fast spin echo images; C: Coronal balanced steady state free precession; D: Coronal fat suppressed post-gadolinium 3D-GRE T1-weighted images. The patient is post distal ileal resection with a low-lying ileocolic anastomosis. The remaining distal ileum displays signs of active inflammation, namely bowel wall thickening and submucosal edema (A and B) associated with mucosal and serosal increased enhancement post-gadolinium (D) in keeping with recurrent Crohn's disease post-surgery. GRE: Gradient recalled echo.

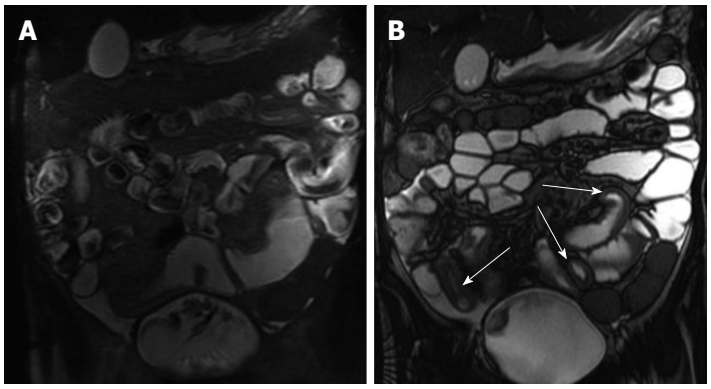

Figure 13 Type 2 Gluten-sensitive enteropathy (Celiac disease). A: Coronal T2-weighted single shot fast spin echo; B: Coronal balanced steady state free precession images show an abnormal ileal fold pattern with substantial decrease in the number of jejunal folds suggesting the diagnosis of celiac disease. Concomitantly, jejunal and ileal segments with increased mural thickening and stratification are seen (arrows, B), consistent with superimposed active inflammation.

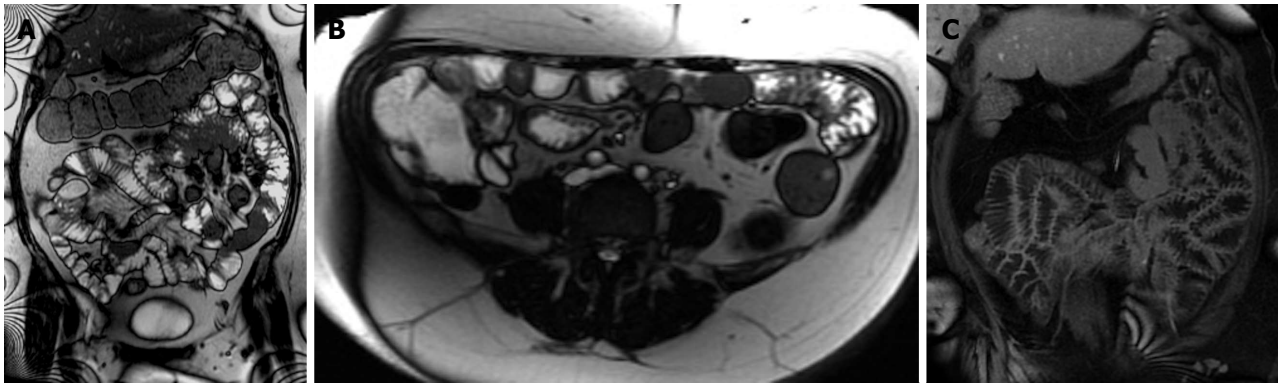

Figure 14 Gluten-sensitive enteropathy (celiac disease). A: Coronal T2-weighted single shot fast spin echo; B: Coronal balanced steady state free precession; C: Coronal fat-suppressed post-gadolinium 3D-GRE T1-weighted images during the interstitial phase. There is abnormal ileal fold pattern with increased number of folds mimicking the appearance of the jejunum (ileal jejunization) in keeping with the diagnosis of celiac disease. GRE: Gradient recalled echo.

diagnosis of celiac disease in symptomatic adult patients. Among these findings, fold-pattern abnormality is the most distinctive[41,42]. Furthermore, because there are diseases that can resemble celiac disease histologically, MRE can help in excluding other disease entities[43], such as lymphoma. Due to greater contrast resolution, MRE may be the preferred method of evaluation.

Fold-pattern abnormalities can best be assessed on bSSFP and single-shot fast/turbo spin-echo T2-weighted pulse sequences. A decreased number of jejunal folds (less than three folds per inch) or complete flattening of the folds can be seen in celiac disease (Figure 13). Also, the ileal folds can be increased (more than 5 folds per inch), a sign called "ileal jejunization" (Figure 14). Jejunoileal fold pattern reversal is present when both ileal jejunization and a decreased number of jejunal folds are present in the same patient. This fold-pattern reversal is very specific for celiac disease[41]. However, less specific imaging findings can be seen including strictures, lymphadenopathy, and perienteric stranding. Also, intussusception, visible as the "double halo sign" of bowel-within-bowel, and enlarged lymph nodes (> 1 cm)[41,42] are frequently encountered.

Small bowel lymphomas are associated with the concomitant presence of celiac disease[44] and should be suspected in cases in which considerable enlargement of lymph nodes (> 2 cm) are identified.

MISCELLANEOUS

Infectious diseases of the small bowel are the most prevalent disease processes in the small bowel after CD. *Yersinia enterocolitica* and *Campylobacter jejuni* represent the most common pathogens. Because of the increasing number of immunocompromised patients, the spectrum of pathogens has become wider during the past decades, including Mycobacterium avium-intracellulare, Cryptosporidium species, and cytomegalovirus. Infectious diseases may mimic CD; because they often manifest as terminal ileitis. Hence, clinical features always need to be considered in order to establish the correct diagnosis[45].

The small bowel is highly sensitive to radiation exposure, with the ileum showing the lowest radiation tolerance. Radiation enteritis typically affects the distal ileum and is often associated with rectosigmoid involvement[46] (Figure 15). The rectum is affected more frequently than the small bowel in pelvic radiotherapy, where proctitis is estimated to occur in 19% of cases[47]. Typical imaging findings include luminal narrowing with small bowel obstruction and pre-stenotic dilatation as well as symmetric wall thickening and edema. Gadolinium-enhanced T1-

Figure 15 Radiation proctocolitis. A: Coronal; B: Axial; C: Sagittal T2-weighted TSE. The rectum and distal sigmoid colon demonstrates increased wall thickness with intermediate signal intensity on T2-weighted images (arrows, A, B and C). This patient underwent hysterectomy and radiation therapy. These findings are compatible with radiation proctocolitis. TSE: Turbo spin echo.

weighted images reveal increased enhancement in the affected bowel wall. Furthermore, submucosal edema can be depicted in early-stage radiation enteritis on T2-weighted images. Care is required to exclude malignancy, especially lymphoma, suggested by mass-like thickening, infiltration of adjacent tissues, and nodal enlargement[45].

PRACTICAL APPROACH TO INFLAMMATORY CONDITIONS-LARGE BOWEL

Inflammatory bowel disease

CD and Ulcerative Colitis (UC) are the two main forms of chronic inflammatory bowel disease (IBD)[48] with 20%-25% of diagnoses being made during childhood[49]. Ileocolonoscopy with biopsy is the primary tool to make the diagnosis of colonic IBD. However, as mentioned above, intramural changes and extra-luminal abnormalities cannot be appreciated. Furthermore, concomitant small bowel involvement must be excluded.

Given the present role of MRE in small bowel CD, we believe that MRE ± colonic enema (MR colonography) might have a similar role in colonic IBD. Often, the degree of distension of the large bowel achieved with oral contrast agents is suboptimal; however, previous reports have shown high sensitivity for differentiating type and severity of colonic IBD with comparable diagnostic accuracy to endoscopy[50]. Furthermore, a recent meta-analysis[51] suggested that MRI is a potentially effective method even without the administration of colonic enema. Recently, Rimola *et al*[36] demonstrated that MRE in combination with a water-based enema is adequately able to assess disease activity in patients with established CD (Figure 16). Current evidence suggests adequate accuracy in evaluating disease activity in established IBD patients. Initial diagnosis and additional differentiation between UC and CD has not been defined yet. MRI findings of UC are similar to those of CD. UC is chronic inflammatory bowel disease restricted to the mucosa and distinctively limited to the colon (Figures 17 and 18) with a predictable distribution, *i.e.*, the disease begins in the rectum and extends proximally in a continuous fashion to involve part or the entire colon (pancolitis). In case of pancolitis, a backwash ileitis may also be present.

Diverticulitis

MRI can effectively diagnose acute diverticulitis, with reported sensitivity of 86% to 94% and specificity of 88% to 92%[52]. It is likely that continually improving MRI techniques may result in higher sensitivity and specificity in the future. Buckley *et al*[53] described MRI findings in patients with acute colonic diverticulitis, identifying findings similar to CT: bowel wall thickening, pericolic stranding, presence of diverticula (Figure 19), and presence of complications such as perforation and abscess formation[53]. MRI is also comparable to CT in its ability to identify alternative diagnoses[54].

Appendicitis

Traditionally, acute appendicitis has been diagnosed on the basis of clinical findings. Despite having high sensitivity (up to 100%), clinical evaluation has relatively low specificity (73%)[55]. The exact role of imaging in the setting of suspected appendicitis is still a matter of debate. CT is the preferred imaging technique for the diagnosis and assessment of appendicitis in the United States[56] and has been shown to reduce the negative-finding appendectomy rate from 24% to 3%[57]. There are several individual CT findings that suggest a diagnosis of appendicitis like appendiceal enlargement (> 6 mm in diameter) that has a high positive predictive value[58]. Likewise, the sensitivity of adjacent fat infiltration is high for the diagnosis of appendicitis[59]. However, the visualization of an appendicolith has been shown to have a low positive predictive value for the diagnosis of appendicitis[58]. Complications, such as perforated appendicitis, extraluminal gas or abscess can be diagnosed with high specificity[60]. If appendicitis can be ruled out, the most common alternative imaging-based diagnoses are gynecologic diseases, diverticulitis, colitis, or epiploic appendagitis[61].

MRI has demonstrated promising accuracy for the

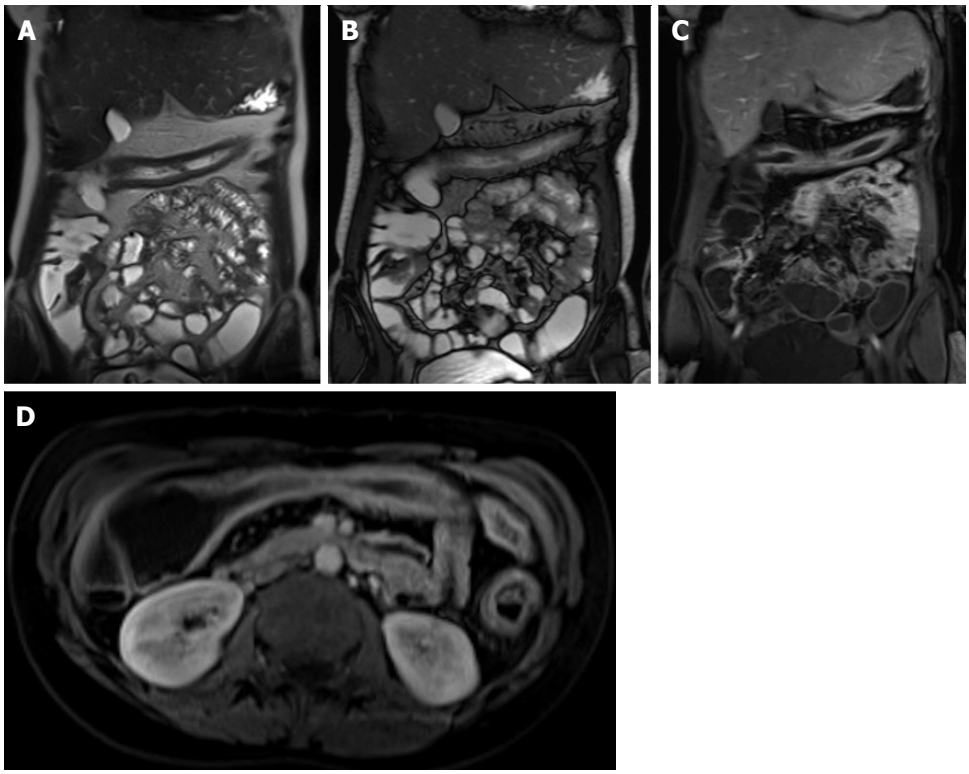

Figure 16 Crohn's colitis. A: Coronal T2-weighted single shot fast spin echo; B: Coronal balanced steady state free precession images; C: Coronal; D: Axial fat-suppressed post-gadolinium 3D-GRE T1-weighted images. There is a segmental uniform thickening of the transverse colon associated with submucosal edema (A and B), mucosal hyper-enhancement, and engorgement of the supplying mesenteric vessels (C and D) in keeping with active Crohn's colitis. Also of note is the focal hyper-enhancement of the terminal ileum (C). GRE: Gradient recalled echo.

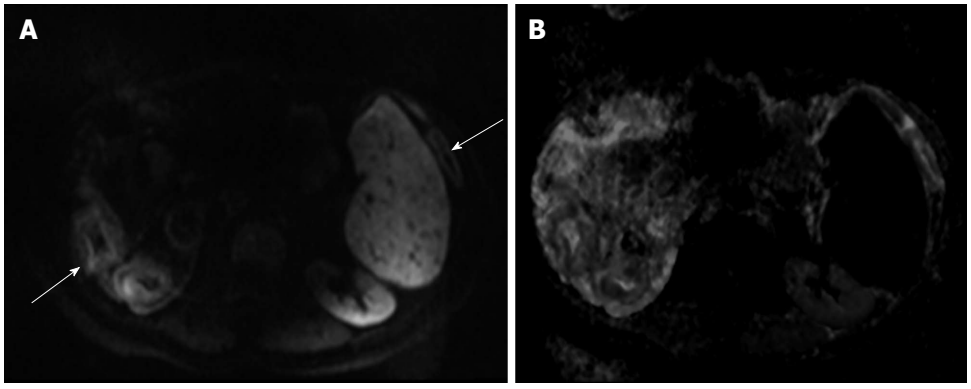

Figure 17 Active colonic ulcerative colitis. A: Axial diffusion-weighted imaging (b = 650 s/mm^2); B: ADC map images. There is diffuse thickening involving the colon associated wish diffuse mucosal diffusion restriction (arrows A) in keeping with active ulcerative colitis. ADC: Analog-digital conversion.

assessment and diagnosis of appendicitis, albeit in a relatively small series of patients, who often were pregnant (Figure 20)[62]. A recent study showed that the accuracy of conditional or immediate MRI was similar to that of conditional CT in patients suspected of having appendicitis[63] However, due to the non-wide availability of MRI systems, relative lack of required expertise and extensive cost-effectiveness studies; the role of MRI is somewhat limited. At this time, MRI is used in only select cases at many institutions, primarily after ultrasound yields nondiagnostic findings in pregnant women.

As in CT, the inflamed appendix and surrounding tissues show marked enhancement on gadolinium-enhanced T1-weighted fat-suppressed images. Recently, Leeuwenburgh *et al*[64] suggested that the most significant MRI features of acute appendicitis include appendix enlargement (diameter > 7 mm), peri-appendiceal fat stranding, and restricted diffusion of appendiceal wall; the presence of all these three features on MRI leads to a correct diagnosis of 96%, whereas their absence practically rules out appendicitis.

GASTRIC AND SMALL BOWEL TUMORS

Gastric tumors

Adenocarcinoma: Gastric carcinoma is one of the most

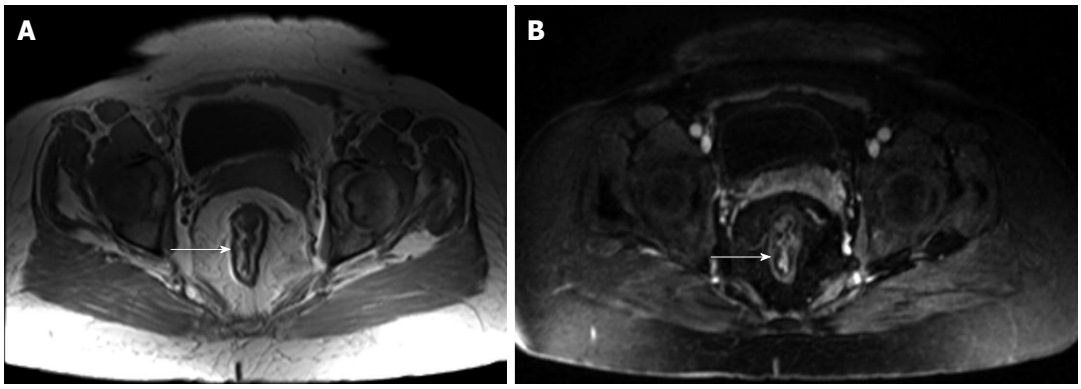

Figure 18 Chronic ulcerative colitis. A: Axial in-phase T1-weighted; B: Axial fat-suppressed post-gadolinium 3D-GRE T1-weighted images. There is diffuse rectal submucosal increased T1 signal (arrow, A), which demonstrates low signal on fat-suppression (arrow, B), but no significant arterial enhancement (B), in keeping with chronic ulcerative colitis. GRE: Gradient recalled echo.

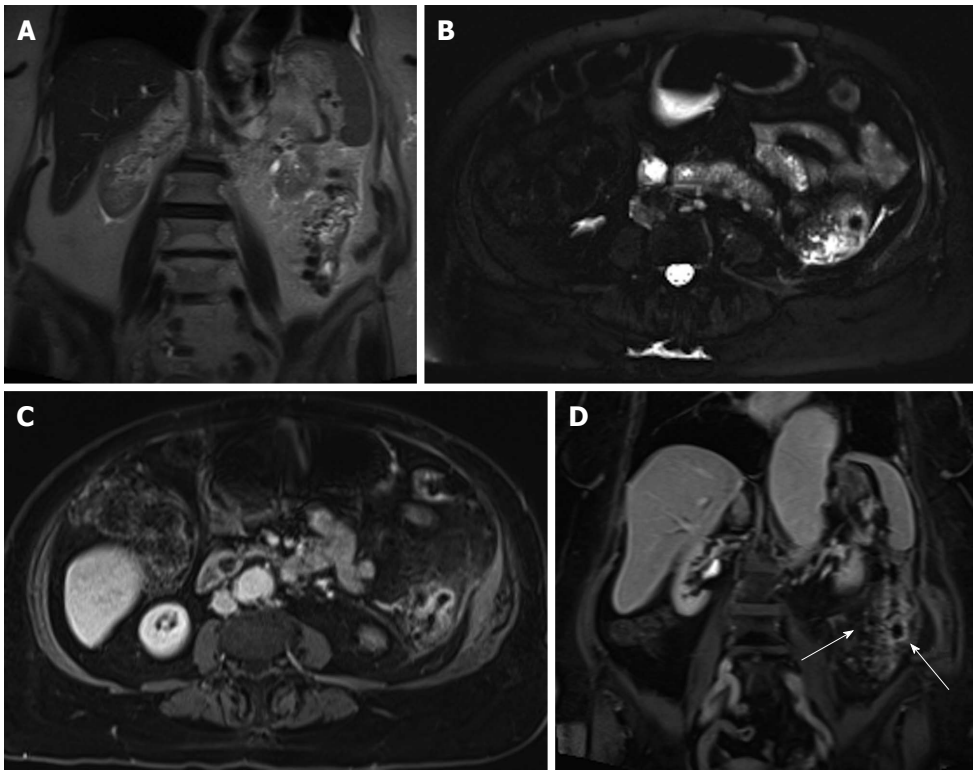

Figure 19 Left colonic diverticulitis. A: Coronal T2-weighted single shot fast spin echo (SSFSE); B: Axial fat-suppressed T2-weighted SSFSE; C: Axial and D: Coronal fat-suppressed post-gadolinium 3D-GRE T1-weighted images during the interstitial phase. There is wall thickening of the descending colon (A), with pericolonic free fluid, better depicted on axial T2-weighted SSFSE image (B). Post-gadolinium images (C and D) show marked enhancement of the left colon, with pericolonic enhancement including the pre-renal fascia. Coronal postgadolinium image (D) shows left colonic diverticula and associated bowel wall and vasa recti engorgement (arrows), consistent with inflammation. GRE: Gradient recalled echo.

common causes of cancer-related death worldwide. Borrmann proposed the original classification of advanced gastric cancer in 1926 based on macroscopic evaluation of the tumor. Advanced gastric cancer was classified by Borrmann as fungating (type 1), excavated (type 2), ulcerated infiltrating (type 3), and diffusely infiltrating (type 4) based on shape and infiltration margin. The prognosis of this disease depends on a variety of factors including Borrmann classification[65].

It is generally accepted that the goals of MRI is to demonstrate the primary tumor, but also assess the depth of invasion and detect extra gastric disease[66,67]. On gadolinium-enhanced fat-suppressed T1-weighted images, the tumor shows heterogeneous enhancement compared to normal gastric wall. Infiltrative tumors (linitis plastica) enhances modestly (Figure 21). In contradistinction, other morphologic types enhance more intensely; however, these tend yet to be better demonstrated in the arterial phase, as normal gastric mucosa tends to enhance substantially. Previous studies have shown that MRI has similar diagnostic accuracy in the in the diagnosis and preoperative staging of gastric cancer compared to

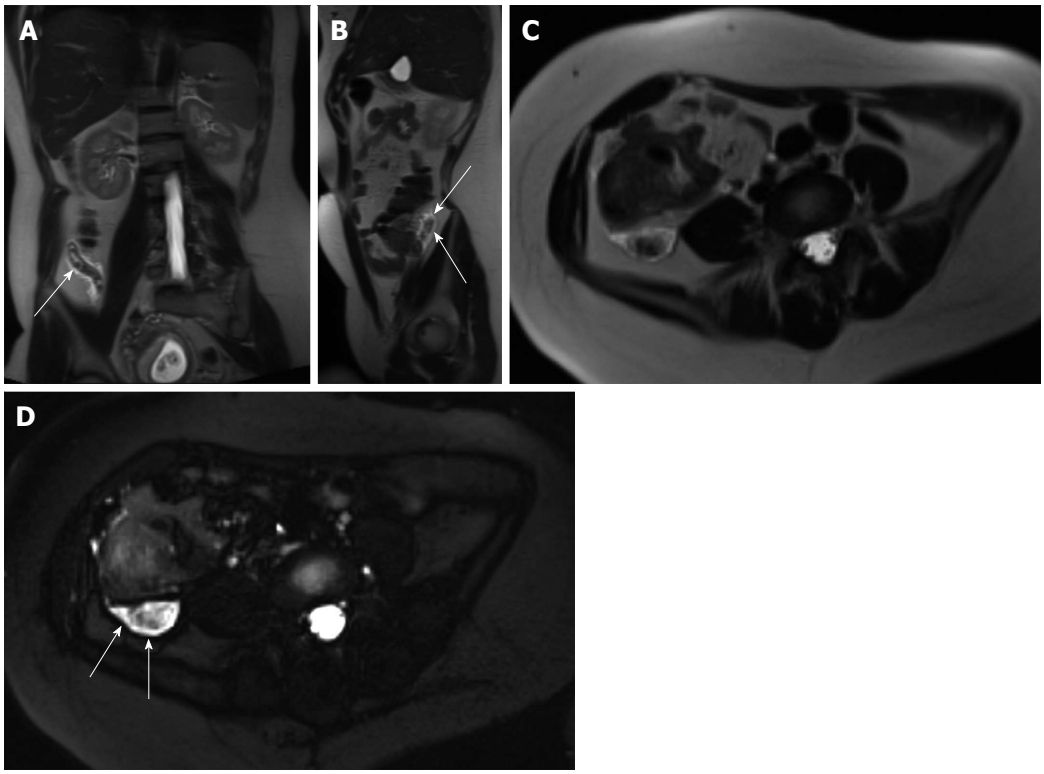

Figure 20 Acute appendicitis in a pregnant patient. A: Coronal; B: Sagittal; and C: Axial single shot fast spin echo (SSFSE) T2 as well as D: fat-suppressed SSFSE T2 images. There is a blind-ended tubular structure at the retrocecal region (arrows, A, B) associated with uniform, diffuse wall thickening and dilatation, reaching up to 13 mm in diameter (C and D) as well as periappendiceal edema and small periappendiceal fluid (A-D) collection, in keeping with acute appendicitis. Edema and fluid appear significantly more conspicuous on fat-suppressed images (arrows, D). Noted is a gravid uterus (A).

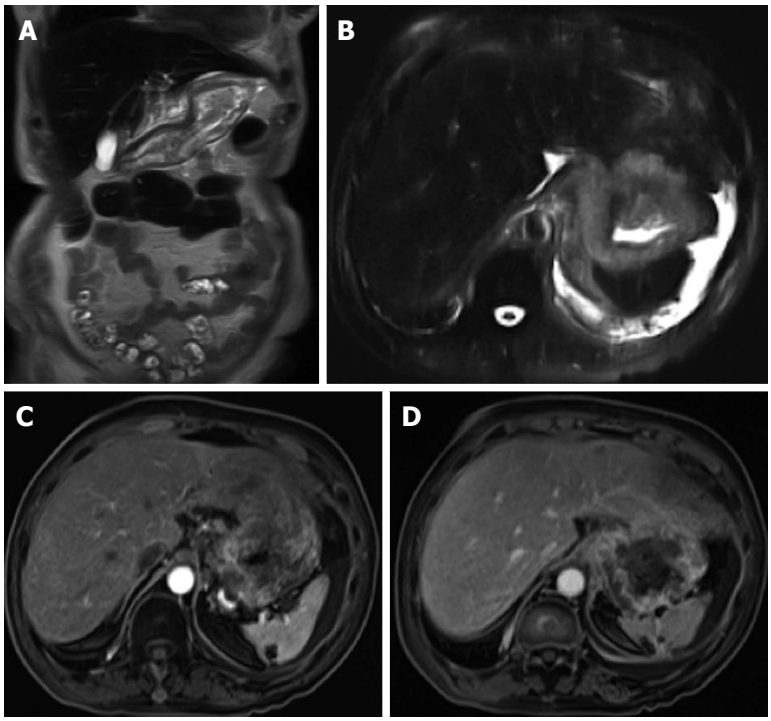

Figure 21 Gastric adenocarcinoma. A: Coronal T2-weighted single shot fast spin echo (SSFSE); B: Axial fat suppressed T2-weighted SSFSE; C: Axial arterial; D: Interstitial post-gadolinium 3D-GRE T1-weighted images. There is diffuse heterogeneous wall thickening of the stomach (A and B) with heterogeneous enhancement (C and D) consistent with linitis plastica. GRE: Gradient recalled echo.

multidetector CT[67]. Maccioni *et al*[67] have shown similar detection rate of gastric lesions; however, the T staging accuracy for gastric cancer was superior for MRI (60% *vs* 48%). This aspect has been previously described by Sohn

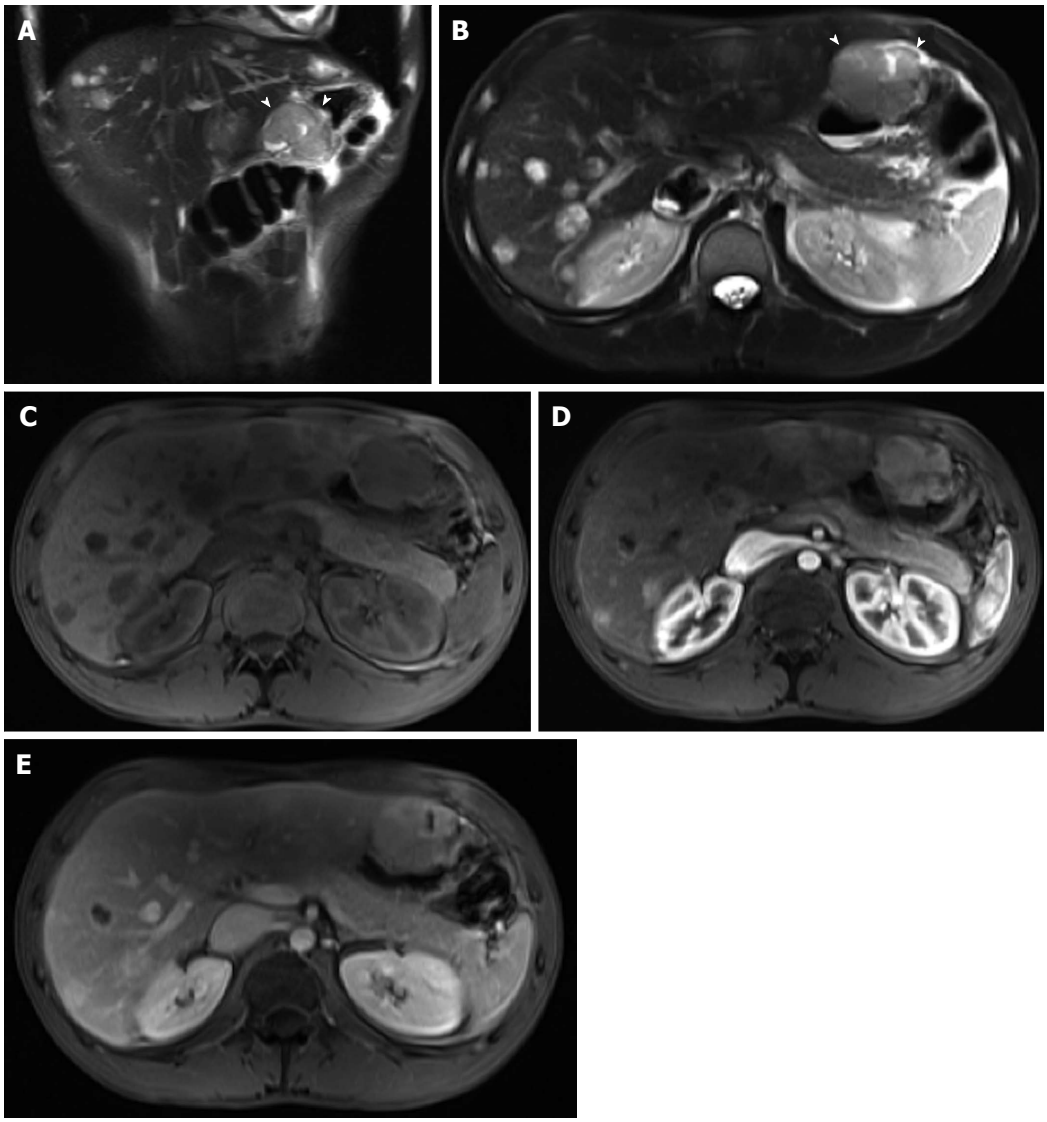

Figure 22 Metastatic malignant gastric gastrointestinal stromal tumors. A: Coronal T2-weighted single shot fast spin echo (SSFSE); B: Axial fat suppressed T2-weighted SSFSE; C: Pre- and post-gadolinium 3D-GRE T1-weighted images during the (D) arterial and (E) interstitial phases. There is a hyperintense mass within the wall of the gastric antrum, which abuts the edge of the left lobe of the liver; Central necrosis is seen (arrowheads, A and B). Multiple liver lesions show heterogeneously increased T2 signal and hypervascular characteristics, fading to isointensity on late phase of enhancement, consistent with metastases. GRE: Gradient recalled echo.

et al[68] showing a slightly improved accuracy with MRI (73.3% *vs* 66.7%). The presence of involved lymph nodes is acknowledged to be an independent factor of poor prognosis. The overall accuracy for nodal staging with MRI is similar to that attained with CT[67,68].

Gastrointestinal stromal tumors: Gastrointestinal stromal tumors (GISTs) are the most common mesenchymal neoplasms, which can occur anywhere in the GI tract. Approximately 60%-70% of GISTs occur in the stomach, followed by the small intestine at 25%-35%[69]. GISTs can either grow into the mucosa causing ulceration or protrude towards the serosal side[70]. These are solid tumors that can undergo liquefactive necrosis and intratumoral hemorrhage. On MRI, the tumor's large size coupled with intense enhancement and regions of necrosis are typical features of GISTs. Moreover, MRI may be helpful in determining the organ of origin in large tumors, as well as detecting metastases of GISTs involving the liver and peritoneum (Figure 22). Also, MRI can provide additional information on the tumor response to medical treatment[71].

Lymphoma: The stomach is the most commonly involved site in GI tract, followed by the small bowel (ileocecal region) and rectum[72]. Diffuse gastric wall thickening is almost always present in gastric lymphoma (Figure 23). Lymphoma also has other characteristics including homogeneous T2 signal intensity, substantial lymph nodes enlargement, and splenomegaly[73].

Small bowel tumors

The incidence of primary tumors is low, accounting for approximately 1% to 3% of all gastrointestinal tumors. Although small bowel tumors are rare, they are commonly considered in the differential diagnosis of small

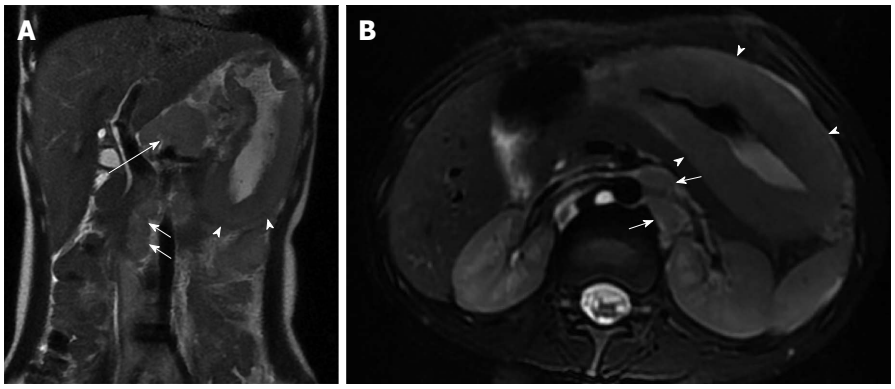

Figure 23 Non-Hodgkin lymphoma of the stomach. A: Coronal T2-weighted single shot fast spin echo (SSFSE) and (B) axial fat-suppressed T2-weighted SSFSE images. There is marked, diffuse, asymmetric gastric wall thickening with smooth outlines, predominantly involving the gastric body and antrum, associated with mildly increased heterogeneous T2 signal intensity (arrowheads, A and B), large conglomerate nodal mass at the gastrohepatic ligament (long arrow, A), and multiple enlarged retroperitoneal lymph nodes (short arrows A and B). Constellation of findings is diagnostic of non-Hodgkin gastric lymphoma with diffuse abdominal lymphadenopathy.

bowel disease because of their nonspecific presenting symptoms such as pain, obstruction, bleeding, and weight loss.

Secondary intestinal tumors, which originate from other parts of the body and metastasize to the small intestine, are clinically common and may cause symptoms similar to primary intestinal neoplasms[74]. MRE has been shown to be a useful technique for the study of suspected bowel masses[75]. Factors that affect the diagnostic performance of a specific modality include the size and characteristics of the tumor, extra-enteric extension, and eventual small bowel obstruction. The degree of distention and motion artifacts also influences the quality of the study. Although there is paucity of data regarding the sensitivity of MRE for the detection of small-bowel masses, one study showed no significant difference between MRI and wireless capsule endoscopy for the detection of large, clinically significant polyps in patients with polyposis syndromes with additional advantage of improved localization with MRE[11].

On MRE, hyper-enhancing masses are usually well depicted when biphasic enteric contrast material is administered. Although any tumor may appear as focal intraluminal mass, location along the GI tract (duodenal, jejunal, or ileal), as well as focal areas of bowel wall thickening or areas of increased mural enhancement, suggest the presence of a tumoral mass. For example, a pedunculated or predominantly exophytic mass suggests a gastrointestinal stromal tumor[76] (Figure 24), while an exophytic mass combined with adjacent lymphadenopathy with or without significant dilatation of the small bowel suggests small bowel lymphoma[76] (Figure 25). Carcinoid tumors arise from neuroendocrine precursors or small bowel wall and may manifest as hypervascular masses, often in the ileum or as enhancing carpet lesions, mimicking the wall thickening of CD. Mesenteric carcinoid metastases demonstrate a desmoplastic reaction that may contain eccentric calcifications (not depicted on MRE) or may be clustered near the mesenteric root[77] (Figure 26). Carcinoid metastases to the liver can appear hypervascular and usually show washout on the delayed imaging mimicking hepatocellular carcinomas (Figure 26). Adenocarcinomas assume a variety of shapes but are generally located in the proximal small bowel (Figure 27) and typically result in proximal dilatation greater than that observed with other neoplasms.

COLORECTAL TUMORS

Colorectal adenocarcinoma

Ninety-six percent of colorectal cancers are adenocarcinomas[78]. A combination of thin-section 3D-GRE fat-suppressed gadolinium-enhanced T1-weighted and high-resolution T2-weighted fast-spin echo (FSE) provides excellent information about tumor size, bowel wall involvement, peri-tumoral extension, and lymph node detection; especially for tumors located proximally to rectal ampulla[79,80].

MRI has established itself as the primary method for local staging as well as preoperative planning and post-neoadjuvant assessment of the rectal cancers. Rectal cancer MRI evaluation requires a dedicated protocol. The only sequence that is required is a high-resolution T2-weighted fast spin echo. Sagittal plane images are initially acquired, followed by axial and coronal images perpendicular to the rectal wall at the level of the tumor, termed short- and long-axis images, respectively. With high-resolution T2-weighted imaging as a gold standard sequence, it proved to be superior in T staging, especially when the patient's comfort and acceptance are taken into consideration[81-83]. The ability of MR to delineate the mesorectal fascia and related structures makes it effective to accurately predict curative resection of the rectal cancer[81,84].

Practical aspects of rectal cancer MR staging include tumor size evaluation, longitudinal and axial localization, tumor extent through the rectal wall layers, extramural invasion of the mesorectal fat and/or mesorectal fascia as well as deep pelvic organs invasion or anal canal extension in case of low lying rectal tumors. Short-axis T2 high-resolution imaging is critical for more accurate tumor (T) staging and yields higher accuracy for deeper tumoral extension (T3-4) (Figure 28); however, transrec-

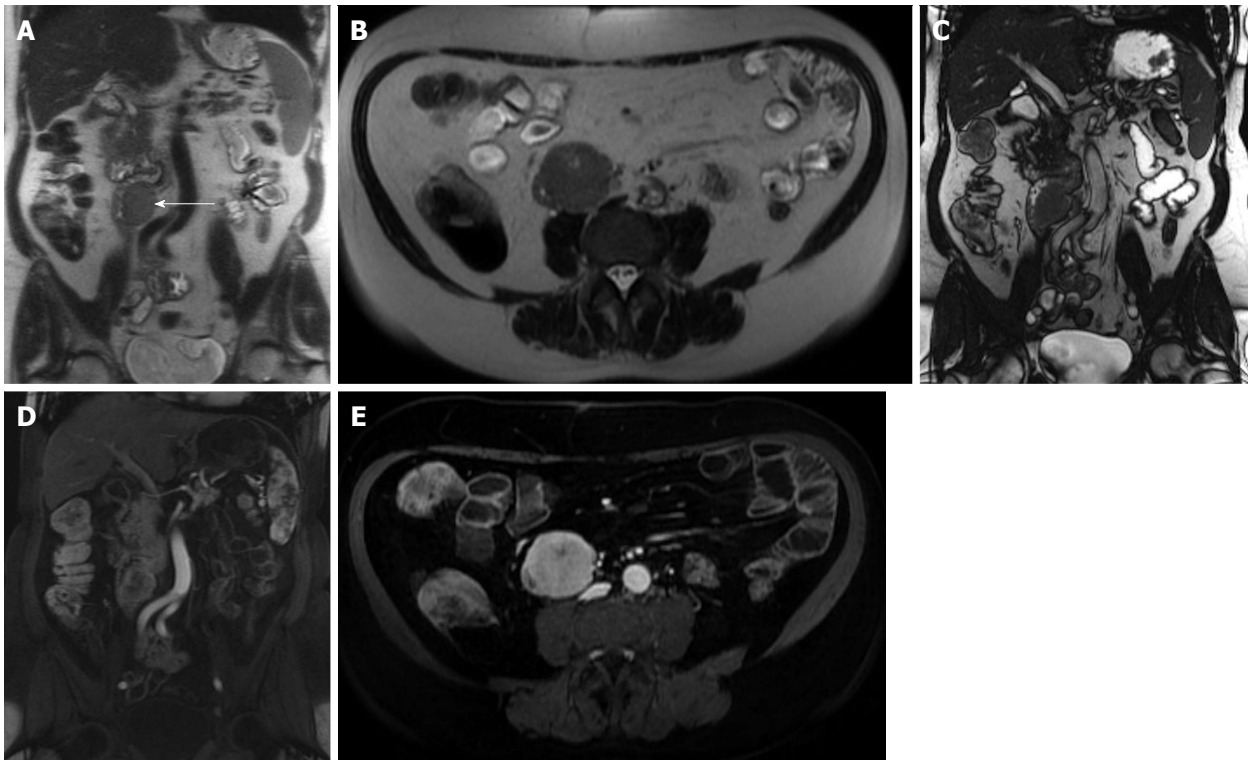

Figure 24 Jejunal gastrointestinal stromal tumor. A: Coronal and (B) axial T2-weighted single shot fast spin echo, and (C) coronal balanced steady state free precession images as well as (D) coronal and (E) axial fat-suppressed post-gadolinium 3D-GRE T1-weighted images. There is a well-defined intramural, exophytic mass lesion arising from the proximal jejunum, in a patient with malrotation, which demonstrates intermediately increased T2 signal (arrow, A, B), early moderate hypervascularity (D) and progressive enhancement (E) post-gadolinium associated with a tiny central area of necrosis in keeping with jejunal gastrointestinal stromal tumor. Lack of proximal bowel obstruction is consistent with its eccentric origin. GRE: Gradient recalled echo.

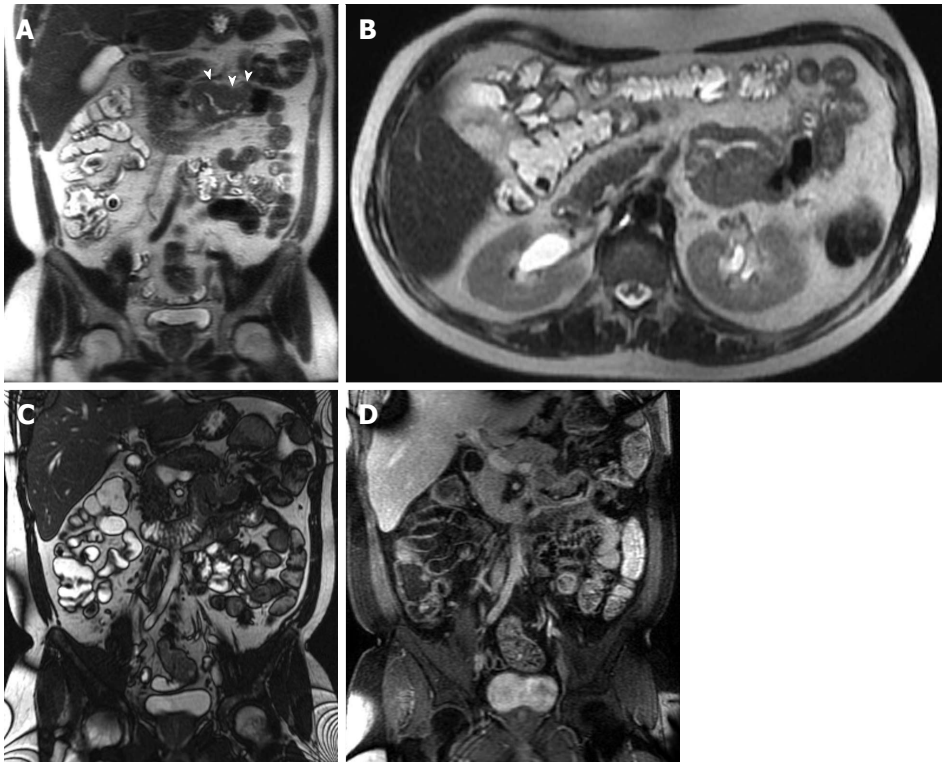

Figure 25 Jejunal lymphoma. A: Coronal and (B) axial T2-weighted single shot fast spin echo, (C) coronal balanced steady state free precession, and (D) coronal fat-suppressed post-gadolinium 3D-GRE T1-weighted images. There is a short segment of proximal jejunal circumferential, irregular, asymmetric wall thickening resulting in luminal narrowing (arrowheads, A) and demonstrates and intermediate T2 signal (A and B) and mild enhancement post-gadolinium (D) in keeping with a pathologically proven jejunal lymphoma. GRE: Gradient recalled echo.

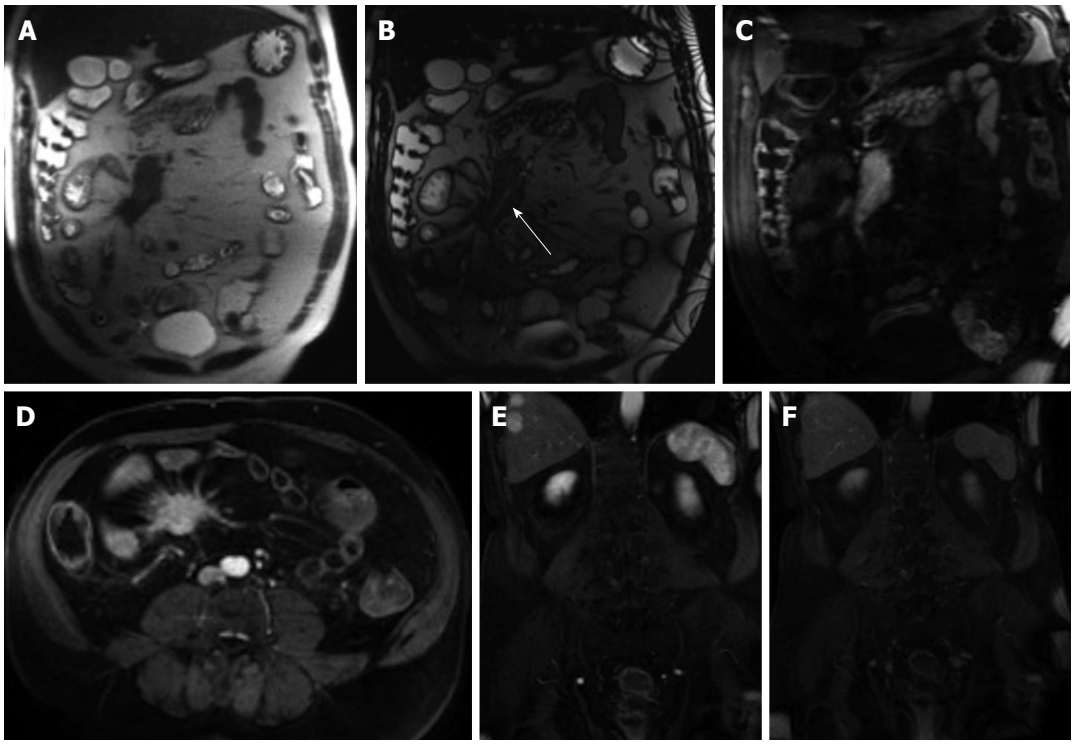

Figure 26 Mesenteric carcinoid. A: Coronal T2-weighted single shot fast spin echo; B: Coronal balanced steady state free precession; C and D: Coronal arterial; E: Axial enteric; F: Coronal interstitial fat-suppressed post-gadolinium 3D-GRE T1-weighted images. There is a large mesenteric mass encasing the superior mesenteric artery and its branches (arrow, B) associated with desmoplastic reaction and small bowel retraction noted on pre-contrast images (A, B), which demonstrates hypervascular (C) and typical sunburst margins (D). Liver metastases are seen with the typical wash-in (D) and washout (F) appearance mimicking the appearance of hepatocellular carcinoma. GRE: Gradient recalled echo.

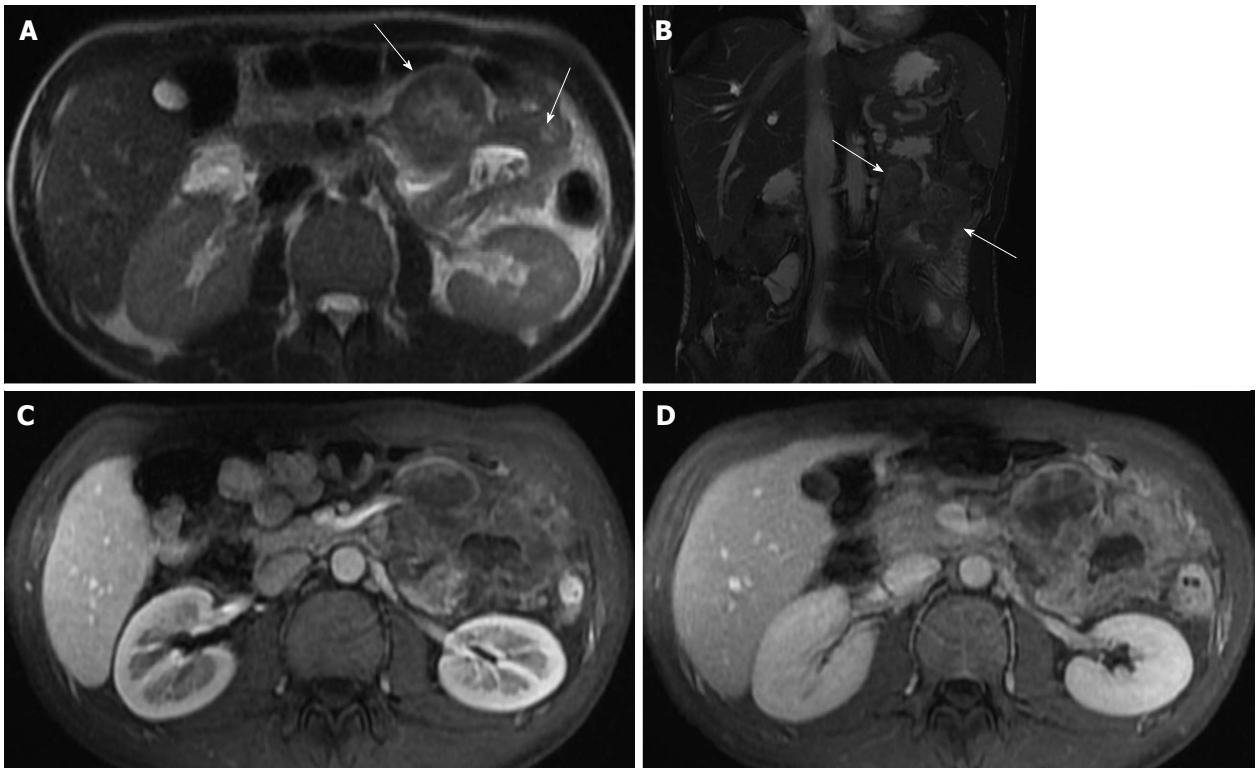

Figure 27 Jejunal adenocarcinoma. A: Axial T2-weighted single shot fast spin echo and (B) coronal balanced steady state free precession images as well as axial fat-suppressed post-gadolinium 3D-GRE T1-weighted images during the (C) hepatic arterial dominant and (D) hepatic venous phases. There is significant circumferential, irregular, asymmetric wall thickening of the proximal jejunum with exophytic extension (arrows, A and B) and hypovascular enhancement pattern (C and D) in keeping with a pathologically proven jejunal adenocarcinoma. GRE: Gradient recalled echo.

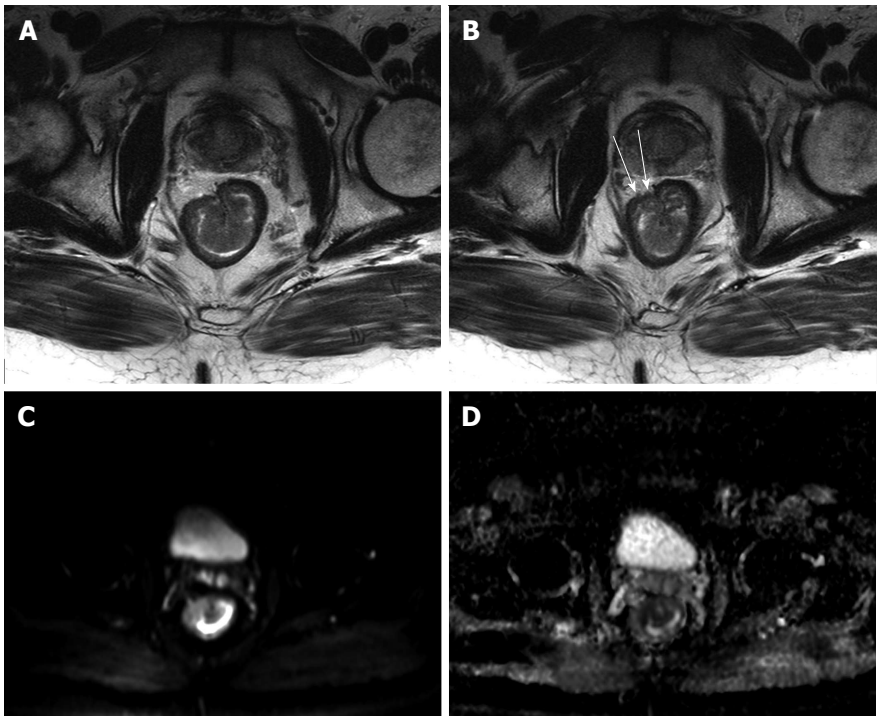

Figure 28 Stage T3 rectal cancer. A and B: Axial high-resolution T2-weighted images as well as axial (C) diffusion-weighted imaging (b = 650 s/mm^2) and (D) ADC map images. There is a large polypoidal mass lesion arising from the right anterolateral lower rectal wall (A and B) with two foci of tumoral extension beyond the low-signal serosal layer (arrows, B) that show diffusion restriction (C and D) in keeping with stage T3 rectal tumor. ADC: Analog-digital conversion.

tal ultrasound has higher reported accuracy in superficial tumors (T1-T2)[85]. A limitation of MR is its inability to easily differentiate T2 from early T3 tumors and certainly cannot differentiate between T1 and T2 cancers[85]. With the advent of endorectal coils, the T staging accuracy has been reported to be between 70%-90%[84,86,87]; however, patient's compliance, limited availability and cost contribute to its less wide application[85]. MRI has 92% accuracy in predicting circumferential resection margin when a cutoff point of 1 mm is used[88]. Nodal involvement can be evaluated using MRI, which rely on short-axis nodal measurement, signal heterogeneity of the cortex, marginal irregularity, or surrounding fat infiltration. The use of superparamagnetic iron oxide particles appears to be promising[89]. Studies also showed that diffusion weighted imaging and perfusion imaging are useful in following-up tumor treatment response including assessing the response to neoadjuvant therapy and determining residual disease or local tumor recurrence[90-93]. The main difficulty in assessing the response to chemoradiation is the distinction between fibrosis with and without residual tumor[94]. Studies evaluating the ability of MRI after chemoradiation to predict tumor clearance from the mesorectal fascia have shown a high negative predictive value of 100%, at the expense of many false-positives leading to a low positive predictive value (PPV) of 50%-60%[95]. Two studies reported a PPV of 83% and 91% and the PPV increased to 94% when > 70% volume downsizing was combined with MR morphological changes[96,97]. The detection of very small volumes of disease remains a problem with techniques that only give information on morphological data. Although 18-Fludeoxyglucose positron emission tomography provides additional functional information, it cannot solve the problem of detection of residual tumor in fibrosis, as shown by a study on the assessment of clearance from the mesorectal fascia[98].

Benign lesions of the small and large bowel

Some lesions have typical features on MR imaging, which is crucial for a correct diagnosis. For instance, hemangiomas are typically strongly hyperintense on T2-weighted MR images; lipomas or tumors with a marked fat content will show high T1 signal intensity that suppresses on fat-suppressed T1-weighted images (Figure 29). However, many other benign neoplasms such as leiomyomas, fibromas and neurogenic tumors may be indistinguishable from other hypervascular lesions on MRE/MRI.

CONCLUSION

The implementation of fast and ultra-fast sequences and dedicated advanced imaging protocols render MRI an excellent tool for GI imaging. State of the art MRI/MRE has rapidly emerged as successful gastrointestinal imaging modality; offering detailed anatomic and morphologic information and also permitting evaluation of extra-luminal manifestation and extension of disease. These features have now been shown to alter physician level of confidence and management procedures including medical or surgical approaches.

The lack of ionizing radiation makes MRI the preferred modality in many GI disease processes, especially

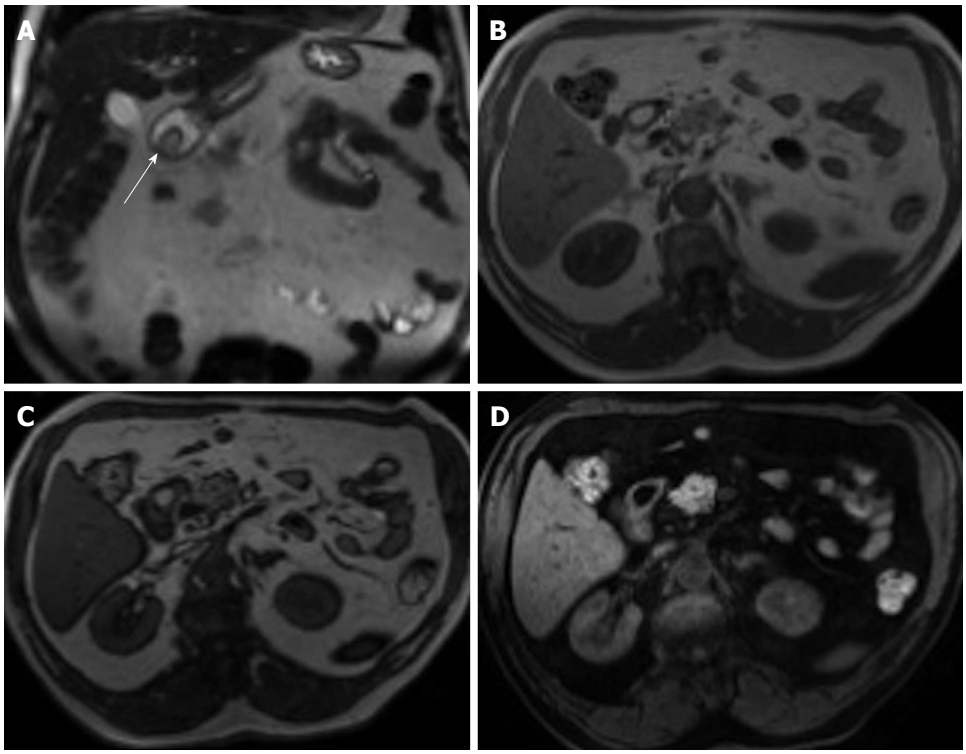

Figure 29 Duodenal lipoma. A: Coronal T2-weighted single shot fast spin echo (SSFSE); B: Axial GRE in-phase; C: Opposed-phase T1-weighted; D: Axial fat-suppressed 3D-GRE T1-weighted images. Small, well-defined, intra-luminal, duodenal mass lesion; which demonstrates intermediately high signal on SSFSE (arrow, A), high signal intensity on the in-phase T1 weighted image (B), no drop of signal on the opposed-phase images (C), and homogenously low signal intensity on the fat-suppressed image (D) in keeping with duodenal lipoma. GRE: Gradient recalled echo.

in young patients in the setting of CD, considering that the majority will undergo frequent imaging evaluation. Pregnant patients and those with iodinated contrast agents allergy or decreased renal function may also benefit from MRI. The main drawbacks may be related to relative non-wide availability at present time, economic constrains, and need for highly subspecialized radiologists.

Whenever cross-sectional imaging is requested, especially MRI or CT, the current trend is to weigh the strengths and weaknesses of both techniques considering a risk-benefit analysis. The choice of a diagnostic technique should be determined taking in account patient's age, clinical status and estimated follow-up exams.

REFERENCES

1 **Umschaden HW**, Szolar D, Gasser J, Umschaden M, Haselbach H. Small-bowel disease: comparison of MR enteroclysis images with conventional enteroclysis and surgical findings. *Radiology* 2000; **215**: 717-725 [PMID: 10831690 DOI: 10.1148/radiology.215.3.r00jn12717]

2 **Rondonotti E**, Herrerias JM, Pennazio M, Caunedo A, Mascarenhas-Saraiva M, de Franchis R. Complications, limitations, and failures of capsule endoscopy: a review of 733 cases. *Gastrointest Endosc* 2005; **62**: 712-716; quiz 752, 754 [PMID: 16246685 DOI: 10.1016/j.gie.2005.05.002]

3 **Brenner DJ**, Hall EJ. Computed tomography--an increasing source of radiation exposure. *N Engl J Med* 2007; **357**: 2277-2284 [PMID: 18046031 DOI: 10.1056/NEJMra072149]

4 **Froehlich JM**, Patak MA, von Weymarn C, Juli CF, Zollikofer CL, Wentz KU. Small bowel motility assessment with magnetic resonance imaging. *J Magn Reson Imaging* 2005; **21**: 370-375 [PMID: 15779029 DOI: 10.1002/jmri.20284]

5 **Cronin CG**, Lohan DG, Browne AM, Roche C, Murphy JM. Does MRI with oral contrast medium allow single-study depiction of inflammatory bowel disease enteritis and colitis? *Eur Radiol* 2010; **20**: 1667-1674 [PMID: 20069426 DOI: 10.1007/s00330-009-1701-2]

6 **Ramalho M**, Herédia V, Cardoso C, Matos AP, Palas J, De Freitas J, Semelka RC. Magnetic resonance imaging of small bowel Crohn's disease. *Acta Med Port* 2012; **25**: 231-240 [PMID: 23079251]

7 **Lee SS**, Kim AY, Yang SK, Chung JW, Kim SY, Park SH, Ha HK. Crohn disease of the small bowel: comparison of CT enterography, MR enterography, and small-bowel follow-through as diagnostic techniques. *Radiology* 2009; **251**: 751-761 [PMID: 19276325 DOI: 10.1148/radiol.2513081184]

8 **Negaard A**, Paulsen V, Sandvik L, Berstad AE, Borthne A, Try K, Lygren I, Storaas T, Klow NE. A prospective randomized comparison between two MRI studies of the small bowel in Crohn's disease, the oral contrast method and MR enteroclysis. *Eur Radiol* 2007; **17**: 2294-2301 [PMID: 17483955 DOI: 10.1007/s00330-007-0648-4]

9 **Schreyer AG**, Geissler A, Albrich H, Schölmerich J, Feuerbach S, Rogler G, Völk M, Herfarth H. Abdominal MRI after enteroclysis or with oral contrast in patients with suspected or proven Crohn's disease. *Clin Gastroenterol Hepatol* 2004; **2**: 491-497 [PMID: 15181618]

10 **Gupta A**, Postgate AJ, Burling D, Ilangovan R, Marshall M, Phillips RK, Clark SK, Fraser CH. A prospective study of MR enterography versus capsule endoscopy for the surveillance of adult patients with Peutz-Jeghers syndrome. *AJR Am J Roentgenol* 2010; **195**: 108-116 [PMID: 20566803 DOI: 10.2214/AJR.09.3174]

11 **Caspari R**, von Falkenhausen M, Krautmacher C, Schild H, Heller J, Sauerbruch T. Comparison of capsule endoscopy and magnetic resonance imaging for the detection of polyps of the small intestine in patients with familial adenomatous polyposis or with Peutz-Jeghers' syndrome. *Endoscopy* 2004;

36: 1054-1059 [PMID: 15578294 DOI: 10.1055/s-2004-826041]
12 **Kinner S**, Kuehle CA, Herbig S, Haag S, Ladd SC, Barkhausen J, Lauenstein TC. MRI of the small bowel: can sufficient bowel distension be achieved with small volumes of oral contrast? *Eur Radiol* 2008; **18**: 2542-2548 [PMID: 18500525 DOI: 10.1007/s00330-008-1041-7]
13 **Kuehle CA**, Ajaj W, Ladd SC, Massing S, Barkhausen J, Lauenstein TC. Hydro-MRI of the small bowel: effect of contrast volume, timing of contrast administration, and data acquisition on bowel distention. *AJR Am J Roentgenol* 2006; **187**: W375-W385 [PMID: 16985108 DOI: 10.2214/AJR.05.1079]
14 **Laghi A**, Paolantonio P, Iafrate F, Borrelli O, Dito L, Tomei E, Cucchiara S, Passariello R. MR of the small bowel with a biphasic oral contrast agent (polyethylene glycol): technical aspects and findings in patients affected by Crohn's disease. *Radiol Med* 2003; **106**: 18-27 [PMID: 12951547]
15 **Ajaj W**, Goehde SC, Schneemann H, Ruehm SG, Debatin JF, Lauenstein TC. Oral contrast agents for small bowel MRI: comparison of different additives to optimize bowel distension. *Eur Radiol* 2004; **14**: 458-464 [PMID: 14634782 DOI: 10.1007/s00330-003-2177-0]
16 **Prassopoulos P**, Papanikolaou N, Grammatikakis J, Rousomoustakaki M, Maris T, Gourtsoyiannis N. MR enteroclysis imaging of Crohn disease. *Radiographics* 2001; **21** Spec No: S161-S172 [PMID: 11598255 DOI: 10.1148/radiographics.21.suppl_1.g01oc02s161]
17 **Martin DR**, Danrad R, Herrmann K, Semelka RC, Hussain SM. Magnetic resonance imaging of the gastrointestinal tract. *Top Magn Reson Imaging* 2005; **16**: 77-98 [PMID: 16314698]
18 **Kiryu S**, Dodanuki K, Takao H, Watanabe M, Inoue Y, Takazoe M, Sahara R, Unuma K, Ohtomo K. Free-breathing diffusion-weighted imaging for the assessment of inflammatory activity in Crohn's disease. *J Magn Reson Imaging* 2009; **29**: 880-886 [PMID: 19306416 DOI: 10.1002/jmri.21725]
19 **Oto A**, Kayhan A, Williams JT, Fan X, Yun L, Arkani S, Rubin DT. Active Crohn's disease in the small bowel: evaluation by diffusion weighted imaging and quantitative dynamic contrast enhanced MR imaging. *J Magn Reson Imaging* 2011; **33**: 615-624 [PMID: 21563245 DOI: 10.1002/jmri.22435]
20 **Maglinte DD**, Gourtsoyiannis N, Rex D, Howard TJ, Kelvin FM. Classification of small bowel Crohn's subtypes based on multimodality imaging. *Radiol Clin North Am* 2003; **41**: 285-303 [PMID: 12659339]
21 **Martin DR**, Kalb B, Sauer CG, Alazraki A, Goldschmid S. Magnetic resonance enterography in Crohn's disease: techniques, interpretation, and utilization for clinical management. *Diagn Interv Radiol* 2012; **18**: 374-386 [PMID: 22517074 DOI: 10.4261/1305-3825.DIR.4893-11.2]
22 **Martin DR**, Lauenstein T, Sitaraman SV. Utility of magnetic resonance imaging in small bowel Crohn's disease. *Gastroenterology* 2007; **133**: 385-390 [PMID: 17681157 DOI: 10.1053/j.gastro.2007.06.036]
23 **Marcos HB**, Semelka RC. Evaluation of Crohn's disease using half-fourier RARE and gadolinium-enhanced SGE sequences: initial results. *Magn Reson Imaging* 2000; **18**: 263-268 [PMID: 10745134]
24 **Albert JG**, Martiny F, Krummenerl A, Stock K, Lesske J, Göbel CM, Lotterer E, Nietsch HH, Behrmann C, Fleig WE. Diagnosis of small bowel Crohn's disease: a prospective comparison of capsule endoscopy with magnetic resonance imaging and fluoroscopic enteroclysis. *Gut* 2005; **54**: 1721-1727 [PMID: 16020490 DOI: 10.1136/gut.2005.069427]
25 **Low RN**, Sebrechts CP, Politoske DA, Bennett MT, Flores S, Snyder RJ, Pressman JH. Crohn disease with endoscopic correlation: single-shot fast spin-echo and gadolinium-enhanced fat-suppressed spoiled gradient-echo MR imaging. *Radiology* 2002; **222**: 652-660 [PMID: 11867781 DOI: 10.1148/radiol.2223010811]
26 **Semelka RC**, Shoenut JP, Silverman R, Kroeker MA, Yaffe CS, Micflikier AB. Bowel disease: prospective comparison of CT and 1.5-T pre- and postcontrast MR imaging with T1-weighted fat-suppressed and breath-hold FLASH sequences. *J Magn Reson Imaging* 1991; **1**: 625-632 [PMID: 1823167]
27 **Low RN**, Francis IR, Politoske D, Bennett M. Crohn's disease evaluation: comparison of contrast-enhanced MR imaging and single-phase helical CT scanning. *J Magn Reson Imaging* 2000; **11**: 127-135 [PMID: 10713944 DOI: 10.1002/(SICI)1522-2586(200002)11:2<127::AID-JMRI8>3.0.CO;2-G]
28 **Masselli G**, Gualdi G. MR imaging of the small bowel. *Radiology* 2012; **264**: 333-348 [PMID: 22821694 DOI: 10.1148/radiol.12111658]
29 **Choi D**, Jin Lee S, Ah Cho Y, Lim HK, Hoon Kim S, Jae Lee W, Hoon Lim J, Park H, Rae Lee Y. Bowel wall thickening in patients with Crohn's disease: CT patterns and correlation with inflammatory activity. *Clin Radiol* 2003; **58**: 68-74 [PMID: 12565208]
30 **Taylor SA**, Punwani S, Rodriguez-Justo M, Bainbridge A, Greenhalgh R, De Vita E, Forbes A, Cohen R, Windsor A, Obichere A, Hansmann A, Rajan J, Novelli M, Halligan S. Mural Crohn disease: correlation of dynamic contrast-enhanced MR imaging findings with angiogenesis and inflammation at histologic examination--pilot study. *Radiology* 2009; **251**: 369-379 [PMID: 19276323 DOI: 10.1148/radiol.2512081292]
31 **Schunk K**, Kern A, Oberholzer K, Kalden P, Mayer I, Orth T, Wanitschke R. Hydro-MRI in Crohn's disease: appraisal of disease activity. *Invest Radiol* 2000; **35**: 431-437 [PMID: 10901105]
32 **Masselli G**, Gualdi G. CT and MR enterography in evaluating small bowel diseases: when to use which modality? *Abdom Imaging* 2013; **38**: 249-259 [PMID: 23011551 DOI: 10.1007/s00261-012-9961-8]
33 **Froehlich JM**, Waldherr C, Stoupis C, Erturk SM, Patak MA. MR motility imaging in Crohn's disease improves lesion detection compared with standard MR imaging. *Eur Radiol* 2010; **20**: 1945-1951 [PMID: 20379822 DOI: 10.1007/s00330-010-1759-x]
34 **Rimola J**, Ordás I, Rodríguez S, Panés J. Colonic Crohn's disease: value of magnetic resonance colonography for detection and quantification of disease activity. *Abdom Imaging* 2010; **35**: 422-427 [PMID: 19536590 DOI: 10.1007/s00261-009-9545-4]
35 **Rimola J**, Ordás I, Rodriguez S, García-Bosch O, Aceituno M, Llach J, Ayuso C, Ricart E, Panés J. Magnetic resonance imaging for evaluation of Crohn's disease: validation of parameters of severity and quantitative index of activity. *Inflamm Bowel Dis* 2011; **17**: 1759-1768 [PMID: 21744431 DOI: 10.1002/ibd.21551]
36 **Rimola J**, Rodriguez S, García-Bosch O, Ordás I, Ayala E, Aceituno M, Pellisé M, Ayuso C, Ricart E, Donoso L, Panés J. Magnetic resonance for assessment of disease activity and severity in ileocolonic Crohn's disease. *Gut* 2009; **58**: 1113-1120 [PMID: 19136510 DOI: 10.1136/gut.2008.167957]
37 **Rimola J**, Ordás I, Rodríguez S, Ricart E, Panés J. Imaging indexes of activity and severity for Crohn's disease: current status and future trends. *Abdom Imaging* 2012; **37**: 958-966 [PMID: 22072290 DOI: 10.1007/s00261-011-9820-z]
38 **Giusti S**, Faggioni L, Neri E, Fruzzetti E, Nardini L, Marchi S, Bartolozzi C. Dynamic MRI of the small bowel: usefulness of quantitative contrast-enhancement parameters and time-signal intensity curves for differentiating between active and inactive Crohn's disease. *Abdom Imaging* 2010; **35**: 646-653 [DOI: 10.1007/s00261-010-9624-6]
39 **Oto A**, Zhu F, Kulkarni K, Karczmar GS, Turner JR, Rubin D. Evaluation of diffusion-weighted MR imaging for detection of bowel inflammation in patients with Crohn's disease. *Acad Radiol* 2009; **16**: 597-603 [PMID: 19282206 DOI: 10.1016/j.acra.2008.11.009]
40 **Ciclitira PJ**, King AL, Fraser JS. AGA technical review on Celiac Sprue. American Gastroenterological Association.

Gastroenterology 2001; **120**: 1526-1540 [PMID: 11313324]
41 **Paolantonio P**, Tomei E, Rengo M, Ferrari R, Lucchesi P, Laghi A. Adult celiac disease: MRI findings. *Abdom Imaging* 2007; **32**: 433-440 [PMID: 16967239 DOI: 10.1007/s00261-006-9089-9]
42 **Tomei E**, Semelka RC, Braga L, Laghi A, Paolantonio P, Marini M, Passariello R, Di Tola M, Sabbatella L, Picarelli A. Adult celiac disease: what is the role of MRI? *J Magn Reson Imaging* 2006; **24**: 625-629 [PMID: 16888777 DOI: 10.1002/jmri.20664]
43 **AGA Institute**. AGA Institute Medical Position Statement on the Diagnosis and Management of Celiac Disease. *Gastroenterology* 2006; **131**: 1977-1980 [PMID: 17087935 DOI: 10.1053/j.gastro.2006.10.003]
44 **Chott A**, Vesely M, Simonitsch I, Mosberger I, Hanak H. Classification of intestinal T-cell neoplasms and their differential diagnosis. *Am J Clin Pathol* 1999; **111**: S68-S74 [PMID: 9894471]
45 **Lauenstein TC**, Umutlu L, Kloeters C, Aschoff AJ, Ladd ME, Kinner S. Small bowel imaging with MRI. *Acad Radiol* 2012; **19**: 1424-1433 [PMID: 22841341 DOI: 10.1016/j.acra.2012.05.019]
46 **Palmer JA**, Bush RS. Radiation injuries to the bowel associated with the treatment of carcinoma of the cervix. *Surgery* 1976; **80**: 458-464 [PMID: 968730]
47 **Miller DG**, Ivey M, Young J. Home parenteral nutrition in treatment of severe radiation enteritis. *Ann Intern Med* 1979; **91**: 858-860 [PMID: 42336]
48 **Beattie RM**, Croft NM, Fell JM, Afzal NA, Heuschkel RB. Inflammatory bowel disease. *Arch Dis Child* 2006; **91**: 426-432 [PMID: 16632672 DOI: 10.1136/adc.2005.080481]
49 **Loftus EV**. Clinical epidemiology of inflammatory bowel disease: Incidence, prevalence, and environmental influences. *Gastroenterology* 2004; **126**: 1504-1517 [PMID: 15168363]
50 **Gandolfi L**. Comparison of magnetic resonance imaging and endoscopy in distinguishing the type and severity of inflammatory bowel disease. *Gastrointest Endosc* 1996; **43**: 86-87 [PMID: 9026433]
51 **Horsthuis K**, Bipat S, Stokkers PC, Stoker J. Magnetic resonance imaging for evaluation of disease activity in Crohn's disease: a systematic review. *Eur Radiol* 2009; **19**: 1450-1460 [PMID: 19189109 DOI: 10.1007/s00330-008-1287-0]
52 **Heverhagen JT**, Sitter H, Zielke A, Klose KJ. Prospective evaluation of the value of magnetic resonance imaging in suspected acute sigmoid diverticulitis. *Dis Colon Rectum* 2008; **51**: 1810-1815 [PMID: 18443876 DOI: 10.1007/s10350-008-9330-4]
53 **Buckley O**, Geoghegan T, McAuley G, Persaud T, Khosa F, Torreggiani WC. Pictorial review: magnetic resonance imaging of colonic diverticulitis. *Eur Radiol* 2007; **17**: 221-227 [PMID: 16625348 DOI: 10.1007/s00330-006-0236-z]
54 **Destigter KK**, Keating DP. Imaging update: acute colonic diverticulitis. *Clin Colon Rectal Surg* 2009; **22**: 147-155 [PMID: 20676257 DOI: 10.1055/s-0029-1236158]
55 **Hong JJ**, Cohn SM, Ekeh AP, Newman M, Salama M, Leblang SD. A prospective randomized study of clinical assessment versus computed tomography for the diagnosis of acute appendicitis. *Surg Infect* (Larchmt) 2003; **4**: 231-239 [PMID: 14588157 DOI: 10.1089/109629603322419562]
56 **Ralls PW**, Balfe DM, Bree RL, DiSantis DJ, Glick SN, Levine MS, Megibow AJ, Saini S, Shuman WP, Greene FL, Laine LA, Lillemoe K. Evaluation of acute right lower quadrant pain. American College of Radiology. ACR Appropriateness Criteria. *Radiology* 2000; **215** Suppl: 159-166 [PMID: 11037421]
57 **Raman SS**, Osuagwu FC, Kadell B, Cryer H, Sayre J, Lu DS. Effect of CT on false positive diagnosis of appendicitis and perforation. *N Engl J Med* 2008; **358**: 972-973 [PMID: 18305278 DOI: 10.1056/NEJMc0707000]
58 **Daly CP**, Cohan RH, Francis IR, Caoili EM, Ellis JH, Nan B. Incidence of acute appendicitis in patients with equivocal CT findings. *AJR Am J Roentgenol* 2005; **184**: 1813-1820 [PMID: 15908536 DOI: 10.2214/ajr.184.6.01841813]
59 **Pereira JM**, Sirlin CB, Pinto PS, Jeffrey RB, Stella DL, Casola G. Disproportionate fat stranding: a helpful CT sign in patients with acute abdominal pain. *Radiographics* 2004; **24**: 703-715 [PMID: 15143223]
60 **Bixby SD**, Lucey BC, Soto JA, Theysohn JM, Ozonoff A, Varghese JC. Perforated versus nonperforated acute appendicitis: accuracy of multidetector CT detection. *Radiology* 2006; **241**: 780-786 [PMID: 17114626 DOI: 10.1148/radiol.2413051896]
61 **Stoker J**, van Randen A, Laméris W, Boermeester MA. Imaging patients with acute abdominal pain. *Radiology* 2009; **253**: 31-46 [PMID: 19789254 DOI: 10.1148/radiol.2531090302]
62 **Wallace GW**, Davis MA, Semelka RC, Fielding JR. Imaging the pregnant patient with abdominal pain. *Abdom Imaging* 2012; **37**: 849-860 [PMID: 22160283 DOI: 10.1007/s00261-011-9827-5]
63 **Leeuwenburgh MM**, Wiarda BM, Wiezer MJ, Vrouenraets BC, Gratama JW, Spilt A, Richir MC, Bossuyt PM, Stoker J, Boermeester MA. Comparison of imaging strategies with conditional contrast-enhanced CT and unenhanced MR imaging in patients suspected of having appendicitis: a multicenter diagnostic performance study. *Radiology* 2013; **268**: 135-143 [PMID: 23481162 DOI: 10.1148/radiol.13121753]
64 **Leeuwenburgh MM**, Jensch S, Gratama JW, Spilt A, Wiarda BM, Van Es HW, Cobben LP, Bossuyt PM, Boermeester MA, Stoker J. MRI features associated with acute appendicitis. *Eur Radiol* 2014; **24**: 214-222 [PMID: 24013847 DOI: 10.1007/s00330-013-3001-0]
65 **Borrmann R**. Geschwulste des Magens und des Duodenums. In: Henke F, Lubarsch O. Handbuch der speziellen pathologischen Anatomie und Histologie. Berlin: Verlag von J Springer, 1926: 812-1054
66 **Marcos HB**, Semelka RC. Stomach diseases: MR evaluation using combined t2-weighted single-shot echo train spin-echo and gadolinium-enhanced spoiled gradient-echo sequences. *J Magn Reson Imaging* 1999; **10**: 950-960 [PMID: 10581508 DOI: 10.1002/(SICI)1522-2586(199912)10:6<950::AID-JMRI7>3.0.CO;2-H]
67 **Maccioni F**, Marcelli G, Al Ansari N, Zippi M, De Marco V, Kagarmanova A, Vestri A, Marcheggiano-Clarke L, Marini M. Preoperative T and N staging of gastric cancer: magnetic resonance imaging (MRI) versus multi detector computed tomography (MDCT). *Clin Ter* 2010; **161**: e57-e62 [PMID: 20499021]
68 **Sohn KM**, Lee JM, Lee SY, Ahn BY, Park SM, Kim KM. Comparing MR imaging and CT in the staging of gastric carcinoma. *AJR Am J Roentgenol* 2000; **174**: 1551-1557 [PMID: 10845479 DOI: 10.2214/ajr.174.6.1741551]
69 **Miettinen M**, Lasota J. Gastrointestinal stromal tumors--definition, clinical, histological, immunohistochemical, and molecular genetic features and differential diagnosis. *Virchows Arch* 2001; **438**: 1-12 [PMID: 11213830]
70 **Chourmouzi D**, Sinakos E, Papalavrentios L, Akriviadis E, Drevelegas A. Gastrointestinal stromal tumors: a pictorial review. *J Gastrointestin Liver Dis* 2009; **18**: 379-383 [PMID: 19795038]
71 **Stroszczynski C**, Jost D, Reichardt P, Chmelik P, Gaffke G, Kretzschmar A, Schneider U, Felix R, Hohenberger P. Follow-up of gastro-intestinal stromal tumours (GIST) during treatment with imatinib mesylate by abdominal MRI. *Eur Radiol* 2005; **15**: 2448-2456 [PMID: 16132930 DOI: 10.1007/s00330-005-2867-x]
72 **Ghimire P**, Wu GY, Zhu L. Primary gastrointestinal lymphoma. *World J Gastroenterol* 2011; **17**: 697-707 [PMID: 21390139 DOI: 10.3748/wjg.v17.i6.697]
73 **Masselli G**, Colaiacomo MC, Marcelli G, Bertini L, Casciani E, Laghi F, D'Amico P, Caprasecca S, Polettini E, Gualdi G. MRI of the small-bowel: how to differentiate primary neo-

plasms and mimickers. *Br J Radiol* 2012; **85**: 824-837 [PMID: 22422388 DOI: 10.1259/bjr/14517468]
74 **Masselli G**, Gualdi G. Evaluation of small bowel tumors: MR enteroclysis. *Abdom Imaging* 2010; **35**: 23-30 [PMID: 19096749 DOI: 10.1007/s00261-008-9490-7]
75 **Minardi AJ**, Zibari GB, Aultman DF, McMillan RW, McDonald JC. Small-bowel tumors. *J Am Coll Surg* 1998; **186**: 664-668 [PMID: 9632155]
76 **Amzallag-Bellenger E**, Oudjit A, Ruiz A, Cadiot G, Soyer PA, Hoeffel CC. Effectiveness of MR enterography for the assessment of small-bowel diseases beyond Crohn disease. *Radiographics* 2012; **32**: 1423-1444 [PMID: 22977028 DOI: 10.1148/rg.325115088]
77 **Hoeffel C**, Crema MD, Belkacem A, Azizi L, Lewin M, Arrivé L, Tubiana JM. Multi-detector row CT: spectrum of diseases involving the ileocecal area. *Radiographics* 2006; **26**: 1373-1390 [PMID: 16973770 DOI: 10.1148/rg.265045191]
78 **Beaumont C**, Pandey T, Gaines Fricke R, Laryea J, Jambhekar K. MR evaluation of rectal cancer: current concepts. *Curr Probl Diagn Radiol* 2013; **42**: 99-112 [PMID: 23683851 DOI: 10.1067/j.cpradiol.2012.08.002]
79 **Shoenut JP**, Semelka RC, Silverman R, Yaffe CS, Micflikier AB. Magnetic resonance imaging evaluation of the local extent of colorectal mass lesions. *J Clin Gastroenterol* 1993; **17**: 248-253 [PMID: 8228088]
80 **Zijta FM**, Bipat S, Stoker J. Magnetic resonance (MR) colonography in the detection of colorectal lesions: a systematic review of prospective studies. *Eur Radiol* 2010; **20**: 1031-1046 [PMID: 19936754 DOI: 10.1007/s00330-009-1663-4]
81 **Taylor FG**, Swift RI, Blomqvist L, Brown G. A systematic approach to the interpretation of preoperative staging MRI for rectal cancer. *AJR Am J Roentgenol* 2008; **191**: 1827-1835 [PMID: 19020255 DOI: 10.2214/AJR.08.1004]
82 **Karatağ O**, Karatağ GY, Özkurt H, Değirmenci HK, Avlanmış Ö, Başak M, Baykan A. The ability of phased-array MRI in preoperative staging of primary rectal cancer: correlation with histopathological results. *Diagn Interv Radiol* 2012; **18**: 20-26 [PMID: 21671218 DOI: 10.4261/1305-3825.DIR.3394-10.2]
83 **Halefoglu AM**, Yildirim S, Avlanmis O, Sakiz D, Baykan A. Endorectal ultrasonography versus phased-array magnetic resonance imaging for preoperative staging of rectal cancer. *World J Gastroenterol* 2008; **14**: 3504-3510 [PMID: 18567078]
84 **MERCURY Study Group**. Diagnostic accuracy of preoperative magnetic resonance imaging in predicting curative resection of rectal cancer: prospective observational study. *BMJ* 2006; **333**: 779 [PMID: 16984925 DOI: 10.1136/bmj.38937.646400.55]
85 **Samee A**, Selvasekar CR. Current trends in staging rectal cancer. *World J Gastroenterol* 2011; **17**: 828-834 [PMID: 21412492 DOI: 10.3748/wjg.v17.i7.828]
86 **Beets-Tan RG**, Beets GL, Vliegen RF, Kessels AG, Van Boven H, De Bruine A, von Meyenfeldt MF, Baeten CG, van Engelshoven JM. Accuracy of magnetic resonance imaging in prediction of tumour-free resection margin in rectal cancer surgery. *Lancet* 2001; **357**: 497-504 [PMID: 11229667]
87 **Hünerbein M**, Pegios W, Rau B, Vogl TJ, Felix R, Schlag PM. Prospective comparison of endorectal ultrasound, three-dimensional endorectal ultrasound, and endorectal MRI in the preoperative evaluation of rectal tumors. Preliminary results. *Surg Endosc* 2000; **14**: 1005-1009 [PMID: 11116406 DOI: 10.1007/s004640000345]
88 **Brown G**, Radcliffe AG, Newcombe RG, Dallimore NS, Bourne MW, Williams GT. Preoperative assessment of prognostic factors in rectal cancer using high-resolution magnetic resonance imaging. *Br J Surg* 2003; **90**: 355-364 [PMID: 12594673 DOI: 10.1002/bjs.4034]
89 **Koh DM**, Brown G, Temple L, Raja A, Toomey P, Bett N, Norman AR, Husband JE. Rectal cancer: mesorectal lymph nodes at MR imaging with USPIO versus histopathologic findings--initial observations. *Radiology* 2004; **231**: 91-99 [PMID: 14976266]
90 **Park MJ**, Kim SH, Lee SJ, Jang KM, Rhim H. Locally advanced rectal cancer: added value of diffusion-weighted MR imaging for predicting tumor clearance of the mesorectal fascia after neoadjuvant chemotherapy and radiation therapy. *Radiology* 2011; **260**: 771-780 [PMID: 21846762 DOI: 10.1148/radiol.11102135]
91 **Gollub MJ**, Gultekin DH, Akin O, Do RK, Fuqua JL, Gonen M, Kuk D, Weiser M, Saltz L, Schrag D, Goodman K, Paty P, Guillem J, Nash GM, Temple L, Shia J, Schwartz LH. Dynamic contrast enhanced-MRI for the detection of pathological complete response to neoadjuvant chemotherapy for locally advanced rectal cancer. *Eur Radiol* 2012; **22**: 821-831 [PMID: 22101743 DOI: 10.1007/s00330-011-2321-1]
92 **Lambregts DM**, Cappendijk VC, Maas M, Beets GL, Beets-Tan RG. Value of MRI and diffusion-weighted MRI for the diagnosis of locally recurrent rectal cancer. *Eur Radiol* 2011; **21**: 1250-1258 [PMID: 21240647 DOI: 10.1007/s00330-010-2052-8]
93 **Sassen S**, de Booij M, Sosef M, Berendsen R, Lammering G, Clarijs R, Bakker M, Beets-Tan R, Warmerdam F, Vliegen R. Locally advanced rectal cancer: is diffusion weighted MRI helpful for the identification of complete responders (ypT0N0) after neoadjuvant chemoradiation therapy? *Eur Radiol* 2013; **23**: 3440-3449 [PMID: 23832319 DOI: 10.1007/s00330-013-2956-1]
94 **Beets-Tan RG**, Beets GL. Local staging of rectal cancer: a review of imaging. *J Magn Reson Imaging* 2011; **33**: 1012-1019 [PMID: 21509856 DOI: 10.1002/jmri.22475]
95 **Chen CC**, Lee RC, Lin JK, Wang LW, Yang SH. How accurate is magnetic resonance imaging in restaging rectal cancer in patients receiving preoperative combined chemoradiotherapy? *Dis Colon Rectum* 2005; **48**: 722-728 [PMID: 15747073 DOI: 10.1007/s10350-004-0851-1]
96 **Dresen RC**, Beets GL, Rutten HJ, Engelen SM, Lahaye MJ, Vliegen RF, de Bruïne AP, Kessels AG, Lammering G, Beets-Tan RG. Locally advanced rectal cancer: MR imaging for restaging after neoadjuvant radiation therapy with concomitant chemotherapy. Part I. Are we able to predict tumor confined to the rectal wall? *Radiology* 2009; **252**: 71-80 [PMID: 19403847 DOI: 10.1148/radiol.2521081200]
97 **Barbaro B**, Fiorucci C, Tebala C, Valentini V, Gambacorta MA, Vecchio FM, Rizzo G, Coco C, Crucitti A, Ratto C, Bonomo L. Locally advanced rectal cancer: MR imaging in prediction of response after preoperative chemotherapy and radiation therapy. *Radiology* 2009; **250**: 730-739 [PMID: 19244043 DOI: 10.1148/radiol.2503080310]
98 **Vliegen RF**, Beets GL, Lammering G, Dresen RC, Rutten HJ, Kessels AG, Oei TK, de Bruïne AP, van Engelshoven JM, Beets-Tan RG. Mesorectal fascia invasion after neoadjuvant chemotherapy and radiation therapy for locally advanced rectal cancer: accuracy of MR imaging for prediction. *Radiology* 2008; **246**: 454-462 [PMID: 18227541 DOI: 10.1148/radiol.2462070042]

P- Reviewer: Chen F, Imbriaco M, Lichtor T **S- Editor**: Ji FF
L- Editor: A **E- Editor**: Liu SQ

World Journal of Radiology

Submit a Manuscript: http://www.wjgnet.com/esps/
Help Desk: http://www.wjgnet.com/esps/helpdesk.aspx
DOI: 10.4329/wjr.v6.i8.567

World J Radiol 2014 August 28; 6(8): 567-582
ISSN 1949-8470 (online)

REVIEW

Imaging of the temporomandibular joint: An update

Asim K Bag, Santhosh Gaddikeri, Aparna Singhal, Simms Hardin, Benson D Tran, Josue A Medina, Joel K Curé

Asim K Bag, Aparna Singhal, Simms Hardin, Benson D Tran, Josue A Medina, Joel K Curé, Section of Neuroradiology, The Department of Radiology, School of Medicine, The University of Alabama at Birmingham, Birmingham, AL 35249-6830, United States
Santhosh Gaddikeri, Department of Radiology, University of Washington, SS-202 Seattle, WA 98195-7117, United States
Author contributions: Bag AK contributed to the arthritis, images and overall integrity, manuscript revision and final approval the manuscript; Gaddikeri S contributed to the internal derangement and manuscript revision; Singhal A contributed to the normal joint anatomy, anatomic variation and manuscript revision; Hardin S contributed to the anatomic variation and manuscript revision; Tran BD contributed to the deposition diseases and tumors, manuscript revision; Medina JA contributed to the imaging techniques, manuscript revision; Curé JK contributed to the images, overall integrity, manuscript revision and final approval.
Correspondence to: Asim K Bag, Assistant Professor, Section of Neuroradiology, The Department of Radiology, School of Medicine, The University of Alabama at Birmingham, JT N432, 619 19th Street South, Birmingham, AL 35249-6830, United States. abag@uabmc.edu
Telephone: +1-205-9349952 Fax: +1-205-9759262
Received: December 28, 2013 Revised: February 27, 2014
Accepted: June 20, 2014
Published online: August 28, 2014

Abstract

Imaging of the temporomandibular joint (TMJ) is continuously evolving with advancement of imaging technologies. Many different imaging modalities are currently used to evaluate the TMJ. Magnetic resonance imaging is commonly used for evaluation of the TMJ due to its superior contrast resolution and its ability to acquire dynamic imaging for demonstration of the functionality of the joint. Computed tomography and ultrasound imaging have specific indication in imaging of the TMJ. This article focuses on state of the art imaging of the temporomandibular joint. Relevant normal anatomy and biomechanics of movement of the TMJ are discussed for better understanding of many TMJ pathologies. Imaging of internal derangements is discussed in detail. Different arthropathies and common tumors are also discussed in this article.

Key words: Temporomandibular joint; Magnetic resonance imaging; Imaging; Computed tomography; Anatomy; Pathologies

Core tip: "Imaging of the temporomandibular joint: An update" is a thorough review of the imaging techniques and imaging appearances of normal anatomy, anatomic variation and pathologies of the temporomandibular joint (TMJ). Numerous images are appropriately used for illustration of the key concepts of TMJ imaging. Nice blend of exquisite details and beautiful illustrative images is the main feature of this article. The purpose of this article is easy understanding of many difficult aspects of imaging of the TMJ.

Bag AK, Gaddikeri S, Singhal A, Hardin S, Tran BD, Medina JA, Curé JK. Imaging of the temporomandibular joint: An update. *World J Radiol* 2014; 6(8): 567-582 Available from: URL: http://www.wjgnet.com/1949-8470/full/v6/i8/567.htm DOI: http://dx.doi.org/10.4329/wjr.v6.i8.567

INTRODUCTION

Pain related to the temporomandibular joint (TMJ) is common in the general population. Only about 3%-7% of the patients with pain related to TMJ seek medical attention[1,2]. Although TMJ disorders or dysfunctions are the most common clinical conditions for imaging referrals, pathologies specific to the bone and the joints are also common. Different imaging modalities are available to image the TMJ, each with inherent strengths and weaknesses. Magnetic resonance imaging (MRI) is the most widely used and is diagnostic technique of choice. In this article, we review the imaging techniques, anatomy pathology involving the TMJ with special emphasis on MRI findings.

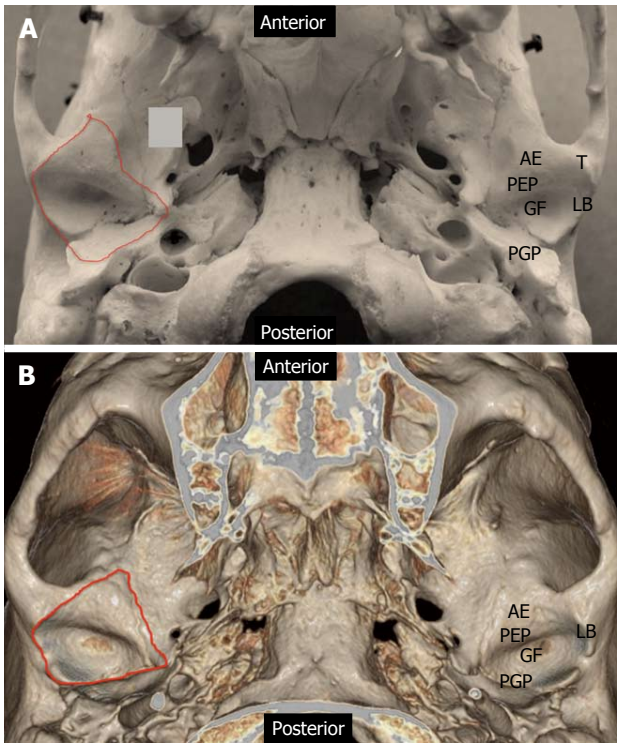

Figure 1 Anatomy of the cranial component of temporomandibular joint. A: Photograph of skull specimen; B: 3-D volume rendered image obtained from a temporal bone Redline demonstrates the capsular attachment. AE: Articular eminence; GF: Glenoid fossa; LB: Lateral border; PEP: Preglenoid plane; PGP: Postglenoid plane; T: Tubercle.

Embryology and development of TMJ

The TMJ is one of the last diarthrodial joints to appear in utero and does not emerge in the craniofacial region until the 8th week of gestation. The maxilla, mandible, muscles of mastication, and biconcave disc develop embryologically from the first branchial arch through the 14th week of gestation. The TMJ is considerably underdeveloped at birth in comparison to other diarthrodial joints making it susceptible to perinatal and postnatal insults. The joint continues developing in the early childhood years as the jaw is utilized for sucking motions and eventually chewing.

ANATOMY OF TMJ

The TMJ is a ginglymoarthrodial synovial joint (latin:ginglymus = hinge joint) that allows both backward and forward translation as well as a gliding motion[3]. Similar to the other synovial joints in the body, the TMJ has a disk, articular surfaces, fibrous capsule, synovial fluid, synovial membrane, and ligaments. What makes this joint unique is the articular surfaces are covered by fibrocartilage instead of hyaline cartilage. The articular surfaces of the TMJ are formed inferiorly by the mandibular condyle and superiorly by the glenoid fossa (also known as mandibular fossa) and articular eminence of the temporal bone.

Articular surfaces

The mandibular component consists of the ovoid condylar process that is 15-20 mm wide in the transverse dimension and 8-10 mm wide in the antero-posterior dimension[3]. The appearance of the mandibular condyle is extremely variable between patients and in different age groups.

The cranial component of the TMJ lies below the squamous portion of the temporal bone anterior to tympanic plate. The articular fossa is formed entirely by the squamous portion of the temporal bone. The posterior part of the articular fossa is elevated to form the posterior articular ridge. In most individuals the posterior articular ridge becomes thicker on the lateral aspect and forms a cone shaped projection known as postglenoid process (PGP). The tympanosquamosal fissure lies at the posterior and lateral part of the glenoid fossa, between the squamous and tympanic portion of the petrous bone and separates the articular surface form the nonarticular surface of the glenoid fossa. Along the medial aspect of the glenoid fossa is the petrotympanic fissure anteriorly and the petrosquamous fissure posteriorly. The articular eminence (AE) forms the anterior boundary of the glenoid fossa. The AE is a transverse bony bar anterior to the glenoid fossa and medial to the posterior margin of the zygomatic process. The anterior slope of the AE is known as the preglenoid plane (PEP) and rises gently from the infratemporal surface of the squamous bone. The mandibular condyle and the articular disk travel anteriorly to the summit of the AE and onto PEP during wide mouth opening. The gentle anterior slope facilitates smooth backward movement of the condyle and disk from the anterior position back to neutral position. The articular tubercle is a small bony knob at the lateral aspect of the AE where the lateral collateral ligament attaches. The lateral border of glenoid fossa is slightly raised from the fossa joining the anterior tubercle with the PGP (Figure 1).

Articular disk

The articular disk is round or oval, biconcave, avascular fibrocartilage between the condyle and glenoid fossa. The disk is considerably thinner centrally in the intermediate zone. The triangular anterior band is approximately 2 mm in thickness and blends with the joint capsule. The posterior band is approximately 3 mm in thickness and continues as bilaminar zone (also known as retrodiscal region and posterior attachment), which consists of superior fibroelastic layer (also known as temporal lamina) that attaches to PGP and an inferior fibrous layer (also known as the inferior lamina) that attaches to the posterior condylar neck. The superior layer prevents slipping of the disk during wide mouth opening and the inferior layer prevents excessive rotation of the disk over the condyle. Both the lamina are separated by loose elastic fibers with blood vessels and nerves. These fibers attach to the posterior joint capsule and augments disk retraction during mouth closing. The bands are longer in the mediolateral dimension than in the antero-posterior dimension[4]. The smaller anterior band attaches anteriorly to the joint

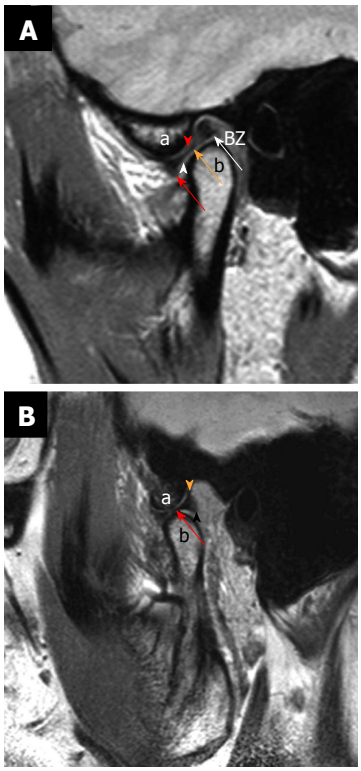

Figure 2 Normal anatomy. Sagittal proton density weighted closed mouth and open mouth view of magnetic resonance imaging. A: On the closed mouth view, the disk is located posterior to the articular eminence (the letter, a). It can be noted that the "bow-tie" shape of the disk: Thicker anterior band (red arrow) and posterior band (white arrow) with a thinner central zone (orange arrow). Bilaminar zone (BZ) is located posterior to the posterior band. It can also be noted that the inferior joint compartment (white arrowhead) between the disk and the mandibular condyle (the letter, b) and superior joint compartment (red arrowhead) between the articular eminence and the disk; B: On the open mouth view (in a different patient), the thinner intermediate zone (red arrow) of the disk is interposed between the articular eminence (the letter, a) and the condylar head (the letter, b) in a "bow-tie" fashion. Orange arrowhead demonstrates temporal lamina and black arrowhead indicate inferior lamina.

capsule, condylar head, and AE. Some patients have an additional antero-medial attachment to the superior belly of the lateral pterygoid muscle. Unlike its anterior and posterior attachments, the disk is not attached to the joint capsule medially and laterally. Instead, the disk is firmly attached to the medial and lateral poles of the mandibular condyle. This allows simultaneous movements of the disk and the condyle (Figure 2).

Muscles

The muscles of mastication (medial and lateral pterygoids, masseter, and temporalis) in addition to other accessory muscles help opening and closing of the jaw[4-6]. The lateral pterygoid in conjunction to the stylohyoid, mylohyoid and geniohyoid muscles is used to open the jaw. The temporalis, medial pterygoid, and masseter muscles close the jaw. The lateral pterygoid, part of the masseter muscle and the medial pterygoid assist in the anterior translation of the mandible. The protrusive muscles (helping forward movement) are used alternately to move the jaw laterally from side to side. Individual muscle origins and attachments are listed below[4,6].

Jaw-closing muscles/adductors

The masseter is the strongest muscle of mastication and has two parts that blend together anteriorly. The superficial part originates from the anterior two-thirds of the zygomatic arch and inserts on the lower one-third of the lateral surface of the mandibular ramus. The deep part originates from the entire zygomatic arch and inserts on the upper two-thirds of the ramus.

The medial pterygoid courses parallel to the masseter along the medial aspect of the mandible. The anterior part arises from the lateral surface of the palatine pyramidal process and the maxillary tuberosity. The posterior part originates from the pterygoid fossa and the medial surface of the lateral pterygoid plate. The medial pterygoid inserts on the inferomedial surface of the mandibular ramus.

The temporalis muscle originates from the temporalis fossa and inserts on the coronoid process and inner side of the mandibular ramus. The fibers also attach directly to the medial side of the coronoid process and ramus.

Jaw-opening muscles/abductors

The lateral pterygoid muscle has two bellies. The superior belly originates from the infratemporal surface of the greater wing of sphenoid. The inferior belly originates from the lateral surface of the lateral pterygoid plate. There is a wide gap between the two heads of the lateral pterygoid muscle that come together anterior to the TMJ. The fibers from the superior head primarily attach to the anteromedial surface of the mandibular neck at the pterygoid fovea. Additionally, in some patients part of the superior head directly attaches to the superomedial aspect of the joint capsule and extends to the anteromedial aspect of the articular surface. All of the fibers of the inferior head attach to the pterygoid fovea. Variability in the attachment of the lateral pterygoid muscle is reported with insertions of the muscle described only to the condyle or to the condyle, capsule, and the disk[7-9].

The superior belly helps maintain the physiologic position of the disk in the open mouth position. This is accomplished by pulling the disk forward with a combined translation and rotation while exerting forward pressure on both the condyle and the disk thus stabilizing their relationship to each other. The inferior belly pulls the condyle forward out of the fossa. When the inferior belly alternately contracts, this produces lateral movement of the jaw.

The digastric muscle has a posterior and an anterior belly united by an conjoined tendon. The posterior belly is attached to the mastoid process of the temporal bone and extends to the hyoid bone becoming continuous with the intermediate tendon. A fibrous loop attached to the hyoid holds the tendon in place. The anterior belly extends from the tendon to the digastric fossa on the lower aspect of mandible near the symphysis. Contraction of the digastric muscles pulls the symphysis menti backwards producing the retrusive and opening movements of the mandible.

The geniohyoid, myolohyoid, stylohyoid and infra-

hyoid muscles also have supportive role in mandibular movements that are beyond the scope of this review.

Biomechanics of TMJ movements

Jaw movement involves a high level of interaction and coordination between bilateral mandibular condyles, disk, muscles, and ligaments of the joints. The functional interactions within the TMJ are complex and incompletely understood[10,11]. A simplistic view of the complex interactions in open and closed mouth positions is described below.

In a normal joint, the thin intermediate zone of the disk is always interposed between the condyle and the temporal bone in both the closed-mouth and open-mouth positions. This is for the prevention of articular damage.

In the closed mouth position, the condyle is centered in the glenoid fossa. The disk is interposed between the condyle inferiorly and the glenoid fossa superiorly. The articular eminence is anterior to the disk (Figure 2). The normal disk is positioned such that the anterior band is in front of the condyle and the junction of the posterior band and bilaminar zone lie immediately above the condylar head near the 12 o'clock position[1,3,4,9,12-14]. However, some controversy exists over the range of normal position of the disk[1,3,4,14-18]. Drace *et al*[15] suggest that the junction of the posterior band and bilaminar zone should fall within 10 degree of vertical to be within 95 percentile of normal. There is significant variation in relationship of the posterior band and bilaminar zone in normal population, resulting in inappropriate classification of anterior disk displacement[16,18]. Rammelsberg *et al*[17] suggest that disk positions of up to +30° from the vertical be considered normal. Many other authors have proposed that the intermediate zone be the point of reference so that in a normal joint it is interposed between the condyle and the temporal bone in all joint positions[4,19,20]. Comparing to the different disk positions of 12, 11 and 10 o'clock, Orsini *et al*[19] found the intermediate zone criterion for disk displacement to be more stringent. Recently Provenzano Mde *et al*[20] have suggested similar conclusions (Figure 2).

IMAGING TECHNIQUES

A variety of modalities can be used to image the TMJ. This includes non-invasive imaging modalities such as conventional radiographs, ultrasound, Computed tomography (CT) and MRI to more invasive imaging such as arthrography. Each imaging modality has its uses.

Conventional radiographs have a limited role in evaluation of the TMJ. They can be used to evaluate only the bony elements of the TMJ. They do not give useful information when it comes to the non-bony elements such as cartilage or adjacent soft tissues. They also do not give useful information concerning joint effusions, which are commonly associated with pain and disc displacements. Another disadvantage concerning conventional radiographs is the problem of superimposition of adjacent structures. Many different views such as the submentovertex, transmaxillary, and the transcranial are used to reduce superimposition.

Ultrasound is a less expensive and easily performed imaging modality that can be used to evaluate the TMJ. This is simple way to look for the presence of a joint effusion[21]. Ultrasound is also used to evaluate cartilage as well as disk displacement with both open and closed mouth imaging[21]. It is used for image-guided injections for both diagnostic and therapeutic purposes[21]. Typically, a linear transducer of 8 MHz or higher is ideal. The patient should be lying supine with the transducer placed parallel to a line extending from the tragus of the ear to the lateral surface of the nose over the TMJ.

CT is useful to evaluate the bony elements of the TMJ as well as the adjacent soft tissues. CT is ideal for the evaluation of fractures, degenerative changes, erosions, infection, invasion by tumor, as well as congenital anomalies[21]. A typical imaging protocol is: 120 kV, 100 mA, 1 mm collimation, 1 mm/rotation (pitch), and imaged with a closed mouth. CT also allows 3D reconstructions, which can be used for evaluating congenital anomalies and fractures[21]. CT is predominantly done when there is suspicion of bony involvement from the MRI and if primary bony pathologies are suspected clinically. Relative advantages of CT over MRI include, exquisite bone details and 3D assessment of congenital, traumatic and postsurgical conditions.

Clinical evaluation of the TMJ can be nonspecific due to overlap of symptoms between internal derangement and myofacial pain dysfunction[1]. MRI should be part of the standard evaluation when an internal structural joint abnormality is suspected because MRI provides high resolution and great tissue contrast. This allows for a detailed evaluation of the anatomy was well as biomechanics of the joint through open and closed mouth imaging[1].

For optimal imaging of the TMJ, small bilateral surface coils with small field of view are used to achieve higher signal to noise ratio and simultaneous bilateral acquisition. Closed mouth coronal and axial T1 sequences are needed to evaluate the overall anatomy and bone marrow as well as the adjacent soft tissues to exclude other adjacent pathology. In our institution, axial T1 is obtained as a localizer[14]. Bilateral closed mouth and open mouth T2, proton density (PD) and dynamic sequences are obtained in a oblique sagittal plane. In our institution, dynamic images are obtained as rapid acquisition of static images using a single shot fast spin echo (SSFSE) proton density sequence during progressive opening and closing of the mouth. These images are displayed sequentially as a cine loop. Mouth opening devices such as Burnett opening devices may be used for incremental opening of the mouth controlled by the patient. It can be argued that passive mouth opening with a Burnet device might not reproduce the physiologic conditions occurring during mouth opening given the possible role of the lateral pterygoid muscle in disc stabilization during mouth opening. Oblique imaging entails 30° medial

Table 1 Temporomandibular joint magnetic resonance imaging protocol

Plane	Sequence	Slice thickness	TR	TE	Mouth open/closed
Axial	T1	2 mm, 0 skip	500	Minimal	Closed
Coronal	T1	3 mm, 0.5 skip	500	Minimal	Closed
Bilateral Sag Oblq	T2 and PD	3 mm	3500	Min and 85	Closed and open
Bilateral Sag Oblq	T2	3 mm	1180-2000	64	Dynamic cine

PD: Proton density; TE: Echo time; TR: Repetition time.

from the true sagittal plane[1]. Please see the table for specific MRI protocol[1]. A total of 8 sequences will need to be performed (Table 1).

Arthrography is an invasive imaging technique to evaluate the TMJ. This imaging modality requires injection of radiopaque contrast into the TMJ under fluoroscopic guidance. Once the contrast is injected, the joint can be evaluated for adhesions, disk dysfunction, as well as disk perforation based on how contrast flows in the joint. This modality is rarely used today because MRI can be used to evaluate the TMJ without being invasive, exposing the patient to a possibility of allergic reaction from the contrast, possibility of infection, or using radiation.

IMAGING APPEARANCE OF NORMAL TMJ

MRI

On MRI, marrow fat in the condyle has a high T1 signal intensity. The cortical bone and the disk have low signal intensity on both T1 and T2 weighted images because of low proton density and short T2[12]. Sometimes high T2 and PD signal intensity can be seen in the central portion of the disk similar to a centrally hydrated vertebral disk[1,4]. The disk is otherwise homogeneous, hypointense and biconcave in shape. The center of the posterior band may be slightly hyperintense due to presence of loose areolar tissue (Figure 2).

The disk's posterior attachment has higher signal intensity than muscle on proton density and T1 weighted images secondary to fatty tissue. The bilaminar zone is visible as intermediate signal intensity structures.

In closed mouth position, the junction of the posterior band and posterior attachment normally lies above the condylar head near the 12 o'clock position. The posterior band and retrodiskal tissue are best depicted in the open mouth position. In open mouth position, the intermediate zone lies between the condyle and the articular eminence and the posterior band is against the posterior surface of the condyle[1,9] (Figure 2).

The superior belly of lateral pterygoid attaches to the anterior band of the disk. The inferior belly of the lateral pterygoid attaches to the anterior surface of the condylar neck with a thin linear hypointense fibrous band. This band is seen just inferior to the position of the disk, and can sometimes be mistaken for the disk, particularly when the disk is medially or laterally displaced[22].

In the coronal plane, the disk is crescent shaped and its medial and lateral borders are attached to the respective aspects of the condylar head and joint capsule. The lateral and medial capsules do not demonstrate any outward bulges beyond the borders in normal condition[1,22].

PATHOLOGIES RELATED TO ANATOMIC VARIATIONS

Anatomic variations in the TMJ can be symptomatic and/or have implications during arthroscopy and surgery. There can also be several variations in the appearance of the mandibular condyles including intra-individual variations between the two sides. The disease processes can be developmental, due to remodeling related to malocclusion, trauma or other secondary developmental abnormalities[3].

Bifid condyle

A bi-lobed or duplicated mandibular head is an infrequently encountered incidental imaging finding. While the etiology is unknown, theories include reminiscence of congenital fibrous septum and peripartum or early childhood trauma. The duplicated heads may lie in either an antero-posterior or transverse orientation. Dennison *et al*[23] have suggested that the term "bifid condyle" should be reserved for describing multiple condyles in the sagittal plane only. No treatment is required for asymptomatic patients. However surgery may be performed if there is displacement of the disc or ankylosis of the joint space (Figure 3).

Foramen of Huschke

In some individuals there may be persistence of a developmental defect in the tympanic plate. The tympanic plate is present as an incomplete U-shaped cartilaginous ring at birth. Over time the ossification proceeds laterally and posteriorly leaving a defect in the floor of the external meatus, called the foramen tympanicum (foramen of Huschke). With growth of the mastoid process, this defect changes in position from inferior to anterior and usually closes by the 5th year of life. Rarely, a 3-4 mm defect persists and is found to be located at the antero-inferior aspect of the external auditory canal and posteromedial to the TMJ. These patients can present with a defect or polyp on the anterior wall of the external auditory canal (EAC) or with salivary otorrhea during mastication. TMJ tissue may also herniate into the EAC during mastication[24,25]. During arthroscopy, there can be inadvertent

Figure 3 Bifid condyle. Coronal reformatted computed tomography image through the temporomandibular joint (TMJ) demonstrates bifid left mandibular condyle. It can be noted that one of the condyles (arrow) is smaller than the other. Advanced degenerative changes are noted in bilateral TMJ.

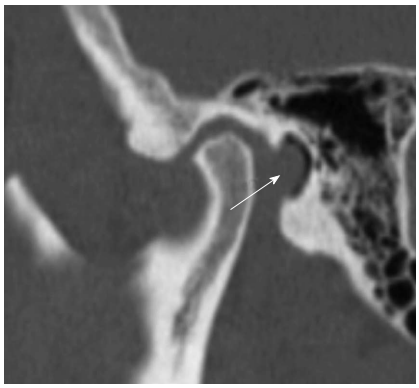

Figure 4 Foramen of Huschke. Sagittal reformatted computed tomography image through the temporomandibular joint demonstrates a focal defect (arrow) in the tympanic plate.

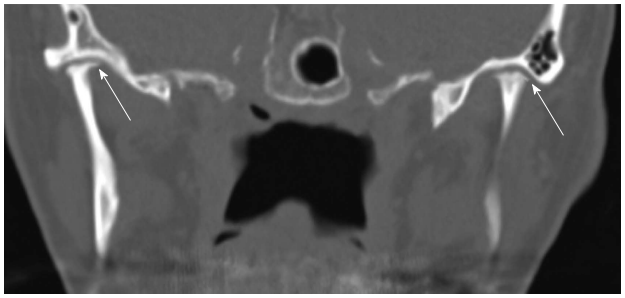

Figure 5 Idiopathic condylar resorption. Coronal reformatted computed tomography image through the temporomandibular joint of a young patient demonstrates bilateral severe condylar resorption (arrows) without any evidence of degenerative changes within the joint.

passage into the EAC resulting in otologic complications. This foramen also can act as a path of communication between the EAC and TMJ or infratemporal fossa allowing the spread of infection, inflammation or tumor[24,25] (Figure 4).

Condylar hypoplasia

Aplasia and hypoplasia of the mandibular condyle is secondary to non-development or underdevelopment of the condyle and can be congenital or acquired. Congenital aplasia or hypoplasia of the mandibular condyles is a rare anomaly and usually occurs as a part of more widespread 1st and 2nd branchial arch anomalies (*e.g.*, Treacher-Collins syndrome). Acquired condylar hypoplasia may be secondary to local factors (trauma, infection, radiation) or systemic factors (toxic agents, rheumatoid arthritis, mucopolysaccharoidosis)[26]. Traumatic vaginal delivery has been implicated as a cause of hypoplasia[27]. Hypoplasia may involve one or both of the condyles. Unilateral disease produces mandibular rotation or tilt and associated facial asymmetry. The diagnosis of bilateral condylar hypoplasia may be delayed secondary to facial symmetry. Hypoplastic condyles are frequently complicated with ankylosis[28].

Idiopathic condylar resorption

Idiopathic condylar resorption (also known as condylysis or "cheerleader syndrome") is primarily a disease of TMJ affecting teenage girls. There is rapidly progressive condylar erosion resulting in widening of the joint space with the chin becoming less prominent from retrognathia[29]. Many causes have been hypothesized including estrogen influence on osteogenesis, avascular necrosis, and TMJ internal derangement. Orthognathic surgery has been implicated as a cause of the disease but also is one of the corrective approaches for idiopathic condylar resorption (Figure 5).

Condylar hyperplasia

Condylar hyperplasia is a rare disorder characterized by increased volume of the mandibular condyle, and is frequently associated with increased volume of the ramus and mandibular body[30]. Condylar hyperplasia is usually a unilateral process. This disease presents in the second and third decades of life during brisk periods of osteogenesis suggesting a hormonal influence upon the growth disturbance. Trauma has also been implicated in asymmetric condylar hyperplasia due to hypervascularity during healing producing inducing excessive osteogenesis. The hyperplasia produces facial asymmetry with the chin rotating away from the affected side[30]. Resection of the hyperplastic condyle causes the abnormal growth to cease and restores facial symmetry (Figure 6).

Extensive pneumatization

Extensive pneumatization of the mastoid bone can involve the glenoid fossa and articular eminence. Knowledge of extensive pneumatization is necessary prior to surgery to prevent perforations. Complications can occur during TMJ surgery due to forceful flap retraction, dissection or with placement of screws in cases where fossa-eminence prostheses are required[31,32]. Pneumatization can also provide a path of minimal resistance and facilitate the spread of pathological tumors, inflammation, infection or fracture into the joint. For these reasons, a CT must be performed prior to TMJ surgery when ex-

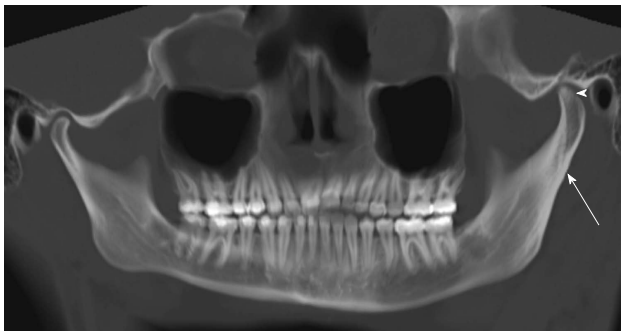

Figure 6 Condylar hyperplasia. Panoramic reformation of the source computed tomography data including both the temporomandibular joints of a young patient demonstrates hyperplasia of the left condyle (arrowhead) in comparison to the right side. Associated hypertrophy of the ramus and the neck (arrow) of the left hemi-mandible is also noted.

Figure 7 Extensive pneumatization. Coronal reformatted computed tomography image through the right temporomandibular joint demonstrates almost complete pneumatization of the glenoid fossa except the central part.

tensive pneumatization is detected in the panoramic radiographs[31,32] (Figure 7).

INTERNAL DERANGEMENT OF TMJ

Internal derangement (ID) is defined as a mechanical fault of the joint that interferes with smooth joint function. This is attributed to abnormal interaction of the articular disc, condyle and articular eminence. Associated clinical features include articular pain and articular noises[33]. Disc displacement is the most common cause of ID, though not all displaced discs are associated with derangement and not all derangements are caused by disc displacement[34]. Additionally, it is not clear whether the displaced disk is related to onset, progression or cessation of the pain. Loose bodies and adhesions in the joint can also result in derangement. Up to 34% of asymptomatic volunteers can have anterior disc displacement and 23% of patients with derangement can have normal disc position[18]. In most large MRI series approximately 80% of patients referred for diagnostic imaging of the TMJ demonstrate some form of disk displacement[35-37]. MRI is the imaging modality of choice for the diagnosis of internal derangement with an accuracy of 95% in assessing the disc position and form and 93% accuracy in assessing the osseous changes[38].

Disc displacement

The disc displacement is categorized based on the relation of the displaced disc with mandibular condyle. The displacement can be anterior, anterolateral, anteromedial, lateral, medial and posterior[39]. The most common pattern of disc displacement are either anterior and anterolateral accounting for more than 80% of the causes[37]. The disc displacement can be subclassified as anterior displacement with reduction (ADR) or anterior displacement with no reduction (ADNR) based on restoration of a normal relationship between the condyle and the disc on mouth opening (Figures 8 and 9). The disc displacement can be either complete or partial[35]. If the entire mediolateral dimension of the disc is displaced, it is referred to as complete displacement. On the other hand if only the medial or lateral portion of the disc is displaced, it is referred to as partial displacement. Partial disc displacement is commonly seen with ADR. Frequently the lateral part of the disc is displaced anteriorly while the medial part of the disc remains in normal position (rotational disk displacement)[40].

In ADR, the anteriorly displaced disc returns to the normal position on mouth opening producing a "reciprocal click" (Figure 9). In ADNR, there is limited mouth opening and deviation of the jaw to the affected side (closed lock). Over time, stretching or perforation of the retrodiscal tissue causes deformation of the disk leading to an improvement in jaw excursion and reduced lateral deviation during mouth opening (Figure 10A). The posterior band of the disc remains anterior to the condyle even with mouth opening[41]. There is increased association of degenerative changes in the TMJ with the ADNR. Although TMJ disorder with ADR and normal condylar cortical bone may be stable for decades, it will eventually progress to ADNR. In a study with 55 patients, de Leeuw *et al*[42] have demonstrated 75% of the patients with long history (approximately 30 years) of TMJ internal derangement have ADNR.

The exact mechanism for a disc displacement is unknown although trauma with injury to the posterior disc attachment is considered to be the most likely cause. Unenhanced MRI is the imaging modality of choice for evaluation of ID. During the early stage of ID the disc retains its normal shape, but over time it becomes deformed by thickening of the posterior band and thinning of the anterior band. This produces in a biconvex, teardrop shaped or a rounded disc. The disc maintains a normal biconcave shape as long as it remains on top of the condyle during mouth opening[42]. Hence, presence of an irregular and rounded disc almost always indicates disc disease[43]. Other MRI findings that suggest disc disease include disc flattening, decrease in the normal intermediate to high signal intensity of the disc[44] and presence of tear or perforation in the chronic stage.

Posterior disc displacement is a rare entity and acco-

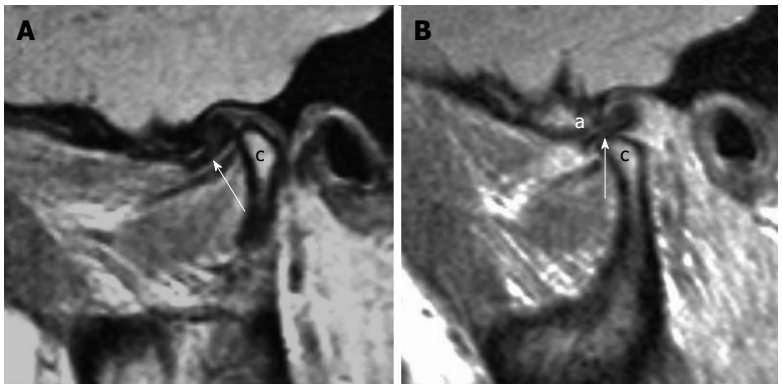

Figure 8 Anterior displacement with reduction. A: Sagittal proton density weighted magnetic resonance imaging (MRI) in the closed mouth position demonstrates anterior displacement of the disk (arrow) in front of the mandibular condyle (the letter, c); B: Sagittal proton density weighted MRI in the open mouth position demonstrates reduction of the disk (arrow) between the articular eminence (the letter, a) and the mandibular condyle (the letter, c).

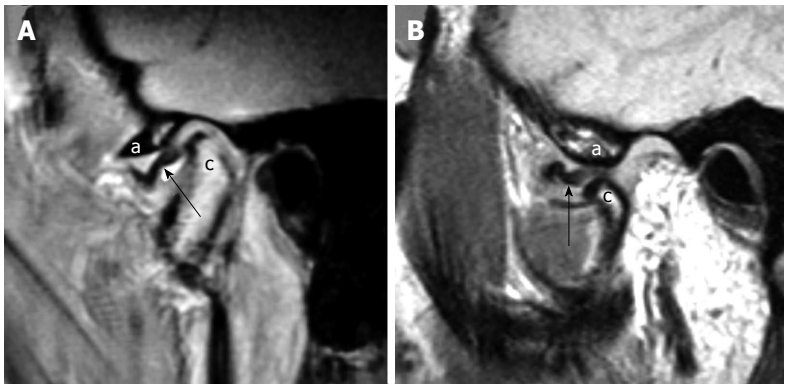

Figure 9 Anterior displacement with no reduction. A: Sagittal proton density weighted magnetic resonance imaging (MRI) in the closed mouth position demonstrates anterior displacement of the disk (arrow) related to the articular eminence (the letter, a) and anterior to the mandibular condyle (the letter c); B: Sagittal proton density weighted MRI in the open mouth position demonstrates no reduction of the disk (arrow) between the articular eminence (the letter, a) and the mandibular condyle (the letter, c).

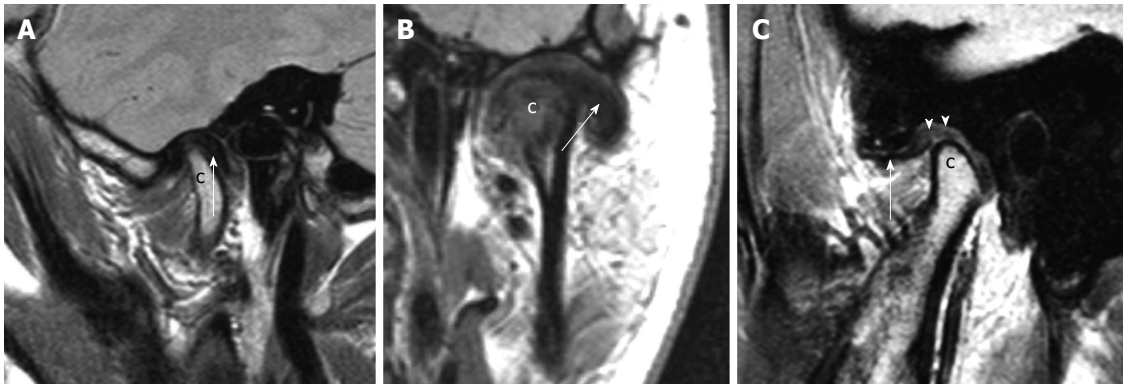

Figure 10 Other types of disk displacement. A: Posterior disk displacement. Sagittal proton density weighted magnetic resonance imaging (MRI) in the closed mouth position demonstrates posterior displacement of the disk (arrow) in relation to the mandibular condyle (the letter, c); B: Lateral disk displacement. Coronal proton density weighted demonstrates lateral displacement of the disk (arrow) in relation to the mandibular condyle (the letter, c); C: Pseudodisk. Sagittal proton density weighted MRI in the closed mouth position demonstrates anterior displacement of the disk (arrow) in front of the mandibular condyle (the letter, c). The thickening of the posterior attachments (arrowheads) superior to the mandibular condyle is seen as "pseudodisk".

unts for only 0.01% to 0.001% of all disc displacements[45]. The major clinical sign is a sudden onset of locked jaw in open position. MRI is helpful in the diagnosis by demonstrating displacement of the posterior band beyond 1° clock position[9] (Figure 10A). Review of patient's clinical information is important before image interpretation as previous posterior disk plication can be mistaken for an acquired posterior disk displacement.

Anterolateral and antero-medial disk displacements are grouped under rotational displacements while the

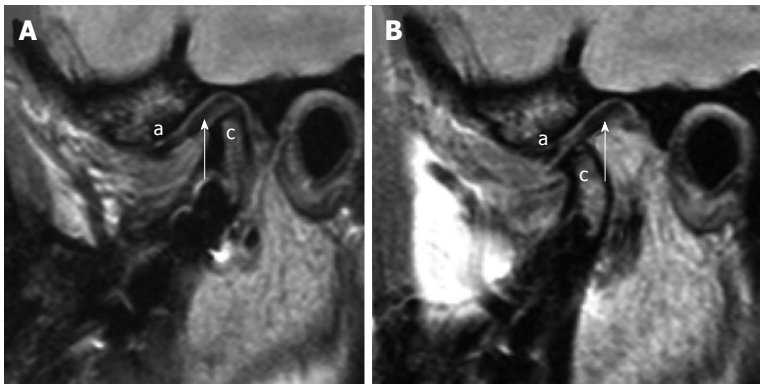

Figure 11 Stuck disk. A: Sagittal proton density weighted magnetic resonance imaging (MRI) in the closed mouth position demonstrates apparently normal position of the disk (arrow) in relation to the mandibular condyle (the letter, c). The letter "a" demonstrates the articular eminence; B: Sagittal proton density weighted MRI in the open mouth position demonstrates no anterior movement of the disk (arrow) with the mandibular condyle (the letter, c), *i.e.*, "stuck" to the glenoid fosssa. The articular eminence is denoted with letter "a".

pure lateral and medial displacements are grouped under sideways displacement[46]. Isolated lateral displacement is rare (Figure 10B). Again these rotational and sideways displacements can be complete or partial and with or without disc reduction. Anterolateral displacement is the most common pattern[37].

Pseudodisk

A pseudo-disk is present in some patients with an anteriorly displaced disk. This has been postulated as an adaptive reaction to anterior disk displacement within the posterior disk attachment followed by subsequent connective tissue hyalinization that[47] appears as a band-like structure of low signal intensity replacing the normally bright signal of the posterior disk attachment[8,9,22] (Figure 10C).

Stuck disc

The "stuck disc" is a pathologic condition characterized by an immobile disc in relation to the glenoid fossa and the articular eminence. This is present in both open and closed mouth positions[9] and is likely related to the adhesions. It can occur with or without disc displacement and can be associated with pain and joint dysfunction due to limitation of condylar translation[48,49]. This diagnosis can be missed unless the TMJ is imaged in both open and closed mouth positions (Figure 11). Sagittal oblique cine imaging is particularly useful in evaluation of stuck disk.

Perforated disc

Disc perforation is reported in 5% to 15% of deranged joints disc displacements[50]. It is more common in patients with ADNR than in ADR[51,52] and is usually seen in patients with advanced arthrosis. The prevalence of a perforated disc is higher in women than in men and prevalent in individuals over 80 years of age[53]. MRI findings of disc perforation include disc deformity (100%), disc displacement (81%), condylar bony changes (68%), joint effusion (23%) and non-visualization of temporal posterior attachment (TPA) of the disc (65%-68%)[54]. Conventional and MR arthrogram can be helpful in the diagnosis of a disc perforation by demonstrating opacification of both the joint compartments from a single lower compartment injection. If the disk perforation is suspected a fat suppressed T2 weighted MRI can be obtained in sagittal and coronal plane[55]. Absence of stretching/straightening of the posterior temporal disk attachment on mouth opening also suggests disk perforation.

Joint effusion

Joint effusion represents an abnormally large accumulation of intra-articular fluid and is commonly seen in symptomatic patients. A small amount of joint fluid can be seen in asymptomatic patients[56]. An effusion is more prevalent in painful than in non-painful joints[16]. Although not all patients with joint pain have effusion, patients with large effusions commonly experience pain and disc displacement[57].

T2 weighted MR sequence is the best sequence for the assessment of joint effusion. An early joint effusion is commonly seen surrounding the anterior band but larger effusions can occupy both superior and inferior joint space. A large effusion may have diagnostic value as it outlines the disc and sometimes even the disc perforation as well as retrodiscal tissue producing "arthrographic effect"[57]. Gadolinium enhanced T1 weighted imaging can be helpful in distinguishing a plain joint effusion from synovial proliferation. In patients with inflammatory arthropathies with associated synovial proliferation, the proliferating synovium enhances while the effusion does not[58].

Thickening of lateral pterygoid muscle attachment (double disk sign)

The exact role of lateral pterygoid muscle (LPM) in the TMJ function is still controversial although its suggested role is in generation of side-to-side and protrusive jaw forces[9]. There are electromyographic studies showing hyperactivity in the inferior attachment of the LPM in patients with TMJ internal derangement[59]. Several mor-

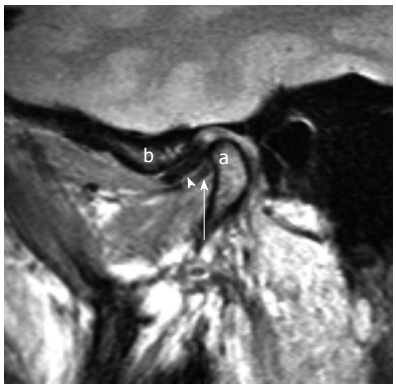

Figure 12 Double disk sign (thickening of the lateral pterygoid muscle). Sagittal closed mouth proton density image demonstrates anterior displacement of the disk (arrow head). The thickened lateral pterygoid muscle near the mandibular condylar (the letter, a) attachment appear as linear hypointense structure (white arrow) inferior to the disk in the same orientation giving the appearance of "double disk". The articular eminence is denoted with letter "b".

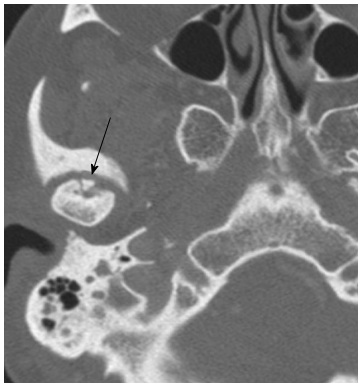

Figure 13 Osteochondritis dessicans. Axial computed tomography scan through the level of the temporomandibular joint demonstrates a tiny bone fragment (arrow) at the anterior aspect of the disk. It can be noted that there are linear lucency surrounding the bone fragment.

Figure 14 Loose bodies. Sagittal reformation of the axial dataset demonstrates multiple "loose bodies" in the joint cavities, anteroinferior to the articular eminence (black arrow) and immediately posterior to the mandibular condyle (white arrow).

phologic changes to the superior and inferior bellies of the LPM on MRI have been described. These include hypertrophy, atrophy and contractures in patients with ADNR of the TMJ with these morphologic changes having a significant association with the clinical symptoms of pain or restricted jaw opening[60]. It is suggested that there is significant association between the anterior disc displacement and attachment of the superior LPM to the disc alone and not to the condyle[61]. The interpreting radiologist should be aware of a potential pitfall of mistaking the thickened inferior LPM to an anteriorly displaced disc ("double disc sign")[9] (Figure 12).

Osteochondritis dissecans and avascular necrosis

Osteochondritis dissecans (OCD) and avascular necrosis (AVN) of the mandibular condyle are similar pathologic entities likely represent a spectrum of the same pathophysiology[62]. Common clinical features of OCD/AVN of the mandibular condyle include pain and joint disability[63]. Pain is commonly over the joint and along the third division of the trigeminal nerve. Other symptoms include ipsilateral headache, earache and spasm of masticator muscles. These can occur with or without limitation of joint movements[63].

MRI is the modality of choice for assessment of OCD/AVN of the mandibular condyle[63]. There is decreased marrow signal on T1 weighted sequences in cases of AVN. T2 weighted sequences demonstrate variable signal characteristics with early AVN, healing and OCD. Early AVN consistently exhibits high signal on T2WI and acute OCD typically demonstrated a hypointense central fragment surrounded by a zone of higher signal on both T1W and T2W sequences[63]. Although MRI is 78% sensitive and 84% specific for the diagnosis of AVN, the positive predictive value is only 54% because condylar sclerosis secondary to advanced TMJ degenerative changes have similar MRI appearances[64]. Radiologic changes of OCD and AVN of the mandibular condyle are frequently associated with joint effusion and internal derangement of the disc[65] (Figure 13).

Loose bodies

Loose bodies in a synovial joint can be due to primary or secondary synovial chondromatosis. The primary type is associated with spontaneous cartilaginous metaplasia in the synovium, while the secondary type is due to incorporation of osteocartilaginous loose bodies in the synovium in the setting of degenerative joint disease[66]. Common clinical symptoms associated with loose bodies include pain, periauricular swelling, decreased range of jaw motion, crepitation and unilateral deviation of the jaw during mouth opening[67].

Panoramic radiographs of the TMJ may or may not demonstrate loose bodies[68]. High resolution CT[69,70] or MRI[70] can demonstrate small loose bodies within the TM joint space (Figure 14).

Hypermobility

Patients with a hypermobile TMJ can present with an inability to close the jaw (open lock) after wide opening of the jaw. This occurs as a result of translation of the

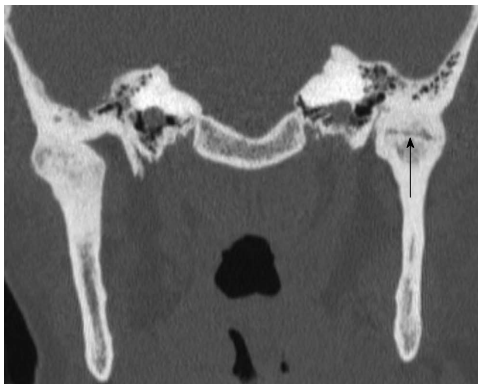

Figure 15 Ankylosis. Coronal reformation of the axial dataset demonstrates complete ankylosis of the right temporomandibular joint (TMJ) and near complete ankylosis of the left TMJ with subtle residual joint space at the center (black arrow).

condyle beyond the margins of the anterior attachment of the TMJ capsule. Entrapment of the condyle along the anterior slope of the articular eminence results due to various biomechanical constraints, particularly masticator muscle activity[71].

In acute cases, there is little need for imaging studies as the open lock is clinically evident with a relevant clinical history of wide jaw opening or trauma. In chronic cases MRI can give information about the height and steepness of the articular eminences as well as the shape and position of the disc[72].

Ankylosis

Ankylosis of the TMJ can be due to fibrous adhesions or a bony fusion resulting in the restriction of jaw motion. It can occur as a sequel of previous infection, trauma surgery[73] and in patients with juvenile idiopathic arthritis or bifid mandibular condyles. MR arthrography is useful for the evaluation of fibrous adhesions and three-dimensional CT scan is necessary for surgical planning when bony fusion is suspected (Figure 15).

TMJ ARTHRITIS

Similar to other synovial joints in body, the TMJ is frequently involved in different inflammatory arthritides. Degenerative arthritis and arthritis secondary to crystalline deposition disease are also common in TMJ. Arthritis secondary to infection or trauma can occur at the TMJ. Arthritis of TMJ is discussed based on the pathophysiologic mechanism.

Inflammatory arthritis

Juvenile idiopathic arthritis: Juvenile idiopathic arthritis (JIA) is the most common rheumatic disease in childhood affecting girls more frequently than boys. The disease predominantly affects synovial joints. There are two peaks of onset, first being between the ages of 1 and 3 years and the second peak between 8 and 12 years[74]. The TMJ is involved in 17% to 87% of patients with JIA[74]. JIA can be systemic, polyarticular and pauciarticular. The TMJ is more commonly involved in patients with polyarticular joint involvement[75]. The typical presentation of TMJ involvement includes pain, joint tenderness, crepitation, stiffness and decreased range of motion. Bony ankylosis can develop in some patients as a late disease manifestation.

Orthopantomogram, CT, MRI and ultrasound have been used to evaluate TMJ JIA. Orthopantomogram and CT predominantly identify the bony erosions secondary to TMJ involvement. Both these techniques involve radiation exposure to young patients. MRI and ultrasound have gained popularity in evaluation of the TMJ in patients with JIA because these techniques have better soft tissue resolution allowing earlier diagnosis of TMJ involvement without any ionizing radiation. Acute TMJ arthritis typically demonstrates joint effusion and synovial thickening on T2 weighted imaging without any bony changes[76]. Enhancement of the joint or periarticular tissue is not a specific sign of acute TMJ arthritis because abnormal joint enhancement can be present even in healthy patients[76]. Condylar resorption can be better evaluated on non-fat suppressed T1 weighted sequence and suggests a more chronic TMJ arthritis[76] (Figure 16).

Rheumatoid arthritis: Rheumatoid arthritis (RA) is a chronic inflammatory disorder that predominantly affects the periarticular tissue such as synovial membrane, joint capsules, tendon, tendon sheaths and ligaments. Internal joint components are secondarily involved. The prevalence of RA in the general population is approximately 2%-2.5% with female predominance. The peak onset of disease is 40-60 years and approximately 50%-75% of patients with RA have TMJ involvement[77].

RA is a slowly progressive disease of insidious onset with progressive destruction of the articular/periarticular soft tissue and the adjacent bones resulting in joint deformity. The TMJ is involved at a later stage of disease. TMJ involvement causes deep, dull aching pain in the preauricular area, especially during chewing. Limited range of motion and morning stiffness can be present[78]. The mandibular condyle gradually resorbs as the disease progresses.

Radiographic features of RA include loss of joint space, condylar destruction, flattening with anterior positioning of the condyle. There may be flattening of the articular eminence and erosion of the glenoid fossa. Synovial proliferation is an early process in RA and can distinguish it from other types of arthritis[79]. Synovial proliferation is readily seen on MRI and can be seen in all patients[79]. A joint effusion is also comparatively more common in RA.

Degenerative (osteo)arthritis

Osteoarthritis (OA) is a chronic degenerative disease that characteristically affects the articular cartilage of synovial joints and is associated with simultaneous remodeling of the underlying subchondral bone with secondary involvement of the synovium. Osteoarthritis is the most

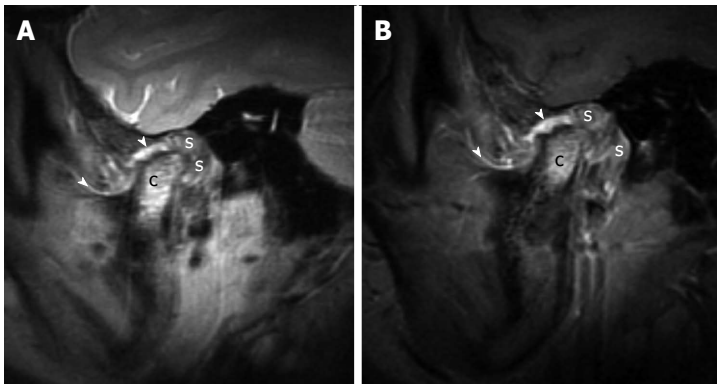

Figure 16 Juvenile idiopathic arthritis. A: Sagittal proton density weighted magnetic resonance imaging (MRI) in the closed mouth position demonstrates increased signal at the mandibular condyle (the letter, c), extensive thickening of the synovium (the letter, s) in the retrodiscal regions. It can be noted that the thickening and increased signal of the synovium at other places (arrowheads); B: Sagittal fat suppressed post contrast T1 weighted MRI in the closed mouth position demonstrates enhancement of signal at the mandibular condyle (the letter, c), enhancement and extensive thickening of the synovium (the letter, s) in the retrodiscal regions. There is thickening and enhancement of the synovium at other places (arrowheads).

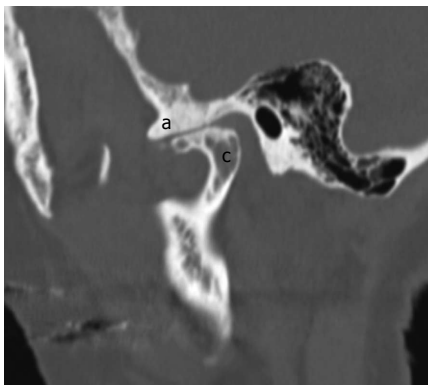

Figure 17 Degenerative changes. Sagittal reformation of the axial dataset demonstrates deformity of the mandibular condyle (the letter, c), extensive sclerosis of the articular eminence (the letter, a) and severe loss of joint space.

common joint pathology affecting the TMJ[80]. There is a clear disparity between radiographic evidence of OA and symptoms. Population based studies demonstrate that minimal condylar flattening is present in up to 35% of asymptomatic patients while approximately 11% of patients have TMJ OA-related symptoms[80].

The most common symptom of TMJ OA is pain during chewing. The pain usually starts in the periarticular soft tissue and the masticator muscles that are in protective reflex spasm. Fatigue of masticator muscles, trismus, decreased range of motion, difficulty opening the mouth and joint crepitations are other common symptoms.

Radiologic hallmarks of TMJ OA are articular surface cortical bone irregularity, erosion and osteophyte formation[81]. Erosion is radiologically defined as focal area of decreased density at the cortical margin of the articular surface of the mandibular condyle and the subchondral region. Osteophyte formation typically occurs at a later stage in the disease and can stabilize and broaden the surface area of the joint in an attempt to better withstand axial loading forces. Different imaging modalities have been used with varying degree of success. There is still no general consensus as to which imaging modality should be the gold standard[81] (Figure 17).

Metabolic arthritis/crystalline arthropathies

Calcium pyrophosphate dehydrate deposition disease: Calcium pyrophosphate dehydrate deposition disease (CPPD) is a metabolic arthropathy caused by the deposition of calcium pyrophosphate dehydrate crystals in and around joints, especially within the articular cartilage and fibrocartilage[82].

The spectrum of TMJ involvement ranges from asymptomatic disk calcification to a marked destruction of the joint with erosive changes in the mandibular condyle and the adjacent skull base. Common symptoms include pain and preauricular swelling with occasional hearing loss. Chewing can exacerbate the pain. Other less common symptoms include TMJ clicking, tinnitus, and malocclusion.

The radiographic appearance of CPPD is variable. Computed tomography demonstrates calcium deposition in the disk or periarticular tissue. On MRI, CPP deposits typically appear as hypointense material both on T1 and T2 weighted sequences. CT and MRI show erosions near both the condyle and fossa with adjacent CPPD deposits[82]. The erosions may extend into the skull base and into the middle cranial fossa. Involvement of other joints with chondrocalcinosis is a clue to the diagnosis. The differential diagnosis includes synovial chondromatosis, synovial osteochondroma, and osteosarcoma (Figure 18).

Infectious arthritis

TMJ infection is usually secondary to direct extension of infection from the adjacent tissue into the joint. Systemic infections such as tuberculosis and syphilis can rarely involve the TMJ. TMJ infection is more common in the setting of immunosuppression and presence of other systematic diseases such as diabetes mellitus, rheumatoid arthritis and intravenous drug use, *etc*.

Figure 18 Calcium pyrophosphate dehydrate deposition disease. Coronal reformation of the axial dataset demonstrates destruction of the left temporomandibular joint with erosion and deformity of both the mandibular condyle and the glenoid fossa. There is extensive extensive calcium pyrophosphate dehydrate deposition disease medial to the joint space (arrow).

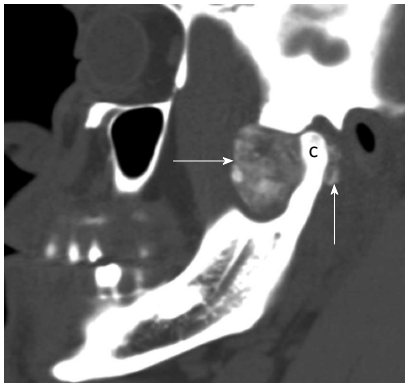

Figure 19 Synovial chondromatosis. Sagittal reformation of the axial dataset demonstrates extensive cloud-like calcification (arrows) filling and expanding the joint space anterior to the mandibular condyle (the letter, c). Calcification is also present posterior to the mandibular condyle.

TUMORS AND TUMOR-LIKE CONDITIONS OF THE TMJ

Tumors and tumor-like conditions can affect the TMJ. These conditions may have similar presentations such as pain, swelling, and limitation of motion.

Synovial chondromatosis

Synovial chondromatosis (SC) is a benign condition with chondrometaplasia of the synovial membrane and formation of cartilaginous nodules. These nodules can become detached and form loose bodies which later calcify. Synovial chondromatosis typically involves large joints, such as the knee, hip, and elbow. It is uncommon for the temporomandibular joint to be affected by SC. SC typically involves the superior compartment of TMJ while involvement of the inferior compartment is rare and secondary to perforation of the articular disc. Uncommon findings include erosion of the mandibular condylar head, temporal skull base, and intracranial extension.

Patients typically present with preauricular pain, swelling, inflammation, limitation of motion, and articular noises. Some patients also report neurologic dysfunction, such as headache and hearing loss.

The diagnosis of TMJ synovial chondromatosis is difficult since it is a rare disease and can have similar findings to more common diseases, such as chondrocalcinosis, osteoarthritis, and chondrosarcoma. The radiologic findings of SC include calcified loose bodies, soft tissue swelling, widening of the joint space, irregularities of the joint surface, and sclerosis of the glenoid fossa and/or mandibular condyle. CT typically shows calcified nodules surrounding the mandibular condyle with degenerative changes of the condyle[83]. MRI typically shows mixed solid and fluid signal related to the metaplasia of the synovial tissue and the fluid component of the accumulated synovial secretions. The calcified nodules are T1/T2 hypointense with a surrounding T2 hyperintense effusion and proliferative synovium, which enhances after contrast administration. MRI is preferred in evaluation of SC over CT because of the ability to detect non-calcified loose bodies, lack of radiation, and visualization of the articular disc[84] (Figure 19).

Treatment is surgical removal of the loose bodies and excision of the metaplastic synovium. In end stage SC without synovial metaplastic activity, the treatment is often non-surgical with therapy aimed towards symptom relief.

Pigmented villonodular synovitis

Pigmented villonodular synovitis (PVNS) is a benign, non-neoplastic proliferative disorder of the synovial membranes of joints, bursae, and tendon sheaths. The disease is typically monoarticular and can involve any joint but is most often seen in the knee. Primary PVNS of the TMJ is rare. There are two forms of PVNS: nodular and diffuse. The most common nodular patterns of PVNS include giant cell tumor, xanthoma, xanthogranuloma, and myeloplaxoma, which affect a focal part of the synovium[85]. Diffuse PVNS affects nearly the entire synovium.

The exact etiology of PVNS is unclear. It was originally postulated to be an inflammatory response to an unknown stimulus. Other theories attribute it to repetitive intra-articular hemorrhage from trauma, altered lipid metabolism, or a benign neoplastic proliferation.

PVNS commonly presents as a slowly growing and non-tender swelling of the affected joint. Patients with involvement of the TMJ, can present with a preauricular mass with swelling, pain, tenderness, clicking, otalgia, and hearing loss.

The most sensitive method for the detection of PVNS is by MRI demonstrating T1/T2 hypointensity and blooming on the GRE sequences from paramagnetic hemosiderin deposition[86]. There may be moderate to intense inhomogeneous enhancement of the synovium. CT findings are usually nonspecific with bone erosion, subchondral cysts, and a soft tissue mass[87]. A joint effusion may be dense from the hemosiderin. The differential diagnosis of PVNS on MRI includes synovial chondrom-

atosis, rheumatoid arthritis, synovial sarcoma, hemophilia, and synovial hemangioma.

Primary and secondary neoplasms, and other lesions

Osteochondroma is the second most common neoplastic lesion affecting the TMJ. Osteochondroma, osteoma, and condylar hyperplasia are often difficult to differentiate both clinically and on imaging. MR and CT may delineate the exact extent of the tumor and its relationship to anatomic structures within the TMJ.

Synovial cysts, ganglion cysts and simple bone cysts may also occur. Many benign primary bone neoplasms, such as chondroblastoma, osteoma, osteoid osteoma, osteoblastoma, ossifying fibroma and aneurysmal bone cyst can also involve the TMJ. Malignant primary bone neoplasms are extremely rare in TMJ but include chondrosarcoma and osteogenic sarcoma. There also can be extension of tumors from adjacent structures into the TMJ. Tumors from the external ear and parotid gland can extend into the TMJ. Less than 1% of all tumors metastasize into the maxillofacial region. Adenocarcinoma is the most common metastatic tumor of the jaw, making up about 70% of cases. Reported metastasis to TMJ includes breast, renal, lung, colon, prostate, thyroid, and testicular primary.

CONCLUSION

Imaging of TMJ should be performed on a case by case basis depending upon clinical signs and symptoms. MRI is the diagnostic study of choice for evaluation of disk position and internal derangement of the joint. CT scan for evaluation of TMJ is indicated if bony involvement is suspected and should be judiciously considered because of radiation risk. Understanding of the TMJ anatomy, biomechanics, and the imaging manifestations of diseases is important to accurately recognize and manage these various pathologies.

REFERENCES

1 **Aiken A**, Bouloux G, Hudgins P. MR imaging of the temporomandibular joint. *Magn Reson Imaging Clin N Am* 2012; **20**: 397-412 [PMID: 22877948 DOI: 10.1016/j.mric.2012.05.002]

2 **Guralnick W**, Kaban LB, Merrill RG. Temporomandibular-joint afflictions. *N Engl J Med* 1978; **299**: 123-129 [PMID: 661872 DOI: 10.1056/NEJM197807202990304]

3 **Alomar X**, Medrano J, Cabratosa J, Clavero JA, Lorente M, Serra I, Monill JM, Salvador A. Anatomy of the temporomandibular joint. *Semin Ultrasound CT MR* 2007; **28**: 170-183 [PMID: 17571700 DOI: 10.1053/j.sult.2007.02.002]

4 **Sommer OJ**, Aigner F, Rudisch A, Gruber H, Fritsch H, Millesi W, Stiskal M. Cross-sectional and functional imaging of the temporomandibular joint: radiology, pathology, and basic biomechanics of the jaw. *Radiographics* 2003; **23**: e14 [PMID: 12920179 DOI: 10.1148/rg.e14]

5 **Sava A**, Scutariu M. Functional anatomy of the temporomandibular joint (II). *Rev Med Chir Soc Med Nat Iasi* 2012; **116**: 1213-1217 [PMID: 23700914]

6 **Van Eijden TM**, Korfage JA, Brugman P. Architecture of the human jaw-closing and jaw-opening muscles. *Anat Rec* 1997; **248**: 464-474 [PMID: 9214565 DOI: 10.1002/(SICI)1097-0185(199707)248:3<464::AID-AR20>3.0.CO;2-M]

7 **Imanimoghaddam M**, Madani AS, Hashemi EM. The evaluation of lateral pterygoid muscle pathologic changes and insertion patterns in temporomandibular joints with or without disc displacement using magnetic resonance imaging. *Int J Oral Maxillofac Surg* 2013; **42**: 1116-1120 [PMID: 23746672 DOI: 10.1016/j.ijom.2013.01.022]

8 **Tomas X**, Pomes J, Berenguer J, Mercader JM, Pons F, Donoso L. Temporomandibular joint soft-tissue pathology, II: Nondisc abnormalities. *Semin Ultrasound CT MR* 2007; **28**: 205-212 [PMID: 17571703 DOI: 10.1053/j.sult.2007.02.005]

9 **Tomas X**, Pomes J, Berenguer J, Quinto L, Nicolau C, Mercader JM, Castro V. MR imaging of temporomandibular joint dysfunction: a pictorial review. *Radiographics* 2006; **26**: 765-781 [PMID: 16702453 DOI: 10.1148/rg.263055091]

10 **Koolstra JH**. Dynamics of the human masticatory system. *Crit Rev Oral Biol Med* 2002; **13**: 366-376 [PMID: 12191962 DOI: 10.1177/154411130201300406]

11 **Lobbezoo F**, Drangsholt M, Peck C, Sato H, Kopp S, Svensson P. Topical review: new insights into the pathology and diagnosis of disorders of the temporomandibular joint. *J Orofac Pain* 2004; **18**: 181-191 [PMID: 15508997]

12 **Harms SE**, Wilk RM. Magnetic resonance imaging of the temporomandibular joint. *Radiographics* 1987; **7**: 521-542 [PMID: 3448646 DOI: 10.1148/radiographics.7.3.3448646]

13 **Katzberg RW**. Temporomandibular joint imaging. *Radiology* 1989; **170**: 297-307 [PMID: 2643133]

14 **Rao VM**, Bacelar MT. MR imaging of the temporomandibular joint. *Magn Reson Imaging Clin N Am* 2002; **10**: 615-630 [PMID: 12685497 DOI: 10.1016/S1064-9689(02)00011-9]

15 **Drace JE**, Enzmann DR. Defining the normal temporomandibular joint: closed-, partially open-, and open-mouth MR imaging of asymptomatic subjects. *Radiology* 1990; **177**: 67-71 [PMID: 2399340]

16 **Katzberg RW**, Westesson PL, Tallents RH, Drake CM. Anatomic disorders of the temporomandibular joint disc in asymptomatic subjects. *J Oral Maxillofac Surg* 1996; **54**: 147-153; discussion 153-155 [PMID: 8604061 DOI: 10.1016/S0278-2391(96)90435-8]

17 **Rammelsberg P**, Pospiech PR, Jäger L, Pho Duc JM, Böhm AO, Gernet W. Variability of disk position in asymptomatic volunteers and patients with internal derangements of the TMJ. *Oral Surg Oral Med Oral Pathol Oral Radiol Endod* 1997; **83**: 393-399 [PMID: 9084204 DOI: 10.1016/S1079-2104(97)90248-1]

18 **Tallents RH**, Katzberg RW, Murphy W, Proskin H. Magnetic resonance imaging findings in asymptomatic volunteers and symptomatic patients with temporomandibular disorders. *J Prosthet Dent* 1996; **75**: 529-533 [PMID: 8709019 DOI: 10.1016/S0022-3913(96)90458-8]

19 **Orsini MG**, Kuboki T, Terada S, Matsuka Y, Yamashita A, Clark GT. Diagnostic value of 4 criteria to interpret temporomandibular joint normal disk position on magnetic resonance images. *Oral Surg Oral Med Oral Pathol Oral Radiol Endod* 1998; **86**: 489-497 [PMID: 9798238 DOI: 10.1016/S1079-2104(98)90380-8]

20 **Provenzano Mde M**, Chilvarquer I, Fenyo-Pereira M. How should the articular disk position be analyzed? *J Oral Maxillofac Surg* 2012; **70**: 1534-1539 [PMID: 22079066 DOI: 10.1016/j.joms.2011.08.004]

21 **Vilanova JC**, Barceló J, Puig J, Remollo S, Nicolau C, Bru C. Diagnostic imaging: magnetic resonance imaging, computed tomography, and ultrasound. *Semin Ultrasound CT MR* 2007; **28**: 184-191 [PMID: 17571701 DOI: 10.1053/j.sult.2007.02.003]

22 **Westesson PL O-YM**, Sano T, Okano T. Anatomy, Pathology, and Imaging of the Temporomandibular Joint. In: Som PM, Curtin HD, ed. Head and Neck Imaging-2 Volume Set, 5th Edition. St. Louis: Mosby, 2011: 1547-613

23 **Dennison J**, Mahoney P, Herbison P, Dias G. The false and the true bifid condyles. *Homo* 2008; **59**: 149-159 [PMID:

18417126 DOI: 10.1016/j.jchb.2008.02.001]
24 **Lacout A**, Marsot-Dupuch K, Smoker WR, Lasjaunias P. Foramen tympanicum, or foramen of Huschke: pathologic cases and anatomic CT study. *AJNR Am J Neuroradiol* 2005; **26**: 1317-1323 [PMID: 15956489]
25 **Tozoglu U**, Caglayan F, Harorli A. Foramen tympanicum or foramen of Huschke: anatomical cone beam CT study. *Dentomaxillofac Radiol* 2012; **41**: 294-297 [PMID: 22517996]
26 **Tank W**, Wright D, Iizuka T. Unilateral dysplasia of the mandibular condyle: report of a case. *J Oral Maxillofac Surg* 1998; **56**: 765-769 [PMID: 9632337]
27 **Berger SS**, Stewart RE. Mandibular hypoplasia secondary to perinatal trauma: report of case. *J Oral Surg* 1977; **35**: 578-582 [PMID: 267174]
28 **Kaneyama K**, Segami N, Hatta T. Congenital deformities and developmental abnormalities of the mandibular condyle in the temporomandibular joint. *Congenit Anom* (Kyoto) 2008; **48**: 118-125 [PMID: 18778456 DOI: 10.1111/j.1741-4520.2008.00191.x]
29 **Wolford LM**. Idiopathic condylar resorption of the temporomandibular joint in teenage girls (cheerleaders syndrome). *Proc* (Bayl Univ Med Cent) 2001; **14**: 246-252 [PMID: 16369629]
30 **Angiero F**, Farronato G, Benedicenti S, Vinci R, Farronato D, Magistro S, Stefani M. Mandibular condylar hyperplasia: clinical, histopathological, and treatment considerations. *Cranio* 2009; **27**: 24-32 [PMID: 19241796]
31 **Ladeira DB**, Barbosa GL, Nascimento MC, Cruz AD, Freitas DQ, Almeida SM. Prevalence and characteristics of pneumatization of the temporal bone evaluated by cone beam computed tomography. *Int J Oral Maxillofac Surg* 2013; **42**: 771-775 [PMID: 23290566]
32 **Miloglu O**, Yilmaz AB, Yildirim E, Akgul HM. Pneumatization of the articular eminence on cone beam computed tomography: prevalence, characteristics and a review of the literature. *Dentomaxillofac Radiol* 2011; **40**: 110-114 [PMID: 21239574]
33 **Rudisch A**, Innerhofer K, Bertram S, Emshoff R. Magnetic resonance imaging findings of internal derangement and effusion in patients with unilateral temporomandibular joint pain. *Oral Surg Oral Med Oral Pathol Oral Radiol Endod* 2001; **92**: 566-571 [PMID: 11709695 DOI: 10.1067/moe.2001.116817]
34 **Cholitgul W**, Nishiyama H, Sasai T, Uchiyama Y, Fuchihata H, Rohlin M. Clinical and magnetic resonance imaging findings in temporomandibular joint disc displacement. *Dentomaxillofac Radiol* 1997; **26**: 183-188 [PMID: 9442605 DOI: 10.1038/sj.dmfr.4600239]
35 **Larheim TA**, Westesson P, Sano T. Temporomandibular joint disk displacement: comparison in asymptomatic volunteers and patients. *Radiology* 2001; **218**: 428-432 [PMID: 11161157 DOI: 10.1148/radiology.218.2.r01fe11428]
36 **Ribeiro RF**, Tallents RH, Katzberg RW, Murphy WC, Moss ME, Magalhaes AC, Tavano O. The prevalence of disc displacement in symptomatic and asymptomatic volunteers aged 6 to 25 years. *J Orofac Pain* 1997; **11**: 37-47 [PMID: 10332309]
37 **Paesani D**, Westesson PL, Hatala M, Tallents RH, Kurita K. Prevalence of temporomandibular joint internal derangement in patients with craniomandibular disorders. *Am J Orthod Dentofacial Orthop* 1992; **101**: 41-47 [PMID: 1731487]
38 **Tasaki MM**, Westesson PL, Raubertas RF. Observer variation in interpretation of magnetic resonance images of the temporomandibular joint. *Oral Surg Oral Med Oral Pathol* 1993; **76**: 231-234 [PMID: 8361737]
39 **Tasaki MM**, Westesson PL, Isberg AM, Ren YF, Tallents RH. Classification and prevalence of temporomandibular joint disk displacement in patients and symptom-free volunteers. *Am J Orthod Dentofacial Orthop* 1996; **109**: 249-262 [PMID: 8607470]
40 **Sano T**, Yamamoto M, Okano T. Temporomandibular joint: MR imaging. *Neuroimaging Clin N Am* 2003; **13**: 583-595 [PMID: 14631692]
41 **Som PM**, Bergeron RT. Head and neck imaging. 2nd ed. St. Louis: Mosby Year Book, 1991
42 **de Leeuw R**, Boering G, Stegenga B, de Bont LG. TMJ articular disc position and configuration 30 years after initial diagnosis of internal derangement. *J Oral Maxillofac Surg* 1995; **53**: 234-241; discussion 241-242 [PMID: 7861272]
43 **Suenaga S**, Hamamoto S, Kawano K, Higashida Y, Noikura T. Dynamic MR imaging of the temporomandibular joint in patients with arthrosis: relationship between contrast enhancement of the posterior disk attachment and joint pain. *AJR Am J Roentgenol* 1996; **166**: 1475-1481 [PMID: 8633468 DOI: 10.2214/ajr.166.6.8633468]
44 **Helms CA**, Kaban LB, McNeill C, Dodson T. Temporomandibular joint: morphology and signal intensity characteristics of the disk at MR imaging. *Radiology* 1989; **172**: 817-820 [PMID: 2772194]
45 **Chossegros C**, Cheynet F, Guyot L, Bellot-Samson V, Blanc JL. Posterior disk displacement of the TMJ: MRI evidence in two cases. *Cranio* 2001; **19**: 289-293 [PMID: 11725853]
46 **Katzberg RW**, Westesson PL, Tallents RH, Anderson R, Kurita K, Manzione JV, Totterman S. Temporomandibular joint: MR assessment of rotational and sideways disk displacements. *Radiology* 1988; **169**: 741-748 [PMID: 3186996]
47 **Konttinen YT**, Ainola M, Valleala H, Ma J, Ida H, Mandelin J, Kinne RW, Santavirta S, Sorsa T, López-Otín C, Takagi M. Analysis of 16 different matrix metalloproteinases (MMP-1 to MMP-20) in the synovial membrane: different profiles in trauma and rheumatoid arthritis. *Ann Rheum Dis* 1999; **58**: 691-697 [PMID: 10531073]
48 **Schellhas KP**, Wilkes CH. Temporomandibular joint inflammation: comparison of MR fast scanning with T1- and T2-weighted imaging techniques. *AJR Am J Roentgenol* 1989; **153**: 93-98 [PMID: 2735304 DOI: 10.2214/ajr.153.1.93]
49 **Roberts D**, Schenck J, Joseph P, Foster T, Hart H, Pettigrew J, Kundel HL, Edelstein W, Haber B. Temporomandibular joint: magnetic resonance imaging. *Radiology* 1985; **154**: 829-830 [PMID: 3969490]
50 **Katzberg RW**, Westesson P-L. Diagnosis of the temporomandibular joint, 1e. Philadelphia: W. B. Saunders Co., 1993
51 **Cholitgul W**, Petersson A, Rohlin M, Akerman S. Clinical and radiological findings in temporomandibular joints with disc perforation. *Int J Oral Maxillofac Surg* 1990; **19**: 220-225 [PMID: 2120363]
52 **Kondoh T**, Westesson PL, Takahashi T, Seto K. Prevalence of morphological changes in the surfaces of the temporomandibular joint disc associated with internal derangement. *J Oral Maxillofac Surg* 1998; **56**: 339-343; discussion 343-344 [PMID: 9496846]
53 **Widmalm SE**, Westesson PL, Kim IK, Pereira FJ, Lundh H, Tasaki MM. Temporomandibular joint pathosis related to sex, age, and dentition in autopsy material. *Oral Surg Oral Med Oral Pathol* 1994; **78**: 416-425 [PMID: 7800370]
54 **Kuribayashi A**, Okochi K, Kobayashi K, Kurabayashi T. MRI findings of temporomandibular joints with disk perforation. *Oral Surg Oral Med Oral Pathol Oral Radiol Endod* 2008; **106**: 419-425 [PMID: 18504154 DOI: 10.1016/j.tripleo.2007.11.020]
55 **Yura S**, Nobata K, Shima T. Diagnostic accuracy of fat-saturated T2-weighted magnetic resonance imaging in the diagnosis of perforation of the articular disc of the temporomandibular joint. *Br J Oral Maxillofac Surg* 2012; **50**: 365-368 [PMID: 21723011 DOI: 10.1016/j.bjoms.2011.05.017]
56 **Larheim TA**, Katzberg RW, Westesson PL, Tallents RH, Moss ME. MR evidence of temporomandibular joint fluid and condyle marrow alterations: occurrence in asymptomatic volunteers and symptomatic patients. *Int J Oral Maxillofac Surg* 2001; **30**: 113-117 [PMID: 11405445 DOI: 10.1054/ijom.2000.0018]
57 **Westesson PL**, Brooks SL. Temporomandibular joint: rela-

tionship between MR evidence of effusion and the presence of pain and disk displacement. *AJR Am J Roentgenol* 1992; **159**: 559-563 [PMID: 1503025 DOI: 10.2214/ajr.159.3.1503025]
58 **Smith HJ**, Larheim TA, Aspestrand F. Rheumatic and nonrheumatic disease in the temporomandibular joint: gadolinium-enhanced MR imaging. *Radiology* 1992; **185**: 229-234 [PMID: 1523314 DOI: 10.1148/radiology.185.1.1523314]
59 **Lafrenière CM**, Lamontagne M, el-Sawy R. The role of the lateral pterygoid muscles in TMJ disorders during static conditions. *Cranio* 1997; **15**: 38-52 [PMID: 9586487]
60 **Yang X**, Pernu H, Pyhtinen J, Tiilikainen PA, Oikarinen KS, Raustia AM. MR abnormalities of the lateral pterygoid muscle in patients with nonreducing disk displacement of the TMJ. *Cranio* 2002; **20**: 209-221 [PMID: 12150268]
61 **Taskaya-Yilmaz N**, Ceylan G, Incesu L, Muglali M. A possible etiology of the internal derangement of the temporomandibular joint based on the MRI observations of the lateral pterygoid muscle. *Surg Radiol Anat* 2005; **27**: 19-24 [PMID: 15750717 DOI: 10.1007/s00276-004-0267-6]
62 **Schellhas KP**, Wilkes CH, Fritts HM, Omlie MR, Heithoff KB, Jahn JA. Temporomandibular joint: MR imaging of internal derangements and postoperative changes. *AJR Am J Roentgenol* 1988; **150**: 381-389 [PMID: 3257330 DOI: 10.2214/ajr.150.2.381]
63 **Schellhas KP**, Wilkes CH, Fritts HM, Omlie MR, Lagrotteria LB. MR of osteochondritis dissecans and avascular necrosis of the mandibular condyle. *AJR Am J Roentgenol* 1989; **152**: 551-560 [PMID: 2783809 DOI: 10.2214/ajr.152.3.551]
64 **Larheim TA**, Westesson PL, Hicks DG, Eriksson L, Brown DA. Osteonecrosis of the temporomandibular joint: correlation of magnetic resonance imaging and histology. *J Oral Maxillofac Surg* 1999; **57**: 888-898; discussion 899 [PMID: 10437715]
65 **Mesgarzadeh M**, Sapega AA, Bonakdarpour A, Revesz G, Moyer RA, Maurer AH, Alburger PD. Osteochondritis dissecans: analysis of mechanical stability with radiography, scintigraphy, and MR imaging. *Radiology* 1987; **165**: 775-780 [PMID: 3685359 DOI: 10.1148/radiology.165.3.3685359]
66 **Xiang S**, Rebellato J, Inwards CY, Keller EE. Malocclusion associated with osteocartilaginous loose bodies of the temporomandibular joint. *J Am Dent Assoc* 2005; **136**: 484-489 [PMID: 15884318]
67 **Von Arx DP**, Simpson MT, Batman P. Synovial chondromatosis of the temporomandibular joint. *Br J Oral Maxillofac Surg* 1988; **26**: 297-305 [PMID: 3048377]
68 **Norman JE**, Stevenson AR, Painter DM, Sykes DG, Feain LA. Synovial osteochondromatosis of the temporomandibular joint. An historical review with presentation of 3 cases. *J Craniomaxillofac Surg* 1988; **16**: 212-220 [PMID: 3042809]
69 **Boccardi A**. CT evaluation of chondromatosis of the temporomandibular joint. *J Comput Assist Tomogr* 1991; **15**: 826-828 [PMID: 1885803]
70 **van Ingen JM**, de Man K, Bakri I. CT diagnosis of synovial chondromatosis of the temporomandibular joint. *Br J Oral Maxillofac Surg* 1990; **28**: 164-167 [PMID: 2135654]
71 **Nitzan DW**. Temporomandibular joint "open lock" versus condylar dislocation: signs and symptoms, imaging, treatment, and pathogenesis. *J Oral Maxillofac Surg* 2002; **60**: 506-11; discussion 512-3 [PMID: 11988925]
72 **DaSilva AF**, Shaefer J, Keith DA. The temporomandibular joint: clinical and surgical aspects. *Neuroimaging Clin N Am* 2003; **13**: 573-582 [PMID: 14631691]
73 **Güven O**. A clinical study on temporomandibular joint ankylosis. *Auris Nasus Larynx* 2000; **27**: 27-33 [PMID: 10648065]
74 **Cannizzaro E**, Schroeder S, Müller LM, Kellenberger CJ, Saurenmann RK. Temporomandibular joint involvement in children with juvenile idiopathic arthritis. *J Rheumatol* 2011; **38**: 510-515 [PMID: 21159837 DOI: 10.3899/jrheum.100325]
75 **Twilt M**, Mobers SM, Arends LR, ten Cate R, van Suijlekom-Smit L. Temporomandibular involvement in juvenile idiopathic arthritis. *J Rheumatol* 2004; **31**: 1418-1422 [PMID: 15229966]
76 **Weiss PF**, Arabshahi B, Johnson A, Bilaniuk LT, Zarnow D, Cahill AM, Feudtner C, Cron RQ. High prevalence of temporomandibular joint arthritis at disease onset in children with juvenile idiopathic arthritis, as detected by magnetic resonance imaging but not by ultrasound. *Arthritis Rheum* 2008; **58**: 1189-1196 [PMID: 18383394 DOI: 10.1002/art.23401]
77 **Koh ET**, Yap AU, Koh CK, Chee TS, Chan SP, Boudville IC. Temporomandibular disorders in rheumatoid arthritis. *J Rheumatol* 1999; **26**: 1918-1922 [PMID: 10493669]
78 **Yoshida A**, Higuchi Y, Kondo M, Tabata O, Ohishi M. Range of motion of the temporomandibular joint in rheumatoid arthritis: relationship to the severity of disease. *Cranio* 1998; **16**: 162-167 [PMID: 9852809]
79 **Kretapirom K**, Okochi K, Nakamura S, Tetsumura A, Ohbayashi N, Yoshino N, Kurabayashi T. MRI characteristics of rheumatoid arthritis in the temporomandibular joint. *Dentomaxillofac Radiol* 2013; **42**: 31627230 [PMID: 22842633 DOI: 10.1259/dmfr/31627230]
80 **Tanaka E**, Detamore MS, Mercuri LG. Degenerative disorders of the temporomandibular joint: etiology, diagnosis, and treatment. *J Dent Res* 2008; **87**: 296-307 [PMID: 18362309]
81 **Hussain AM**, Packota G, Major PW, Flores-Mir C. Role of different imaging modalities in assessment of temporomandibular joint erosions and osteophytes: a systematic review. *Dentomaxillofac Radiol* 2008; **37**: 63-71 [PMID: 18239033 DOI: 10.1259/dmfr/16932758]
82 **Matsumura Y**, Nomura J, Nakanishi K, Yanase S, Kato H, Tagawa T. Synovial chondromatosis of the temporomandibular joint with calcium pyrophosphate dihydrate crystal deposition disease (pseudogout). *Dentomaxillofac Radiol* 2012; **41**: 703-707 [PMID: 23166363 DOI: 10.1259/dmfr/24183821]
83 **Kahraman AS**, Kahraman B, Dogan M, Firat C, Samdanci E, Celik T. Synovial chondromatosis of the temporomandibular joint: radiologic and histopathologic findings. *J Craniofac Surg* 2012; **23**: 1211-1213 [PMID: 22801131 DOI: 10.1097/SCS.0b013e3182564a6e]
84 **Wang P**, Tian Z, Yang J, Yu Q. Synovial chondromatosis of the temporomandibular joint: MRI findings with pathological comparison. *Dentomaxillofac Radiol* 2012; **41**: 110-116 [PMID: 22116129 DOI: 10.1259/dmfr/36144602]
85 **Giannakopoulos H**, Chou JC, Quinn PD. Pigmented villonodular synovitis of the temporomandibular joint. *Ear Nose Throat J* 2013; **92**: E10-E13 [PMID: 23904309]
86 **Kim KW**, Han MH, Park SW, Kim SH, Lee HJ, Jae HJ, Kang JW, Chang KH. Pigmented villonodular synovitis of the temporomandibular joint: MR findings in four cases. *Eur J Radiol* 2004; **49**: 229-234 [PMID: 14962652 DOI: 10.1016/S0720-048X(03)00099-8]
87 **Le WJ**, Li MH, Yu Q, Shi HM. Pigmented villonodular synovitis of the temporomandibular joint: CT imaging findings. *Clin Imaging* 2014; **38**: 6-10 [PMID: 24100118 DOI: 10.1016/j.clinimag.2013.08.011]

P- Reviewer: Franco AL, Rattan V, Ramirez Aristeguieta LM
S- Editor: Ji FF **L- Editor**: A **E- Editor**: Liu SQ

World Journal of Radiology

Submit a Manuscript: http://www.wjgnet.com/esps/
Help Desk: http://www.wjgnet.com/esps/helpdesk.aspx
DOI: 10.4329/wjr.v6.i8.583

World J Radiol 2014 August 28; 6(8): 583-588
ISSN 1949-8470 (online)

REVIEW

Pathophysiology, clinical features and radiological findings of differentiation syndrome/all-trans-retinoic acid syndrome

Luciano Cardinale, Francesco Asteggiano, Federica Moretti, Federico Torre, Stefano Ulisciani, Carmen Fava, Giovanna Rege-Cambrin

Luciano Cardinale, Francesco Asteggiano, Federica Moretti, Federico Torre, Institute of Radiology, Department of Clinical and Biological Sciences, University of Turin, AOU S.Luigi Gonzaga, 10043 Orbassano, Torino, Italy
Stefano Ulisciani, Carmen Fava, Giovanna Rege-Cambrin, Division of Hematology and Internal Medicine, Department of Clinical and Biological Sciences of University of Turin, AOU S.Luigi Gonzaga, 10043 Orbassano, Torino, Italy
Author contributions: Cardinale L planned the research; Asteggiano F and Torre F collected the materials; Ulisciani S, Fava C, Rege-Cambrin G were involved in the collection of clinical data; Moretti F and Ulisciani S wrote the paper assisted by Fava C; Cardinale L and Rege-Cambrin G reviewed this commentary and supervised its publication; Asteggiano F, Moretti F and Torre F were involved in the language translation.
Correspondence to: Luciano Cardinale, PhD, Institute of Radiology, Department of Clinical and Biological Sciences, University of Turin, AOU S.Luigi Gonzaga, Regione Gonzole 10, 10043 Orbassano, Torino, Italy. luciano.cardinale@gmail.com
Telephone: +39-11-90261 Fax: +39-11-9026303
Received: December 28, 2013 Revised: July 9, 2014
Accepted: July 17, 2014
Published online: August 28, 2014

Abstract

In acute promyelocytic leukemia, differentiation therapy based on all-trans-retinoic acid can be complicated by the development of a differentiation syndrome (DS). DS is a life-threatening complication, characterized by respiratory distress, unexplained fever, weight gain, interstitial lung infiltrates, pleural or pericardial effusions, hypotension and acute renal failure. The diagnosis of DS is made on clinical grounds and has proven to be difficult, because none of the symptoms is pathognomonic for the syndrome without any definitive diagnostic criteria. As DS can have subtle signs and symptoms at presentation but progress rapidly, end-stage DS clinical picture resembles the acute respiratory distress syndrome with extremely poor prognosis; so it is of absolute importance to be conscious of these complications and initiate therapy as soon as it was suspected. The radiologic appearance resembles the typical features of cardiogenic pulmonary edema. Diagnosis of DS remains a great skill for radiologists and haematologist but it is of an utmost importance the cooperation in suspect DS, detect the early signs of DS, examine the patients' behaviour and rapidly detect the complications.

Key words: Differentiation syndrome; All-trans-retinoic acid syndrome; Chest X-ray and computed tomography; Lungleukemic infiltrates; Acute promyelocytic leukaemia; Promyelocytic leukemia/retinoic acid receptor-α

Core tip: Aim of this review is to illustrate the spectrum of chest imaging findings which lead to suspect a diagnosis of differentiation syndrome, which arise in patients suffering of Acute Promyelocytic Leukemia after treatment with all-trans-retinoic acid or other differentiating drugs, in order to facilitate the differential diagnosis with other life-threatening pulmonary complications occurring in this subset of highly immunocompromised patients.

Cardinale L, Asteggiano F, Moretti F, Torre F, Ulisciani S, Fava C, Rege-Cambrin G. Pathophysiology, clinical features and radiological findings of differentiation syndrome/all-trans-retinoic acid syndrome. *World J Radiol* 2014; 6(8): 583-588 Available from: URL: http://www.wjgnet.com/1949-8470/full/v6/i8/583.htm DOI: http://dx.doi.org/10.4329/wjr.v6.i8.583

LEARNING OBJECTIVES

The treatment of acute promyelocytic leukemia with agents capable of inducing the differentiation of leu-

kemic cells can be complicated by a peculiar syndrome, named differentiation syndrome (DS); this was previously classified as retinoic acid syndrome, as all-trans-retinoic acid (ATRA) was the first agent to be involved in this complication. DS is a syndrome of cardiac and respiratory distress which represents a life-threatening complication, and is associated with severe morbidity and mortality; so early diagnosis and immediate therapeutic intervention are essential in reducing the risk of death[1].

In this work we illustrate the imaging findings on chest X-ray, and in standard or high-resolution computed tomography (CT) useful to suggest this uncommon diagnosis. The aim of this work is to underline the importance of an early diagnosis of DS, to show how radiologists can confirm the diagnosis of DS, to stimulate the cooperation and communication between radiologists and clinicians.

BACKGROUND

Acute promyelocytic leukemia (APL), identified as acute myeloid leukaemia (AML) M3 by the French-American-English classification, is an acute myeloid disorder due to a maturative block of myeloid precursor at the promyelocytic stage, leading to peculiar clinical manifestations, and characterized by a reciprocal balanced translocation between chromosome 15 and 17 *t*(15, 17)[2]. APL represents about 10% of all AML in United States and Europe and is more frequent in adults; median age at diagnosis is 40[3,4].

The finding of a translocation *t*(15, 17), with a consequent transcriptional fusion between promyelocytic leukaemia (*PML*) gene and retinoic acid receptor-α (*RARα*) gene, responsible of the maturative and differentiative stop, offered the basis to develop a specific target therapy with retinoic acid. PML-RARα rearrangement is detectable in approximately 95% of APL cases[2,3].

APL is usually a primitive disorder, but there are also cases of APL arising following a previous exposure to chemotherapy or radiotherapy[5,6].

On the clinical side APL represents a hematologic emergency because of its typical presentation with pancytopenia and a life-threatening disseminated intravascular coagulation, that enforces a quick start of treatment, even before a cytogenetic and molecular diagnosis. Diagnosis of APL is usually based on peripheral blood and bone marrow morphology, supported by typical laboratory and clinical picture. Confirmation then comes from the molecular finding of PML-RARα rearrangement. Treatment of APL is based on the association of ATRA with conventional chemotherapy (usually anthracyclines), or with arsenic trioxide (ATO). Since the introduction of ATRA in the treatment, the complete remission rate raised up to 90% and the 5-year disease free survival to 74%[7-9].

Induction treatment with ATRA and ATO, either as a single agent or in combination with cytotoxic drugs, can induce the DS[10] in 2% to 31% of APL patients[10,11], while the association with chemotherapy compared with ATRA as single-agent lead to a reduction risk of DS (9% *vs* 18%-25%)[12,13]. Mortality due to DS has declined from 30% to 2%-10% because of the early recognition and clinical intervention[10]. Notably, DS is rarely seen during consolidation and maintenance phases[12,14,15].

Table 1 Signs and symptoms

Differentiation syndrome: Sign and symptoms	
Elevated white blood cell count	Weight gain > 5 kg
Dyspnea	Bone pain
Respiratory distress	Headache
Fever	Hypotension
Pulmonary edema	Congestive heart failure
Pulmonary infiltrates	Acute renal failure
Pleural and pericardial effusion	Hepatotoxicity

The pathophysiology of DS is not completely understood. Both ATRA and ATO exert their action by degradation of the PML-RARα fusion product. As a consequence, malignant leukemic cells undergo differentiation and final maturation[16,17].

Exposition to ATRA and ATO cause continued generation of inflammatory cytokines and adhesion molecules, with the consequent extravasation into the tissues from the blood. Increased in cytokine and adhesion molecules level also occurs in liver, heart and spleen[11,18].

DS is typically diagnosed during the first induction treatment, more often 10 to 12 d after therapy start, with a range of 2 to 46 d[10,11,18-20]. Main symptoms at presentation are fever, respiratory failure and fluid retention with weight increase, occurring in around 80% of the cases[10,18]. Additional common findings are lung infiltrates (50%), pericardial and pleural effusions (30%) and acute renal failure (10% of the cases)[18]. DS has to be distinguished from other clinical conditions which may occur in the setting of acute leukaemia, including pulmonary infection, leukostasis, and heart failure. Diagnosis of DS is made when three or more of the symptoms and signs listed in Table 1 are present. Clinical management and outcome are greatly influenced by early pharmacological treatment. Dexamethasone must be used at a dosage of 10 mg twice daily *iv* as soon as DS is suspected. Steroid treatment should continue until DS resolves, and then the dosage can be gradually tapered in the following weeks[21,22]. Hemodynamic and ventilatory support is also indicated in severe cases, which may require admission at the intensive care unit. In Table 2, modified from[1], the measures to be taken at suspicion of DS are reported. Discontinuation of treatment with ATRA (or ATO) is mandatory in severe DS cases[4]. Corticosteroid are commonly used as DS prophylaxis, although there is no evidence that such treatment may ameliorate the morbidity and mortality of DS. However, in patients with leukocytosis at diagnosis (white blood cells > 5×10^9/L), preemptive steroids administration has been shown useful in reducing incidence and severity of DS. No definite risk factors for developing DS were found, but a close monitoring of patients presenting with hyperleukocytosis

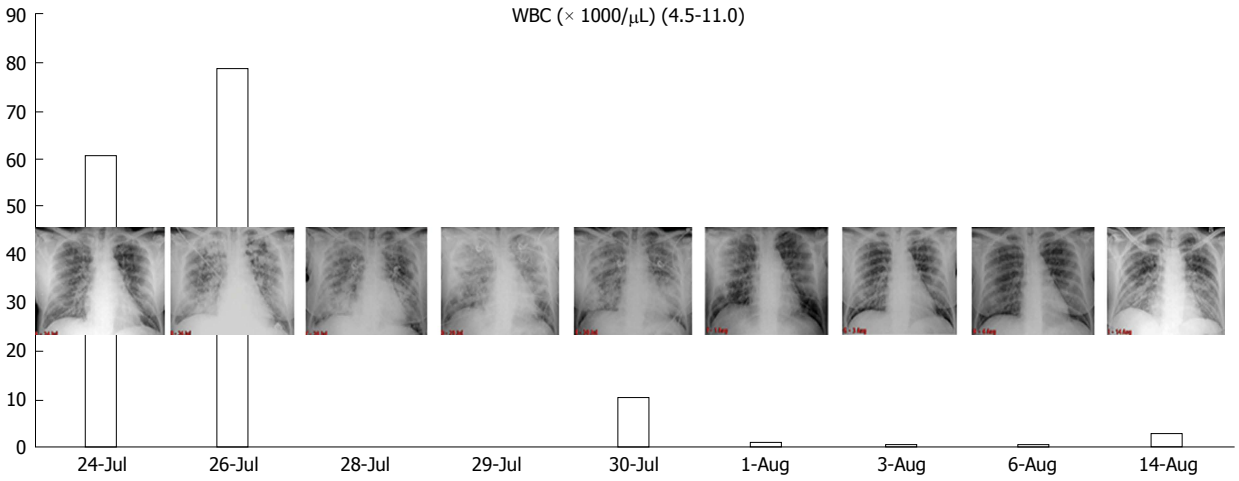

Figure 1 Correlation between white blood cell count and chest X-ray. Note that the worsening of chest X-ray is directly linked with the fall of white blood cell due to the massive differentiation during the onset of differentiation syndrome. References: Institute of Radiology, Department of Clinical and Biological Sciences of University of Turin, AOU S. Luigi Gonzaga, Regione Gonzole 10, 10043 Orbassano, Torino, Italy. WBC: White blood cells.

Table 2 Measures at suspicion of differentiation syndrome

Measures at suspicion of DS
Chest X-ray, renal function (creatinine and urea), hepatic function (amino transferases and bilirubin), blood cell counts, coagulation test, oxygen saturation
Weight monitoring
Ventilatory support/O_2 supplementation
Blood pressure maintenance measures
Fluid restriction (renal failure)
Steroid administration at first suspicion: dexamethasone 10 mg twice daily until clinical resolution, then tapered dose for a few days
Suspend ATRA or ATO in severe cases, which can be restarted after clinical improvement. If DS recurs after restart, ATRA must be definitively discontinued during induction

Some patients have DS that is refractory to corticosteroids. There are yet no widely accepted alternatives to it. It seems reasonable to employ, in the future, agents that block migration, adhesion or transmigration of APL cells. References: Institute of Radiology, Department of Clinical and Biological Sciences of University of Turin, AOU S.Luigi Gonzaga, Regione Gonzole 10, 10043 Orbassano, Torino, Italy. DS: Differentiation syndrome; ATRA: All-trans-retinoic acid; ATO: Arsenic-trioxide.

is recommended[22,23].

A better knowledge and early identification of DS, with rapid initiation of treatment, allowed to obtain a decrease in mortality associated with APL in the recent years.

IMAGING FINDINGS

As stated before, there are no clinical signs or laboratory tests to diagnose DS, nor is there a radiological finding pathognomonic for DS.

Radiologic features may be explained by the proposed hypotheses of pathophysiology of the DS[24]. Most of the patients with DS showed cardiomegaly, widening of the vascular pedicle width, increased pulmonary blood volume, peribronchial cuff, ground-glass opacity, septal lines, and pleural effusion: these findings are similar to those of congestive heart failure with pulmonary edema, but they could also probably be produced by leukemic lung infiltration and endothelial leakage[24].

If the disease progresses, acute respiratory distress syndrome develops. Diffuse alveolar damage and massive intra-alveolar hemorrhage were found in a necropsy patient study by Frankel *et al*[25]. Endothelial cell damage, including intra-alveolar oedema, intra-alveolar hemorrhage, and fibrinous exudate, were found by Tallman *et al*[26] and by Nicolls *et al*[27]. Others histological analysis of lungs reported extensive interstitial and alveolar lung infiltration by maturing myeloid cells, endothelial cells damage, oedema, hemorrhage, and fibrinous exudates that correspond in poorly defined centrolobular nodules and ground-glass opacity with or without interlobular septal thickening.

To our knowledge only a few cases are reported describing the CT aspect in DS: Davis *et al*[28] reported CT findings in three patients with DS. CT findings were peripheral nodules reticular and ground-glass opacity and pleural effusions. They also reported the case of a patient with DS who developed pneumothorax[28].

In mild DS, lesions are prevalent in the lower lobes, while in severe DS, lesions are ubiquitary, with no difference within peripheral or central regions[6,9].

In Figure 1, we present the correlation with radiological findings and white blood cells (WBC). The pathogenesis of DS suggest that this syndrome is due to a massive lung interstitial invasion by leukemic cells. The finding of a negative peak of WBC nearly contemporary to the massive lung oedema seems to confirm this theory.

Patients with PML and DS have an highly compromised immune system; therefore, it is not a rare event to find other concurrent pathologic conditions as pneumonia or fungine infections which can confound the radiological picture of DS/ATRA syndrome.

CT findings of ATRA syndrome are nonspecific (Figure 2).

All findings have differential diagnoses: leukemic infiltrates, drug toxicity, pulmonary edema, hemorrhage, can all have similar appearances.

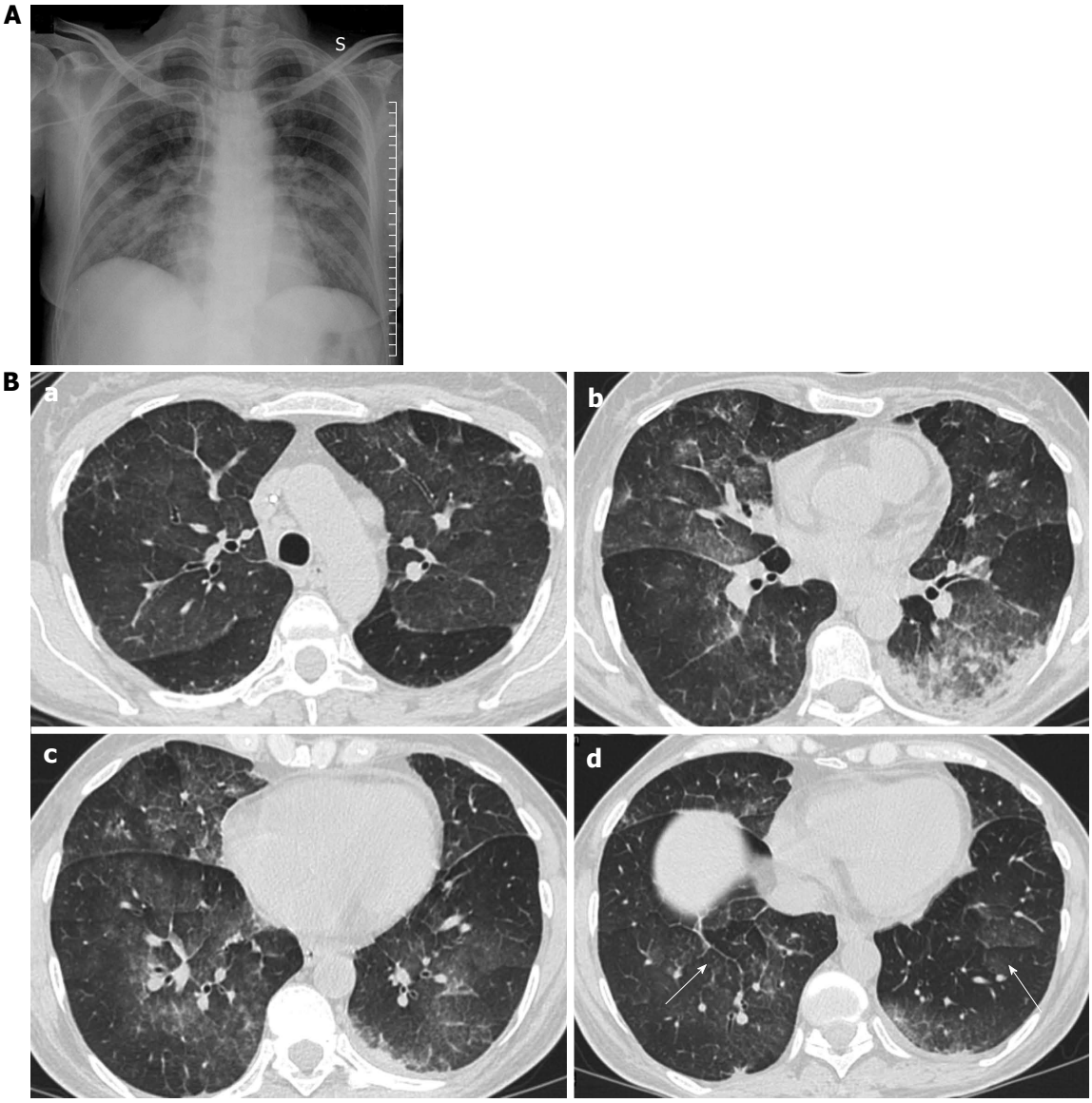

Figure 2 Photograph. A: Chest X-ray shows subtile patchy ground glass opacities of the middle inferior lung fields; B: Computed tomography scans of the same patient as Figure 4 shows patchy ground glass opacities (a, b and c) with interlobar septal thickening (arrows in d). References: Institute of Radiology, Department of Clinical and Biological Sciences of University of Turin, AOU S.Luigi Gonzaga, Regione Gonzole 10, 10043 Orbassano, Torino, Italy.

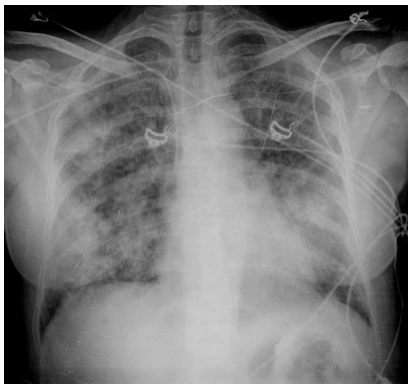

Figure 3 Supine Chest X-ray showing bilateral, asymmetrical patchy consolidation. Septal lines and pleural effusions are absent. Based on the only radiologic features, it would be difficult to differentiate one fromacute respiratory distress syndrome or hemorrhage on these findings. References: Institute of Radiology, Department of Clinical and Biological Sciences of University of Turin, AOU S.Luigi Gonzaga, Regione Gonzole 10, 10043 Orbassano, Torino, Italy.

Although the imaging features are not characteristic, in combination with the clinical picture, they may contribute to the early identification of DS and consequently to its fast resolution (Figures 3 and 4).

CONCLUSION

Diagnosis of DS requires a great skill for radiologists and hematologists, and cooperation and treatment is of utmost importance when DS is confirmed.

Chest X-ray still remains the first imaging step, but often, in mild cases, it is not sufficient.

In summary chest X-ray features include increased cardiothoracic ratio and vascular pedicle width, interstitial edema with peribronchial cuffing and Kerley lines.

The chest CT is useful to evaluate the lung parenchyma and also to discover other signs of severity, as pericardial and pleural effusions, and sometimes to find

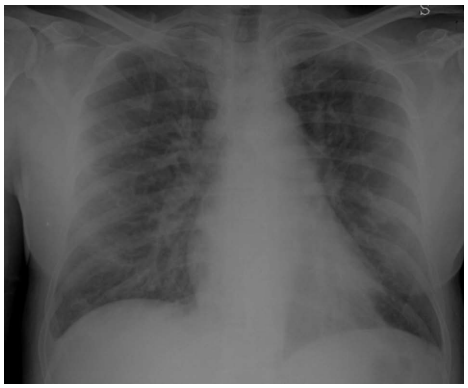

Figure 4 Chest X-ray in patient with differentiation syndrome showed mild cardiomegaly and increased pulmonary vascular marking in both lungs with thickening of small fissure and minimal pleural effusion on the right side seen as obliteration of right costo-phrenic angle: These findings are similar to those of congestive heart failure with pulmonary edema. In contrast with congestive heart failure the time for the complete healing is long, and is similar to that of interstitial pneumonia or acute respiratory distress syndrome. References: Institute of Radiology, Department of Clinical and Biological Sciences of University of Turin, AOU S.Luigi Gonzaga, Regione Gonzole 10, 10043 Orbassano, Torino, Italy.

others concurrent lung infections.

Take home message: (1) Suspect DS in patient with acute APL under treatment with ATRA and/or arsenic trioxide; (2) Detect the early signs of DS to confirm the clinical diagnosis; (3) Examine the patient's behaviour; and (4) Rapidly detect and treat the complications.

REFERENCES

1 **Rego EM**, De Santis GC. Differentiation syndrome in promyelocytic leukemia: clinical presentation, pathogenesis and treatment. *Mediterr J Hematol Infect Dis* 2011; **3**: e2011048 [PMID: 22110898 DOI: 10.4084/MJHID.2011.048]

2 **Melnick A**, Licht JD. Deconstructing a disease: RARalpha, its fusion partners, and their roles in the pathogenesis of acute promyelocytic leukemia. *Blood* 1999; **93**: 3167-3215 [PMID: 10233871]

3 **Rogers JE**, Yang D. Differentiation syndrome in patients with acute promyelocytic leukemia. *J Oncol Pharm Pract* 2012; **18**: 109-114 [PMID: 21364078 DOI: 10.1177/1078155211399163]

4 **Sanz MA**, Grimwade D, Tallman MS, Lowenberg B, Fenaux P, Estey EH, Naoe T, Lengfelder E, Büchner T, Döhner H, Burnett AK, Lo-Coco F. Management of acute promyelocytic leukemia: recommendations from an expert panel on behalf of the European LeukemiaNet. *Blood* 2009; **113**: 1875-1891 [PMID: 18812465 DOI: 10.1182/blood-2008-04-150250]

5 **Pulsoni A**, Pagano L, Lo Coco F, Avvisati G, Mele L, Di Bona E, Invernizzi R, Leoni F, Marmont F, Mele A, Melillo L, Nosari AM, Pogliani EM, Vignetti M, Visani G, Zagonel V, Leone G, Mandelli F. Clinicobiological features and outcome of acute promyelocytic leukemia occurring as a second tumor: the GIMEMA experience. *Blood* 2002; **100**: 1972-1976 [PMID: 12200354]

6 **Mistry AR**, Felix CA, Whitmarsh RJ, Mason A, Reiter A, Cassinat B, Parry A, Walz C, Wiemels JL, Segal MR, Adès L, Blair IA, Osheroff N, Peniket AJ, Lafage-Pochitaloff M, Cross NC, Chomienne C, Solomon E, Fenaux P, Grimwade D. DNA topoisomerase II in therapy-related acute promyelocytic leukemia. *N Engl J Med* 2005; **352**: 1529-1538 [PMID: 15829534]

7 **Wang ZY**, Chen Z. Acute promyelocytic leukemia: from highly fatal to highly curable. *Blood* 2008; **111**: 2505-2515 [PMID: 18299451 DOI: 10.1182/blood-2007-07-102798]

8 **Bennett JM**, Catovsky D, Daniel MT, Flandrin G, Galton DA, Gralnick HR, Willman CL. Hypergranular promyelocytic leukemia: correlation between morphology and chromosomal translocations including t(15; 17) and t(11; 17). *Leukemia* 2000; **14**: 1197-1200 [PMID: 10914542]

9 **de la Serna J**, Montesinos P, Vellenga E, Rayón C, Parody R, León A, Esteve J, Bergua JM, Milone G, Debén G, Rivas C, González M, Tormo M, Díaz-Mediavilla J, González JD, Negri S, Amutio E, Brunet S, Lowenberg B, Sanz MA. Causes and prognostic factors of remission induction failure in patients with acute promyelocytic leukemia treated with all-trans retinoic acid and idarubicin. *Blood* 2008; **111**: 3395-3402 [PMID: 18195095]

10 **Patatanian E**, Thompson DF. Retinoic acid syndrome: a review. *J Clin Pharm Ther* 2008; **33**: 331-338 [PMID: 18613850]

11 **Luesink M**, Pennings JL, Wissink WM, Linssen PC, Muus P, Pfundt R, de Witte TJ, van der Reijden BA, Jansen JH. Chemokine induction by all-trans retinoic acid and arsenic trioxide in acute promyelocytic leukemia: triggering the differentiation syndrome. *Blood* 2009; **114**: 5512-5521 [PMID: 19828696 DOI: 10.1182/blood-2009-02-204834]

12 **De Botton S**, Dombret H, Sanz M, Miguel JS, Caillot D, Zittoun R, Gardembas M, Stamatoulas A, Condé E, Guerci A, Gardin C, Geiser K, Makhoul DC, Reman O, de la Serna J, Lefrere F, Chomienne C, Chastang C, Degos L, Fenaux P. Incidence, clinical features, and outcome of all trans-retinoic acid syndrome in 413 cases of newly diagnosed acute promyelocytic leukemia. The European APL Group. *Blood* 1998; **92**: 2712-2718 [PMID: 9763554]

13 **de Botton S**, Chevret S, Coiteux V, Dombret H, Sanz M, San Miguel J, Caillot D, Vekhoff A, Gardembas M, Stamatoulas A, Conde E, Guerci A, Gardin C, Fey M, Cony Makhoul D, Reman O, de la Serna J, Lefrere F, Chomienne C, Degos L, Fenaux P. Early onset of chemotherapy can reduce the incidence of ATRA syndrome in newly diagnosed acute promyelocytic leukemia (APL) with low white blood cell counts: results from APL 93 trial. *Leukemia* 2003; **17**: 339-342 [PMID: 12592333]

14 **Rust DM**, Soignet SL. Risk/benefit profile of arsenic trioxide. *Oncologist* 2001; **6** Suppl 2: 29-32 [PMID: 11331438]

15 **Gupta V**, Yi QL, Brandwein J, Lipton JH, Messner HA, Schuh AC, Wells RA, Minden MD. Role of all-trans-retinoic acid (ATRA) in the consolidation therapy of acute promyelocytic leukaemia (APL). *Leuk Res* 2005; **29**: 113-114 [PMID: 15541484]

16 **Roche Laboratories, Inc**. Vesanoid (tretinoin) package insert. Nutley, NJ, 2004. Available from: URL: http: // www.accessdata.fda.gov/drugsatfda_docs/label/2004/20438s004lbl.pdf

17 **Nasr R**, Lallemand-Breitenbach V, Zhu J, Guillemin MC, de Thé H. Therapy-induced PML/RARA proteolysis and acute promyelocytic leukemia cure. *Clin Cancer Res* 2009; **15**: 6321-6326 [PMID: 19808868 DOI: 10.1158/1078-0432.CCR-09-0209]

18 **Larson RS**, Tallman MS. Retinoic acid syndrome: manifestations, pathogenesis, and treatment. *Best Pract Res Clin Haematol* 2003; **16**: 453-461 [PMID: 12935962]

19 **Luesink M**, Jansen JH. Advances in understanding the pulmonary infiltration in acute promyelocytic leukaemia. *Br J Haematol* 2010; **151**: 209-220 [PMID: 20735400 DOI: 10.1111/j.1365-2141.2010.08325.x]

20 **Montesinos P**, Bergua JM, Vellenga E, Rayón C, Parody R, de la Serna J, León A, Esteve J, Milone G, Debén G, Rivas C, González M, Tormo M, Díaz-Mediavilla J, González JD, Negri S, Amutio E, Brunet S, Lowenberg B, Sanz MA. Differentiation syndrome in patients with acute promyelocytic leukemia treated with all-trans retinoic acid and anthracy-

cline chemotherapy: characteristics, outcome, and prognostic factors. *Blood* 2009; **113**: 775-783 [PMID: 18945964 DOI: 10.1182/blood-2008-07-168617]
21 Acute Myeloid Leukemia NCCN Clinical Practice Guidelines in Oncology (Version 2.2014)
22 **Wiley JS**, Firkin FC. Reduction of pulmonary toxicity by prednisolone prophylaxis during all-trans retinoic acid treatment of acute promyelocytic leukemia. Australian Leukaemia Study Group. *Leukemia* 1995; **9**: 774-778 [PMID: 07769839]
23 **Sanz MA**, Martín G, González M, León A, Rayón C, Rivas C, Colomer D, Amutio E, Capote FJ, Milone GA, De La Serna J, Román J, Barragán E, Bergua J, Escoda L, Parody R, Negri S, Calasanz MJ, Bolufer P. Risk-adapted treatment of acute promyelocytic leukemia with all-trans-retinoic acid and anthracycline monochemotherapy: a multicenter study by the PETHEMA group. *Blood* 2004; **103**: 1237-1243 [PMID: 14576047]
24 **Jung JI**, Choi JE, Hahn ST, Min CK, Kim CC, Park SH. Radiologic features of all-trans-retinoic acid syndrome. *AJR Am J Roentgenol* 2002; **178**: 475-480 [PMID: 11804921]
25 **Frankel SR**, Eardley A, Lauwers G, Weiss M, Warrell RP. The "retinoic acid syndrome" in acute promyelocytic leukemia. *Ann Intern Med* 1992; **117**: 292-296 [PMID: 1637024]
26 **Tallman MS**, Andersen JW, Schiffer CA, Appelbaum FR, Feusner JH, Ogden A, Shepherd L, Rowe JM, François C, Larson RS, Wiernik PH. Clinical description of 44 patients with acute promyelocytic leukemia who developed the retinoic acid syndrome. *Blood* 2000; **95**: 90-95 [PMID: 10607690]
27 **Nicolls MR**, Terada LS, Tuder RM, Prindiville SA, Schwarz MI. Diffuse alveolar hemorrhage with underlying pulmonary capillaritis in the retinoic acid syndrome. *Am J Respir Crit Care Med* 1998; **158**: 1302-1305 [PMID: 9769296]
28 **Davis BA**, Cervi P, Amin Z, Moshi G, Shaw P, Porter J. Retinoic acid syndrome: pulmonary computed tomography (CT) findings. *Leuk Lymphoma* 1996; **23**: 113-117 [PMID: 9021693]

P- Reviewer: Agarwal R, Sureka B **S- Editor**: Wen LL
L- Editor: A **E- Editor**: Liu SQ

World Journal of Radiology

Submit a Manuscript: http://www.wjgnet.com/esps/
Help Desk: http://www.wjgnet.com/esps/helpdesk.aspx
DOI: 10.4329/wjr.v6.i8.589

World J Radiol 2014 August 28; 6(8): 589-597
ISSN 1949-8470 (online)

REVIEW

Measuring consciousness in coma and related states

Carol Di Perri, Aurore Thibaut, Lizette Heine, Andrea Soddu, Athena Demertzi, Steven Laureys

Carol Di Perri, Neuroradiology, National Neurological Institute C Mondino, 27100 Pavia, Italy
Carol Di Perri, Aurore Thibaut, Lizette Heine, Athena Demertzi, Steven Laureys, Cyclotron Research Center and Neurology Department, Coma Science Group, University of Liège, 4000 Liège, Belgium
Andrea Soddu, Brain and Mind Institute, Physics and Astronomy Department, Western University, London, Ontario, N6A 3K7, Canada
Author contributions: Di Perri C designed and wrote the manuscript; Thibaut A, Heine L, Soddu A and Demertzi A were involved in designing and editing the manuscript; Laureys S supervised the manuscript design and writing; all authors were involved in literature search.
Supported by The European Commission; the James McDonnell Foundation; the European Space Agency; Mind Science Foundation; the French Speaking Community Concerted Research Action; the Belgian interuniversity attraction pole; the Public Utility Foundation "Université Européenne du Travail"; "Fondazione Europea di Ricerca Biomedica" and the University and University Hospital of Liège
Correspondence to: Carol Di Perri, MD, Cyclotron Research Center and Neurology Department, Coma Science Group, University of Liège, Allée du 6 août 8, Sart Tilman B30, 4000 Liège, Belgium. caroldiperri@hotmail.com
Telephone: +32-43-662316 Fax: +32-43-662946
Received: February 28, 2014 Revised: May 9, 2014
Accepted: June 14, 2014
Published online: August 28, 2014

Abstract

Consciousness is a prismatic and ambiguous concept that still eludes any universal definition. Severe acquired brain injuries resulting in a disorder of consciousness (DOC) provide a model from which insights into consciousness can be drawn. A number of recent studies highlight the difficulty in making a diagnosis in patients with DOC based only on behavioral assessments. Here we aim to provide an overview of how neuroimaging techniques can help assess patients with DOC. Such techniques are expected to facilitate a more accurate understanding of brain function in states of unconsciousness and to improve the evaluation of the patient's cognitive abilities by providing both diagnostic and prognostic indicators.

Key words: Disorders of consciousness; Neuroimaging; Magnetic resonance imaging; Transcranial magnetic stimulation/electroencephalography; Minimally conscious state; Vegetative state/unresponsive wakefulness syndrome

Core tip: In this review we show the main ways neuroimaging techniques contribute to both understanding the neural correlates of consciousness and detecting possible consciousness residual in severly traumatic brain injured patients. In particular, we make reference to the latest research in terms of both improving the diagnosis of patients with disorder of consciousness, and understanding the brain processes underlining consciousness, such as a broad and more complex than previously thought alteration of brain connectivity architecture.

Di Perri C, Thibaut A, Heine L, Soddu A, Demertzi A, Laureys S. Measuring consciousness in coma and related states. *World J Radiol* 2014; 6(8): 589-597 Available from: URL: http://www.wjgnet.com/1949-8470/full/v6/i8/589.htm DOI: http://dx.doi.org/10.4329/wjr.v6.i8.589

INTRODUCTION

Consciousness is a multifaceted and ambiguous concept, which is often the focus of passionate multi-disciplinant debates. Consciousness is thought to represent an emergent property of reciprocal connections between specialized areas of the grey matter within cortical and subcortical networks[1]. To date, there is no universal definition for consciousness covering all its essential characteristics[2], making everything particularly tricky and challenging when facing this specific topic and the related disorders.

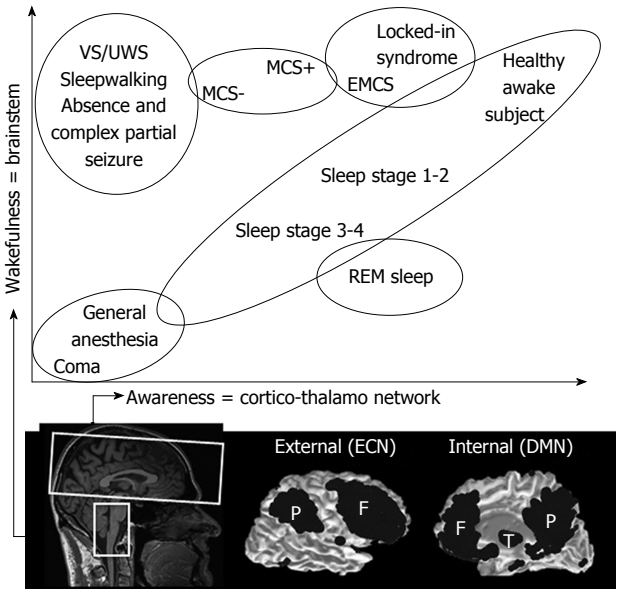

Figure 1 The two main components of consciousness: wakefulness and awareness. Correlation between wakefulness, related to the brainstem, and awareness, related to the cortico-thalamic network. In most pathological and physiological states, the two components are linearly correlated along the spectrum of consciousness. However, they are dissociated in some cases. Vegetative state/unresponsive wakefulness syndrome (VS/UWS); minimally conscious state (MCS); emergence of MCS, EMCS. Adapted from ref. [3,4]. EMCS: Emerge from minimally conscious state; ECN: Executive control network; DMN: Default mode network; REM: Rapid eyes movement.

We here adopt a perspective where consciousness is clinically defined as having two components: awareness and arousal[3]. Arousal, also called wakefulness, refers to the level of alertness (clinically determined by eye opening), whereas awareness refers to the content of consciousness (clinically determined by command following or non-reflex motor behaviour such as eye tracking or localized responses to pain)[3]. Arousal is anatomically related to structures in the brain and specifically in the brainstem and hypothalamus, whereas awareness has been shown to be related to a wide fronto-parietal network encompassing associative cortices and, more specifically, to the intrinsic connectivity of this network and the connectivity between the fronto-parietal associative cortices and the thalamus[4,5]. In physiological states, there is an intimate positive correlation between arousal and awareness. Sleep is the best way to describe the relationship between these two components: the less awake we become as we move towards deep sleep, the less aware we become of our surroundings and ourselves[3]. Based on this, subjects in pathological and pharmacological coma (*i.e.*, anesthesia) are not conscious because they cannot be awakened, even after noxious stimulation[3]. Similarly, under sedation (a drug-dose dependent impairment of consciousness) and in hypnotic state (a suggestion-dependent alteration of conscious experience), subjects report an altered state of awareness as they move towards lower levels of arousal[6-8]. Hence, arousal seems to be essential for awareness to emerge, *i.e.*, one needs to be awake in order to be aware. However, being awake is not sufficient in order to be aware.

There are, in fact, some exceptional cases in which these two components are dissociated. On the one hand, in the rapid eye movement stage of sleep, wakefulness is impaired while internal awareness is relatively spared. On the other hand, in vegetative state (VS), now also coined unresponsive wakefulness syndrome (UWS)[9], in minimally conscious state (MCS) and in some more transient states such as absence seizures, complex partial seizures or somnambulism, awareness is impaired while wakefulness is spared (Figure 1)[10-13]. The interest in understanding the neuropathology of such latter states, and in particular VS/UWS, is twofold. Firstly, VS/UWS patients offer a lesion approach to the study of human consciousness in terms of identifying the neural correlate of awareness[3]. These patients represent cases of awareness suppression but, unlike coma patients, exhibit intact wakefulness. Secondly, VS/UWS patients represent a clinical challenge, in terms of both diagnosis,and prognosis.

We aim to review here the knowledge of (un) consciousness obtained by studying disorders of consciousness (DOC) following brain injury (coma, VS/UWS, and MCS). We will focus mainly on structural and functional neuroimaging studies and we will pinpoint how developing such techniques could improve both scientific and clinical perspectives in DOC (Table 1).

We searched the MEDLINE database for English-language reports published between 2002 and April 2014 which used the terms "disorders of consciousness", "vegetative state", "minimally conscious state", "neuroimaging", "magnetic resonance imaging (MRI)", "positron emission tomography (PET)", "transcranial magnetic stimulation (TMS)" and "TMS/electroencephalography (TMS/EEG)". We reviewed the full text of all the original articles, reviews, early-release publications and associated citations retrieved, and relevant papers found in the authors' own files.

CLINICAL ENTITIES OF DISORDERS OF CONSCIOUSNESS

Disorders of consciousness are characterized by a prolonged impaired unconsciousness following an acquired severe brain injury. These conditions are more and more frequent in the clinical setting due to progress in emergency medicine and lifesaving technologies which have led to a better survival rate after severe brain damage[14].

Patients surviving severe brain damage may end up in a coma. This state may arise following structural or metabolic lesions to the brainstem reticular system or due to widespread bilateral cerebral damage[1]. Patients in coma show continuous absence of eye opening and any spontaneous or stimulus induced arousal or voluntary behavioural responses. Hence, they are neither awake nor aware. Coma is a time-limited condition (it usually does not last longer than a few weeks) leading either to brain death (*i.e.*, permanent loss of brainstem functions), a VS/UWS or the recovery of consciousness. Patients in a VS/UWS have recovered wakefulness (as evinced by

Table 1 Key points of the review

Novel neuroimaging techniques in patients with DOC give important key insights into both the understanding of consciousness and the differential diagnosis of clinical DOC entities, given that behavioural assessment alone can sometimes be incorrect and imprecise
Conventional MRI and DTI investigates the structural properties of the brain and the white matter integrity. These studies showed mainly a predictive rather than diagnostic value
PET activations show a critical role of a wide frontoparietal associative network for the emergence of consciousness
fMRI employing active paradigm detects covert awareness in approximately 17% of unresponsive patients at bedside. However, there is a high risk of false negative. fMRI employing passive paradigm shows also a prognostic value. fMRI during resting state shows a broad alteration of brain connectivity, implying both decreased and increased connectivity in patients with DOC
TMS-EEG shows a high diagnostic value even at single subject level

DOC: Disorders of consciousness; MRI: Magnetic resonance imaging; DTI: Diffusion tensor imaging; PET: Positron emission tomography; fMRI: Functional magnetic resonance imaging; TMS-EEG: Transcranial magnetic stimulation coupled with electroencephalography.

eye opening) but their motor responses are only reflexive and, therefore, do not indicate conscious awareness[15]. VS/UWS has been said to be permanent 12 mo after traumatic brain injury and 3 mo following non-traumatic brain damage, making chances of recovery very low[16]. However, this has recently been challenged[9]. It is now suggested that one substitute the term "permanent" with the association of the injury etiology (traumatic *vs* non traumatic) and the length of time since onset, as these factors appear to influence outcome. Non traumatic patients generally have the worst outcome. From VS/UWS, patients may progress into a MCS. This may either be the endpoint of their improvement or a provisional stage on the way to further recovery of consciousness[17]. MCS is a condition of severely altered consciousness characterized by minimal, inconstant yet definite behavioural signs of awareness of self and the surroundings. Based on the level of their purposeful behavioural signs, MCS patients were recently subcategorized as MCS plus (showing command following, intelligible verbalizations or non-functional communication) and MCS minus (showing visual pursuit, localization of noxious stimulation or contingent behaviour such as appropriate smiling or crying to emotional stimuli)[18]. Patients may emerge from MCS once they regain the ability to reliably communicate and/or use objects in a functional manner[17]. Although there is some evidence suggesting that patients in a MCS have better chances of recovery than patients in a VS/UWS, at present, we are not in a position to refer to possible temporal boundaries of irreversible MCS[19].

DOC must be differentiated from locked in syndrome (LIS). This is a rare state which usually follows a brain stem lesion with massive damage to the cortico-spinal and cortico-bulbar pathways, and classically results in loss of control of all voluntary muscles except for extrinsic eye muscles, making it possible for them only to communicate with small eyelid movements[20,21].

Differential diagnosis of the above mentioned clinical DOC entities raises important ethical and medical questions such as end-of-life decision and pain treatment[14,22,23]. Nowadays, the gold standard for assessing the level of consciousness is the clinical assessment of patients' behavioural responsiveness. Since responsiveness is only indirect proof of consciousness (lack of responsiveness does not necessarily imply lack of consciousness), reliance on these behavioural markers entails significant challenges and may lead to misdiagnoses. Clinical studies have shown that up to 40% of patients with a diagnosis of VS/UWS may in fact retain some level of awareness[24-26], and the main causes of misdiagnosis are associated with patient's disabilities, such as paralysis and aphasia, fluctuation in arousal level, difficulty differentiating between reflexive and involuntary movements and the non-use of standardized and sensitive clinical scales such as the Coma Recovery Scale-Revised (CRS-R)[27]. Furthermore, conventional brain structural imaging studies have shown highly variable and heterogeneous results in patients with DOC, suggesting that a specific brain region cannot be unequivocally related to awareness[28]. This knowledge has lead to the search for other non-clinical assessment techniques which can enable us to better understand brain function in these patients and to overcome the limits of behavioural assessment in the detection of possible retained consciousness in unresponsive patients.

NEUROIMAGING STUDIES IN DOC

Functional neuroimaging methods have made it possible to objectively study cognitive processing in the absence of behavioural reports. PET measures different aspects of metabolic function according to the type of administered radioactive tracer. Structural conventional MRI and diffusion tensor imaging (DTI) reveal the structural properties of the brain and the white matter integrity respectively. Functional MRI (fMRI) quantifies brain function derived from blood-oxygen-level dependent (BOLD) changes. TMS/EEG allows us to non-invasively stimulate a subset of cortical neurons and to measure the effects of this perturbation on the rest of the brain[29-33] (Table 2).

Below we will refer to the neuroimaging studies that have been most frequently adopted to infer covert cognitive abilities in behaviourally non responsive DOC patients.

PET

^{18}Fluorodesoxyglucose-PET (FDG-PET) studies were the first to demonstrate massive decrease in brain metabolism in patients with DOC. Using PET in resting state conditions, it was shown that patients in VS/UWS exhibit a decrease in brain metabolism of up to 40% of the normal value[3]. Nevertheless, recovery from the

Table 2 Main strength and limits of the different techniques

Technique	Strenght	Limits
PET	Relatively direct measure of brain activity	Ionizing, radioactive tracer, low spatial and temporal resolution expensive
MRI	No use of ionizing. Permits both high resolution study of structural brain (DTI) and fMRI employing active, passive and resting state paradigms	Indirect measure of brain activity (functional) Sensitive to movement and artifacts, impractical (application precluded in patients with contraindication), expensive
TMS-EEG	Practical (no important contraindications) gives information at single subject level	Sensitive to muscle artifacts

PET: Positron emission tomography; MRI: Magnetic resonance imaging; TMS-EEG: Transcranial magnetic stimulation coupled with electroencephalography; DTI: Diffusion tensor imaging; fMRI: Functional magnetic resonance imaging.

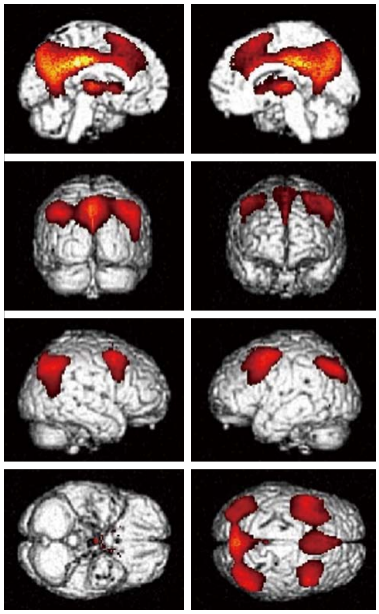

Figure 2 Brain areas where metabolism is impaired in vegetative state/unresponsive wakefulness syndrome patients compared to controls (areas in red), superimposed in a structural 3D image. $P < 0.05$, family wise error corrected.

VS/UWS does not coincide with the recovery of global metabolic levels. Instead it seems that some areas are more important to consciousness than others. In fact, patients suffering from DOC show decreased metabolism in a widespread network encompassing frontoparietal areas, such as in the lateral prefrontal and posterior parietal regions as well as midline anterior cingulate/mesiofrontal and posterior cingulate/precuneal associative cortices (Figure 2)[34,35]. Importantly, recovery from the VS/UWS parallels connectivity restoration in these areas (cortico-cortical) and between these regions and the thalamus (thalamo-cortical)[36].

FDG-PET cannot yet disentangle between VS/UWS and MCS at the single subject. However, it has shown to be highly sensitive in identifying patients in MCS[37] and displaying a correlation between metabolism in the above mentioned awareness network and the CRS-R score of the patients[38].

There is now growing evidence suggesting that this awareness network can be subdivided into two different networks: the intrinsic [default mode network (DMN)] and the extrinsic awareness network [executive control network (ECN)]. The extrinsic awareness network encompasses the lateral fronto-parietal brain regions and is related to sensory awareness or awareness of the environment. The intrinsic awareness network (most widely known as the DMN) encompasses mainly the medial prefrontal cortex and the precuneus and bilateral posterior parietal cortices and is related to internal awareness or self-related processes, such as mind-wandering and autobiographical thinking[39-41]. More recently, it has been demonstrated that patients in MCS retain metabolism in the lateral fronto-parietal areas whilst midline regions are highly dysfunctional[42]. As such, this data suggests that, at group level, patients in MCS display altered self-awareness besides their abilities to, at least to a certain extent, interact (but not communicate) with their surroundings. Furthermore, patients who are considered to be in MCS minus showed impairment of the left dominant hemisphere, possibly correlated to aphasia, consistent with their command-following impairment[18].

$^{15}H_2O$-PET studies using passive auditory and noxious stimulation[43,44], have furthermore highlighted a peculiar disconnection in VS/UWS patients between the primary sensory areas and these large-scale associative fronto-parietal cortices, which are thought to be essential for conscious perception[3]. In contrast, patients in MCS show a partial preservation of this large-scale associative fronto-parietal network[45]. Furthermore, PET studies employing nociceptive stimuli have highlighted an activation of the pain matrix in MCS patients similar to that observed in healthy controls, suggesting a possible perception of pain in this patient category. By contrast, activation in VS/UWS was limited to the primary sensory areas[46].

Structural MRI

MRI with conventional sequences (T1-TSE, T2-TSE, FLAIR) is the method of choice to detect brain edema, contusion, hematomas, herniation, hemorrhage, hydrocephalus, or hemorrhagic shearing lesion due to diffuse axonal injuries common in post-traumatic patients (T2* sequences). Nevertheless, in an emergency setting, the computed tomography scan is preferable in some cases due to its accessibility, speed of acquisition, and sensitivity to acute hemorrhagic lesions that require a surgical approach[38,47].

Some studies have highlighted the predictive value

of the classical conventional sequences. For example, the number of lesions detected by FLAIR and T2* sequences has been shown to be inversely correlated with the Glasgow Coma Scale (GCS) of traumatic patients in a coma. The presence of lesions in the corpus callosum and the dorsal midbrain has been shown to be correlated with lack of recovery at group level in coma patients[47,48]. However, these methods have failed to explain why some patients in a VS/UWS and/or in a MCS have no or minimal brain lesions. This highlights the lack of specificity and sensitivity of conventional MRI in DOC, which alone cannot be considered a reliable tool for assessing this patient category.

Recently developed DTI techniques can reveal structural damage in tissue that appears normal in conventional-MRI.

These techniques have been able to predict scores on the GCS and successfully classify VS/UWS and MCS patients into their appropriate diagnostic categories with an accuracy of 95%[49]. Furthermore, recent multicentric studies have demonstrated that DTI is better at predicting outcome for both traumatic and anoxic patients at 1 year follow up from injury than structural and clinical assessment[50,51]. An other study evaluated the combination of DTI and MR-spectroscopy as a tool for predicting long-term outcome of traumatic patients[52], showing that a prediction of non-recovery after 1 year could be calculated with up to 86% sensitivity and 97% specificity when taking into account both DTI and MR-spectroscopy values.

With regards to diagnostic accuracy, a recent study used DTI to assess the neuropathology of patients in VS/UWS and MCS *in vivo* and to identify measurements that could potentially distinguish the patients in these two groups[49]. The MCS and VS/UWS patients appeared to differ significantly in subcortical white matter and thalamic regions (measured using diffusivity maps) but appeared not to differ in the brainstem. DTI results predicted scores on the GCS and successfully classified the patients into their appropriate diagnostic categories with an accuracy of 95%[49]. Furthermore, DTI proved to be helpful for characterizing etiologic differences in patients in VS/UWS, demonstrating that DTI abnormalities in the brainstem were confined to the traumatic brain injured group[53].

These studies suggest that DTI-MRI techniques can quantify white matter integrity and support the possible benefit of using these methods for an early classification of this patient population.

fMRI

In the last few years PET activation studies have been largely replaced by fMRI non-ionizing techniques. Activation studies using visual, auditory and somatosensory stimuli have revealed high level cortical activation encompassing the associative cortices in patients in MCS, similar to that observed in healthy controls[54,55]. In contrast, only low level cortical activation, limited to the primary sensory areas, was detected in VS/UWS. The minority of patients in VS/UWS with high level cortical activation often showed signs of recovery on the long term follow up[55,56]. Besides the prognostic value of this technique, active fMRI paradigms have recently been performed to detect covert awareness in patients who are behaviourally unresponsive by investigating signs which are independent from motor command following, and in some cases even establishing yes-no communication[57-59].

For instance, a recent fMRI study using mental imagery tasks (imagining playing tennis *vs* spatial navigation around one's house) showed that in a large cohort of 54 patients with DOC, 5 were able to willfully modulate their brain activity. Furthermore, one behaviourally VS/UWS patient was able to use this technique to correctly respond with yes (by imagining playing tennis) or no (by imagining visiting the rooms of his house) to autobiographical questions during the fMRI scanning[57]. Approximately 17% of patients diagnosed as in VS/UWS following behavioural assessment seem to be able to follow commands when the commands involve a change in blood oxygenation level dependent response, rather than overt motoric behaviour. Similarly, a further study using selective auditory attention showed that 3 patients (2 in MCS and 1 in VS/UWS) were able to convey their ability to follow commands, and the one in VS/UWS was even able to correctly communicate answers to several autobiographic binary questions[60].

Despite their potential diagnostic and prognostic value, active fMRI paradigm in terms of detecting covert awareness has remained mostly controversial. Indeed, without a comprehensive understanding of the neural correlates of awareness, the absence of cortical activation to external stimuli does not necessarily coincide with absence of awareness. Indeed, out of 31 MCS patients described in the study by Monti *et al*[57], only one was able to willfully modulate his brain activity. This could be due to the fact that patients may be asleep during the scan, or due to patients' disabilities, such as aphasia (patients cannot understand the task), *etc*[57].

In this context, the other fMRI paradigms commonly performed which partially overcome this latter limit are passive, measuring brain responses to external sensory stimulation (*e.g.*, auditory, somatosensory and visual) whilst the subject is not performing any mental task. An example is the brain activation elicited by the patient's own name spoken by a familiar voice. This is a salient auditory stimulus which has been preferred due to its attention-grabbing properties. For example, using the own-name paradigm, it was shown that 2 out of 7 patients in VS/UWS and all 4 patients in MCS not only showed activation in the primary auditory cortex, but also in higher order associative temporal areas, which are thought to be implicated in the conscious processing of the incoming stimuli[55]. Interestingly, these 2 patients in VS/UWS subsequently recovered to MCS. The absence of higher activation did not unequivocally coincide with the absence of awareness as sensory deficits, such as deafness, could have led to a false negative.

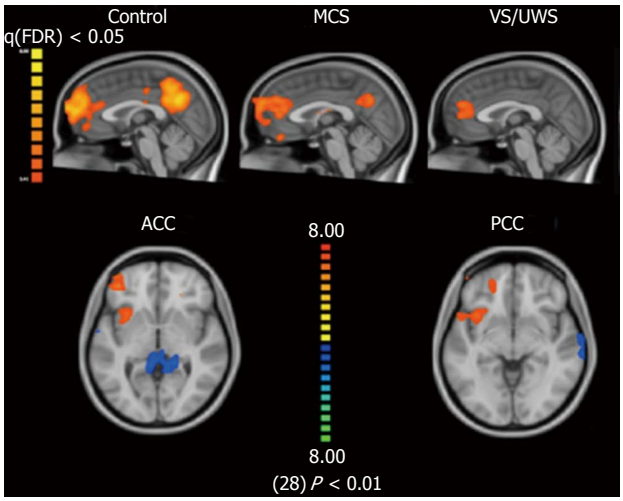

Figure 3 Default mode network in vegetative state/unresponsive wakefulness syndrome, minimally conscious state, healthy controls-sagittal view[68]. In vegetative state/unresponsive wakefulness syndrome (VS/UWS), the anterior cingulate cortex (ACC) and posterior cingulate cortex (PCC) are hypoconnected to the default mode network (in blue) and hyperconnected to the fronto-insular cortex (in red), axial view. Correlation from random effect (P < 0.01) and clustered corrected (P < 0.05) results based on general linear model maps with seed region of interest comparing VS/UWS to healthy controls[60]. MCS: Minimally conscious state.

Resting-state fMRI is a non invasive technique used to investigate the spontaneous temporal coherence in BOLD fluctuations related to the amount of synchronized neural activity (*i.e.*, functional connectivity) between distinct brain locations, in the absence of input or output tasks[61]. This technique has been increasingly used in the analysis of patients with DOC, mainly because it is not invasive and it surpasses the requirement for motor output or language comprehension. Among the several functional networks that have been detected so far[62], DMN has been the first to attract scientific attention. To date, resting state fMRI studies suggest that activity of this network is generally lower as a function of the level of consciousness. It has been demonstrated, for example, that the connectivity of this network is correlated to the level of consciousness, ranging from patients in VS/UWS (low connectivity) to patients in MCS and to healthy controls (higher connectivity)[63] (Figure 3). In addition, DMN connectivity could not be found in a brain dead patient, which highlights the neural origin of these MRI signals[64]. Recently, more networks at resting state have been investigated in DOC, such as the bilateral fronto-parietal or executive control networks, salience, sensorimotor, auditory, visual systems, and the cerebellar network. It was found that, besides DMN, the bilateral executive control networks and the auditory system were also significantly less identifiable (in terms of spatial and neural properties) in patients with DOC compared to healthy controls, and showed consciousness-level dependent decreases in functional connectivity across the spectrum of DOC[65].

Interestingly, it has been found that the resting brain is characterized by a switch between the dominance of the DMN (linked to "internal" or self-awareness) and the ECN (linked to "external" or environmental awareness[66,67]; when one shows activation, the other does not and vice-versa. More recently, it was found that such spontaneous anticorrelated patterns are closely related to mentation and behavioral status. This means that DMN activity is linked to behaviorally report of internal awareness whereas ECN activity is related to behavioural ratings for external awareness[39]. The decrease in anticorrelated pattern in disordered consciousness supports the functional relevance of anticorrelated patterns to the phenomenological complexity of consciousness[29].

Alongside the investigation of reduced connectivity is the presence of hyper-connectivity patterns, which might also be indicative of brain function. In fact, it has recently been demonstrated that, together with DMN hypoconnectivity, the subcortical limbic system (including the orbitofrontal cortex, insula and hypothalamus) exhibits paradoxically increased fMRI connectivity in patients with DOC when compared to healthy controls[68] (Figure 3). This could point to a more complex scenario of brain connectivity architecture in the emergence of consciousness, where hypoconnectivity may only represent a single aspect.

TMS-EEG

Unfortunately, fMRI-based techniques are impractical. The fact that a scanner is needed limits its use to hospital settings and precludes use in patients with pace makers, metal implants or those in a critical condition in intensive care units.

In this context, EEG recording associated with TMS is a promising way to assess cerebral connectivity and it may be especially useful for assessing the level of consciousness in patients with DOC as it does not require a scanner and it does not rely on the subject's ability to process sensory stimuli, to understand and follow instructions or to communicate. In addition, this technique permits consciousness assessment at single subject level, unlike the majority of fMRI and PET studies[33,69].

TMS-EEG can measure brain complexity by non-invasively stimulating a subset of cortical neurons (through TMS) and can immediately measure the effects of this perturbation on the rest of the brain (through high density EEG)[32,33].

Based on the level of consciousness, the perturbation will show either cortical interaction related to preservation or loss of information and/or integration. For example, in patients in VS/UWS, when stimulating a superficial region of the cerebral cortex, TMS either induced no response or triggered a simple, local EEG response, indicating a breakdown of effective connectivity (*i.e.*, of the influence that one brain region exerts on another[70,71], similar to that observed in deep sleep and anesthesia[33,72]). In contrast, for patients in MCS, TMS triggered complex EEG activations which sequentially involved distant cortical areas, similar to activations recorded in patients in LIS and healthy awake subjects. Recently, these TMS-EEG responses have been practically quantified by the

perturbational complexity index (PCI)[32]. This index has demonstrated its potential as a unified measurement scale to grade the level of consciousness. The PCI, in fact, estimates the amount of information contained in the integrated response of the thalamo-cortical system to a direct TMS perturbation[32]. Empirically, it showed to provide a data-driven metric that can discriminate level of consciousness in single subjects under different conditions: below 0.31 for unconsciousness, above 0.51 for healthy consciousness and in the between for MCS.

CONCLUSION

In the last decade we have witnessed the development and the validation of standardized behavioural scales, together with neuroimaging and neurophysiological techniques to better understand the variable conditions of patients with DOC. The need to objectively measure phenomena associated with consciousness has promoted an increased use of these neuroimaging and neurophysiological tools in this patient population. Here we have reviewed the basic principles of how the main neuroimaging techniques (PET, structural MRI, fMRI and TMS-EEG), provide us with important insights into brain function in DOC patients. Since every single technique gives us specific and different information, we support the integration of structural and functional neuroimaging techniques, in order to have a broader and more holistic vision of both the disease and the single patient under our care. Furthermore, we expect that in the near future, with a wider use of standardized behavioural scales and the development of multimodal neuroimaging techniques, there will be a drop in diagnosis-error. Finally, the application of these methodologies at the single subject level, as clinical reality requires, is one of the next challenges.

ACKNOWLEDGMENTS

The authors thank Ziggy Kennel for english revision.

REFERENCES

1 **Laureys S**, Owen AM, Schiff ND. Brain function in coma, vegetative state, and related disorders. *Lancet Neurol* 2004; **3**: 537-546 [PMID: 15324722]
2 **Zeman A**. Consciousness. *Brain* 2001; **124**: 1263-1289 [PMID: 11408323]
3 **Laureys S**. The neural correlate of (un)awareness: lessons from the vegetative state. *Trends Cogn Sci* 2005; **9**: 556-559 [PMID: 16271507 DOI: 10.1016/j.tics.2005.10.010]
4 **Di Perri C**, Stender J, Laureys S, Gosseries O. Functional neuroanatomy of disorders of consciousness. *Epilepsy Behav* 2014; **30**: 28-32 [PMID: 24100252]
5 **Laureys S**, Faymonville ME, Luxen A, Lamy M, Franck G, Maquet P. Restoration of thalamocortical connectivity after recovery from persistent vegetative state. *Lancet* 2000; **355**: 1790-1791 [PMID: 10832834 DOI: 10.1016/S0140-6736(00)02271-6]
6 **Faymonville ME**, Boly M, Laureys S. Functional neuroanatomy of the hypnotic state. *J Physiol Paris* 2006; **99**: 463-469 [PMID: 16750615 DOI: 10.1016/j.jphysparis.2006.03.018]
7 **Vanhaudenhuyse A**, Boveroux P, Boly M, Schnakers C, Bruno MA, Kirsch M, Demertzi A, Lamy M, Maquet P, Laureys S, Faymonville ME. [Hypnosis and pain perception]. *Rev Med Liege* 2008; **63**: 424-428 [PMID: 18669215]
8 **Boly M**, Sanders RD, Mashour GA, Laureys S. Consciousness and responsiveness: lessons from anaesthesia and the vegetative state. *Curr Opin Anaesthesiol* 2013; **26**: 444-449 [PMID: 23743554 DOI: 10.1097/ACO.0b013e3283628b5d]
9 **Laureys S**, Celesia GG, Cohadon F, Lavrijsen J, León-Carrión J, Sannita WG, Sazbon L, Schmutzhard E, von Wild KR, Zeman A, Dolce G. Unresponsive wakefulness syndrome: a new name for the vegetative state or apallic syndrome. *BMC Med* 2010; **8**: 68 [PMID: 21040571 DOI: 10.1186/1741-7015-8-68]
10 **Salek-Haddadi A**, Lemieux L, Merschhemke M, Friston KJ, Duncan JS, Fish DR. Functional magnetic resonance imaging of human absence seizures. *Ann Neurol* 2003; **53**: 663-667 [PMID: 12731002 DOI: 10.1002/ana.10586]
11 **Blumenfeld H**. Epilepsy and the consciousness system: transient vegetative state? *Neurol Clin* 2011; **29**: 801-823 [PMID: 22032662 DOI: 10.1016/j.ncl.2011.07.014]
12 **Blumenfeld H**. Impaired consciousness in epilepsy. *Lancet Neurol* 2012; **11**: 814-826 [PMID: 22898735 DOI: 10.1016/S1474-4422(12)70188-6]
13 **Bassetti C**, Vella S, Donati F, Wielepp P, Weder B. SPECT during sleepwalking. *Lancet* 2000; **356**: 484-485 [PMID: 10981896 DOI: 10.1016/S0140-6736(00)02561-7]
14 **Laureys S**. Science and society: death, unconsciousness and the brain. *Nat Rev Neurosci* 2005; **6**: 899-909 [PMID: 16261182 DOI: 10.1038/nrn1789]
15 **Boveroux P**, Bonhomme V, Boly M, Vanhaudenhuyse A, Maquet P, Laureys S. Brain function in physiologically, pharmacologically, and pathologically altered states of consciousness. *Int Anesthesiol Clin* 2008; **46**: 131-146 [PMID: 18617821 DOI: 10.1097/AIA.0b013e318181a8b3]
16 Medical aspects of the persistent vegetative state (2). The Multi-Society Task Force on PVS. *N Engl J Med* 1994; **330**: 1572-1579 [PMID: 8177248 DOI: 10.1056/NEJM199406023302206]
17 **Giacino JT**, Ashwal S, Childs N, Cranford R, Jennett B, Katz DI, Kelly JP, Rosenberg JH, Whyte J, Zafonte RD, Zasler ND. The minimally conscious state: definition and diagnostic criteria. *Neurology* 2002; **58**: 349-353 [PMID: 11839831 DOI: 10.1212/WNL.58.3.349]
18 **Bruno MA**, Vanhaudenhuyse A, Thibaut A, Moonen G, Laureys S. From unresponsive wakefulness to minimally conscious PLUS and functional locked-in syndromes: recent advances in our understanding of disorders of consciousness. *J Neurol* 2011; **258**: 1373-1384 [PMID: 21674197 DOI: 10.1007/s00415-011-6114-x]
19 **Laureys S**, Boly M. The changing spectrum of coma. *Nat Clin Pract Neurol* 2008; **4**: 544-546 [PMID: 18762800 DOI: 10.1038/ncpneuro0887]
20 **Laureys S**, Pellas F, Van Eeckhout P, Ghorbel S, Schnakers C, Perrin F, Berré J, Faymonville ME, Pantke KH, Damas F, Lamy M, Moonen G, Goldman S. The locked-in syndrome : what is it like to be conscious but paralyzed and voiceless? *Prog Brain Res* 2005; **150**: 495-511 [PMID: 16186044 DOI: 10.1016/S0079-6123(05)50034-7]
21 **Bauer G**, Gerstenbrand F, Rumpl E. Varieties of the locked-in syndrome. *J Neurol* 1979; **221**: 77-91 [PMID: 92545]
22 **Demertzi A**, Ledoux D, Bruno MA, Vanhaudenhuyse A, Gosseries O, Soddu A, Schnakers C, Moonen G, Laureys S. Attitudes towards end-of-life issues in disorders of consciousness: a European survey. *J Neurol* 2011; **258**: 1058-1065 [PMID: 21221625 DOI: 10.1007/s00415-010-5882-z]
23 **Demertzi A**, Schnakers C, Ledoux D, Chatelle C, Bruno MA, Vanhaudenhuyse A, Boly M, Moonen G, Laureys S. Different beliefs about pain perception in the vegetative and mini-

mally conscious states: a European survey of medical and paramedical professionals. *Prog Brain Res* 2009; **177**: 329-338 [PMID: 19818911 DOI: 10.1016/S0079-6123(09)17722-1]
24 **Schnakers C**, Vanhaudenhuyse A, Giacino J, Ventura M, Boly M, Majerus S, Moonen G, Laureys S. Diagnostic accuracy of the vegetative and minimally conscious state: clinical consensus versus standardized neurobehavioral assessment. *BMC Neurol* 2009; **9**: 35 [PMID: 19622138 DOI: 10.1186/1471-2377-9-35]
25 **Andrews K**, Murphy L, Munday R, Littlewood C. Misdiagnosis of the vegetative state: retrospective study in a rehabilitation unit. *BMJ* 1996; **313**: 13-16 [PMID: 8664760 DOI: 10.1136/bmj.313.7048.13]
26 **Childs NL**, Mercer WN, Childs HW. Accuracy of diagnosis of persistent vegetative state. *Neurology* 1993; **43**: 1465-1467 [PMID: 8350997 DOI: 10.1212/WNL.43.8.1465]
27 **Giacino JT**, Kalmar K, Whyte J. The JFK Coma Recovery Scale-Revised: measurement characteristics and diagnostic utility. *Arch Phys Med Rehabil* 2004; **85**: 2020-2029 [PMID: 15605342 DOI: 10.1016/j.apmr.2004.02.033]
28 **Tshibanda L**, Vanhaudenhuyse A, Boly M, Soddu A, Bruno MA, Moonen G, Laureys S, Noirhomme Q. Neuroimaging after coma. *Neuroradiology* 2010; **52**: 15-24 [PMID: 19862509 DOI: 10.1007/s00234-009-0614-8]
29 **Heine L**, Soddu A, Gómez F, Vanhaudenhuyse A, Tshibanda L, Thonnard M, Charland-Verville V, Kirsch M, Laureys S, Demertzi A. Resting state networks and consciousness: alterations of multiple resting state network connectivity in physiological, pharmacological, and pathological consciousness States. *Front Psychol* 2012; **3**: 295 [PMID: 22969735 DOI: 10.3389/fpsyg.2012.00295]
30 **Tshibanda L**, Vanhaudenhuyse A, Bruno MA, Boly M, Soddu A, Laureys S, Moonen G. [MRI in coma survivors]. *Rev Med Liege* 2009; **64** Spec No: 42-48 [PMID: 20085015]
31 **Tshibanda L**, Vanhaudenhuyse A, Galanaud D, Boly M, Laureys S, Puybasset L. Magnetic resonance spectroscopy and diffusion tensor imaging in coma survivors: promises and pitfalls. *Prog Brain Res* 2009; **177**: 215-229 [PMID: 19818904 DOI: 10.1016/S0079-6123(09)17715-4]
32 **Casali AG**, Gosseries O, Rosanova M, Boly M, Sarasso S, Casali KR, Casarotto S, Bruno MA, Laureys S, Tononi G, Massimini M. A theoretically based index of consciousness independent of sensory processing and behavior. *Sci Transl Med* 2013; **5**: 198ra105 [PMID: 23946194]
33 **Massimini M**, Ferrarelli F, Huber R, Esser SK, Singh H, Tononi G. Breakdown of cortical effective connectivity during sleep. *Science* 2005; **309**: 2228-2232 [PMID: 16195466 DOI: 10.1126/science.1117256]
34 **Nakayama N**, Okumura A, Shinoda J, Nakashima T, Iwama T. Relationship between regional cerebral metabolism and consciousness disturbance in traumatic diffuse brain injury without large focal lesions: an FDG-PET study with statistical parametric mapping analysis. *J Neurol Neurosurg Psychiatry* 2006; **77**: 856-862 [PMID: 16549415 DOI: 10.1136/jnnp.2005.080523]
35 **Silva S**, Alacoque X, Fourcade O, Samii K, Marque P, Woods R, Mazziotta J, Chollet F, Loubinoux I. Wakefulness and loss of awareness: brain and brainstem interaction in the vegetative state. *Neurology* 2010; **74**: 313-320 [PMID: 20101037 DOI: 10.1212/WNL.0b013e3181cbcd96]
36 **Laureys S**, Lemaire C, Maquet P, Phillips C, Franck G. Cerebral metabolism during vegetative state and after recovery to consciousness. *J Neurol Neurosurg Psychiatry* 1999; **67**: 121 [PMID: 10454871 DOI: 10.1136/jnnp.67.1.121]
37 **Stender J**, Gosseries O, Bruno MA, Charland-Verville V, Vanhaudenhuyse A, Demertzi A, Chatelle C, Thonnard M, Thibaut A, Heine L, Soddu A, Boly M, Schnakers C, Gjedde A, Laureys S. Diagnostic precision of PET imaging and functional MRI in disorders of consciousness: a clinical validation study. *Lancet* 2014; **384**: 514-522 [PMID: 24746174]
38 **Giacino JT**, Fins JJ, Laureys S, Schiff ND. Disorders of consciousness after acquired brain injury: the state of the science. *Nat Rev Neurol* 2014; **10**: 99-114 [PMID: 24468878]
39 **Vanhaudenhuyse A**, Demertzi A, Schabus M, Noirhomme Q, Bredart S, Boly M, Phillips C, Soddu A, Luxen A, Moonen G, Laureys S. Two distinct neuronal networks mediate the awareness of environment and of self. *J Cogn Neurosci* 2011; **23**: 570-578 [PMID: 20515407 DOI: 10.1162/jocn.2010.21488]
40 **Demertzi A**, Soddu A, Laureys S. Consciousness supporting networks. *Curr Opin Neurobiol* 2013; **23**: 239-244 [PMID: 23273731 DOI: 10.1016/j.conb.2012.12.003]
41 **Demertzi A**, Vanhaudenhuyse A, Brédart S, Heine L, di Perri C, Laureys S. Looking for the self in pathological unconsciousness. *Front Hum Neurosci* 2013; **7**: 538 [PMID: 24027519]
42 **Thibaut A**, Bruno MA, Chatelle C, Gosseries O, Vanhaudenhuyse A, Demertzi A, Schnakers C, Thonnard M, Charland-Verville V, Bernard C, Bahri M, Phillips C, Boly M, Hustinx R, Laureys S. Metabolic activity in external and internal awareness networks in severely brain-damaged patients. *J Rehabil Med* 2012; **44**: 487-494 [PMID: 22366927 DOI: 10.2340/16501977-0940]
43 **Laureys S**, Faymonville ME, Peigneux P, Damas P, Lambermont B, Del Fiore G, Degueldre C, Aerts J, Luxen A, Franck G, Lamy M, Moonen G, Maquet P. Cortical processing of noxious somatosensory stimuli in the persistent vegetative state. *Neuroimage* 2002; **17**: 732-741 [PMID: 12377148 DOI: 10.1006/nimg.2002.1236]
44 **Laureys S**, Faymonville ME, Degueldre C, Fiore GD, Damas P, Lambermont B, Janssens N, Aerts J, Franck G, Luxen A, Moonen G, Lamy M, Maquet P. Auditory processing in the vegetative state. *Brain* 2000; **123** (Pt 8): 1589-1601 [PMID: 10908189]
45 **Laureys S**, Perrin F, Faymonville ME, Schnakers C, Boly M, Bartsch V, Majerus S, Moonen G, Maquet P. Cerebral processing in the minimally conscious state. *Neurology* 2004; **63**: 916-918 [PMID: 15365150 DOI: 10.1212/01.WNL.0000137421.30792.9B]
46 **Boly M**, Faymonville ME, Schnakers C, Peigneux P, Lambermont B, Phillips C, Lancellotti P, Luxen A, Lamy M, Moonen G, Maquet P, Laureys S. Perception of pain in the minimally conscious state with PET activation: an observational study. *Lancet Neurol* 2008; **7**: 1013-1020 [PMID: 18835749 DOI: 10.1016/S1474-4422(08)70219-9]
47 **Kampfl A**, Schmutzhard E, Franz G, Pfausler B, Haring HP, Ulmer H, Felber S, Golaszewski S, Aichner F. Prediction of recovery from post-traumatic vegetative state with cerebral magnetic-resonance imaging. *Lancet* 1998; **351**: 1763-1767 [PMID: 9635948 DOI: 10.1016/S0140-6736(97)10301-4]
48 **Hoelper BM**, Soldner F, Choné L, Wallenfang T. Effect of intracerebral lesions detected in early MRI on outcome after acute brain injury. *Acta Neurochir Suppl* 2000; **76**: 265-267 [PMID: 11450021]
49 **Fernández-Espejo D**, Bekinschtein T, Monti MM, Pickard JD, Junque C, Coleman MR, Owen AM. Diffusion weighted imaging distinguishes the vegetative state from the minimally conscious state. *Neuroimage* 2011; **54**: 103-112 [PMID: 20728553 DOI: 10.1016/j.neuroimage.2010.08.035]
50 **Galanaud D**, Perlbarg V, Gupta R, Stevens RD, Sanchez P, Tollard E, de Champfleur NM, Dinkel J, Faivre S, Soto-Ares G, Veber B, Cottenceau V, Masson F, Tourdias T, André E, Audibert G, Schmitt E, Ibarrola D, Dailler F, Vanhaudenhuyse A, Tshibanda L, Payen JF, Le Bas JF, Krainik A, Bruder N, Girard N, Laureys S, Benali H, Puybasset L. Assessment of white matter injury and outcome in severe brain trauma: a prospective multicenter cohort. *Anesthesiology* 2012; **117**: 1300-1310 [PMID: 23135261 DOI: 10.1097/ALN.0b013e3182755558]
51 **Luyt CE**, Galanaud D, Perlbarg V, Vanhaudenhuyse A, Stevens RD, Gupta R, Besancenot H, Krainik A, Audibert G, Combes A, Chastre J, Benali H, Laureys S, Puybasset L. Diffusion tensor imaging to predict long-term outcome after

cardiac arrest: a bicentric pilot study. *Anesthesiology* 2012; **117**: 1311-1321 [PMID: 23135257 DOI: 10.1097/ALN.0b013e318275148c]

52 **Tollard E**, Galanaud D, Perlbarg V, Sanchez-Pena P, Le Fur Y, Abdennour L, Cozzone P, Lehericy S, Chiras J, Puybasset L. Experience of diffusion tensor imaging and 1H spectroscopy for outcome prediction in severe traumatic brain injury: Preliminary results. *Crit Care Med* 2009; **37**: 1448-1455 [PMID: 19242330 DOI: 10.1097/CCM.0b013e31819cf050]

53 **Newcombe VF**, Williams GB, Scoffings D, Cross J, Carpenter TA, Pickard JD, Menon DK. Aetiological differences in neuroanatomy of the vegetative state: insights from diffusion tensor imaging and functional implications. *J Neurol Neurosurg Psychiatry* 2010; **81**: 552-561 [PMID: 20460593 DOI: 10.1136/jnnp.2009.196246]

54 **Di H**, Boly M, Weng X, Ledoux D, Laureys S. Neuroimaging activation studies in the vegetative state: predictors of recovery? *Clin Med* 2008; **8**: 502-507 [PMID: 18975482 DOI: 10.7861/clinmedicine.8-5-502]

55 **Di HB**, Yu SM, Weng XC, Laureys S, Yu D, Li JQ, Qin PM, Zhu YH, Zhang SZ, Chen YZ. Cerebral response to patient's own name in the vegetative and minimally conscious states. *Neurology* 2007; **68**: 895-899 [PMID: 17372124 DOI: 10.1212/01.wnl.0000258544.79024.d0]

56 **Owen AM**, Coleman MR, Menon DK, Johnsrude IS, Rodd JM, Davis MH, Taylor K, Pickard JD. Residual auditory function in persistent vegetative state: a combined PET and fMRI study. *Neuropsychol Rehabil* 2005; **15**: 290-306 [PMID: 16350973 DOI: 10.1080/09602010443000579]

57 **Monti MM**, Vanhaudenhuyse A, Coleman MR, Boly M, Pickard JD, Tshibanda L, Owen AM, Laureys S. Willful modulation of brain activity in disorders of consciousness. *N Engl J Med* 2010; **362**: 579-589 [PMID: 20130250 DOI: 10.1056/NEJMoa0905370]

58 **Monti MM**, Coleman MR, Owen AM. Executive functions in the absence of behavior: functional imaging of the minimally conscious state. *Prog Brain Res* 2009; **177**: 249-260 [PMID: 19818906 DOI: 10.1016/S0079-6123(09)17717-8]

59 **Bekinschtein TA**, Manes FF, Villarreal M, Owen AM, Della-Maggiore V. Functional imaging reveals movement preparatory activity in the vegetative state. *Front Hum Neurosci* 2011; **5**: 5 [PMID: 21441977]

60 **Naci L**, Owen AM. Making every word count for nonresponsive patients. *JAMA Neurol* 2013; **70**: 1235-1241 [PMID: 23939634]

61 **Biswal BB**, Van Kylen J, Hyde JS. Simultaneous assessment of flow and BOLD signals in resting-state functional connectivity maps. *NMR Biomed* 1997; **10**: 165-170 [PMID: 9430343]

62 **Beckmann CF**, DeLuca M, Devlin JT, Smith SM. Investigations into resting-state connectivity using independent component analysis. *Philos Trans R Soc Lond B Biol Sci* 2005; **360**: 1001-1013 [PMID: 16087444 DOI: 10.1098/rstb.2005.1634]

63 **Vanhaudenhuyse A**, Noirhomme Q, Tshibanda LJ, Bruno MA, Boveroux P, Schnakers C, Soddu A, Perlbarg V, Ledoux D, Brichant JF, Moonen G, Maquet P, Greicius MD, Laureys S, Boly M. Default network connectivity reflects the level of consciousness in non-communicative brain-damaged patients. *Brain* 2010; **133**: 161-171 [PMID: 20034928]

64 **Boly M**, Tshibanda L, Vanhaudenhuyse A, Noirhomme Q, Schnakers C, Ledoux D, Boveroux P, Garweg C, Lambermont B, Phillips C, Luxen A, Moonen G, Bassetti C, Maquet P, Laureys S. Functional connectivity in the default network during resting state is preserved in a vegetative but not in a brain dead patient. *Hum Brain Mapp* 2009; **30**: 2393-2400 [PMID: 19350563 DOI: 10.1002/hbm.20672]

65 **Demertzi A**, Gómez F, Crone JS, Vanhaudenhuyse A, Tshibanda L, Noirhomme Q, Thonnard M, Charland-Verville V, Kirsch M, Laureys S, Soddu A. Multiple fMRI system-level baseline connectivity is disrupted in patients with consciousness alterations. *Cortex* 2014; **52**: 35-46 [PMID: 24480455]

66 **Fox MD**, Snyder AZ, Vincent JL, Corbetta M, Van Essen DC, Raichle ME. The human brain is intrinsically organized into dynamic, anticorrelated functional networks. *Proc Natl Acad Sci USA* 2005; **102**: 9673-9678 [PMID: 15976020 DOI: 10.1073/pnas.0504136102]

67 **Fransson P**. Spontaneous low-frequency BOLD signal fluctuations: an fMRI investigation of the resting-state default mode of brain function hypothesis. *Hum Brain Mapp* 2005; **26**: 15-29 [PMID: 15852468 DOI: 10.1002/hbm.20113]

68 **Di Perri C**, Bastianello S, Bartsch AJ, Pistarini C, Maggioni G, Magrassi L, Imberti R, Pichiecchio A, Vitali P, Laureys S, Di Salle F. Limbic hyperconnectivity in the vegetative state. *Neurology* 2013; **81**: 1417-1424 [PMID: 24049132 DOI: 10.1212/WNL.0b013e3182a43b78]

69 **Massimini M**, Ferrarelli F, Murphy M, Huber R, Riedner B, Casarotto S, Tononi G. Cortical reactivity and effective connectivity during REM sleep in humans. *Cogn Neurosci* 2010; **1**: 176-183 [PMID: 20823938]

70 **Ragazzoni A**, Pirulli C, Veniero D, Feurra M, Cincotta M, Giovannelli F, Chiaramonti R, Lino M, Rossi S, Miniussi C. Vegetative versus minimally conscious states: a study using TMS-EEG, sensory and event-related potentials. *PLoS One* 2013; **8**: e57069 [PMID: 23460826]

71 **Rosanova M**, Gosseries O, Casarotto S, Boly M, Casali AG, Bruno MA, Mariotti M, Boveroux P, Tononi G, Laureys S, Massimini M. Recovery of cortical effective connectivity and recovery of consciousness in vegetative patients. *Brain* 2012; **135**: 1308-1320 [PMID: 22226806]

72 **Ferrarelli F**, Massimini M, Sarasso S, Casali A, Riedner BA, Angelini G, Tononi G, Pearce RA. Breakdown in cortical effective connectivity during midazolam-induced loss of consciousness. *Proc Natl Acad Sci USA* 2010; **107**: 2681-2686 [PMID: 20133802 DOI: 10.1073/pnas.0913008107]

P- Reviewer: Boy C, Howren MB, Serafini G **S- Editor**: Ji FF
L- Editor: A **E- Editor**: Liu SQ

World Journal of Radiology

Submit a Manuscript: http://www.wjgnet.com/esps/
Help Desk: http://www.wjgnet.com/esps/helpdesk.aspx
DOI: 10.4329/wjr.v6.i8.598

World J Radiol 2014 August 28; 6(8): 598-606
ISSN 1949-8470 (online)

REVIEW

Incorporating GSA-SPECT into CT-based dose-volume histograms for advanced hepatocellular carcinoma radiotherapy

Shintaro Shirai, Morio Sato, Yasutaka Noda, Yoshitaka Kumayama, Noritaka Shimizu

Shintaro Shirai, Morio Sato, Yasutaka Noda, Yoshitaka Kumayama, Noritaka Shimizu, Department of Radiology, Wakayama Medical University, Wakayama Shi, Wakayama 641-8510, Japan
Author contributions: Shirai S, Sato M, Noda Y, Kumayama Y and Shimizu N contributed to this paper.
Correspondence to: Morio Sato, MD, Professor, Department of Radiology, Wakayama Medical University, 811-1 Kimiidera, Wakayama Shi, Wakayama 641-8510, Japan. morisato@mail.wakayama-med.ac.jp
Telephone: +81-73-4410604 Fax: +81-73-4443110
Received: December 26, 2013 Revised: April 15, 2014
Accepted: May 28, 2014
Published online: August 28, 2014

Abstract

In single photon emission computed tomography-based three-dimensional radiotherapy (SPECT-B-3DCRT), images of Tc-99m galactosyl human serum albumin (GSA), which bind to receptors on functional liver cells, are merged with the computed tomography simulation images. Functional liver is defined as the area of normal liver where GSA accumulation exceeds that of hepatocellular carcinoma (HCC). In cirrhotic patients with a gigantic, proton-beam-untreatable HCC of $\geqslant$ 14 cm in diameter, the use of SPECT-B-3DCRT in combination with transcatheter arterial chemoembolization achieved a 2-year local tumor control rate of 78.6% and a 2-year survival rate of 33.3%. SPECT-B-3DCRT was applied to HCC to preserve as much functional liver as possible. Sixty-four patients with HCC, including 30 with Child B liver cirrhosis, received SPECT-B-3DCRT and none experienced fatal radiation-induced liver disease (RILD). The Child-Pugh score deteriorated by 1 or 2 in > 20% of functional liver volume that was irradiated with $\geqslant$ 20 Gy. The deterioration in the Child-Pugh score decreased when the radiation plan was designed to irradiate $\leqslant$ 20% of the functional liver volume in patients given doses of $\geqslant$ 20 Gy ($_{FL}V_{20Gy}$). Therefore, $_{FL}V_{20Gy} \leqslant$ 20% may represent a safety index to prevent RILD during 3DCRT for HCC. To supplement $_{FL}V_{20Gy}$ as a qualitative index, we propose a quantitative indicator, F_{20Gy}, which was calculated as F_{20Gy} = 100% × (the GSA count in the area irradiated with $\geqslant$ 20 Gy)/(the GSA count in the whole liver).

Key words: Functional image-guided radiotherapy; Galactosyl human serum albumin; Dose-volume histogram; Three-dimensional radiotherapy; Hepatocellular carcinoma

Core tip: Three-dimensional conformal radiotherapy, which is designed to preserve functional liver, can be visualized by single photon emission computed tomography with Tc-99m-galactosyl human serum albumin (GSA). This treatment modality has promising therapeutic effects for hepatocellular carcinomas (HCCs) of > 14 cm in diameter that are unmanageable by proton beam therapy. A treatment plan designed to irradiate $\leqslant$ 20% of the functional liver volume ($_{FL}V_{20Gy} \leqslant$ 20%) did not cause radiation-induced liver disease. Therefore, $_{FL}V_{20Gy} \leqslant$ 20% may be a useful safety marker for three-dimensional radiotherapy of HCC of various sizes. It is also possible to estimate the effects of radiotherapy on the liver by dividing the GSA count in the region of the liver irradiated with $\geqslant$ 20 Gy by the GSA count of the entire liver.

Shirai S, Sato M, Noda Y, Kumayama Y, Shimizu N. Incorporating GSA-SPECT into CT-based dose-volume histograms for advanced hepatocellular carcinoma radiotherapy. *World J Radiol* 2014; 6(8): 598-606 Available from: URL: http://www.wjgnet.com/1949-8470/full/v6/i8/598.htm DOI: http://dx.doi.org/10.4329/wjr.v6.i8.598

INTRODUCTION

The development of computed tomography (CT) has contributed to radiation treatment (RT) planning by its ability to reveal the precise location of target tissue and at-risk organs in three dimensions, thus enabling dose-volume histograms (DVHs) to be created[1]. The introduction of DVHs has had significant benefits in terms of better target control and reduced adverse effects. However, even in cases where a DVH was used, RT may cause radiation-induced liver disease (RILD), which is sometimes fatal, in patients with advanced hepatocellular carcinoma (HCC)[2,3]. In the normal tissue complication probability model, which is used to predict disorders based on the DVH, the volume-adverse effect coefficient is relatively large (0.32-0.40)[4,5]. Therefore, attempts to reduce the irradiation volume do not always prevent RILD[2,3]. Furthermore, the proportion of irradiated normal liver relative to the entire normal liver ($_{NL}V_{Gy}$) often fails to predict RILD[2,3,6].

The onset of RILD was commonly attributed to the presence of liver cirrhosis in patients with HCC[2,3]. For example, Ikai *et al*[7] reported marked variability in the function of normal liver in patients with liver cirrhosis and in patients with portal vein tumor thrombus (PVTT), which led to the adoption of a surgical therapeutic strategy. Radiation oncologists generally use and rely upon CT-based DVH. Many radiation oncologists may not acknowledge or cope with the possible variations in liver function in normal liver.

Because single photon emission computed tomography (SPECT) with liver scintigraphy reflects the function of normal liver[7-9], we anticipated that SPECT could be used to evaluate localized liver function. Nanashima *et al*[8] reported that SPECT images obtained using Tc-99m-galactosyl human serum albumin (GSA) provided a better assessment of local liver function than conventional CT images. Furthermore, Shuke *et al*[9] reported that GSA was the best radioisotope for evaluating liver function by scintigraphy. Therefore, we merged SPECT images obtained using GSA (GSA-SPECT) with CT simulation images to prepare isodose curves. We then used the merged images for treatment planning for HCC, including cases with PVTT, hepatic vein tumor thrombus (HVTT) and/or bile tract tumor thrombus (BTTT)[10,11]. We refer to this approach as SPECT-based three-dimensional conformal radiotherapy (SPECT-B-3DCRT).

The aim of this article is to describe the technical details, safety and efficacy of SPECT-B-3DCRT. We also describe its potential limitations and possible strategies to overcome its limitations.

COMBINING RT WITH TRANSCATHETER ARTERIAL CHEMOEMBOLIZATION

Transcatheter arterial chemoembolization (TACE) is perhaps the most widely performed multidisciplinary therapy for unresectable HCC[12]. However, because TACE is commonly ineffective in patients with HCC ≥ 5 cm in diameter or HCC with blood vessel invasion[12,13], we combined SPECT-B-3DCRT together with TACE in such patients, with the aim of improving treatment outcomes[10,11]. Namely, TACE was applied for intrahepatic metastasis out of the radiation field. RT is also applied to metastases in bone, liver and brain. Accordingly, TACE plus RT is an effective multidisciplinary therapy for patients with otherwise limited treatment options[10,11,14-16].

DEFINITION OF FUNCTIONAL LIVER

There is increasing research into the use of GSA in internal medicine and surgery in the context of hepatology[17,18], but it has been overlooked in relation to RT. When we first considered applying GSA-SPECT to RT, we found no reliable studies describing the potential relationship between GSA and RT. However, we found some studies describing the use of Tc-99m-macroaggregated albumin in RT of lung cancer. Although different radioisotopes are used for different cancers, these earlier reports highlighted the need to select an appropriate radioisotope and evaluate organ function before commencing RT[19,20,21]. The first step for evaluating liver function involved fusing the SPECT image to the CT simulation image. The state of the liver varies considerably in HCC patients, ranging from normal liver function to Child C cirrhotic liver[17]. Therefore, the next step was to establish a definition of functional liver. Unfortunately, a universal definition of functional liver cannot be used because the extent of cirrhotic liver varies considerably among patients. Christian *et al*[19] proposed a threshold for organ function in individual organs. Based on a study by Sawamura *et al*[22], we defined functional liver as the region of the liver in which radioisotope accumulation exceeded that of the HCC, while dysfunctional liver was defined as the region of the liver in which radioisotope accumulation was similar to that of the HCC[10,11] (Figures 1 and 2). This definition of functional liver was therefore qualitative but not quantitative.

SPECT-B-3DCRT TECHNIQUE

The current Japanese guidelines for RT of HCC recommend that small HCCs are irradiated with 80-90 Gy in 40-45 fractions[23]. However, surgical hepatectomy and radiofrequency ablation (RFA) are also used to treat small HCCs. At our institute, RT is generally requested for HCCs that cannot be managed surgically or by RFA, especially in patients with giant HCCs with intrahepatic metastasis and liver cirrhosis. All the patients in this series were asked by the surgeon and/or hepatologists to undergo radiotherapy because of the presence of PVTT. The administration of sorafenib was limited to liver function of Child-Pugh A classification and the cost of sorafenib, approximately 6000 dollars per month, was a financial burden on the patients. Surgical hepatic lobectomy was not scheduled because of the presence of

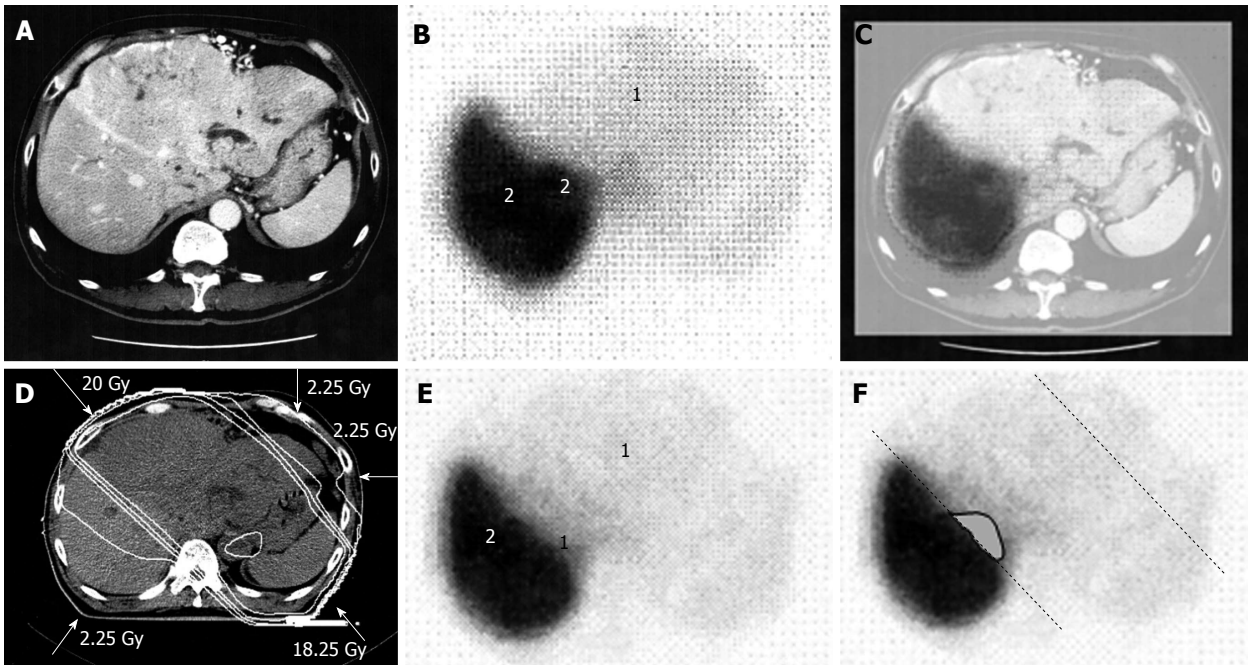

Figure 1 A 58-year-old man with hepatocellular carcinoma with a maximum diameter of 18.0 cm. A: Contrast-enhanced computed tomography; B: Single photon emission computed tomography with Tc-99m-galactosyl human serum albumin before radiotherapy; C: The merged image of A and B. The regions (1) without GSA accumulation in B correspond to main tumor located in the left lobe. The regions (2) of high accumulation in B correspond to functional liver. These regions were identified using the merged image (C); D: Dose distribution based on the CT simulation; E: GSA-SPECT image obtained 2 mo after RT shows regions without GSA accumulation (1) along the two high-dose beams, with preservation of functional liver (2); F: The extent of radiation-induced dysfunctional liver is shown as the gray area with a black border and was determined by comparing B and E. GSA: Galactosyl human serum albumin; SPECT: Single photon emission computed tomography; CT: Computed tomography; RT: Radiotherapy.

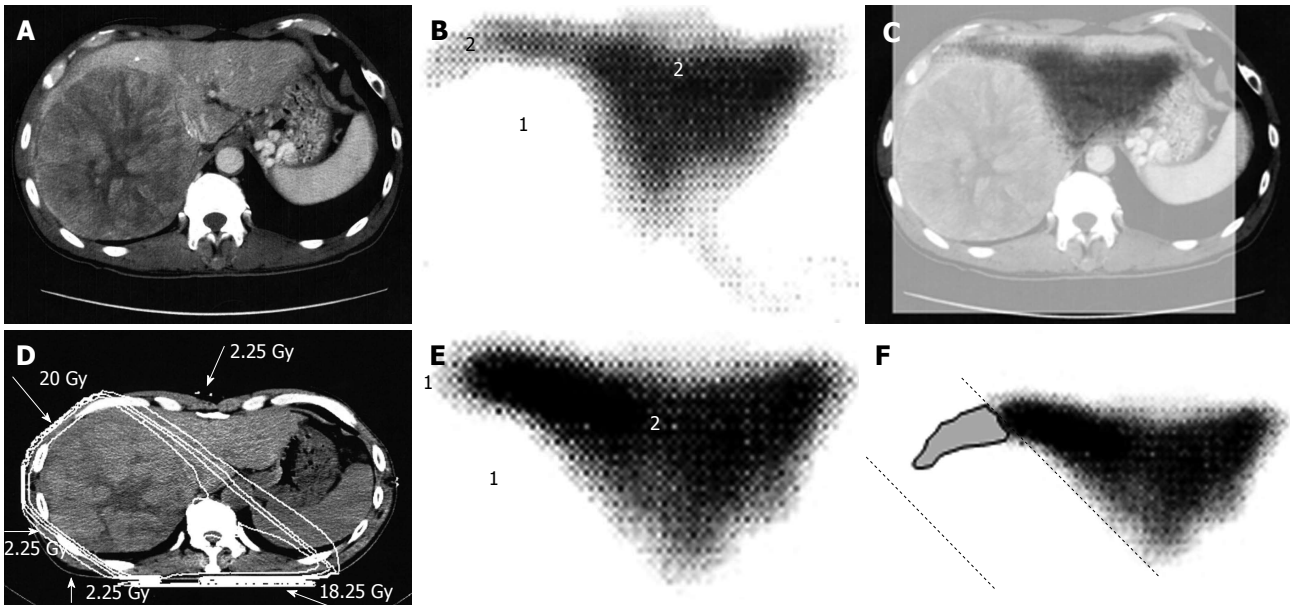

Figure 2 A 53-year-old man with hepatocellular carcinoma with a maximum diameter of 16.5 cm. A: Contrast-enhanced computed tomography; B: Single photon emission computed tomography with Tc-99m-galactosyl human serum albumin before radiotherapy; C: The merged image of A and B; The regions (1) without GSA accumulation in B correspond to main tumor located in the right lobe. The regions (2) of high accumulation in B correspond to functional liver. These regions were identified using the merged image (C); D: Dose distribution based on the CT simulation; E: GSA-SPECT image obtained 2 mo after RT shows regions without GSA accumulation (1) along the two high-dose beams, with preservation of functional liver (2); F: The extent of radiation-induced dysfunctional liver is shown as the gray area with a black border and was determined by comparing B and E. GSA: Galactosyl human serum albumin; SPECT: Single photon emission computed tomography; CT: Computed tomography; RT: Radiotherapy.

intrahepatic metastases in the other lobe. Namely, treatment of surgery and internal medicine were not indicated for medical and social reasons. Therefore, we prescribed 45 Gy (18 fractions, 2.5 Gy/fraction) for the main tumor

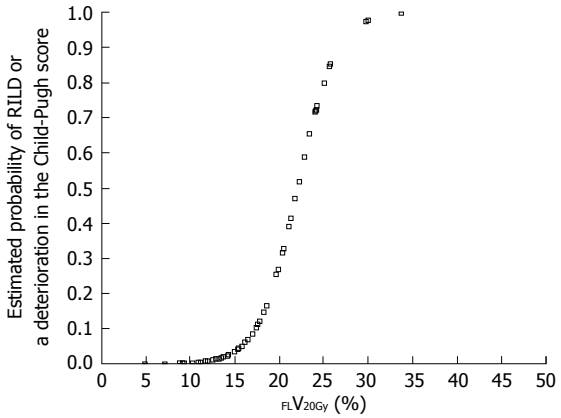

Figure 3 Estimated probability of radiation-induced liver disease or a deterioration in the Child-Pugh score by ⩾ 1 point according to percentage of functional liver irradiated with ⩾ 20 Gy ($_{FL}V_{20Gy}$). Probability values were estimated by logistic regression analysis. RILD: Radiation-induced liver disease.

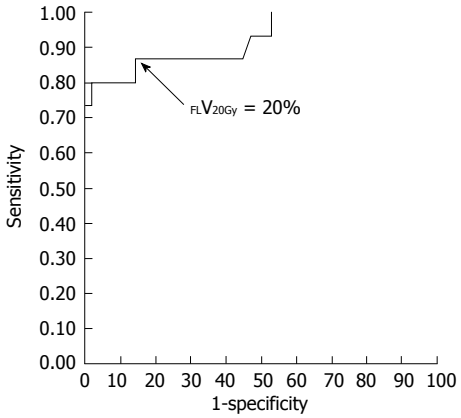

Figure 4 Receiver-operating characteristic curve for the percentage of functional liver volume irradiated with ⩾ 20 Gy ($_{FL}V_{20Gy}$). The optimal cutoff value for $_{FL}V_{20Gy}$ was 20% for predicting radiation-induced liver disease or a deterioration in the Child-Pugh score of ⩾ 1 point. At this cutoff value, sensitivity and specificity were 0.867 and 0.857, respectively. The area under the receiver-operating characteristic curve was 0.923 ($P < 0.001$). *Journal of Gastroenterology and Hepatology* Research gave assurance that the copyright for this figure is retained by the authors.

and the vessel tumor thrombus to prevent RILD[11,15] (Figures 1 and 2). If the tumor size and/or type necessitated applying a greater dose to functional liver than was initially planned, we decided to omit some of the tumor from the irradiation field, providing that the omitted volume was < 5% of the whole tumor and was treated by TACE[13]. Our objective was to avoid RILD in such cases. Furthermore, to account for respiratory mobilization[2,3], the clinical target volume margin was routinely set 2-3 cm greater than the gross tumor volume margin. We also reduced the margin for respiration mobilization from 2-3 cm to 1 cm by asking the patients to hold their breath at the end of expiration[10,11]. To minimize the effects of respiration, the patient practiced breath holding for 10-15 s at the end of expiration until the position could be maintained with a maximum variance of 5 mm under X-ray fluoroscopic monitoring. Treatment planning was also designed to reduce the radiation exposure to the liver[10,11]. In short, the beam angle and dose preserved the functional volume visualized using the merged SPECT-CT image. We conducted SPECT-B-3DCRT in 64 patients with HCC, including 30 patients with Child B liver cirrhosis. We confirmed that a deterioration in the Child-Pugh score of 1 or 2 only occurred in patients when > 20% of the entire functional liver volume was irradiated with ⩾ 20 Gy (Figures 3 and 4)[16]. Figure 3 depicted the abrupt rise of $_{FL}V_{20Gy}$ from approximately 20% and Figure 4 depicted $_{FL}V_{20Gy}$ of 20% corresponded to the cutoff value in receiver operating characteristic analysis. Therefore, our treatment plan specified that ⩽ 20% of the functional liver volume would be irradiated with ⩾ 20 Gy to minimize the deterioration in the Child-Pugh score.

The stomach, intestine, spinal cord and kidneys are at-risk organs during liver RT[24,25]. The use of supplementary beams and/or setting a couch angle of ⩽ 90° helped to reduce irradiation of the stomach, intestine and spinal cord to ⩽ 38.25 Gy, while ⩽ 30% of the total volume of both kidneys was exposed to ⩾ 20 Gy[10,11].

The merged SPECT-CT images provided us with an unexpected but promising finding. The growth of gigantic HCCs is coupled with significant destruction of functional liver, especially of the tissue surrounding the tumor. Consequently, the target tissue becomes greater and it becomes easier to preserve functional liver with appropriate treatment planning[14].

TREATMENT OF HCC ⩾ 14 CM IN DIAMETER

Japanese RT guidelines suggest proton beam irradiation to treat HCC of ⩾ 5 cm[23]. Sugahara *et al*[26] reported that proton beam therapy brought about 2-year local tumor control rate of 87% and 2-year survival rate of 36%. These results seem to surpass our results below. However, median tumor size of their study was 11 cm (range, 10-14 cm) and proton beam therapy is not indicated for HCC of ⩾ 14 cm[26]. That is the reason why we introduced treating HCC of ⩾ 14 cm using SPECT-B-3DCRT. We assessed the merged SPECT-CT images for HCC of ⩾ 14 cm in diameter and found that the majority of functional liver was localized to the non-main HCC-bearing lobe rather than the main HCC-bearing lobe[15] (Figures 1 and 2). Our clinical research indicated that SPECT-B-3DCRT did not affect liver function when ⩾ 80% of functional liver was located in the non-main HCC-bearing lobe[15]. In 12 patients who received SPECT-B-3DCRT, the local tumor control rate was 78.6% and the 2-year survival rate was 33.3%, without serious adverse effects (Figure 5). Based on these findings, we recommend the use of SPECT-B-3DCRT for patients with gigantic (⩾ 14 cm) HCC that cannot be managed by resection or proton beam therapy.

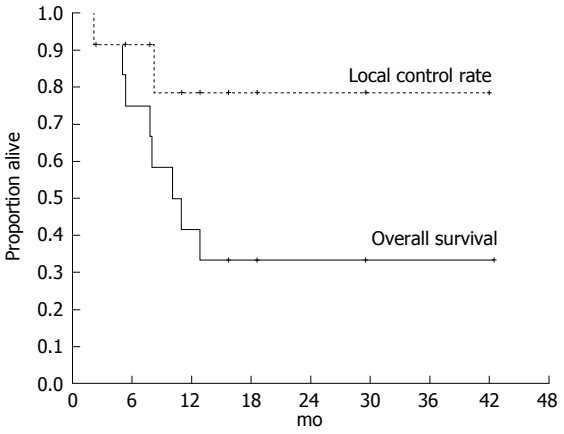

Figure 5 Kaplan-Meier analysis of the local control rate of the irradiated tumor and the survival in 12 cases of hepatocellular carcinoma exceeding 14 cm following single photon emission computed tomography-based three-dimensional radiotherapy. Cancer and Clinical oncology gave assurance that the copyright for this figure is retained by the authors.

TREATMENT OF HCC 5-14 CM IN DIAMETER

If functional liver is predominantly located in the non-main HCC-bearing lobe, SPECT-B-3DCRT can be performed without significant concerns, as described above. However, in some patients, the majority of functional liver is located in the main HCC-bearing lobe. If the main HCC-bearing lobe is the right lobe and > 50% of functional liver volume is in the main HCC-bearing lobe, the treatment strategy should be developed very carefully.

We treated 26 patients with HCCs of 5-14 cm with PVTT, leading to the control rate of 92.2% of the PVTT and 1-year and 2-year survival rate of 44.4% and 30%, respectively[10]. Figure 6 shows a typical patient with an HCC of 5-14 cm in diameter. This patient had a right PVTT. SPECT revealed that 85% of functional liver was in the right lobe adjacent to the PVTT. If the RT plan was prepared for normal liver using CT images alone, we would expect that short-axis beams (hypothetical main beams, Figure 6F) would result in less irradiation of normal liver than that with long-axis beams (actual main beams, Figure 6C). $_{NL}V_{20Gy}$ would be 30.8% for the long-axis beam plan and 23.1% for the short-axis beam plan. However, $_{FL}V_{20Gy}$ based on SPECT images was 23.8% for the long-axis beam plan and 43.7% for the short-axis beam plan (Figure 7). Therefore, in this patient, RT using short-axis beams would likely cause RILD.

Cheng *et al*[2] reported that 17/89 (19.1%) and 7/89 (7.9%) patients who received 3DCRT with treatment planning without SPECT experienced RILD and fatal RILD, respectively. In the study by Liang *et al*[3], 17/109 (15.6%) and 13/109 (11.9%) patients developed RILD and fatal RILD, respectively. In our series, 3/64 (4.7%) and 0 patients (0%) who received SPECT-B-3DCRT experienced RILD and fatal RILD, respectively[16]. Therefore, we believe that GSA-SPECT helps to predict and may ultimately reduce the risk of non-fatal and fatal RILD.

TREATMENT OF HCC < 5 CM IN DIAMETER

SPECT-B-3DCRT can be applied to HCC of ≤ 5 cm with PVTT, HVTT and/or BTTT. In this situation, functional liver surrounds the main tumor and is therefore likely to be damaged by RT. Regrettably, as we encountered no patient with HCC < 5 cm with PVTT[10,11], we described the content of radiotherapy for HCC < 5 cm by referring to other manuscripts. Mornex *et al*[27] reported that 3DCRT caused Grade 4 toxicity in 2/11 (22%) Child B patients and Grade 3 toxicity in 3/16 (19%) Child A patients with a HCC ≤ 5 cm in diameter. Therefore, smaller HCCs require more careful treatment planning than larger HCCs. In this context, we consider that treatment planning with $_{FL}V_{20Gy}$ ≤ 20% is an important approach for preserving functional liver (Figures 3 and 4). If $_{FL}V_{20Gy}$ is > 20% of the planned volume of the main tumor to be irradiated, we suggest that the treatment plan is revised to omit part of the main tumor. This residual part of the tumor can be treated by TACE instead[16].

LIMITATIONS OF FUNCTIONAL LIVER

If merged SPECT-CT images are available, the concept of functional liver is particularly useful for treatment planning in individual patients. However, functional liver is a qualitative rather than quantitative concept, making it difficult to compare data on functional liver among institutes. Therefore, an objective definition of functional liver should be established and standardized.

DOSE-FUNCTION HISTOGRAM AND FUNCTIONAL COUNT RATE (F_{Gy})

Sugahara *et al*[17] used GSA SPECT to evaluate the function of the right and left lobes before surgical hepatectomy in a quantitative manner by determining the liver uptake of GSA relative to the total dose of GSA injections. Christian *et al*[19] and Seppenwoolde *et al*[21] used lung perfusion SPECT for treatment planning and evaluated the extent of functional lung. Therefore, software has been developed to determine the dose-function histograms (DFH) from perfusion SPECT images for use in treatment planning for lung cancer[20].

Based on these previous reports, we propose functional count rate (F_{Gy}) as a quantitative index of functional liver. F_{Gy} is defined as the percentage of the functional liver rate in the DFH and is based on V_{Gy}, the percentage of liver volume in the DVH. F_{Gy} is calculated using the following formula: F_{Gy} = 100 × (GSA count in the area of the liver indicated by the isodose curve)/(GSA count for the entire liver). Because we use $_{FL}V_{20Gy}$ ≤ 20% as a qualitative safety marker, F_{20Gy} was calculated for the patient presented in Figure 8. For this patient, F_{20Gy}, $_{NL}V_{20Gy}$ and $_{FL}V_{20Gy}$ were 22.2, 20.6 and 18.1, respectively. We consider that, because DFH and F_{Gy} link the area of the isodose curve to liver

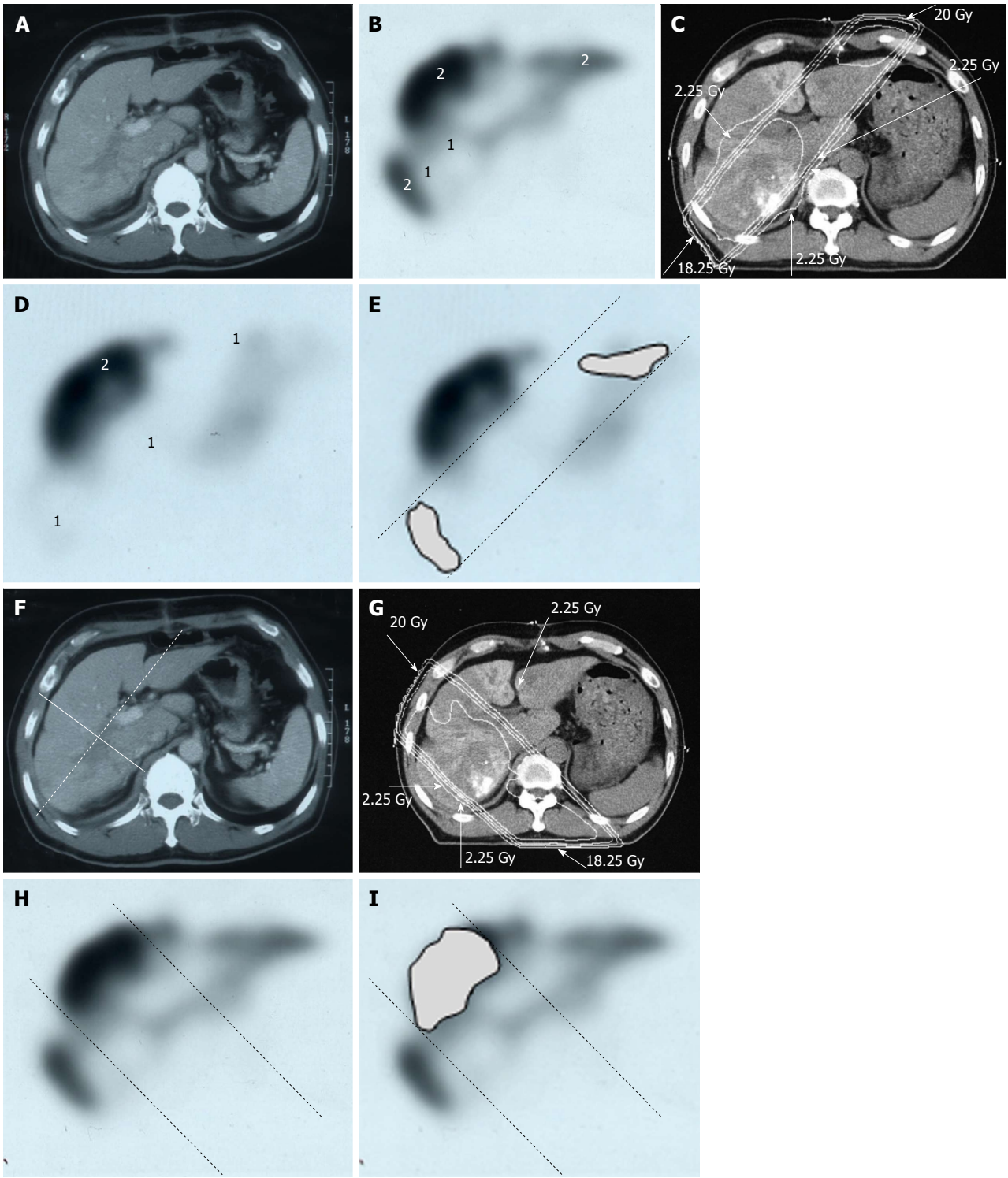

Figure 6 Distribution of functional liver and treatment planning for a 60-year-old male with hepatocellular carcinoma and liver cirrhosis of Child-Pugh grade A. A: Contrast-enhanced computed tomography shows a PVTT in the right first portal vein originating from the right posterior sub-segment branch of the portal vein; B: GSA-SPECT taken before RT at the same level as A confirms that functional liver (2) is unevenly distributed between the anterior and lateral sides of the right PVTT. 1 = dysfunctional liver; C: The two main radiation beams were angled in the left-anterior to right-posterior direction (20 Gy) and in the right-posterior to left-anterior direction (18.25 Gy beam); D: GSA-SPECT image obtained 2 mo after RT shows functional liver (2) and preservation of the right anterior sub-segment. This image also shows that the extent of dysfunctional liver has increased in the right posterior and left medial sub-segments; E: The extent of radiation-induced dysfunctional liver is shown as the dark gray area; F-I: Hypothetical treatment planning; F: The hypothetical main beams are angled in the right-anterior to left-posterior direction (solid lines), unlike the actual beams (dotted lines); G: The hypothetical radiation beams are angled in the right-anterior to left-posterior direction (20 Gy) and in the left-posterior to right-anterior direction (18.25 Gy). Although the radiation-induced destruction of normal liver can be estimated, it is difficult to predict the extent of radiation-induced destruction of functional liver from CT simulation alone; H: GSA-SPECT image together with the hypothetical main beams; I: The gray area indicates the extent of radiation-induced dysfunctional liver likely to be induced by the hypothetical main beams. The relative difference in the destruction of functional liver between the real and the hypothetical treatment plans can be estimated by comparing E and I. PVTT: Portal vein tumor thrombus; GSA-SPECT: Galactosyl human serum albumin-single photon emission computed tomography with Tc-99m-galactosyl human serum albumin image; RT: Radiotherapy; CT: Computed tomography.

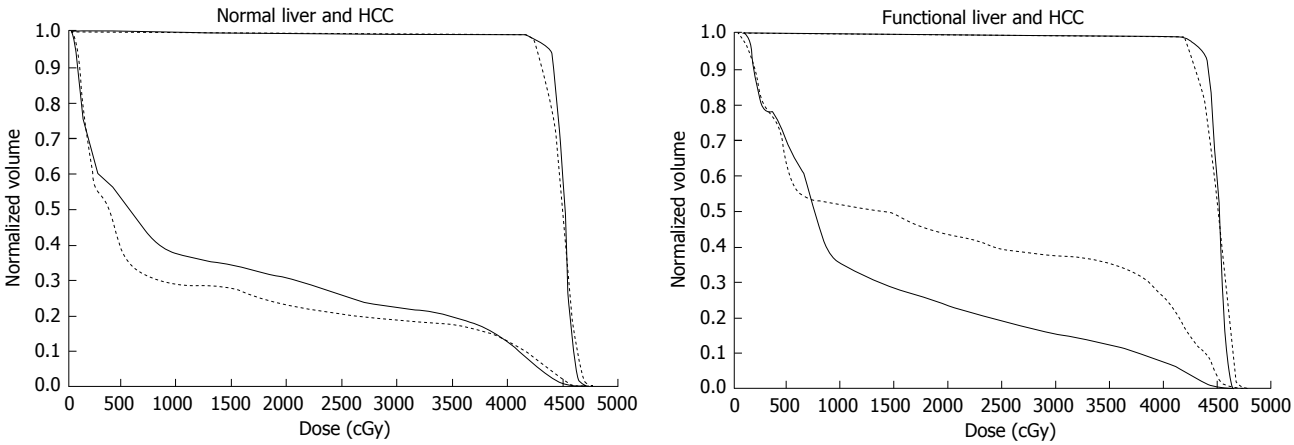

Figure 7 Comparison of dose-volume histograms between actual treatment plans (solid lines) and hypothetical treatment plans (dotted lines). A: Comparison of the DVH for normal liver. In this case, the percentage of the normal liver irradiated with ⩾ 20 Gy ($_{NL}V_{20Gy}$) was 23.1% for the hypothetical treatment plan *vs* 30.8% for the actual treatment plan. Therefore, irradiation of normal liver is lower for the hypothetical treatment plan than for the actual treatment plan; B: Comparison of the DVH for functional liver. In this case, the percentage of functional liver irradiated with ⩾ 20 Gy ($_{FL}V_{20Gy}$) was 43.7% for the hypothetical treatment plan *vs* 23.8% for the actual treatment plan. Therefore, irradiation of functional liver is lower for the actual treatment plan than for the hypothetical treatment plan. The difference between $_{NL}V_{20Gy}$ and $_{FL}V_{20Gy}$ in these two settings is due to the uneven distribution of functional liver. DVH: Dose-volume histograms; HCC: Hepatocellular carcinoma.

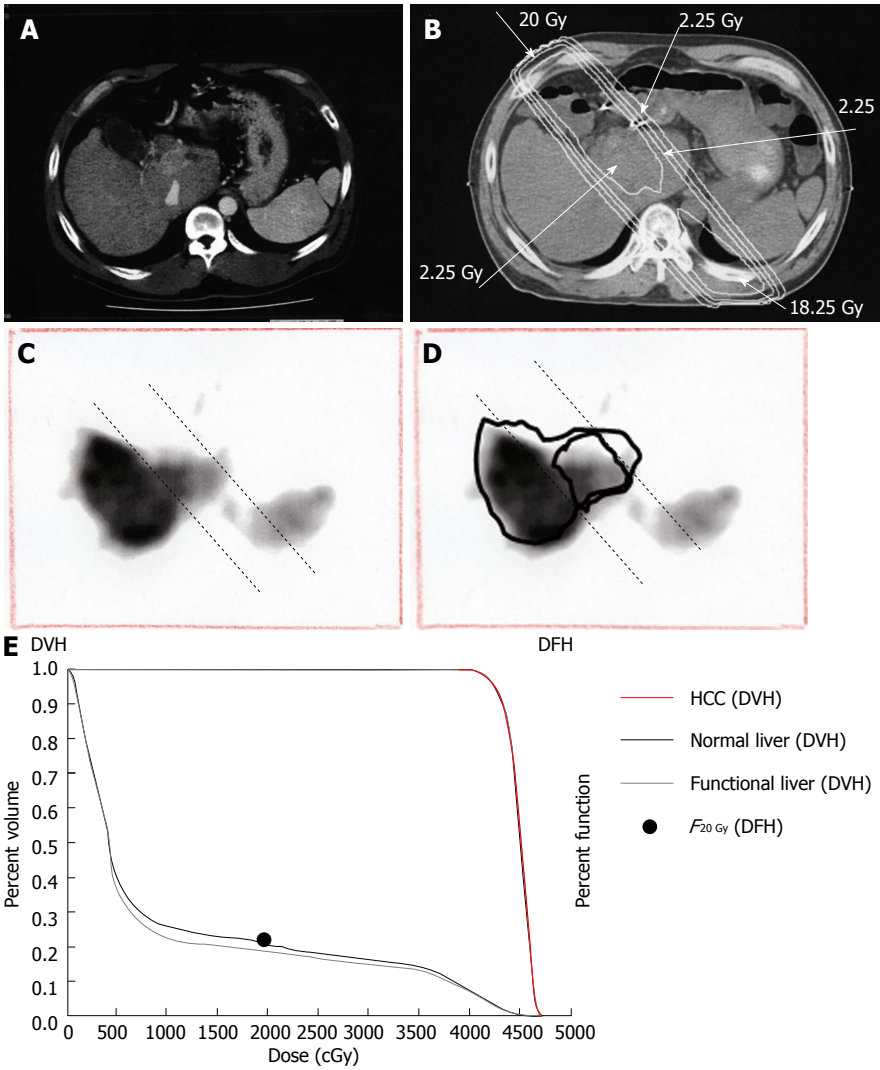

Figure 8 Quantitative analysis of radiation-induced dysfunctional liver. A: Computed tomographic image of a 52-year-old man with a recurrent tumor thrombus in the main portal vein after undergoing left hepatectomy for hepatocellular carcinoma; B: Isodose curves used for treatment planning; C: F_{20Gy} was calculated from the GSA count of the entire liver and the area within the 20 Gy isodose curve; D: $F_{20\ Gy}$ was calculated from a single photon emission computed tomography with Tc-99m-galactosyl human serum albumin image using the formula: $F_{20\ Gy}$ = 100 × (GSA count in the area of the liver within the 20 Gy isodose curve)/(GSA count for the entire liver); E: In this patient, F_{20Gy} was 22.2%. GSA: Galactosyl human serum albumin; DVH: Dose volume histogram; DFH: Dose function histogram; HCC: Hepatocellular carcinoma.

function in a quantitative manner, they could replace DVH and V_{Gy} as gold-standard methods for evaluating the effects of RT on liver function. However, further studies are needed to confirm the clinical utility of DFH and F_{Gy} in treatment planning for patients with HCC and liver dysfunction.

CONCLUSION

SPECT-B-3DCRT combined with TACE can be performed in patients with HCC of any size, together with a PVTT, HVTT and/or BTTT, offering improved safety and therapeutic outcomes compared with existing modalities. Although $_{FL}V_{20Gy} \leqslant 20\%$ is a qualitative assessment, it is a useful safety marker for predicting the risk of RILD. We also consider that DFH and F_{Gy} are promising quantitative markers for predicting the effects of SPECT-B-3DCRT in patients with HCC.

ACKNOWLEDGMENTS

Journal of Gastroenterology and Hepatology Research gave assurance that the copyright for this figure is retained by the authors.

REFERENCES

1 **Mohan R**, Brewster LJ, Barest GD. A technique for computing dose volume histograms for structure combinations. *Med Phys* 1987; **14**: 1048-1052 [PMID: 3696069 DOI: 10.1118/1.595984]
2 **Cheng JC**, Wu JK, Lee PC, Liu HS, Jian JJ, Lin YM, Sung JL, Jan GJ. Biologic susceptibility of hepatocellular carcinoma patients treated with radiotherapy to radiation-induced liver disease. *Int J Radiat Oncol Biol Phys* 2004; **60**: 1502-1509 [PMID: 15590181 DOI: 10.1016/j.ijrobp.2004.05.048]
3 **Liang SX**, Zhu XD, Xu ZY, Zhu J, Zhao JD, Lu HJ, Yang YL, Chen L, Wang AY, Fu XL, Jiang GL. Radiation-induced liver disease in three-dimensional conformal radiation therapy for primary liver carcinoma: the risk factors and hepatic radiation tolerance. *Int J Radiat Oncol Biol Phys* 2006; **65**: 426-434 [PMID: 16690430 DOI: 10.1016/j.ijrobp.2005.12.031]
4 **Burman C**, Kutcher GJ, Emami B, Goitein M. Fitting of normal tissue tolerance data to an analytic function. *Int J Radiat Oncol Biol Phys* 1991; **21**: 123-135 [PMID: 2032883 DOI: 10.1016/0360-3016(91)90172-Z]
5 **Lyman JT**. Complication probability as assessed from dose-volume histograms. *Radiat Res Suppl* 1985; **8**: S13-S19 [PMID: 3867079 DOI: 10.2307/3583506]
6 **Kim TH**, Kim DY, Park JW, Kim SH, Choi JI, Kim HB, Lee WJ, Park SJ, Hong EK, Kim CM. Dose-volumetric parameters predicting radiation-induced hepatic toxicity in unresectable hepatocellular carcinoma patients treated with three-dimensional conformal radiotherapy. *Int J Radiat Oncol Biol Phys* 2007; **67**: 225-231 [PMID: 17056199]
7 **Ikai I**, Yamaoka Y, Yamamoto Y, Ozaki N, Sakai Y, Satoh S, Shinkura N, Yamamoto M. Surgical intervention for patients with stage IV-A hepatocellular carcinoma without lymph node metastasis: proposal as a standard therapy. *Ann Surg* 1998; **227**: 433-439 [PMID: 9527067]
8 **Nanashima A**, Yamaguchi H, Shibasaki S, Morino S, Ide N, Takeshita H, Tsuji T, Sawai T, Nakagoe T, Nagayasu T, Ogawa Y. Relationship between CT volumetry and functional liver volume using technetium-99m galactosyl serum albumin scintigraphy in patients undergoing preoperative portal vein embolization before major hepatectomy: a preliminary study. *Dig Dis Sci* 2006; **51**: 1190-1195 [PMID: 16944008 DOI: 10.1007/s10620-006-8031-x]
9 **Shuke N**, Aburano T, Nakajima K, Yokoyama K, Sun BF, Matsuda H, Muramori A, Michigishi T, Tonami N, Hisada K. [The utility of quantitative 99mTc-GSA liver scintigraphy in the evaluation of hepatic functional reserve: comparison with 99mTc-PMT and 99mTc-Sn colloid]. *Kaku Igaku* 1992; **29**: 573-584 [PMID: 1434071]
10 **Shirai S**, Sato M, Suwa K, Kishi K, Shimono C, Kawai N, Tanihata H, Minamiguchi H, Nakai M. Single photon emission computed tomography-based three-dimensional conformal radiotherapy for hepatocellular carcinoma with portal vein tumor thrombus. *Int J Radiat Oncol Biol Phys* 2009; **73**: 824-831 [PMID: 18755560 DOI: 10.1016/j.ijrobp.2008.04.055]
11 **Shirai S**, Sato M, Suwa K, Kishi K, Shimono C, Sonomura T, Kawai N, Tanihata H, Minamiguchi H, Nakai M. Feasibility and efficacy of single photon emission computed tomography-based three-dimensional conformal radiotherapy for hepatocellular carcinoma 8 cm or more with portal vein tumor thrombus in combination with transcatheter arterial chemoembolization. *Int J Radiat Oncol Biol Phys* 2010; **76**: 1037-1044 [PMID: 19540053 DOI: 10.1016/j.ijrobp.2009.03.023]
12 **Yamada R**, Sato M, Kawabata M, Nakatsuka H, Nakamura K, Takashima S. Hepatic artery embolization in 120 patients with unresectable hepatoma. *Radiology* 1983; **148**: 397-401 [PMID: 6306721]
13 **Arata S**, Tanaka K, Okazaki H, Kondo M, Morimoto M, Saito S, Numata K, Nakamura S, Sekihara H. Risk factors for recurrence of large HCC in patients treated by combined TAE and PEI. *Hepatogastroenterology* 2001; **48**: 480-485 [PMID: 11379338]
14 **Shirai S**, Sato M, Noda Y, Kishi K, Kawai N, Minamiguchi H, Nakai M, Sanda H, Sahara S, Ikoma A, Sonomura T. Distribution of functional liver volume in hepatocellular carcinoma patients with portal vein tumor thrombus in the 1st branch and main trunk using single photon emission computed tomography-application to radiation therapy. *Cancers* (Basel) 2011; **3**: 4114-4126 [DOI: 10.3390/cancers3044114]
15 **Shirai S**, Sato M, Noda Y, Kishi K, Ikoma A, Sanda H, Sonomura T, Minamiguchi H, Nakai M, Kawai N. SPECT-based radiation therapy and transcatheter arterial chemoembolization for unresectable hepatocellular carcinoma sized 14 cm or greater. *Cancer Clin Oncol* 2012; **1**: 65-76 [DOI: 10.5539/cco.v1n1p65]
16 **Shirai S**, Sato M, Noda Y, Kumayama Y, Sonomura T, Kawai N, Minamiguchi H, Nakai M, Sanda H, Tanaka F. The safety indicator of radiotherapy for advanced hepatoma with liver cirrhosis. *J Gastroenterol Hepatol Res* 2013; **2**: 730-736
17 **Sugahara K**, Togashi H, Takahashi K, Onodera Y, Sanjo M, Misawa K, Suzuki A, Adachi T, Ito J, Okumoto K, Hattori E, Takeda T, Watanabe H, Saito K, Saito T, Sugai Y, Kawata S. Separate analysis of asialoglycoprotein receptors in the right and left hepatic lobes using Tc-GSA SPECT. *Hepatology* 2003; **38**: 1401-1409 [PMID: 14647051 DOI: 10.1053/jhep.2003.09031]
18 **Kaibori M**, Ha-Kawa SK, Maehara M, Ishizaki M, Matsui K, Sawada S, Kwon AH. Usefulness of Tc-99m-GSA scintigraphy for liver surgery. *Ann Nucl Med* 2011; **25**: 593-602 [PMID: 21800021 DOI: 10.1007/s12149-011-0520-0]
19 **Christian JA**, Partridge M, Nioutsikou E, Cook G, McNair HA, Cronin B, Courbon F, Bedford JL, Brada M. The incorporation of SPECT functional lung imaging into inverse radiotherapy planning for non-small cell lung cancer. *Radiother Oncol* 2005; **77**: 271-277 [PMID: 16274762 DOI: 10.1016/j.radonc.2005.08.008]
20 **Marks LB**, Sherouse GW, Munley MT, Bentel GC, Spencer DP. Incorporation of functional status into dose-volume analysis. *Med Phys* 1999; **26**: 196-199 [PMID: 10076973 DOI: 10.1118/1.598503]

21 **Seppenwoolde Y**, Muller SH, Theuws JC, Baas P, Belderbos JS, Boersma LJ, Lebesque JV. Radiation dose-effect relations and local recovery in perfusion for patients with non-small-cell lung cancer. *Int J Radiat Oncol Biol Phys* 2000; **47**: 681-690 [PMID: 10837952 DOI: 10.1016/S0360-3016(00)00454-5]

22 **Sawamura T**, Nakada H, Hazama H, Shiozaki Y, Sameshima Y, Tashiro Y. Hyperasialoglycoproteinemia in patients with chronic liver diseases and/or liver cell carcinoma. Asialoglycoprotein receptor in cirrhosis and liver cell carcinoma. *Gastroenterology* 1984; **87**: 1217-1221 [PMID: 6092193]

23 **Japanese Society for Therapeutic Radiology and Oncology**. Hepatocellular carcinoma. In: Radiotherapy planning guideline 2012 (in Japanese). Tokyo: Kinbara Pub, 2012: 161-164

24 **Emami B**, Lyman J, Brown A, Coia L, Goitein M, Munzenrider JE, Shank B, Solin LJ, Wesson M. Tolerance of normal tissue to therapeutic irradiation. *Int J Radiat Oncol Biol Phys* 1991; **21**: 109-122 [PMID: 2032882 DOI: 10.1016/0360-3016(91)90171-Y]

25 **Park W**, Lim DH, Paik SW, Koh KC, Choi MS, Park CK, Yoo BC, Lee JE, Kang MK, Park YJ, Nam HR, Ahn YC, Huh SJ. Local radiotherapy for patients with unresectable hepatocellular carcinoma. *Int J Radiat Oncol Biol Phys* 2005; **61**: 1143-1150 [PMID: 15752895 DOI: 10.1016/j.ijrobp.2004.08.028]

26 **Sugahara S**, Oshiro Y, Nakayama H, Fukuda K, Mizumoto M, Abei M, Shoda J, Matsuzaki Y, Thono E, Tokita M, Tsuboi K, Tokuuye K. Proton beam therapy for large hepatocellular carcinoma. *Int J Radiat Oncol Biol Phys* 2010; **76**: 460-466 [PMID: 19427743 DOI: 10.1016/j.ijrobp.2009.02.030]

27 **Mornex F**, Girard N, Beziat C, Kubas A, Khodri M, Trepo C, Merle P. Feasibility and efficacy of high-dose three-dimensional-conformal radiotherapy in cirrhotic patients with small-size hepatocellular carcinoma non-eligible for curative therapies--mature results of the French Phase II RTF-1 trial. *Int J Radiat Oncol Biol Phys* 2006; **66**: 1152-1158 [PMID: 17145534 DOI: 10.1016/j.ijrobp.2006.06.015]

P- Reviewer: Francica G, Kumar P, Picardi A **S- Editor**: Ji FF
L- Editor: Roemmele A **E- Editor**: Liu SQ

World Journal of Radiology

Submit a Manuscript: http://www.wjgnet.com/esps/
Help Desk: http://www.wjgnet.com/esps/helpdesk.aspx
DOI: 10.4329/wjr.v6.i8.607

World J Radiol 2014 August 28; 6(8): 607-612
ISSN 1949-8470 (online)

MINIREVIEWS

Bone mineral density in cone beam computed tomography: Only a few shades of gray

Marcio José da Silva Campos, Thainara Salgueiro de Souza, Sergio Luiz Mota Júnior, Marcelo Reis Fraga, Robert Willer Farinazzo Vitral

Marcio José da Silva Campos, Thainara Salgueiro de Souza, Sergio Luiz Mota Júnior, Marcelo Reis Fraga, Robert Willer Farinazzo Vitral, Department of Orthodontics, Juiz de Fora Federal University, 36036-900, Minas Gerais, Brasil
Author contributions: Campos MJS and de Souza TS contributed equally to this work, drafted and wrote the manuscript; Mota Júnior SL and Fraga MR revised the manuscript; Campos MJS and Vitral RWF were responsible for final approval of the version to be published.
Correspondence to: Robert Willer Farinazzo Vitral, DDS, MD, PhD, Professor and Chair of Orthodontics, Department of Orthodontics, Juiz de Fora Federal University, Juiz de Fora, 36036-900, Minas Gerais, Brasil. robertvitral@gmail.com
Telephone: +55-32-21023879 Fax: +55-32-21023879
Received: December 27, 2013 Revised: March 11, 2014
Accepted: April 25, 2014
Published online: August 28, 2014

Abstract

Cone beam computed tomography (CBCT) has often been used to determine the quality of craniofacial bone structures through the determination of mineral density, which is based on gray scales of the images obtained. However, there is no consensus regarding the accuracy of the determination of the gray scales in these exams. This study aims to provide a literature review concerning the reliability of CBCT to determine bone mineral density. The gray values obtained with CBCT show a linear relationship with the attenuation coefficients of the materials, Hounsfield Units values obtained with medical computed tomography, and density values from dual energy X-ray absorciometry. However, errors are expected when CBCT images are used to define the quality of the scanned structures because these images show inconsistencies and arbitrariness in the gray values, particularly when related to abrupt change in the density of the object, X-ray beam hardening effect, scattered radiation, projection data discontinuity-related effect, differences between CBCT devices, changes in the volume of the field of view (FOV), and changes in the relationships of size and position between the FOV and the object evaluated. A few methods of mathematical correction of the gray scales in CBCT have been proposed; however, they do not generate consistent values that are independent of the devices and their configurations or of the scanned objects. Thus, CBCT should not be considered the examination of choice for the determination of bone and soft tissue mineral density at the current stage, particularly when values obtained are to be compared to predetermined standard values. Comparisons between symmetrically positioned structures inside the FOV and in relation to the exomass of the object, as it occurs with the right and left sides of the skull, seem to be viable because the effects on the gray scale in the regions of interest are the same.

Key words: Tomography; Cone-Beam computed tomography; Bone mineral density; Reproducibility of results

Core tip: The development of cone beam computed tomography (CBCT) has allowed for more frequent use of these images in dentistry for the evaluation of dentomaxillofacial structures. Yet, there is no consensus regarding the accuracy of CBCT to determine mineral density of craniofacial bone structures, although this technique has been used for this purpose in several types of analyses. According to the studies available to date, it may be concluded that CBCT should not be considered the examination of choice for the determination of mineral density of osseous and soft tissues, especially when values obtained are compared with predetermined standard values.

RWF. Bone mineral density in cone beam computed tomography: Only a few shades of gray. *World J Radiol* 2014; 6(8): 607-612 Available from: URL: http://www.wjgnet.com/1949-8470/full/v6/i8/607.htm DOI: http://dx.doi.org/10.4329/wjr.v6.i8.607

INTRODUCTION

Bidimensional radiographic methods (periapical, occlusal, panoramic and cephalometric radiographs) are widely used in dentistry; however, they do not provide visualization of the regions of interest without the superimposition of structures and consequent camouflage of anatomical details. The advent of images acquired from computed tomography (CT) has made more precise quantitative and qualitative evaluation of the adjacent structures possible[1,2].

Although the use of CT is routine in medical practice, this examination has not been extensively widespread in dentistry, due to the presence of image artifacts, high cost, complexity of the examination and high dose radiation[3].

The development of cone beam computed tomography (CBCT), used for the evaluation of dentomaxillofacial structures, has allowed for more frequent use of these images in dentistry because it is a less complex device that produces images with satisfactory resolution, with little artifact incidence and lower dose of radiation[4].

Multislice and cone beam CT images are frequently used to determine mineral density of craniofacial bone structures[5-10]. Yet, there is no consensus regarding the accuracy of CBCT for this type of analysis. While some studies advocate its use[10-15], others advocate that CBCT is not an adequate tool for this type of evaluation because the intensity values of CBCT are influenced by the characteristics of the system[4,13,16] and by the scanned object[16-18]. This study aims to provide a literature review concerning the reliability of CBCT for the determination of bone mineral density of craniofacial structures.

BONE MINERAL DENSITY

Mineral density is determined by the amount of mineral mass contained in a certain volume of a structure, described in units of mass per area (in bidimensional images) or per volume (in tridimensional images), where only mineral content is considered[19]. Several methods may be used to determine bone mineral density, including digital image analysis of microradiographs, single photon absorciometry, dual photon absorciometry, dual energy X-ray absorciometry (DEXA) and quantitative ultrasound[20-22]. However, these procedures present with limitations inherent to the techniques used because density is determined through images of superimposed structures, not producing tridimensional information[23,24].

Nowadays, multislice computed tomography (MSCT) is one of the most useful medical imaging techniques for the acquisition of data regarding not only bone density, but the density of all the tissues of the body. In these examinations, density is described in hounsfield units (HU) and represents the relative density of a body tissue according to a calibrated gray-level scale based on HU values of the air (-1000 HU), water (0 HU) and dense bone (+1000 HU)[25]. HU values are directly related to the mass absorption coefficient of different tissues[26] and, despite some variation[27], these values may be used for the determination of density of the tissues with a high degree of accuracy[10] and sensitivity, detecting density differences of 1% or less[28]. However, the gray scale can vary between different scanners and with different energies on the same MSCT scanner[25]. The factor with the highest influence on the determination of the gray scale is the energy of the X-ray beam (kVp), which is directly related to the capacity of penetration of the primary beam. The bigger the energy of the X-ray beam, the bigger and more uniform its penetration will be, resulting in smaller variation of attenuation, smaller contrast of images, and smaller density of the structures evaluated. The adequate setting of the energy applied allows for the determination of a correct density[29].

CONE BEAM CT

After the development of CBCT, a less complex device with low operational cost and reduced radiation emission[30-32] used for the acquisition of tridimensional images of dentomaxillofacial structures by Mozzo *et al*[33], the indication of medical CT for the evaluation of these structures decreased considerably, especially due to the higher radiation dose applied to the patient during image acquisition[10,32]. Thus, CBCT has been proposed as a diagnostic method for the determination of bone mineral density[10,11,18,34-36]. Gray values obtained with CBCT are used in an analog way as the HU values for the determination of mineral density[16] and show a linear relationship with the attenuation coefficients of the materials[13,15], HU values obtained with medical CT[11,12,37,38], and density values from DEXA[14].

Despite the correlation between gray values obtained with MSCT and CBCT, errors are expected when CBCT images are used to define the density of scanned structures[39] because these images present with inconsistencies and arbitrariness of gray values[16,40], especially when related to abrupt changes of density in the object[41,42], X-ray beam hardening effect[39,43], scattered radiation[43] and projection data discontinuity-related effect[16], making the validity of the measurements obtained questionable (Table 1).

In CBCT, the abrupt and discrepant variation of the attenuation coefficient of the X-rays in the scanned structures, as occurs in the presence of metallic structures, creates artifacts in the images, which are characterized by dark and bright streaks in the vicinity of the metal object. Once these artifacts exhibit a different color from that of the structure to be analyzed, they are responsible for the inconsistencies in the gray values in the areas where they are present[15,41,42].

Another source of artifacts in CBCT images is the

Table 1 Factors that might lead to inconsistencies and arbitrariness of grey values on cone beam computed tomography images

Ref.	Factors
Nackaerts *et al*[4]	Variation in the devices
	Image-acquisition settings
	Relationship between the object evaluated and FOV
	The position held by the region of interest
Mah *et al*[13]	Variation in the devices
Reeves *et al*[15]	Abrupt changes of density in the object
Katsumata *et al*[16]	Projection data discontinuity-related effect
	Variation in the CBCT devices
	Image-acquisition settings
	Relationship between the object evaluated and FOV
Bryant *et al*[17]	Projection data discontinuity-related effect
	Relationship between the object evaluated and FOV
	The amount of exomass
Katsumata *et al*[18]	The dimensions of the FOV
	The amount of exomass
Pauwels *et al*[39]	X-ray beam hardening effect
	Projection data discontinuity-related effect
	Variation in the devices
Schulze *et al*[41]	Abrupt changes of density in the object
	X-ray beam hardening effect
	Scattered radiation
Pauwels *et al*[42]	Abrupt changes of density in the object
Goodsitt *et al*[43]	X-ray beam hardening effect
	Scattered radiation
Liu *et al*[50]	The position held by the region of interest

CBCT: Cone beam computed tomography; FOV: Field of view.

phenomenon of X-ray beam hardening. In CBCT, when the beam of X-rays made up of broad spectrum photons reaches a certain material, the low energy photons are easily absorbed, altering the spectrum of the beam. Once the X-ray beam reaches a specific point or area of the object by different angles, varied alterations in the intensity of its energy spectrum occur before it strikes the detector, generating different readings of the attenuation coefficient of this point, and may produce dark streaks in the images obtained[41]. Besides causing artifacts in the images, when the low energy photons are absorbed, the X-ray beam gains energy, passing through the tissues more easily, causing an underestimation of the attenuation coefficient and producing dark areas in the images[42].

An underestimation of the attenuation coefficient due to the occurrence of darker gray values also occurs as a consequence of scattered radiation. When the X-ray beam interacts with the object being evaluated, some photons are diffracted from their original position and strike the detector in a random way. This scattered radiation is added to the primary radiation of the X-ray beam, overestimating the intensity measured by the system and underestimating the attenuation coefficient of the object, affecting the obtained values of density[41]. CBCT devices have bigger detectors than the MSCT because the X-ray beam of the former is conical and of the latter is in the shape of a fan, favoring the occurrence of scattered radiation[44].

Another type of artifact related to CBCT images is known as projection data discontinuity-related artifact, which occurs when FOV is smaller than the scanned object. First, during the system rotation for the image acquisition, the X-ray beam strikes the parts of the object located outside the FOV, creating peripheral bright-band near the boundary of the FOV[16,39], this effect being directly related to the mass and spatial distribution of materials or tissues outside the FOV[17].

Besides the presence of artifacts and the inconsistency of the gray values attributed to the characteristics of CBCT, variation in the devices[4,13,16], image-acquisition settings[4,16], and the relationship between the object evaluated and FOV[4,16-18] may also influence in the images obtained because alterations of these variables are associated with low reproducibility of gray values. Due mainly to the integration between some of these characteristics, in most instances, variables are not adequately controlled in the studies of reliability of values of density in CBCT.

At present, there are several models of CBCT devices in the market and significant fluctuations in gray values were demonstrated when different equipment was compared[4,13]. Each CBCT scanner has its own factors of exposition and image reconstruction (FOV, kVp, mA, voxel size, exposure time). Some are fixed, others are variable[13,39], making it difficult or even impossible for studies on determination of density in CBCT to draw conclusions for all the systems used[39].

According to Pauwels *et al*[39], some CBCT devices with specific protocols of exposition generate stable gray values which may be related to HU and density. However, as with medical CT, the determination of gray values is specific to the scanner, depending on the calibration of the devices.

The determination of the dimensions of the FOV in CBCT is very variable due to its different applicability in dentistry. This adaptation of the size of the FOV according to the demand of the examination is a great advantage of the system because it exposes the patient to a minimum amount of radiation in order to evaluate the region of interest. However, it may have significant implications in the gray values of the structures, with small volume FOVs associated with reduced values of density[18].

The decrease of gray values in the smallest FOV may be explained by the reduction of the diameter of the X-ray beam so as to irradiate only the region of interest[45-48]. This X-ray beam limitation may lead to the decrease of the amount of low-energy photons and to the increase in the capacity of penetration of X-rays[49], resulting in a relative reduction of the value of attenuation of X-rays and gray values[43].

The manipulation of the dimensions of the FOV may also alter the amount of exomass, mass present outside the FOV during image acquisition, which is associated with the variability of the gray values in CBCT examinations[17,18]. Katsumata *et al*[18] reported a significant variation of the gray values when objects of different mass were evaluated with different FOV volumes, where the greater volume FOV provided the elimination of the exomass, resulting in less variability of the gray values.

The variability of the gray values associated with the exomass may be explained by the projection data discontinuity caused by the variation of the superimpositions of the non-homogeneous and non-symmetrical tissues outside the FOV along the rotation of the X-ray beam during image acquisition[16,39].

Another factor that may be related to the variability of the gray values in CBCT is the position held by the region of interest (specific area of measurement of density) inside the FOV. This variability occurred when density was determined in various places of a homogeneous structure[4,50] and with more intensity when the same object was scanned repeatedly in different positions inside the FOV under the same exposure conditions[4].

Despite the many variables that may affect image quality and the determination of gray values in CBCT examinations, great effort has been made in obtaining valid gray values in these images. Studies have described methods for mathematical correction of gray levels in CBCT examination using as reference X-ray attenuation coefficients of standardized materials[13,15], gray values obtained in conventional CT examination[50,51], and even correction algorithms during or after image acquisition[51,52]. Yet, owing to different configurations of image acquisition, which may be specific for each CBCT device or altered for several applications of these examinations in dentistry, the correction methods of gray values obtained in CBCT still do not generate consistent values which are independent of the devices and their configurations or of the scanned objects[15,50].

CONCLUSION

According to the studies available to date, it may be concluded that CBCT should not be considered the examination of choice for the determination of mineral density of osseous and soft tissues, especially when values obtained are compared with predetermined standard values. Comparisons between symmetrically positioned structures inside the FOV and in relation to the exomass of the object, as with the right and left sides of the skull, seem to be viable because the effects on the gray values in the regions of interest are the same.

REFERENCES

1 **Schwarz MS**, Rothman SL, Rhodes ML, Chafetz N. Computed tomography: Part I. Preoperative assessment of the mandible for endosseous implant surgery. *Int J Oral Maxillofac Implants* 1987; **2**: 137-141 [PMID: 3481354]

2 **Velvart P**, Hecker H, Tillinger G. Detection of the apical lesion and the mandibular canal in conventional radiography and computed tomography. *Oral Surg Oral Med Oral Pathol Oral Radiol Endod* 2001; **92**: 682-688 [PMID: 11740486 DOI: 10.1067/moe.2001.118904]

3 **Marques AP**, Perrella A, Arita ES, Pereira MF, Cavalcanti Mde G. Assessment of simulated mandibular condyle bone lesions by cone beam computed tomography. *Braz Oral Res* 2010; **24**: 467-474 [PMID: 21180970 DOI: 10.1590/S1806-83242010000400016]

4 **Nackaerts O**, Maes F, Yan H, Couto Souza P, Pauwels R, Jacobs R. Analysis of intensity variability in multislice and cone beam computed tomography. *Clin Oral Implants Res* 2011; **22**: 873-879 [PMID: 21244502 DOI: 10.1111/j.1600-0501.2010.02076.x]

5 **Lindh C**, Obrant K, Petersson A. Maxillary bone mineral density and its relationship to the bone mineral density of the lumbar spine and hip. *Oral Surg Oral Med Oral Pathol Oral Radiol Endod* 2004; **98**: 102-109 [PMID: 15243479 DOI: 10.1016/S1079-2104(03)00460-8]

6 **Turkyilmaz I**, Tözüm TF, Tumer C. Bone density assessments of oral implant sites using computerized tomography. *J Oral Rehabil* 2007; **34**: 267-272 [PMID: 17371564 DOI: 10.1111/j.1365-2842.2006.01689.x]

7 **de Oliveira RC**, Leles CR, Normanha LM, Lindh C, Ribeiro-Rotta RF. Assessments of trabecular bone density at implant sites on CT images. *Oral Surg Oral Med Oral Pathol Oral Radiol Endod* 2008; **105**: 231-238 [PMID: 18230392 DOI: 10.1016/j.tripleo.2007.08.007]

8 **Park HS**, Lee YJ, Jeong SH, Kwon TG. Density of the alveolar and basal bones of the maxilla and the mandible. *Am J Orthod Dentofacial Orthop* 2008; **133**: 30-37 [PMID: 18174068 DOI: 10.1016/j.ajodo.2006.01.044]

9 **Choi JH**, Park CH, Yi SW, Lim HJ, Hwang HS. Bone density measurement in interdental areas with simulated placement of orthodontic miniscrew implants. *Am J Orthod Dentofacial Orthop* 2009; **136**: 766.e1-766.e12; discussion 766-767 [PMID: 19962594 DOI: 10.1016/j.ajodo.2009.04.019]

10 **Hsu JT**, Chang HW, Huang HL, Yu JH, Li YF, Tu MG. Bone density changes around teeth during orthodontic treatment. *Clin Oral Investig* 2011; **15**: 511-519 [PMID: 20393863 DOI: 10.1007/s00784-010-0410-1]

11 **Aranyarachkul P**, Caruso J, Gantes B, Schulz E, Riggs M, Dus I, Yamada JM, Crigger M. Bone density assessments of dental implant sites: 2. Quantitative cone-beam computerized tomography. *Int J Oral Maxillofac Implants* 2005; **20**: 416-424 [PMID: 15973953]

12 **Lagravère MO**, Carey J, Ben-Zvi M, Packota GV, Major PW. Effect of object location on the density measurement and Hounsfield conversion in a NewTom 3G cone beam computed tomography unit. *Dentomaxillofac Radiol* 2008; **37**: 305-308 [PMID: 18757714 DOI: 10.1259/dmfr/65993482]

13 **Mah P**, Reeves TE, McDavid WD. Deriving Hounsfield units using grey levels in cone beam computed tomography. *Dentomaxillofac Radiol* 2010; **39**: 323-335 [PMID: 20729181 DOI: 10.1259/dmfr/19603304]

14 **Marquezan M**, Lau TC, Mattos CT, Cunha AC, Nojima LI, Sant'Anna EF, Souza MM, Araújo MT. Bone mineral density. *Angle Orthod* 2012; **82**: 62-66 [PMID: 21774580 DOI: 10.2319/031811-192.1]

15 **Reeves TE**, Mah P, McDavid WD. Deriving Hounsfield units using grey levels in cone beam CT: a clinical application. *Dentomaxillofac Radiol* 2012; **41**: 500-508 [PMID: 22752324 DOI: 10.1259/dmfr/31640433]

16 **Katsumata A**, Hirukawa A, Okumura S, Naitoh M, Fujishita M, Ariji E, Langlais RP. Effects of image artifacts on gray-value density in limited-volume cone-beam computerized tomography. *Oral Surg Oral Med Oral Pathol Oral Radiol Endod* 2007; **104**: 829-836 [PMID: 17448704]

17 **Bryant JA**, Drage NA, Richmond S. Study of the scan uniformity from an i-CAT cone beam computed tomography dental imaging system. *Dentomaxillofac Radiol* 2008; **37**: 365-374 [PMID: 18812597 DOI: 10.1259/dmfr/13227258]

18 **Katsumata A**, Hirukawa A, Okumura S, Naitoh M, Fujishita M, Ariji E, Langlais RP. Relationship between density variability and imaging volume size in cone-beam computerized tomographic scanning of the maxillofacial region: an in vitro study. *Oral Surg Oral Med Oral Pathol Oral Radiol Endod* 2009; **107**: 420-425 [PMID: 18715805 DOI: 10.1016/j.tripleo.2008.05.049]

19 **NIH Consensus Development Panel on Osteoporosis Prevention, Diagnosis, and Therapy**. Osteoporosis prevention, diagnosis, and therapy. *JAMA* 2001; **285**: 785-795 [PMID: 11176917 DOI: 10.1001/jama.285.6.785]

20 **Genant HK**, Engelke K, Fuerst T, Glüer CC, Grampp S, Harris ST, Jergas M, Lang T, Lu Y, Majumdar S, Mathur A, Takada M. Noninvasive assessment of bone mineral and structure: state of the art. *J Bone Miner Res* 1996; **11**: 707-730 [PMID: 8725168 DOI: 10.1002/jbmr.5650110602]

21 **Jäger A**, Radlanski RJ, Taufall D, Klein C, Steinhöfel N, Döler W. Quantitative determination of alveolar bone density using digital image analysis of microradiographs. *Anat Anz* 1990; **170**: 171-179 [PMID: 2375496]

22 **Hans D**, Fuerst T, Uffmann M. Bone density and quality measurement using ultrasound. *Curr Opin Rheumatol* 1996; **8**: 370-375 [PMID: 8864591 DOI: 10.1097/00002281-199607000-00016]

23 **Choël L**, Duboeuf F, Bourgeois D, Briguet A, Lissac M. Trabecular alveolar bone in the human mandible: a dual-energy x-ray absorptiometry study. *Oral Surg Oral Med Oral Pathol Oral Radiol Endod* 2003; **95**: 364-370 [PMID: 12627111 DOI: 10.1067/moe.2003.119]

24 **Chang HW**, Huang HL, Yu JH, Hsu JT, Li YF, Wu YF. Effects of orthodontic tooth movement on alveolar bone density. *Clin Oral Investig* 2012; **16**: 679-688 [PMID: 21519883 DOI: 10.1007/s00784-011-0552-9]

25 **White SC**, Pharoah MJ. Oral radiology: principles and interpretation. 5th ed. Philadelphia: Mosby, 2004

26 **Homolka P**, Beer A, Birkfellner W, Nowotny R, Gahleitner A, Tschabitscher M, Bergmann H. Bone mineral density measurement with dental quantitative CT prior to dental implant placement in cadaver mandibles: pilot study. *Radiology* 2002; **224**: 247-252 [PMID: 12091691 DOI: 10.1148/radiol.2241010948]

27 **Lecomber AR**, Yoneyama Y, Lovelock DJ, Hosoi T, Adams AM. Comparison of patient dose from imaging protocols for dental implant planning using conventional radiography and computed tomography. *Dentomaxillofac Radiol* 2001; **30**: 255-259 [PMID: 11571544 DOI: 10.1038/sj.dmfr.4600627]

28 **Kravitz ND**, Kusnoto B. Risks and complications of orthodontic miniscrews. *Am J Orthod Dentofacial Orthop* 2007; **131**: S43-S51 [PMID: 17448385 DOI: 10.1016/j.ajodo.2006.04.027]

29 **Wolbarst AB**, Biwer BM, Cady R, Chen SY, Domotor S, Egidi P, LePoire DJ, Mo T, Peterson J, Walker S. ISCORS Catalog of References to Parameter Values and Distributions Used in Environmental Pathway Modeling for Cleanup of Sites Contaminated with Radioactivity. *Health Phys* 2005; **89**: S91-S99 [PMID: 16224267 DOI: 10.1097/01.HP.0000177683.93443.f4]

30 **Mah J**, Hatcher D. Three-dimensional craniofacial imaging. *Am J Orthod Dentofacial Orthop* 2004; **126**: 308-309 [PMID: 15356493 DOI: 10.1016/j.ajodo.2004.06.024]

31 **Scarfe WC**, Farman AG, Sukovic P. Clinical applications of cone-beam computed tomography in dental practice. *J Can Dent Assoc* 2006; **72**: 75-80 [PMID: 16480609]

32 **Ludlow JB**, Ivanovic M. Comparative dosimetry of dental CBCT devices and 64-slice CT for oral and maxillofacial radiology. *Oral Surg Oral Med Oral Pathol Oral Radiol Endod* 2008; **106**: 106-114 [PMID: 18504152 DOI: 10.1016/j.tripleo.2008.03.018]

33 **Mozzo P**, Procacci C, Tacconi A, Martini PT, Andreis IA. A new volumetric CT machine for dental imaging based on the cone-beam technique: preliminary results. *Eur Radiol* 1998; **8**: 1558-1564 [PMID: 9866761 DOI: 10.1007/s003300050586]

34 **Lee S**, Gantes B, Riggs M, Crigger M. Bone density assessments of dental implant sites: 3. Bone quality evaluation during osteotomy and implant placement. *Int J Oral Maxillofac Implants* 2007; **22**: 208-212 [PMID: 17465345]

35 **Campos MJ**, de Albuquerque EG, Pinto BC, Húngaro HM, Gravina MA, Fraga MR, Vitral RW. The role of orthodontic tooth movement in bone and root mineral density: a study of patients submitted and not submitted to orthodontic treatment. *Med Sci Monit* 2012; **18**: CR752-CR757 [PMID: 23197239 DOI: 10.12659/MSM.883604]

36 **Salimov F**, Tatli U, Kürkçü M, Akoğlan M, Oztunç H, Kurtoğlu C. Evaluation of relationship between preoperative bone density values derived from cone beam computed tomography and implant stability parameters: a clinical study. *Clin Oral Implants Res* 2013; Epub ahead of print [PMID: 23772811 DOI: 10.1111/clr.12219]

37 **Naitoh M**, Hirukawa A, Katsumata A, Ariji E. Evaluation of voxel values in mandibular cancellous bone: relationship between cone-beam computed tomography and multislice helical computed tomography. *Clin Oral Implants Res* 2009; **20**: 503-506 [PMID: 19250241 DOI: 10.1111/j.1600-0501.2008.01672.x]

38 **Nomura Y**, Watanabe H, Honda E, Kurabayashi T. Reliability of voxel values from cone-beam computed tomography for dental use in evaluating bone mineral density. *Clin Oral Implants Res* 2010; **21**: 558-562 [PMID: 20443807 DOI: 10.1111/j.1600-0501.2009.01896.x]

39 **Pauwels R**, Nackaerts O, Bellaiche N, Stamatakis H, Tsiklakis K, Walker A, Bosmans H, Bogaerts R, Jacobs R, Horner K. Variability of dental cone beam CT grey values for density estimations. *Br J Radiol* 2013; **86**: 20120135 [PMID: 23255537 DOI: 10.1259/bjr.20120135]

40 **Hassan B**, Metska ME, Ozok AR, van der Stelt P, Wesselink PR. Comparison of five cone beam computed tomography systems for the detection of vertical root fractures. *J Endod* 2010; **36**: 126-129 [PMID: 20003950 DOI: 10.1016/j.joen.2009.09.013]

41 **Schulze R**, Heil U, Gross D, Bruellmann DD, Dranischnikow E, Schwanecke U, Schoemer E. Artefacts in CBCT: a review. *Dentomaxillofac Radiol* 2011; **40**: 265-273 [PMID: 21697151 DOI: 10.1259/dmfr/30642039]

42 **Pauwels R**, Stamatakis H, Bosmans H, Bogaerts R, Jacobs R, Horner K, Tsiklakis K. Quantification of metal artifacts on cone beam computed tomography images. *Clin Oral Implants Res* 2013; **24** Suppl A100: 94-99 [PMID: 22168574 DOI: 10.1111/j.1600-0501.2011.02382.x]

43 **Goodsitt MM**, Chan HP, Way TW, Larson SC, Christodoulou EG, Kim J. Accuracy of the CT numbers of simulated lung nodules imaged with multi-detector CT scanners. *Med Phys* 2006; **33**: 3006-3017 [PMID: 16964879 DOI: 10.1118/1.2219332]

44 **Kalender WA**, Kyriakou Y. Flat-detector computed tomography (FD-CT). *Eur Radiol* 2007; **17**: 2767-2779 [PMID: 17587058 DOI: 10.1007/s00330-007-0651-9]

45 **Palomo JM**, Rao PS, Hans MG. Influence of CBCT exposure conditions on radiation dose. *Oral Surg Oral Med Oral Pathol Oral Radiol Endod* 2008; **105**: 773-782 [PMID: 18424119 DOI: 10.1016/j.tripleo.2007.12.019]

46 **Pauwels R**, Beinsberger J, Collaert B, Theodorakou C, Rogers J, Walker A, Cockmartin L, Bosmans H, Jacobs R, Bogaerts R, Horner K. Effective dose range for dental cone beam computed tomography scanners. *Eur J Radiol* 2012; **81**: 267-271 [PMID: 21196094 DOI: 10.1016/j.ejrad.2010.11.028]

47 **Siewerdsen JH**, Jaffray DA. Cone-beam computed tomography with a flat-panel imager: magnitude and effects of x-ray scatter. *Med Phys* 2001; **28**: 220-231 [PMID: 11243347 DOI: 10.1118/1.1339879]

48 **Spies L**, Evans PM, Partridge M, Hansen VN, Bortfeld T. Direct measurement and analytical modeling of scatter in portal imaging. *Med Phys* 2000; **27**: 462-471 [PMID: 10757598 DOI: 10.1118/1.598914]

49 **Kheruka S**, Naithani U, Maurya A, Painuly N, Aggarwal L, Gambhir S. A study to improve the image quality in low-dose computed tomography (SPECT) using filtration. *Indian J Nucl Med* 2011; **26**: 14-21 [PMID: 21969774 DOI: 10.4103/0972-3919.84595]

50 **Liu Y**, Bäuerle T, Pan L, Dimitrakopoulou-Strauss A, Strauss LG, Heiss C, Schnettler R, Semmler W, Cao L. Calibration of

cone beam CT using relative attenuation ratio for quantitative assessment of bone density: a small animal study. *Int J Comput Assist Radiol Surg* 2013; **8**: 733-739 [PMID: 23225074 DOI: 10.1007/s11548-012-0803-5]

51 **Naitoh M**, Aimiya H, Hirukawa A, Ariji E. Morphometric analysis of mandibular trabecular bone using cone beam computed tomography: an in vitro study. *Int J Oral Maxillofac Implants* 2010; **25**: 1093-1098 [PMID: 21197484]

52 **Kachelriess M**, Sourbelle K, Kalender WA. Empirical cupping correction: a first-order raw data precorrection for cone-beam computed tomography. *Med Phys* 2006; **33**: 1269-1274 [PMID: 16752561 DOI: 10.1118/1.2188076]

P- Reviewer: Chang Z, Kamishima T, Kwok YM, Neves FS, Peremans K
S- Editor: Ji FF **L- Editor**: Roemmele A **E- Editor**: Wu HL

World Journal of Radiology

Submit a Manuscript: http://www.wjgnet.com/esps/
Help Desk: http://www.wjgnet.com/esps/helpdesk.aspx
DOI: 10.4329/wjr.v6.i8.613

World J Radiol 2014 August 28; 6(8): 613-618
ISSN 1949-8470 (online)

Upper gastrointestinal barium evaluation of duodenal pathology: A pictorial review

Pankaj Gupta, Uma Debi, Saroj Kant Sinha, Kaushal Kishor Prasad

Pankaj Gupta, Department of Radiodiagnosis, Postgraduate Institute of Medical Education and Research, Chandigarh 160012, India
Uma Debi, Division of GE Radiology, Department of Superspeciality of Gastroenterology, Postgraduate Institute of Medical Education and Research, Chandigarh 160012, India
Saroj Kant Sinha, Department of Superspeciality of Gastroenterology, Postgraduate Institute of Medical Education and Research, Chandigarh 160012, India
Kaushal Kishor Prasad, Division of GE Histopathology, Department of Superspeciality of Gastroenterology, Postgraduate Institute of Medical Education and Research, Chandigarh 160012, India
Author contributions: Gupta P and Debi U contributed in generating the figures and writing the article; Sinha SK contributed in writing the article; and Prasad KK contributed in writing the article, revising the article critically and gave final approval of the version to be published.
Correspondence to: Kaushal Kishor Prasad, MD, PDC, CFN, MAMS, FICPath, Additional Professor, Chief, Division of GE Histopathology, Department of Superspeciality of Gastroenterology, Postgraduate Institute of Medical Education and Research, Sector-12, Chandigarh 160012, India. kaushalkp10@hotmail.com
Telephone: +91-172-2756604 Fax: +91-172-2744401
Received: February 11, 2014 Revised: April 15, 2014
Accepted: July 18, 2014
Published online: August 28, 2014

Abstract

Like other parts of the gastrointestinal tract (GIT), duodenum is subject to a variety of lesions both congenital and acquired. However, unlike other parts of the GIT *viz.* esophagus, rest of the small intestine and large intestine, barium evaluation of duodenal lesions is technically more challenging and hence not frequently reported. With significant advances in computed tomography technology, a thorough evaluation including intraluminal, mural and extramural is feasible in a single non-invasive examination. Notwithstanding, barium evaluation still remains the initial and sometimes the only imaging study in several parts of the world. Hence, a thorough acquaintance with the morphology of various duodenal lesions on upper gastrointestinal barium examination is essential in guiding further evaluation. We reviewed our experience with various common and uncommon barium findings in duodenal abnormalities.

Key words: Barium study; Duodenum; Upper gastrointestinal tract; Small bowel; Pathology

Core tip: Barium evaluation of duodenal pathologies is technically more challenging than rest of gastrointestinal tract. Barium study still forms an initial and integral part of evaluation as it provide useful clues to the diagnosis and guide further evaluation. This article should alert the radiologist to consider various common and uncommon duodenal pathologies in the correct clinical setting to guide the clinician for further investigations to ensure correct diagnosis and enable appropriate treatment.

Gupta P, Debi U, Sinha SK, Prasad KK. Upper gastrointestinal barium evaluation of duodenal pathology: A pictorial review. *World J Radiol* 2014; 6(8): 613-618 Available from: URL: http://www.wjgnet.com/1949-8470/full/v6/i8/613.htm DOI: http://dx.doi.org/10.4329/wjr.v6.i8.613

INTRODUCTION

Duodenum is often an overlooked segment of the gastrointestinal tract (GIT) as much of the GIT Radiology literature has focused on the esophagus, stomach, distal small bowel and colon. Duodenum like other parts of the GIT is affected by a variety of pathologic conditions including congenital, inflammatory and neoplastic diseases. While some of the congenital abnormities like duplications and diverticulae are usually asymptomatic, others

Figure 1 Upper gastrointestinal barium study reveals that the duodenojejunal flexure does not cross the left of the midline suggestive of malrotation.

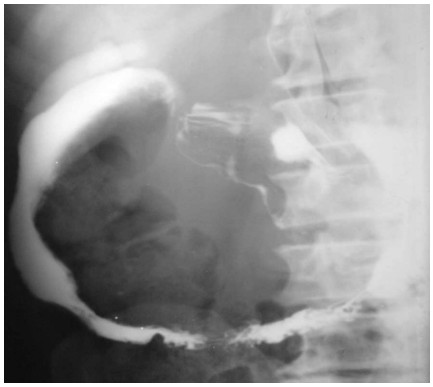

Figure 2 Widening of the duodenal C-loop is noted. Ultrasonography (not shown) showed a well-defined cystic lesion suggestive of duplication. This is a non-specific barium finding.

like annular pancreas and malrotation may manifest in the first decade of life. Inflammatory involvement of the duodenum results from peptic ulcer disease, Crohn's disease (CD) and adjacent inflammatory conditions. Duodenal neoplasms are rare and malignant tumors are much more common than benign tumors. Although, there are no specific signs of the various duodenal pathologies on upper GIT barium series, barium evaluation still forms an integral part of evaluation of patients in several parts of the world due to easy availability and relatively less cost. However, computed tomography (CT) and endoscopy have a greater sensitivity and specificity in detecting duodenal pathologies. CT, in particular provides information about both intramural and extramural disease processes. When used as an initial imaging tool, barium examination does provide useful clues to the underlying pathophysiological processes and as such guide the choice of further tests. Barium examination of duodenum may be contraindicated in suspected leak, history of recent surgery or acute trauma. In these situations, water soluble contrast study replaces barium study. Correct diagnosis requires a thorough knowledge of the appearance of disease processes of duodenum on barium studies. We present a brief barium pictorial review of common and uncommon duodenal lesions.

ANATOMY

Except for the bulb, duodenum is a retroperitoneal structure. It lies within the anterior pararenal space. Forming a C-loop segment around the pancreatic head, this 30 cm tube extends from pylorus to the ligament of Treitz. It is arbitrarily divided into four parts based on their anatomic orientation. The relationship of the proximal and distal end to the spine is important. The pyloric end of the duodenum lies to the right of the spine and the duodenojejunal (DJ) flexure to the left of the pedicle of the spine.

CONGENITAL ANOMALIES

Midgut malrotation

The embryological basis is inadequate rotation of the intestinal loop around the axis of the superior mesenteric artery (SMA) during fetal life, around 10th week of development. Malrotation may occur as an isolated congenital anomaly or as a part of visceral situs anomalies[1]. In practical terms, malrotation can be classified into three types: non-rotation, malrotation and reverse rotation[2]. Former, the most common type is usually asymptomatic and incidentally detected and is imprecisely labeled as non-rotation. Reverse rotation is rare.

Upper gastrointestinal (UGI) barium study is accurate for detection of malrotation. The DJ junction does not cross the midline and is below the duodenal bulb (Figure 1). Delayed evaluation usually shows abnormal location of the right colon. Though abnormal position of caecum is suggestive, normal position does not exclude the diagnosis as it can be normally location in 20% cases[3].

Duplication

Most common site for duplication in the GIT is ileocecal region. Duodenal duplication is relatively uncommon congenital anomaly, accounting for less than 10% of all GIT duplications[4]. It is typically located along the mesenteric aspect of the first and second parts of the duodenum. On barium evaluation, extrinsic mass effect is noted on the duodenum and greater curvature of the stomach (Figure 2). Though rare, communication with the duodenum can be found. The barium findings are non-specific. Differential diagnosis include choledochal cyst, pancreatic lesions including pancreatic masses, pseudocyst, *etc.* and large duodenal diverticulum. A specific diagnosis can be made on high resolution ultrasonography if classical multi-layered appearance (gut signature) is seen[5].

Diverticulum

Duodenal diverticulum can be congenital or acquired. It is a frequent incidental finding detected in about 5% of upper GIT barium studies[6]. The most common site is along mesenteric border of second part of duodenum near the ampulla of Vater. It is seen as barium filled out pouching along the medial aspect of the second part of duodenum, although other locations are not uncommon (Figure 3).

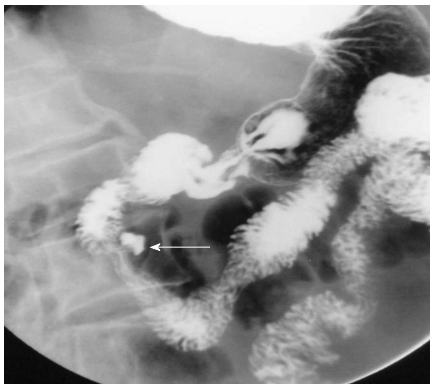

Figure 3 Barium filled out pouching is noted along the medial aspect of the second part of the duodenum (arrow) suggestive of a duodenal diverticulum.

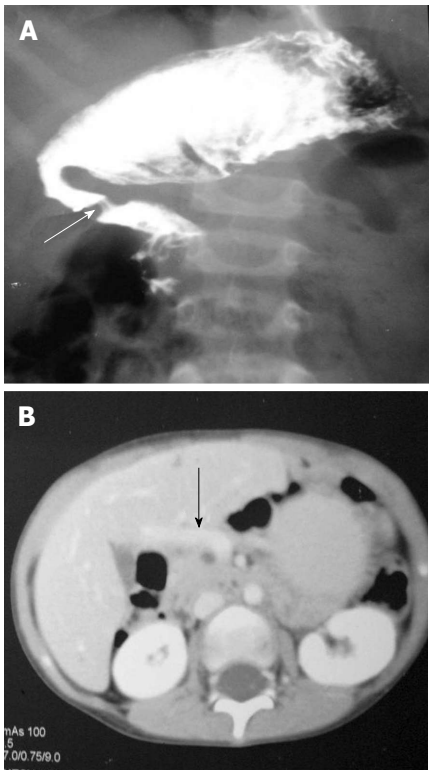

Figure 4 Upper gastrointestinal barium study (A) shows a band like extrinsic narrowing of the first part of the duodenum (arrow), axial computed tomography image (B) reveals the anomalous position of the portal vein anterior to the duodenum (arrow) suggestive of preduodenal portal vein.

Preduodenal portal vein

It usually occurs in association with other congenital malformation, most commonly malrotation, pancreatic, splenic and cardiac anomalies. The portal vein passes anterior to the duodenum and pancreatic head[7]. On barium study, it appears as an extrinsic linear impression on the proximal duodenum or obstruction of the proximal duodenum (Figure 4A). The correct diagnosis is made by contrast enhanced CT that shows the abnormal location of portal vein (Figure 4B).

Annular pancreas

The embryologic basis of the annular pancreas is a defect

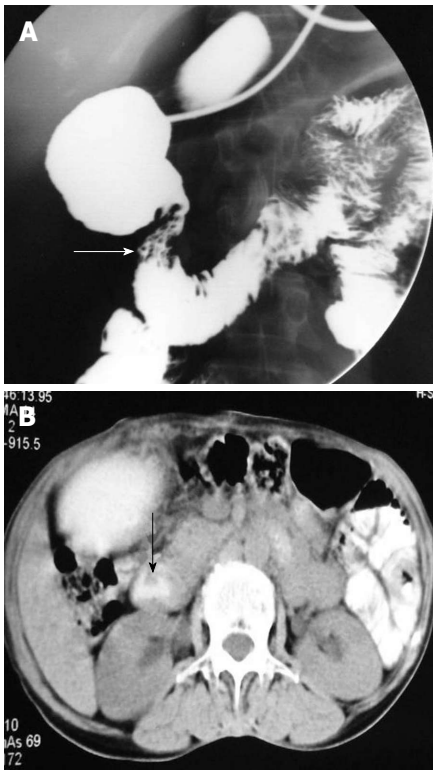

Figure 5 Upper gastrointestinal barium study (A) demonstrates smooth circumferential extrinsic narrowing of the second part of the duodenum (arrow), axial computed tomography image (B) shows pancreatic parenchyma incompletely surrounding the duodenum (arrow), features suggestive of partial annular pancreas.

in the normal rotation of the ventral pancreatic anlage. The result of this aberration is encircling of the second part of duodenum by pancreatic tissue. The annulus encircles the duodenum partially or completely[8]. Pathologically, it is usually loosely applied to the serosa of the duodenum. In extreme cases, the pancreatic tissue is interdigitated with the wall of the duodenum. On barium study, it produces a smooth or tapered narrowing of the second part of the duodenum (Figure 5A). The diagnosis is confirmed by cross-sectional imaging, usually a CT scan (Figure 5B).

Duodenal web

There are several varieties of webs: complete duodenal atresias (imperforate webs), wind sock webs and webs with central or eccentric apertures. The most common sites of web are in vicinity of the ampulla either preampullary or postampullary location[8] (Figure 6). Upper GIT barium study shows the abnormality as a short segment transverse filling defect in the descending duodenum.

Brunner gland hyperplasia

Brunner's gland hyperplasia is a frequent asymptomatic finding on upper GIT barium evaluation. It is seen as solitary or multiple nodular filling defects that are typically less than 5 mm in diameter in the proximal duodenum[9]. When extensive, the nodules lead to a cobblestone or Swiss-cheese pattern (Figure 7). The differential diagnoses for such filling defects in the duodenum include heterotopia,

Figure 6 A short segment narrowing (arrow) suggestive of a web is noted at the junction of first and second part of duodenum. In addition, multiple diverticula are seen at the medial aspect of the second part of the duodenum (arrowheads).

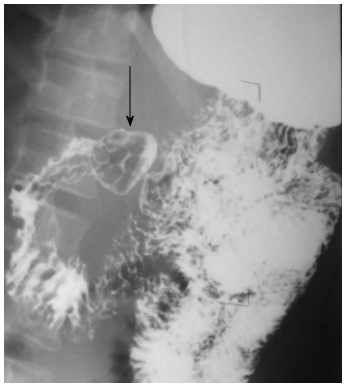

Figure 7 Multiple nodular filling defects are noted in the duodenal cap (arrow) along with fold thickening in the second part of the duodenum. These findings suggest a diagnosis of Brunner gland hyperplasia.

nodular lymphoid hyperplasia, multiple adenomas in familial adenomatous polyposis, hamartomas in Peutz-Jeghers syndrome, carcinoid tumors and metastatic deposits.

ACQUIRED DISEASES

Inflammatory diseases

Peptic ulcer disease: Duodenal ulcers (DUs) are common and affect nearly one-tenth of the adult population. DUs are almost always benign. This is unlike gastric ulcers where 5% of the ulcers can be malignant. Though endoscopy is the most sensitive and specific method for diagnosis of suspected DUs, it is invasive and costly. Double-contrast UGI barium study still remains a useful alternative to endoscopy[10]. More than 90% of DUs occur in the duodenal bulb and nearly 50% of these occur on the anterior wall. Ulcer craters are seen as well-defined round or ovoid pools of barium, surrounded by a symmetrical mound of edematous mucosa. Adjacent radiating mucosal folds converge to the edge of the crater. Healed ulcer leads to deformity of the bulb (Figure 8A). The uncommon variety of DUs, postbulbar ulcers are usually located along the medial aspect of the second part of duodenum above the ampulla of Vater (Figure 8B). Diagnosis on barium study is hampered by location; however indentation of the lateral wall of the duodenum opposite the ulcer due to spasm offers a clue[10].

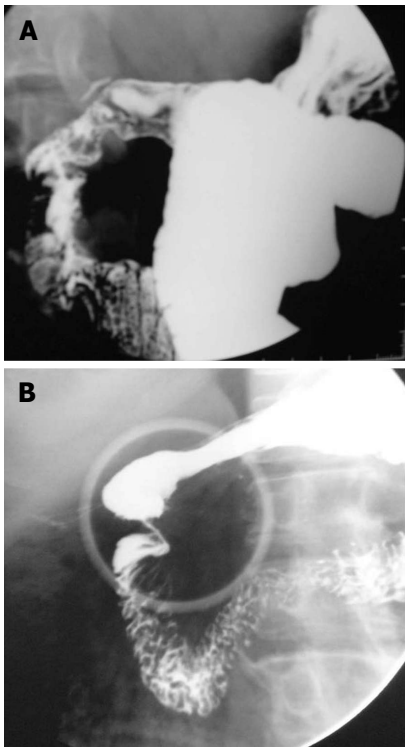

Figure 8 Upper gastrointestinal barium study shows deformity of the duodenal cap (A), stricture is noted at the junction of first and second part of the duodenum (B). These findings are secondary to healed bulbar (A) and post bulbar duodenal ulcers (B).

Tuberculosis: Duodenal tuberculosis (TB) comprises 2% of gastrointestinal TB. Clinically, the patients are divided into two groups: those having dyspeptic symptoms and those with obstructive symptoms. In the former group, barium findings include: luminal narrowing, ulcerations and extrinsic compression. These changes typically spare the proximal duodenum. Less frequently, scarring of duodenal cap, widening of the C-loop are noted. In the group with obstructive symptoms, findings include luminal narrowing of varying degrees (Figure 9) or cut off at junction of second and third part of duodenum resembling the SMA syndrome.

Concomitant tuberculous involvement of rest of the GIT is fairly common. Associated involvement of biliary tract can be noted (Figure 9). This takes the form of air in the common bile duct or reflux of barium into the biliary tree.

CD: CD affects the upper GIT mucosa in 20%-40% of patients. Early disease leads to irregular thickening, edema and cobblestone appearance. With disease progression, there is fibrosis and stenosis of the involved segment. Finally a string sign may develop. There are three patterns of involvement in advanced disease. The first and the most common pattern is the contiguous involvement of stomach and duodenum[11]. Other two patterns are isolat-

Figure 9 There is narrowing of the distal second part of the duodenum with reflux of barium into the common bile ducts. This patient had concomitant involvement of the ileocecal junction (not shown). Histopathology revealed a diagnosis of gastrointestinal tuberculosis.

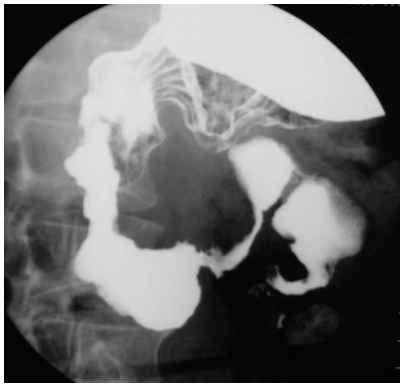

Figure 10 A long segment narrowing with irregular outline and proximal dilatation is noted in the fourth part of duodenum. In addition few strictures are also noted in proximal jejunum. Detailed evaluation in this patient revealed a diagnosis of Crohn's disease.

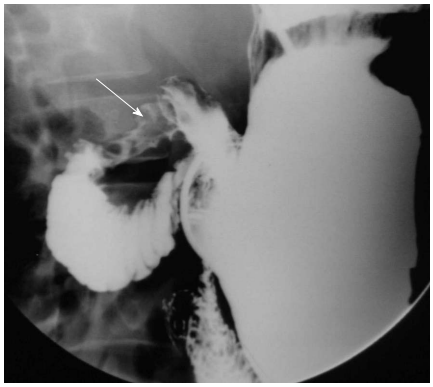

Figure 11 Mild luminal narrowing with ulceration is noted in the proximal duodenum. Computed tomography of this patient (not shown) revealed mural thickening of the duodenum with cystic changes suggestive of cystic dystrophy.

ed involvement of proximal and distal duodenum (Figure 10). Less common findings are development of fissures, pseudodiverticulae and reflux of contrast into the biliary tree. Advanced gastroduodenal involvement may lead to pseudo-Billroth I appearance.

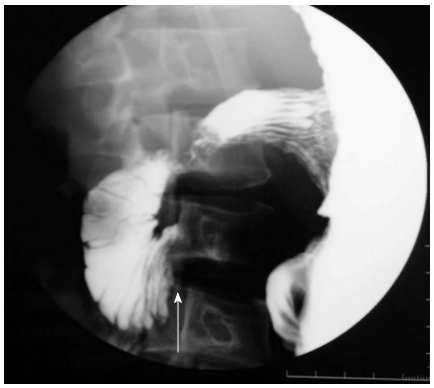

Figure 12 Upper gastrointestinal barium study shows cut off of the duodenum at the junction of second and third part with collapsed distal duodenum suggestive of superior mesenteric artery syndrome.

Extrinsic inflammatory or neoplastic diseases affecting the duodenum: Nonspecific duodenal wall thickening may occur in inflammatory conditions of pancreas or gall bladder. In addition, adjacent neoplastic processes can involve duodenum, *e.g.*, pancreatic adenocarcinoma.

Duodenal dystrophy: This entity is associated with groove pancreatitis, a variant of chronic pancreatitis. It is characterised by the presence of multiple cystic lesions in the duodenal wall that is thickened because of chronic inflammation[12]. Barium findings are non-specific and demonstrate only stenosis of the involvement segment with or without irregularity of outline (Figure 11). Endoscopic ultrasound is the modality of choice. CT shows thickened duodenal wall between the duodenal lumen and pancreas. Cystic lesions are noted within the thickened wall.

SMA syndrome

SMA syndrome is a rare condition characterised by acute angulation of SMA leading to compression of the third part of the duodenum between the SMA and the aorta[13]. The basic etiological factor is loss of abdominal fat due to a variety of debilitating conditions. Upper GIT barium study shows extrinsic compression of the third part, dilatation of the proximal duodenum and a collapsed small bowel distal to the impression of SMA (Figure 12).

Neoplasms

Duodenal tumors account for about one-third of small bowel neoplasm. Overall small bowel tumors comprise only 5% of the gastrointestinal tumors. Benign tumors are rare. These include adenomatous polyp, lipoma and leiomyoma. Primary adenocarcinoma is the most common malignant lesion of the duodenum and is usually found in the periampullary region[14] (Figure 13). It presents as either a polypoidal mass causing filling defect or an irregular, annular constricting lesion with deformity of the lumen and mucosal irregularity. Rare malignant lesions include lymphoma (Figure 14) and malignant gastrointestinal stromal tumors.

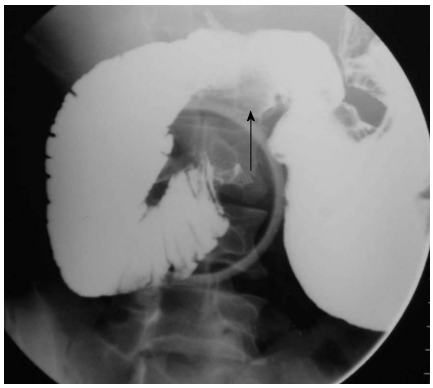

Figure 13 A mass is noted in relation to the medial aspect of the first and second part of the duodenum with ulceration (arrow). In addition stricture with mucosal irregularity is seen in distal third part of duodenum. Endoscopic biopsy revealed adenocarcinoma.

CONCLUSION

Duodenal pathologies are distinct from those in rest of the GIT. Upper gastrointestinal barium study comprises one of the initial methods of evaluation of duodenal pathologies. Though, not entirely specific for a particular pathological entity, barium studies do provide a fairly good idea about the underlying disease pattern and guide further management.

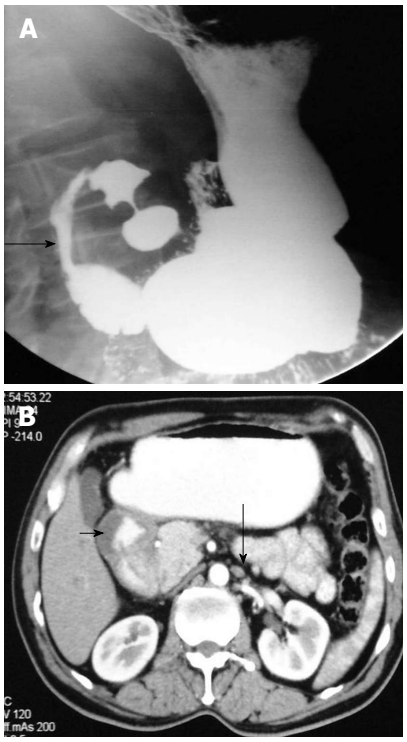

Figure 14 A long segment narrowing of the second part (arrow) of the duodenum is noted (A), axial computed tomography image (B) shows circumferential mural thickening of the duodenum (short arrow) with few paraaortic lymph nodes (long arrow). Endoscopic biopsy revealed a diagnosis of non-Hodgkin lymphoma.

REFERENCES

1 **Snyder WH**, Chaffin L. Embryology and pathology of the intestinal tract: presentation of 40 cases of malrotation. *Ann Surg* 1954; **140**: 368-379 [PMID: 13198074 DOI: 10.1097/00000658-195409000-00013]
2 **Maxson RT**, Franklin PA, Wagner CW. Malrotation in the older child: surgical management, treatment, and outcome. *Am Surg* 1995; **61**: 135-138 [PMID: 7856973]
3 **Berdon WE**. The diagnosis of malrotation and volvulus in the older child and adult: a trap for radiologists. *Pediatr Radiol* 1995; **25**: 101-103 [PMID: 7596651]
4 **Macpherson RI**. Gastrointestinal tract duplications: clinical, pathologic, etiologic, and radiologic considerations. *Radiographics* 1993; **13**: 1063-1080 [PMID: 8210590 DOI: 10.1148/radiographics.13.5.8210590]
5 **Fidler JL**, Saigh JA, Thompson JS, Habbe TG. Demonstration of intraluminal duodenal diverticulum by computed tomography. *Abdom Imaging* 1998; **23**: 38-39 [PMID: 9437060 DOI: 10.1007/s002619900281]
6 **Stone EE**, Brant WE, Smith GB. Computed tomography of duodenal diverticula. *J Comput Assist Tomogr* 1989; **13**: 61-63 [PMID: 2492039 DOI: 10.1097/00004728-198901000-00012]
7 **Talus H**, Roohipur R, Depaz H, Adu AK. Preduodenal portal vein causing duodenal obstruction in an adult. *J Am Coll Surg* 2006; **202**: 552-553 [PMID: 16500261 DOI: 10.1016/j.jamcollsurg.2005.08.022]
8 **Hwang JI**, Chiang JH, Yu C, Cheng HC, Chang CY, Mueller PR. Pictorial review: Radiological diagnosis of duodenal abnormalities. *Clin Radiol* 1998; **53**: 323-332 [PMID: 9630268 DOI: 10.1016/S0009-9260(98)80002-0]
9 **Gore RM**, Levine MS. Textbook of gastrointestinal radiology. 2nd ed. Philadelphia, PA: Saunders. 2000: 593-595
10 **Levine MS**, Creteur V, Kressel HY, Laufer I, Herlinger H. Benign gastric ulcers: diagnosis and follow-up with double-contrast radiography. *Radiology* 1987; **164**: 9-13 [PMID: 3588932 DOI: 10.1148/radiology.164.1.3588932]
11 **Nugent FW**, Richmond M, Park SK. Crohn's disease of the duodenum. *Gut* 1977; **18**: 115-120 [PMID: 856671 DOI: 10.1136/gut.18.2.115]
12 **Procacci C**, Graziani R, Zamboni G, Cavallini G, Pederzoli P, Guarise A, Bogina G, Biasiutti C, Carbognin G, Bergamo-Andreis IA, Pistolesi GF. Cystic dystrophy of the duodenal wall: radiologic findings. *Radiology* 1997; **205**: 741-747 [PMID: 9393530 DOI: 10.1148/radiology.205.3.9393530]
13 **Lippl F**, Hannig C, Weiss W, Allescher HD, Classen M, Kurjak M. Superior mesenteric artery syndrome: diagnosis and treatment from the gastroenterologist's view. *J Gastroenterol* 2002; **37**: 640-643 [PMID: 12203080 DOI: 10.1007/s005350200101]
14 **Kazerooni EA**, Quint LE, Francis IR. Duodenal neoplasms: predictive value of CT for determining malignancy and tumor resectability. *AJR Am J Roentgenol* 1992; **159**: 303-309 [PMID: 1632344 DOI: 10.2214/ajr.159.2.1632344]

P- Reviewer: El-Sayed M, Li YY, Maglinte DDT, Perju-Dumbrava D, Slomiany BL
S- Editor: Wen LL **L- Editor**: A **E- Editor**: Liu SQ

World Journal of Radiology

Submit a Manuscript: http://www.wjgnet.com/esps/
Help Desk: http://www.wjgnet.com/esps/helpdesk.aspx
DOI: 10.4329/wjr.v6.i8.619

World J Radiol 2014 August 28; 6(8): 619-624
ISSN 1949-8470 (online)

RETROSPECTIVE STUDY

Balloon test occlusion of internal carotid artery: Angiographic findings predictive of results

Kazufumi Kikuchi, Takashi Yoshiura, Akio Hiwatashi, Osamu Togao, Koji Yamashita, Hiroshi Honda

Kazufumi Kikuchi, Takashi Yoshiura, Akio Hiwatashi, Osamu Togao, Koji Yamashita, Hiroshi Honda, Department of Clinical Radiology, Graduate School of Medical Sciences, Kyushu University, Fukuoka 812-8582, Japan

Author contributions: All the authors were involved in designing the study and editing; Kikuchi K made substantial contributions to data analysis and interpretation, performed the statistical analysis, wrote the manuscript draft, and revised it critically according the suggestions of the other authors; Hiwatashi A, Togao O, Yamashita K and Honda H made substantial contributions to data analysis, interpretation, finding the pictures, and helped draft the manuscript; Yoshiura T made substantial contributions to the study conception and design, critically revised the manuscript draft for important intellectual content, and gave final approval of the version to be published; all the authors read and approved the final manuscript.

Supported by JSPS KAKENHI, No. 26461828

Correspondence to: Takashi Yoshiura, MD, PhD, Department of Clinical Radiology, Graduate School of Medical Sciences, Kyushu University, 3-1-1 Maidashi, Higashi-ku, Fukuoka 812-8582, Japan. tyoshiu@radiol.med.kyushu-u.ac.jp
Telephone: +81-92-6425695 Fax: +81-92-6425708

Received: April 28, 2014 Revised: June 24, 2014
Accepted: July 17, 2014
Published online: August 28, 2014

Abstract

AIM: To reveal angiographic findings to predict the result of balloon test occlusion (BTO).

METHODS: The cerebral angiograms of 42 consecutive patients who underwent cerebral angiography including both the Matas and Allcock maneuvers and BTO were retrospectively analyzed. Visualization of the anterior cerebral artery (ACA) and the middle cerebral artery (MCA) by the cross flow on the tested side during the Matas or Allcock maneuver was graded on a 5-point scale. Circle of Willis (COW) anatomy with respect to the presence/absence of a collateral path to reach the tested internal carotid artery (ICA) was classified into four categories. A univariate logistic analysis was used to analyze the associations between each angiographic finding and the BTO result. Sensitivity, specificity, accuracy, positive predictive value, and negative predictive value for each finding were calculated.

RESULTS: Five patients (12%) were BTO-positive and the remaining 37 patients (88%) were BTO-negative. Visualizations of the ACA and MCA as well as the COW anatomy were significantly associated with the BTO result ($P = 0.0051$ for ACA, $P = 0.0002$ for MCA, and $P < 0.0001$ for COW anatomy). In particular, good MCA visualization and the presence of an anterior connection (collateral path to the tested ICA from the contralateral ICA *via* the anterior communicating artery) in the COW were highly predictive for negative BTO (negative predictive value = 100% for both).

CONCLUSION: A BTO result may be predicted by angiographic findings including ACA/MCA visualization and COW anatomy.

Key words: Balloon test occlusion; Cross flow; Circle of Willis; Anterior circulation; Posterior circulation

Core tip: Balloon test occlusion (BTO) is widely performed to assess the ischemic tolerance among preoperative patients. It is safe and useful, however, it sometimes carries the risk of thrombosis, dissection and infarction. Our study revealed that visualizations of the anterior cerebral artery and middle cerebral artery (MCA) as well as the circle of Willis (COW) anatomy were significantly associated with the BTO result. In particular, good MCA visualization and/or the presence of an anterior connection [collateral path to the tested internal carotid artery (ICA) from the contralateral ICA *via* the anterior communicating artery] in the COW were highly predictive for negative BTO.

Kikuchi K, Yoshiura T, Hiwatashi A, Togao O, Yamashita K, Honda H. Balloon test occlusion of internal carotid artery: Angiographic findings predictive of results. *World J Radiol* 2014; 6(8): 619-624 Available from: URL: http://www.wjgnet.com/1949-8470/full/v6/i8/619.htm DOI: http://dx.doi.org/10.4329/wjr.v6.i8.619

INTRODUCTION

The treatment of skull base lesions such as tumors, aneurysms, and traumatic lesions may require internal carotid artery (ICA) sacrifice[1,2]. Pretherapeutic knowledge of carotid artery dependence is essential in these patients, since vascular bypass or alternative surgical approaches may be necessary in those unable to tolerate ICA sacrifice. Balloon test occlusion (BTO) is an angiographic test to evaluate ischemic tolerance after permanent occlusion of an ICA[1,2]. During BTO, the cerebral hemisphere ipsilateral to the tested ICA may be perfused by collateral blood flow, depending on the development of collateral pathways including the circle of Willis (COW). Although BTO is widely accepted, it sometimes carries the risk of thrombosis, dissection and infarction[2,3]. We hypothesized that the BTO results can be predicted by angiographic findings. Therefore the purpose of the present study was to test whether angiographic findings can be used to predict BTO results.

MATERIALS AND METHODS

Subjects

Kyushu University Institutional Review Board for Clinical Research approved this retrospective study. Between 1996 and 2011, BTO was performed in 77 patients at Kyushu University Hospital. Among them, those who underwent both the Matas maneuver (angiography of the non-tested ICA during manual carotid compression on the tested side) and the Allcock maneuver (angiography of the vertebral artery during manual carotid compression on the tested side) were selected. The cerebral angiograms of 42 consecutive patients (17 male and 25 female patients; mean age, 54.2 years; median, 57 years; range 25-70 years) were thus included in this retrospective analysis. Of the 42 BTO procedures, the right ICA was tested in 23 patients, and the left ICA was tested in 19 patients. The diagnosis at the time of treatment included 13 ICA aneurysms and 29 tumors (18 meningiomas, 3 schwannomas, 2 pituitary adenomas, 2 cervical lymph node metastatic tumors, 2 thyroid tumors, 1 chondrosarcoma and 1 hemangiopericytoma).

Angiographic procedure

A 5 Fr or 5.5 Fr femoral introducer was inserted in the right femoral artery to perform the cerebral angiography using a digital subtraction angiography (DSA) unit (DFP-200A; Toshiba Medical Systems, Tokyo, Japan and AXIOM Artis zee Biplane system; Siemens AG, Healthcare Sector, Forchheim, German) with a 5 Fr diagnostic catheter (TERUMO Clinical Supply, Gifu, Japan and Hanaco Medical, Tokyo). After the femoral punctures, 3000 IU of heparin was systematically administered intra-arterially by bolus, followed by an additional intra-arterial infusion of 1000 IU/h. For each patient, both Matas and Allcock maneuvers as well as a complete biplane DSA study including bilateral common and ICAs and vertebrobasilar system were performed. Angiogram of external carotid artery was added when necessary. A total of 8 to 10 mL of iodinate contrast [iopamidol 300 mgI/mL (Iopamiron™, Bayer, Osaka, Japan)] was injected at 4 to 5 mL/s for the ICA angiography, and 10 to 12 mL at 5 to 6 mL/s was used for the vertebral artery (VA) angiography.

BTO procedure

The cervical portion of the tested ICA was occluded up to 20 min using a 5 Fr balloon catheter (balloon size 8 mm; head hunter/BHW type, MOIYAN balloon catheter; Miyano Medical Corp., Kobe, Japan). The balloon was carefully inflated under fluoroscopic observation. Complete occlusion was confirmed by an angiogram through the balloon catheter. The patient then underwent a continuous neurologic evaluation throughout the examination. The neurologic evaluations were performed by clinical neurospecialists who maintained continuous verbal dialogues with the patient and were continuously evaluating the patient's muscle strength, sensation, cognition, and cranial nerve function during the testing period. Electroencephalographic (EEG) monitoring was performed in 36 patients. The balloon was immediately deflated when any neurologic deficit or EEG abnormality was detected. In such cases, the BTO was judged to be positive. The BTO was considered negative when the patient tolerated the 20-min occlusion.

Image evaluation

Two board-certified radiologists (Kazufumi Kikuchi and Osamu Togao) reviewed all angiographic images obtained during the Matas and Allcock maneuvers in a consensus reading, and they evaluated the visualization of the anterior cerebral artery (ACA) and the middle cerebral artery (MCA) on the tested side by the cross flow. Visualization of the ACA and the MCA was graded on a 5-point scale according to the established anatomical segment of each artery (A1-4 for the ACA and M1-4 for the MCA[4]). It was graded as A0/M0 when no visualization of each artery was noted. The best arterial visualization during the Matas and Allcock maneuver was chosen as the representative of each artery (ACA and MCA). Subsequently, the Grading was classified as either poor (Grades 0-2) or good (Grades 3-4). The same two board-certified radiologists evaluated the COW anatomy. The COW anatomy was classified into four types (Types 0-3) according to the presence/absence of an anterior connection (connection between the right and left ICAs *via* the anterior communicating artery) and the presence/absence of a posterior

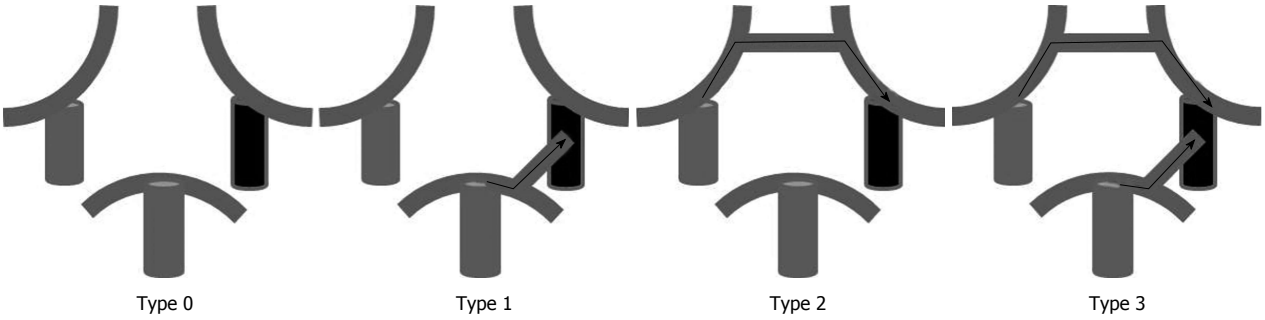

Figure 1 Classification of circle of Willis anatomy. Type 0: Neither an anterior connection nor a posterior connection is present; Type 1: Only a posterior connection is present; Type 2: Only an anterior connection is present; Type 3: Both anterior and posterior connections are present. Note the black vessel represents the tested internal carotid artery.

Table 1 Results of anterior cerebral artery visualization by cross flow and the balloon test occlusion outcome

ACA visualization		BTO-positive (%)	BTO-negative (%)	Total (%)
Poor	Grade 0	2 (5)	0 (0)	2 (5)
	Grade 1	0 (0)	0 (0)	0 (0)
	Grade 2	1 (2)	1 (2)	2 (5)
Good	Grade 3	0 (0)	5 (12)	5 (12)
	Grade 4	2 (5)	31 (74)	33 (78)
Total		5 (12)	37 (88)	42 (100)

Significant differences (P = 0.0051; 95%CI: 0.13-7.61) was seen between the ACA visualization and the BTO outcome. ACA: Anterior cerebral artery; BTO: Balloon test occlusion.

Table 2 Results of middle cerebral artery visualization by cross flow and the balloon test occlusion outcome

MCA visualization		BTO-positive (%)	BTO-negative (%)	Total (%)
Poor	Grade 0	3 (7)	1 (2)	4 (9)
	Grade 1	1 (2)	0 (0)	1 (2)
	Grade 2	1 (2)	3 (7)	4 (9)
Good	Grade 3	0 (0)	12 (29)	12 (29)
	Grade 4	0 (0)	21 (50)	21 (50)
Total		5 (12)	37 (88)	42 (100)

Significant differences (P = 0.0002; 95%CI: 0.07-14.19) was seen between the MCA visualization and the BTO outcome. MCA: Middle cerebral artery; BTO: Balloon test occlusion.

connection (connection between the tested ICA and basilar artery) (Figure 1). Subsequently, the COW anatomy was classified into poorly-developed (either Type 0 or 1) and well-developed (either Type 2 or 3).

Statistical analysis

We performed a univariate logistic analysis to determine the associations between each angiographic finding and the BTO result (positive *vs* negative). We calculated the sensitivity, specificity, accuracy, positive predictive value, and negative predictive value of ACA/MCA visualization by cross flow (poor *vs* good) and COW anatomy (poorly developed *vs* well-developed) for predicting the BTO result. For all analyses, $P < 0.05$ was considered significant.

RESULTS

Five patients (12%) were BTO-positive and the remaining 37 patients (88%) were BTO-negative. The BTO-induced abnormalities were hyposthenia (n = 3), aphasia (n = 3), loss of consciousness (n = 2), slow brain waves (n = 2) and facial paralysis (n = 1). In all patients, the neurological deficits disappeared immediately after balloon deflation.

Tables 1 and 2 summarize the visualization of the ACA and MCA, respectively. Among the four patients with poor ACA visualization, three (75%) were BTO-positive, whereas among the 38 cases with good ACA visualization, only two (5%) were BTO-positive (Table 1). Among the nine patients with poor MCA visualization, 5 (56%) were BTO-positive, whereas none (0%) of the 37 patients with good MCA visualization were BTO-positive. For both the ACA and the MCA, poor visualization by cross flow was significantly associated with a positive BTO result (P = 0.0051; 95%CI: 0.13-7.61 for ACA, P = 0.0002; 95%CI: 0.07-14.19 for MCA, respectively). Visualization of cross flow to the ACA (either poor or good) predicted BTO results with a sensitivity of 60.0%, a specificity of 97.3%, an accuracy of 92.9%, a positive predictive value (PPV) of 75.0%, and a negative predictive value (NPV) of 94.7%. Similarly, visualization of cross flow to the MCA showed a sensitivity of 100%, a specificity of 89.2%, an accuracy of 90.5%, a PPV of 55.6%, and an NPV of 100%.

Table 3 shows the comparison of COW anatomy and BTO results. Both (100%) of the two patients with Type 0 COW anatomy had a positive BTO outcome. Among the six patients with Type 1 anatomy, 3 (50%) were BTO-positive. Among the 34 patients with well-developed COW (either Type 2 or Type 3 anatomy), none (0%) was BTO-positive. The logistic analysis showed that poorly-developed COW was significantly associated with positive BTO result ($P < 0.0001$; 95%CI: 0.31-3.21).

When the COW anatomy was classified into poorly-developed and well-developed, the sensitivity, specificity, accuracy, PPV, and NPV were 100%, 91.9%, 92.9%, 62.5%, and 100%, respectively.

Figures 2 and 3 show representative patients with

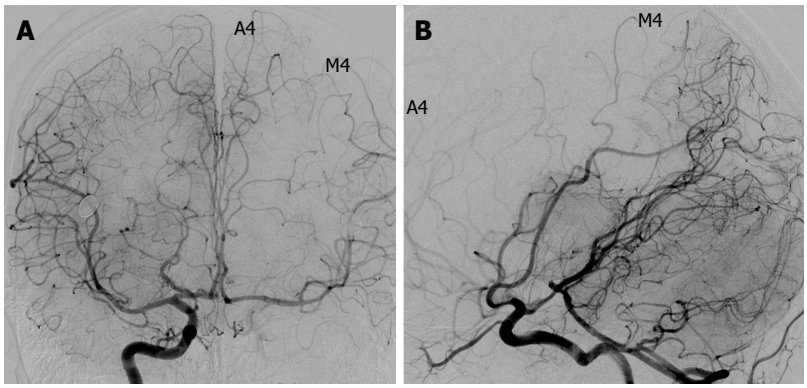

Figure 2 A 30-year-old patient with left skull base meningioma (Grade A4, M4; circle of Willis Type 3; balloon test occlusion negative). In the right internal carotid artery injection, both the anterior cerebral artery and the middle cerebral artery on the left are well visualized by a cross flow via the anterior communicating artery (A) and the posterior communicating artery (B).

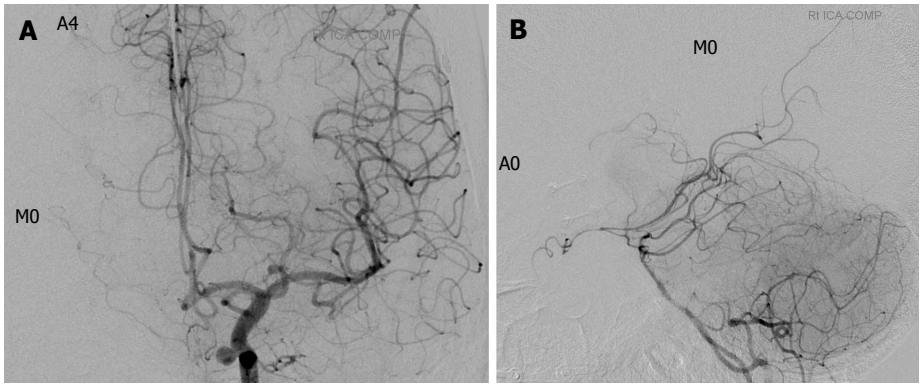

Figure 3 A 50-year-old patient with left skull base meningioma and an incidental left internal carotid artery aneurysm (Grade A4, M0; circle of Willis Type 1; balloon test occlusion negative). No cross flow is visualized in the right middle cerebral artery by either left internal carotid artery (ICA) (A) or vertebral artery (VA) (B) injection. The right anterior cerebral artery is well visualized by left ICA injection (A) but not by VA injection (B). This patient complained of right facial paralysis and aphasia 8 min after the balloon occlusion was inflated.

Table 3 Circle of Willis anatomy and the balloon test occlusion outcome

COW anatomy		BTO-positive (%)	BTO-negative (%)	Total (%)
Poorly-developed	Type 0	2 (5)	0 (0)	2 (5)
	Type 1	3 (7)	3 (7)	6 (14)
Well-developed	Type 2	0 (0)	4 (10)	4 (10)
	Type 3	0 (0)	30 (71)	30 (71)
Total		5 (12)	37 (88)	42 (100)

Significant differences ($P < 0.0001$; 95%CI: 0.31-3.21) was seen between the COW anatomy and the BTO outcome. COW: Circle of Willis; BTO: Balloon test occlusion.

negative and positive BTO, respectively.

DISCUSSION

Therapeutic occlusion of the ICA remains an important procedure[5-11]. In such cases, temporary BTO is imperative to evaluate ischemic risks before complete blockage is performed[11-14]. The introduction of clinical BTO of the ICA was associated with significant reduction in post-occlusion morbidity; a review of the literature comprising 516 patients demonstrated that the use of BTO of the ICA reduced the morbidity of permanent ICA occlusion from 26% to 13%[15]. However, complications due to BTO have been reported, and the incidence of neurological deficits during BTO ranges from 3.2% (3) to 3.7% (2). The risk of complication would rise when the wall of the ICA is under a pathological condition such as severe atheromatous disease[16] or vulnerability due to Ehlers-Danlos syndrome[17].

Our present results demonstrate that for both the ACA and the MCA, poor visualization by cross flow was significantly associated with a positive BTO result. In particular, MCA visualization showed a high sensitivity (100%) and NPV (100%). Poor development of the COW was significantly associated with a positive BTO result. Similarly to MCA visualization, COW anatomy showed a high sensitivity (100%) and NPV (100%). Both of the two patients with Type 0 COW anatomy were BTO-positive. Among the patients with Type 1 anatomy (only a posterior connection is present), 50% (3/6) were BTO-positive, whereas none of those with Type 2 (only an anterior connection is present) anatomy (0/4) were BTO-positive. This finding indicates that the anterior circulation has a greater effect on the risk of ischemic compared to the posterior circulation, as indicated in other

studies[18-21].

Our results showed that good MCA cross-flow visualization and well-developed COW anatomy (*i.e.*, the presence of the anterior connection) were highly predictive of a negative BTO result. In this study, angiographic findings during the Matas and Allcock maneuvers were evaluated. However, it is apparent that the predictive value of these two findings (good MCA cross-flow visualization and well-developed COW anatomy) would be applicable to angiograms obtained without carotid compression. When either of these two predictive findings is present, avoidance of BTO may be considered, especially in patients at a high risk for complications associated with BTO. Conversely, poor visualization of ACA/MCA and poorly-developed COW anatomy were frequently associated with a positive BTO result (Tables 1-3). BTO should be performed carefully in patients with those angiographic findings.

This study has several limitations. First, the number of patients is limited. Moreover, due to the retrospective nature, patient selection biases may be present. There may be technical variability in manual carotid compression. Incomplete compression might have resulted in poor cross flow visualization. We compared the angiographic findings with BTO results, but not directly with ischemic events following permanent ICA occlusion. In the majority of our patients, subsequent permanent occlusion was not performed. Neurological evaluation and EEG monitoring were used to detect ischemia during the BTO. We did not use perfusion imaging techniques during the BTO, which would provide precise information about localized ischemia that may not be detected by neurological assessment.

In conclusion, angiographic findings during Matas and Allcock maneuvers including the ACA/MCA visualization by cross flow and the COW anatomy were significantly correlated with the BTO result. Good visualization of the MCA by cross flow and the presence of the anterior connection in the COW are predictive for negative BTO.

COMMENTS

Background

Balloon test occlusion (BTO) is an angiographic test to evaluate ischemic tolerance after permanent occlusion of an internal carotid artery (ICA). BTO is widely accepted, it sometimes carries the risk of thrombosis, dissection and infarction. The authors hypothesized that the BTO results can be predicted by angiographic findings.

Research frontiers

The data revealed that visualizations of the anterior cerebral artery (ACA) and middle cerebral artery (MCA) as well as the circle of Willis (COW) anatomy were significantly associated with the BTO result. In particular, good MCA visualization and the presence of an anterior connection (collateral path to the tested ICA from the contralateral ICA *via* the anterior communicating artery) in the COW were highly predictive for negative BTO.

Innovations and breakthroughs

This study represents a BTO result may be predicted by angiographic findings including ACA/MCA visualization and COW anatomy.

Applications

The results may be useful for avoiding the risk of complication when the wall of the ICA is under a pathological condition such as severe atheromatous disease or vulnerability due to Ehlers-Danlos syndrome.

Peer review

The authors have performed a good study, the manuscript is interesting.

REFERENCES

1 **Erba SM**, Horton JA, Latchaw RE, Yonas H, Sekhar L, Schramm V, Pentheny S. Balloon test occlusion of the internal carotid artery with stable xenon/CT cerebral blood flow imaging. *AJNR Am J Neuroradiol* 1988; **9**: 533-538 [PMID: 3132827]

2 **Tarr RW**, Jungreis CA, Horton JA, Pentheny S, Sekhar LN, Sen C, Janecka IP, Yonas H. Complications of preoperative balloon test occlusion of the internal carotid arteries: experience in 300 cases. *Skull Base Surg* 1991; **1**: 240-244 [PMID: 17170842 DOI: 10.1055/s-2008-1057104]

3 **Mathis JM**, Barr JD, Jungreis CA, Yonas H, Sekhar LN, Vincent D, Pentheny SL, Horton JA. Temporary balloon test occlusion of the internal carotid artery: experience in 500 cases. *AJNR Am J Neuroradiol* 1995; **16**: 749-754 [PMID: 7611033]

4 **Osborn AG**. Diagnostic cerebral angiography. Lippincott Williams & Wilkins, 1998

5 **Adams GL**, Madison M, Remley K, Gapany M. Preoperative permanent balloon occlusion of internal carotid artery in patients with advanced head and neck squamous cell carcinoma. *Laryngoscope* 1999; **109**: 460-466 [PMID: 10089976 DOI: 10.1097/00005537-199903000-00022]

6 **Nayak UK**, Donald PJ, Stevens D. Internal carotid artery resection for invasion of malignant tumors. *Arch Otolaryngol Head Neck Surg* 1995; **121**: 1029-1033 [PMID: 7646855 DOI: 10.1001/archotol.1995.01890090067013]

7 **Sanna M**, Piazza P, Ditrapani G, Agarwal M. Management of the internal carotid artery in tumors of the lateral skull base: preoperative permanent balloon occlusion without reconstruction. *Otol Neurotol* 2004; **25**: 998-1005 [PMID: 15547433 DOI: 10.1097/00129492-200411000-00023]

8 **Larson JJ**, Tew JM, Tomsick TA, van Loveren HR. Treatment of aneurysms of the internal carotid artery by intravascular balloon occlusion: long-term follow-up of 58 patients. *Neurosurgery* 1995; **36**: 26-30; discussion 30 [PMID: 7708164 DOI: 10.1227/00006123-199501000-00002]

9 **Fox AJ**, Viñuela F, Pelz DM, Peerless SJ, Ferguson GG, Drake CG, Debrun G. Use of detachable balloons for proximal artery occlusion in the treatment of unclippable cerebral aneurysms. *J Neurosurg* 1987; **66**: 40-46 [PMID: 3783258 DOI: 10.3171/jns.1987.66.1.0040]

10 **Field M**, Jungreis CA, Chengelis N, Kromer H, Kirby L, Yonas H. Symptomatic cavernous sinus aneurysms: management and outcome after carotid occlusion and selective cerebral revascularization. *AJNR Am J Neuroradiol* 2003; **24**: 1200-1207 [PMID: 12812955]

11 **Lubicz B**, Gauvrit JY, Leclerc X, Lejeune JP, Pruvo JP. Giant aneurysms of the internal carotid artery: endovascular treatment and long-term follow-up. *Neuroradiology* 2003; **45**: 650-655 [PMID: 12923666 DOI: 10.1007/s00234-003-1047-4]

12 **Brunberg JA**, Frey KA, Horton JA, Deveikis JP, Ross DA, Koeppe RA. [15O]H2O positron emission tomography determination of cerebral blood flow during balloon test occlusion of the internal carotid artery. *AJNR Am J Neuroradiol* 1994; **15**: 725-732 [PMID: 8010276]

13 **Michel E**, Liu H, Remley KB, Martin AJ, Madison MT, Kucharczyk J, Truwit CL. Perfusion MR neuroimaging in patients undergoing balloon test occlusion of the internal carotid artery. *AJNR Am J Neuroradiol* 2001; **22**: 1590-1596 [PMID: 11559513]

14 **van der Schaaf IC**, Brilstra EH, Buskens E, Rinkel GJ. Endovascular treatment of aneurysms in the cavernous sinus: a systematic review on balloon occlusion of the parent vessel and embolization with coils. *Stroke* 2002; **33**: 313-318 [PMID:

11779933 DOI: 10.1161/hs0102.101479]
15 **Linskey ME**, Jungreis CA, Yonas H, Hirsch WL, Sekhar LN, Horton JA, Janosky JE. Stroke risk after abrupt internal carotid artery sacrifice: accuracy of preoperative assessment with balloon test occlusion and stable xenon-enhanced CT. *AJNR Am J Neuroradiol* 1994; **15**: 829-843 [PMID: 8059649]
16 **Hankey GJ**, Warlow CP, Sellar RJ. Cerebral angiographic risk in mild cerebrovascular disease. *Stroke* 1990; **21**: 209-222 [PMID: 2406993 DOI: 10.1161/01.str.21.2.209]
17 **North KN**, Whiteman DA, Pepin MG, Byers PH. Cerebrovascular complications in Ehlers-Danlos syndrome type IV. *Ann Neurol* 1995; **38**: 960-964 [PMID: 8526472 DOI: 10.1002/ana.410380620]
18 **Mount LA**, Taveras JM. Arteriographic demonstration of the collateral circulation of the cerebral hemispheres. *AMA Arch Neurol Psychiatry* 1957; **78**: 235-253 [PMID: 13457498 DOI: 10.1001/archneurpsyc.1957.02330390017003]
19 **Kluytmans M**, van der Grond J, van Everdingen KJ, Klijn CJ, Kappelle LJ, Viergever MA. Cerebral hemodynamics in relation to patterns of collateral flow. *Stroke* 1999; **30**: 1432-1439 [PMID: 10390319 DOI: 10.1161/01.str.30.7.1432]
20 **Doblar DD**, Plyushcheva NV, Jordan W, McDowell H. Predicting the effect of carotid artery occlusion during carotid endarterectomy: comparing transcranial doppler measurements and cerebral angiography. *Stroke* 1998; **29**: 2038-2042 [PMID: 9756578 DOI: 10.1161/01.str.29.10.2038]
21 **Liebeskind DS**, Flint AC, Budzik RF, Xiang B, Smith WS, Duckwiler GR, Nogueira RG; for the MERCI and Multi-MERCI Investigators. Carotid I's, L's and T's: collaterals shape the outcome of intracranial carotid occlusion in acute ischemic stroke. *J Neurointerv Surg* 2014; Epub ahead of print [PMID: 24789707 DOI: 10.1136/neurintsurg-2014-011231]

P- Reviewer: Kettering K, Paraskevas KI **S- Editor**: Ji FF
L- Editor: A **E- Editor**: Liu SQ

World Journal of Radiology

Submit a Manuscript: http://www.wjgnet.com/esps/
Help Desk: http://www.wjgnet.com/esps/helpdesk.aspx
DOI: 10.4329/wjr.v6.i8.625

World J Radiol 2014 August 28; 6(8): 625-628
ISSN 1949-8470 (online)

CASE REPORT

Characterization of ureteral stents by dual-energy computed tomography: Clinical implications

El-Sayed H Ibrahim, William E Haley, Maria A Jepperson, Michael J Wehle, Joseph G Cernigliaro

El-Sayed H Ibrahim, William E Haley, Division of Nephrology and Hypertension, Mayo Clinic, Jacksonville, FL 32224, United States
Maria A Jepperson, Joseph G Cernigliaro, Department of Radiology, Mayo Clinic, Jacksonville, FL 32224, United States
Michael J Wehle, Department of Urology, Mayo Clinic, Jacksonville, FL 32224, United States
Author contributions: Ibrahim EH contributed with image reconstruction, data analysis, and manuscript writing; Haley WE contributed with study design, results interpretation, and manuscript writing; Jepperson MA contributed with data analysis; Wehle MJ contributed with results interpretation; Cernigliaro JG contributed with study design and results interpretation.
Correspondence to: El-Sayed H Ibrahim, MD, Division of Nephrology and Hypertension, Mayo Clinic, Jacksonville, FL 32224, United States. ibrahim.elsayed@mayo.edu
Telephone: +1-904-9536037 Fax: +1-904-9536581
Received: February 12, 2014 Revised: April 3, 2014
Accepted: July 12, 2014
Published online: August 28, 2014

Abstract

Dual-energy computed-tomography (DECT) has been suggested as the method of choice for imaging urinary calculi due to the modality's high sensitivity for detecting stones and its capability of accurately differentiating between uric-acid (UA) and non-UA (predominantly calcium) stones. The clinical significance of the latter feature relates to the differences in management of UA *vs* non-UA calculi. Like calculi, ureteral stents are assigned color by the dual-energy post-processing algorithm, which may lead to improved or worsened stone visualization based on the resulting stent/stone contrast. Herein we depict the case of a nephrolithiasis patient with bilateral stents, each with different color, clearly displaying the effect of stent color on stone visualization. Further, three-dimensional reconstruction of the DECT images illustrates advantages of this enhancement compared to conventional two-dimensional computed tomography. The resulting stent/stone contrast produces an unanticipated potential advantage of DECT in patients with urolithiasis and stents and may promote improved management decision-making.

Key words: Ureteral stent; Dual-energy computed-tomography; Dual-energy computed-tomography; Kidney stones; Nephrolithiasis

Core tip: Dual-energy computed-tomography is a recently introduced technique for imaging kidney stones. Ureteral stents are also characterized by the dual-energy (DE) algorithm and, like calculi, are assigned color. The resulting stent/stone color contrast may lead to either improved or worsened stone visualization in patients with urolithiasis and stents. This case report illustrates different DE characterization of stents based on their type, and the resulting effects on stent/stone contrast. The awareness of the DE characterization of different stent types allows for stent selection that improves stone visualization.

Ibrahim EH, Haley WE, Jepperson MA, Wehle MJ, Cernigliaro JG. Characterization of ureteral stents by dual-energy computed tomography: Clinical implications. *World J Radiol* 2014; 6(8): 625-628 Available from: URL: http://www.wjgnet.com/1949-8470/full/v6/i8/625.htm DOI: http://dx.doi.org/10.4329/wjr.v6.i8.625

INTRODUCTION

Dual-energy computed-tomography (DECT) is a recently introduced technique for imaging urinary calculi. This technology utilizes the material change in attenuation between two peak X-ray energies to create color-coded material-specific images; in the case of urinary calculi, it is capable of distinguishing uric acid (UA) from non-UA

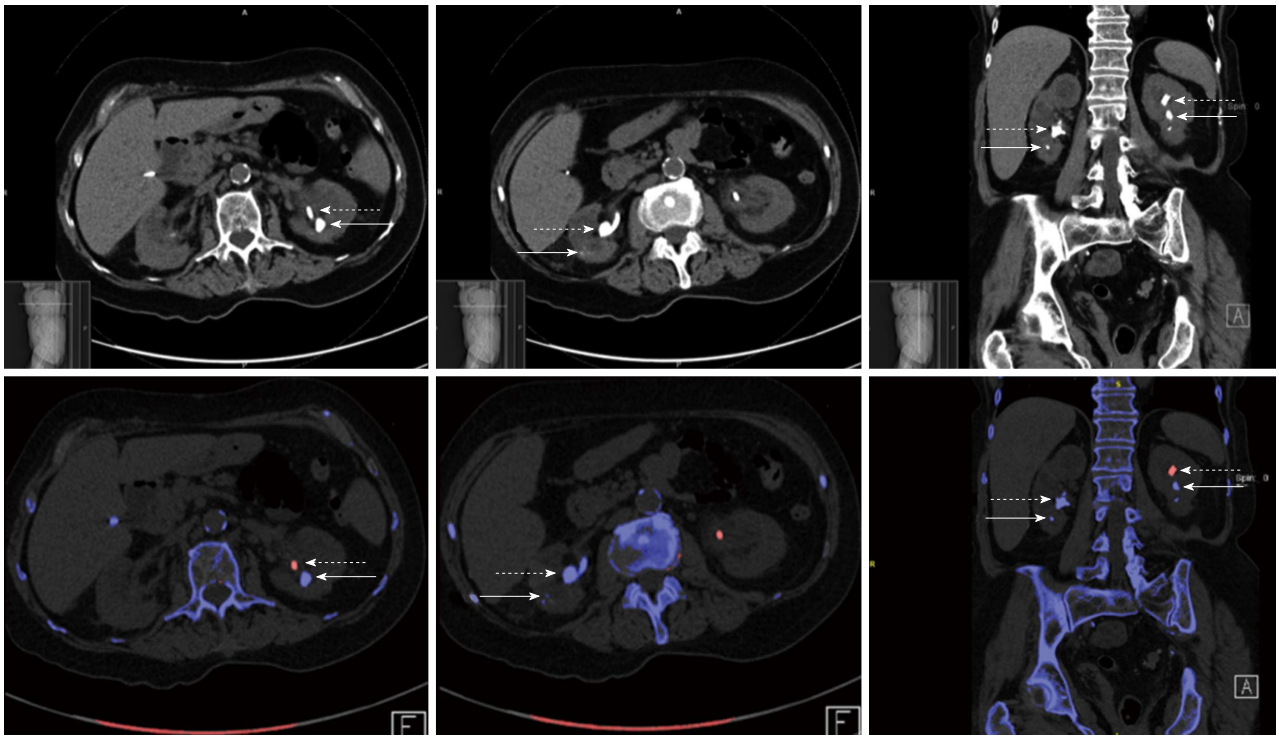

Figure 1 Conventional and dual-energy computed tomography images of kidney stones and ureteral stents. Conventional computed tomography (top) and dual-energy computed-tomography (DECT, bottom) images showing the advantage of DECT for stone visualization and identification of composition. The solid and dashed arrows point to stones and stents, respectively. The different stent and stone colors in the left kidney enhanced stone visualization, while the visualization of the stone in the right kidney is compromised because it has the same color as the stent. The small cubes in the bottom show the view orientation in the 3D [Anterior (A); and Foot (F)].

stones[1-3]. Prior to the introduction of this technology, urinary stone composition could not be reliably determined except by attaining stone material for analysis[4,5]. The clinical significance of pre-intervention determination of stone composition lies in the fact that medical dissolution therapy may be helpful in the case of UA calculi, and may obviate the need for surgical procedures that are often required for treatment of non-UA calculi[6,7].

In cases of ureteral obstruction or procedures involving the ureter, stent placement is commonly required. Ureteral stents are also characterized by the dual-energy (DE) algorithm; those with similar attenuation change as UA stones are assigned one color (*e.g.*, red) while those with change in attenuation similar to non-UA stones are assigned another color (*e.g.*, blue). We have previously reported a list of the DE characteristics of commonly-used ureteral stents[8]. The resulting potential for stent/stone color contrast creates an unanticipated advantage of DECT in patients with urolithiasis and stents. The stent/stone contrast may either lead to enhanced (the stent and stone have different colors) or camouflaged (both stent and stone have the same color) stone visualization. In this report, we present, to our knowledge for the first time, an interesting case of a patient with bilateral stents characterized by DECT with different colors, for whom DECT helped identify the calculi and stone composition.

CASE REPORT

The protocol for conducting this study was approved by the Mayo Clinic institutional review board. A 78-year-old female presented with bilateral ureteral stents following ureteroscopic removal of obstructing left-side ureteral calculus, and prior stenting on right-side for obstructing renal pelvis calculus (left-side stent: Boston-Scientific; right-side stent: Cook-Amplatz). The images were acquired on a Definition-Flash Siemens computed tomography (CT) scanner in dual-energy mode. The DECT peak tube potentials (kVp) were set to 80 kV and 140 kV, and the scan was conducted using a dedicated renal stone imaging protocol. Continuous non-contrast images were obtained from the level of the diaphragms to the pubic symphysis. The data was reconstructed on a workstation provided by the manufacturer using the Syngo software (VE 36A). Axial and coronal reconstructions were made using a mixed (low and high kVp) dataset with 5 mm slice-thickness/2.5 mm slice-interval (axial) and 3 mm slice-thickness/2.5 mm slice-interval (coronal). Material-specific image reconstructions in the axial- and coronal-planes were made at 1 mm slice-thickness/0.8 mm slice-interval and D30f convolution kernel. The DE post-processing algorithm assigns color based on the ratio of X-ray attenuations from the two tube potentials using a 3-material (UA, calcium, urine) decomposition algorithm. The capability of DECT to characterize (and color code) the stones and stents is appreciated when conventional CT images are compared to the DECT characterized images, as shown in Figure 1. Note also the limitation of the two-dimensional images in Figure 1 as they show only parts of the stents and stones that lie inside the imaging

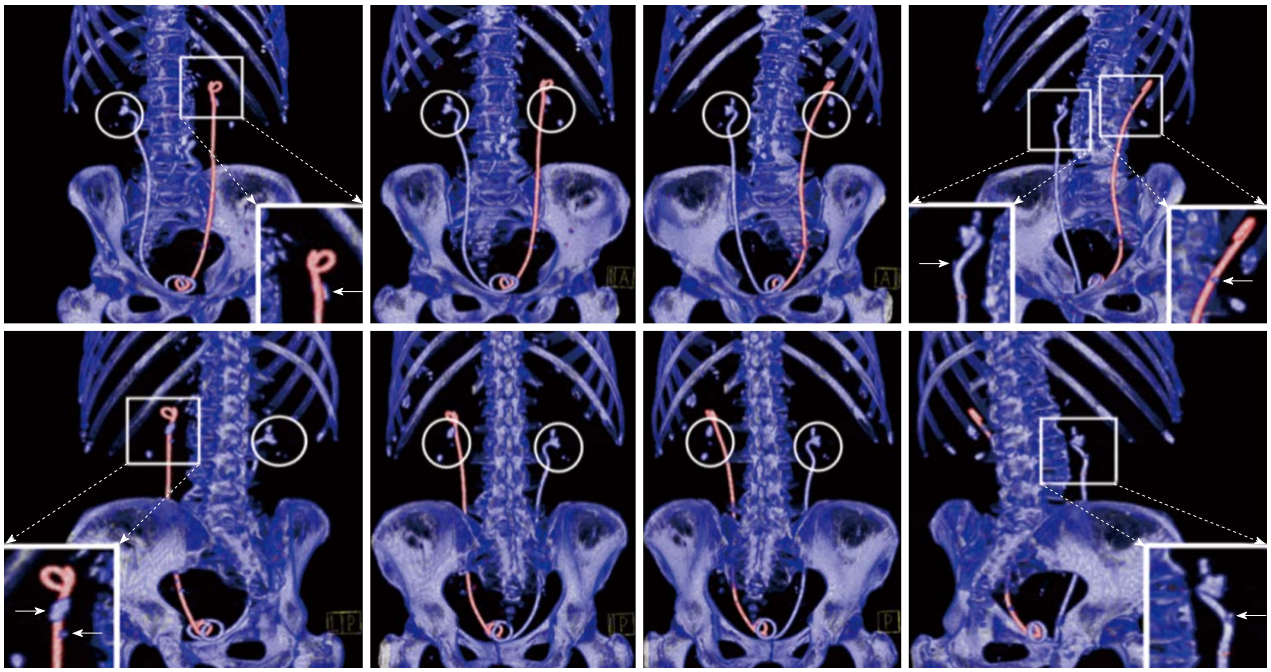

Figure 2 Three-dimensional reconstruction of dual-energy computed tomography images of kidney stones and different types of ureteral stents. Different views of the stent/stone boundary from three-dimensional reconstruction of the dual-energy computed-tomography images. The left and right stents appear red and blue, respectively, while all stones appear blue due to their non-uric-acid composition. The different colors of the stent and stone in the left kidney allow for better stone visualization (arrows) than in the right kidney where both the stent and stone have the same color. [Anterior (A)-Posterior (P); and Left (L)]

plane; this is better resolved by three-dimensional image reconstruction as shown in Figure 2.

The scan revealed a 1 cm calculus in the posterior interpolar region of the left kidney and a 9 mm calculus in the left anterior lower pole calyx, as well as several non-obstructing calculi bilaterally. The dual-energy characterization showed all calculi to be of non-UA composition (blue color), while the left and right stents appeared red and blue, respectively. While the images showed excellent stent/calculus color contrast in the left kidney (stent appears red and calculi appear blue), there was virtually no observed color contrasting in the right kidney (both stent and calculi appear blue). The effect of the stent/stone contrast on calculus visualization is appreciated when the images are viewed from different angles as illustrated in the three-dimensional reconstructed images in Figure 2, where calculus in the right kidney is totally camouflaged by the stent when viewed from certain angles.

DISCUSSION

DECT scanners acquire data simultaneously from two X-ray tubes (operating at different potentials) and detector arrays that are mounted near perpendicular angles[1,2]. DECT is advantageous compared to conventional CT for nephrolithiasis imaging due to the modality's additional capability of characterizing the stone composition a priori and without increasing radiation dose, which allows for optimizing the treatment decision-making (DECT is nearly 100% accurate for distinguishing UA from non-UA stones > 3 mm)[4-6]. Nevertheless, the situation is more complicated in patients requiring stents, as they appear colored in the resulting images based on their individual DE characterization[8]. Herein, we depict an interesting and illustrative case with bilateral stents that were assigned different colors in the resulting DECT images (Boston Scientific stent left ureter and Cook-Amplatz stent right ureter). Stent coloring may be an advantage when the stent and calculus are assigned different colors, as the stone is better recognized with better appreciation of its size and shape. On the other hand, the situation may be worsened when both stent and stone are assigned the same color, as the stent may conceal or camouflage the stone and/or its boundary. In the latter case, premature stent removal in the presence of potential obstructing stone fragments could follow. Accordingly, awareness of the DE characterization of different stent types allows for appropriate stent selection in patients with known stone composition. The potential for stent/stone color contrast connotes a possible advantage of DECT in patients with urolithiasis requiring a stent and may thereby promote improved management decision-making.

COMMENTS

Case characteristics

A 78-year-old kidney stone female patient with bilateral ureteral stents.

Clinical diagnosis

Nephrolithiasis with dysuria, hematuria, and bilateral flank pain.

Differential diagnosis

Acute kidney injury with bilateral obstructing stones requiring bilateral stents.

Laboratory diagnosis

Lab results showed serum creatine of 2.8 mg/dL; urine culture: > 100000 cfu/mL *Escherichia coli*; urinalysis: > 182 wbc/hpf, > 182 rbc/hpf, pH 5.5, 2+

protein.

Imaging diagnosis

Bilateral moderate hydronephrosis and hydroureter and multiple large renal calculi bilaterally: large right renal pelvic stone 2 cm × 1.6 cm × 1.2 cm with dilated calyces distally; 7 mm ureteral calculus mid/distal left ureter.

Pathological diagnosis

Stone analysis by infrared spectroscopy revealed stone composition of 90%/10% of calcium oxalate monohydrate/calcium phosphate (apatite).

Treatment

The patient underwent ureteroscopic removal of obstructing left-side ureteral calculus with stent placement as well as stent placement on the right side for obstructing renal pelvis calculus.

Related reports

Dual-energy computed-tomography (DECT) is capable of distinguishing uric acid (UA) from non-UA stones; moreover, a recent report provided dual-energy characteristics of commonly used ureteral stents.

Term explanation

DECT is a recently introduced technique for imaging urinary calculi, whereby the material change in attenuation between two peak X-ray energies is used to create color-coded material-specific images.

Experiences and lessons

This case report shows the potential advantage of DECT in patients with urolithiasis requiring a stent, where selection of the stent type based on its dual-energy characteristics improves the resulting stent/stone color contrast for better management decision-making.

Peer review

This report shows the capability of DECT to distinguish kidney stones by color-coding the stones and ureteral stents as compared to conventional computed tomography. This technology is novel and useful in determining the stone type, a distinction that is important for determining the optimal treatment strategy.

REFERENCES

1 **Matlaga BR**, Kawamoto S, Fishman E. Dual source computed tomography: a novel technique to determine stone composition. *Urology* 2008; **72**: 1164-1168 [PMID: 18619656 DOI: 10.1016/j.urology.2008.03.051]

2 **Hartman R**, Kawashima A, Takahashi N, Silva A, Vrtiska T, Leng S, Fletcher J, McCollough C. Applications of dual-energy CT in urologic imaging: an update. *Radiol Clin North Am* 2012; **50**: 191-205, v [PMID: 22498438 DOI: 10.1016/j.rcl.2012.02.007]

3 **Boll DT**, Patil NA, Paulson EK, Merkle EM, Simmons WN, Pierre SA, Preminger GM. Renal stone assessment with dual-energy multidetector CT and advanced postprocessing techniques: improved characterization of renal stone composition--pilot study. *Radiology* 2009; **250**: 813-820 [PMID: 19244048 DOI: 10.1148/radiol.2503080545]

4 **Kulkarni NM**, Eisner BH, Pinho DF, Joshi MC, Kambadakone AR, Sahani DV. Determination of renal stone composition in phantom and patients using single-source dual-energy computed tomography. *J Comput Assist Tomogr* 2013; **37**: 37-45 [PMID: 23321831 DOI: 10.1097/RCT.0b013e3182720f66]

5 **Ascenti G**, Siragusa C, Racchiusa S, Ielo I, Privitera G, Midili F, Mazziotti S. Stone-targeted dual-energy CT: a new diagnostic approach to urinary calculosis. *AJR Am J Roentgenol* 2010; **195**: 953-958 [PMID: 20858824 DOI: 10.2214/AJR.09.3635]

6 **Stolzmann P**, Kozomara M, Chuck N, Müntener M, Leschka S, Scheffel H, Alkadhi H. In vivo identification of uric acid stones with dual-energy CT: diagnostic performance evaluation in patients. *Abdom Imaging* 2010; **35**: 629-635 [PMID: 19727931 DOI: 10.1007/s00261-009-9569-9]

7 **Primak AN**, Fletcher JG, Vrtiska TJ, Dzyubak OP, Lieske JC, Jackson ME, Williams JC, McCollough CH. Noninvasive differentiation of uric acid versus non-uric acid kidney stones using dual-energy CT. *Acad Radiol* 2007; **14**: 1441-1447 [PMID: 18035274]

8 **Jepperson MA**, Thiel DD, Cernigliaro JG, Broderick GA, Parker AS, Haley WE. Determination of ureter stent appearance on dual-energy computed tomography scan. *Urology* 2012; **80**: 986-989 [PMID: 22921702 DOI: 10.1016/j.urology.2012.07.005]

P- Reviewer: Sakhaee K **S- Editor**: Wen LL
L- Editor: A **E- Editor**: Liu SQ

World Journal of Radiology

Submit a Manuscript: http://www.wjgnet.com/esps/
Help Desk: http://www.wjgnet.com/esps/helpdesk.aspx
DOI: 10.4329/wjr.v6.i8.629

World J Radiol 2014 August 28; 6(8): 629-635
ISSN 1949-8470 (online)

CASE REPORT

Percutaneous thrombin embolization of a pancreatico-duodenal artery pseudoaneurysm after failing of the endovascular treatment

Giulio Barbiero, Michele Battistel, Ana Susac, Diego Miotto

Giulio Barbiero, Michele Battistel, Ana Susac, Diego Miotto, University Radiology, Department of Medicine, University Hospital of Padua, 35128 Padova, Italy
Author contributions: Barbiero G, Battistel M and Susac A performed the case report; Barbiero G and Susac A wrote the manuscript; Miotto D did the supervision.
Correspondence to: Giulio Barbiero, MD, University Radiology, Department of Medicine, University Hospital of Padua, 2 Via Giustiniani, 35128 Padova, Italy. giuliobarbiero@katamail.com
Telephone: +39-049-8212366 Fax: +39-049-8218172
Received: April 8, 2014 Revised: May 24, 2014
Accepted: June 18, 2014
Published online: August 28, 2014

Abstract

Pancreatico-duodenal artery (PDA) pseudoaneurysms are rare vascular conditions with high mortality rates after rupture and they are frequently secondary to pancreatitis, surgery, trauma or infection. Due to the high risk of rupture and bleeding, it is mandatory to treat all pseudoaneurysms, regardless of their size or symptomatology. First option of treatment is open surgical repair, but it has high mortality rate, especially in hemodynamically unstable patients. In the recent years, percutaneous ultrasonography (US)- or computed tomography-guided thrombin injection was proposed as an alternative method for treating visceral aneurysms and pseudoaneurysms, but few reports described this therapy in case of peri-pancreatic pseudoaneurysms. We present a rare case of pseudoaneurysm of the PDA in a patient with no previous history of pancreatitis nor major surgery but with an occlusive lesion of the celiac axis. To the best of our knowledge this is the first reported case of PDA pseudoaneurysm successfully treated in emergency by single transabdominal US-guided injection of thrombin after failed attempts of percutaneous catheterization of the feeding vessel of the pseudoaneurysm.

Key words: Pancreatico-duodenal artery; Pseudoaneurysm embolization; Percutaneous thrombin injection; Endovascular treatment; Arterial intervention

Core tip: We present a rare case of pseudoaneurysm of the pancreatico-duodenal artery (PDA) in a patient with no risk factors but with an occlusive lesion of the celiac axis. To the best of our knowledge this is the first reported case of PDA pseudoaneurysm successfully treated in emergency by single transabdominal ultrasonography-guided injection of thrombin after failed attempts of percutaneous catheterization of the feeding vessel of the pseudoaneurysm.

Barbiero G, Battistel M, Susac A, Miotto D. Percutaneous thrombin embolization of a pancreatico-duodenal artery pseudoaneurysm after failing of the endovascular treatment. *World J Radiol* 2014; 6(8): 629-635 Available from: URL: http://www.wjgnet.com/1949-8470/full/v6/i8/629.htm DOI: http://dx.doi.org/10.4329/wjr.v6.i8.629

INTRODUCTION

Pancreatico-duodenal artery (PDA) pseudoaneurysms are potentially life-threatening but rare vascular conditions, accounting for 2% of splanchnic artery aneurysms and with mortality rates after rupture of 15%-50%[1-4].

They are mostly due to pancreatitis, surgery, trauma, infection, iatrogenic lesions, vasculitis and atherosclerosis[5], but also to the presence of a celiac axis or common haepatic artery stenosis/occlusion, known as Sutton-Kadir syndrome[6,7]. These lesions may be identified by means of different imaging techniques [ultrasonography (US), computed tomography (CT), magnetic resonance

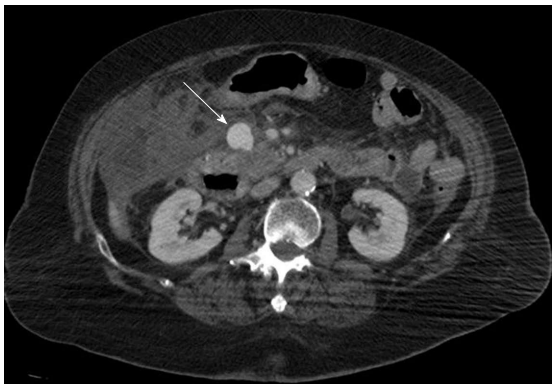

Figure 1 Axial contrast-enhanced computed tomography showing pancreatico-duodenal artery pseudoaneurysm (arrow) before the treatment.

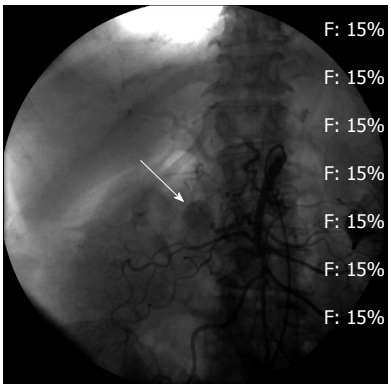

Figure 2 Selective superior mesenteric artery catheterization showing pancreatico-duodenal artery pseudoaneurysm (arrow) but the feeding vessel could not be identified.

imaging (MRI) and digital subtraction angiography (DSA)].

Due to the high risk of rupture and bleeding and the absence of predictive factors, it is recommended to treat all pseudoaneurysms, regardless of their size or symptomatology[8]. Open surgical repair, consisting of resection, ligation, exclusion, bypass or endo/organ resection, has high-mortality rate and is applied in hemodynamically unstable patients or as secondary approach after failed transcatheter embolization[9].

In the recent years, with the development of materials and techniques in the field of interventional radiology, percutaneous endovascular management of such a pseudoaneurysm is becoming the first-line treatment, with low morbidity and mortality[10,11].

Percutaneous US- or CT-guided injection is an alternative method for treating visceral aneurysms and pseudoaneurysms[12-23], but few reports described this therapy in case of superior mesenteric artery (SMA) or PDA pseudoaneurysms[9,24-28].

To the best of our knowledge, this is the first reported case of a PDA pseudoaneurysm percutaneously treated by direct thrombin injection by US guidance after failing of endovascular treatment.

CASE REPORT

An 82-year-old woman was in a peripheral hospital two days before for cerebral haemorrhage and was admitted in emergency to our central hospital with the suspicion of acute bleeding. During the hospital stay routine laboratory investigation revealed severe anaemia with haemoglobin drop to 6.0 g/dL and contrast-enhanced thoraco-abdominal CT scan was performed on a 64-slice multidetector Siemens scanner. It identified an oval, rounded mass within the pancreatic head with slow centrifugal contrast-enhancement, presumed to be a bleeding pseudoaneurysm with a haematoma and a small haemoperitoneum around the spleen (Figure 1). The feeding artery to the pseudoaneurysm was identified as a PDA, given the area of distribution and the origin from SMA. The patient's surgical history was unremarkable and did not have history of chronic pancreatitis.

At the admission the patient underwent to endotracheal intubation but was hemodynamically stable. Due to her age and clinical co-morbidities, open surgery was not the best option and an attempt with endovascular procedure was decided.

Angiography was performed using Siemens equipment (Axiom Artis U, Siemens AG, Forchheim, Germany). Under local anaesthesia (lidocaine 2%), using the Seldinger technique, a selective SMA catheterization (Cobra Glidecath, 5F, 65-cm-long, Terumo, Tokyo, Japan) with a hydrophilic guidewire (0.035", 150-cm-long, Terumo) confirmed the pseudoaneurysm of 2-cm on diameter of the PDA area (Figure 2). Both the examination of the SMA made in different projections, including the lateral view and superselective catheterization (Progreat, 2.7F, 130-cm-long, Terumo, Tokyo, Japan) of at least 4 proximal branches did not show the pseudoaneurysm so that the feeding vessel could not be identified.

Selective catheterization (Radifocus guidewire, 0.035", 150-cm-long, and Cobra Glidecath, 5F, 65-cm-long, Terumo) of the celiac artery (CA) was performed, but the gastroduodenal artery (GDA) was not depicted, because of a close stenosis of the take-off of CA from the abdominal aorta.

Since we were not able to identify and catheterize the feeding vessel, and considering the patient's high-risk clinical condition, percutaneous embolization with thrombin injection was suggested. The procedure was performed after local anaesthesia (lidocaine 2%) and a Chiba needle (Ecojekt 18G, 20-cm-long, HS Hospital Service, Aprilia, Latina, Italy) was inserted into the pseudoaneurysmal sac through the anterior abdominal wall under US guidance (MyLab, Esaote, Genova, Italy) and 2 mL (1000 IU) of human thrombin (Tisseel, Baxter AG, Rome, Italy) were injected. During the injection, the anechoic area of pseudoaneurysm turned into hypoechoic area and the colour signals disappeared because of immediate thrombosis was achieved on the US control (Figure 3).

A final SMA selective control DSA performed at the end of the procedure confirmed complete exclusion of

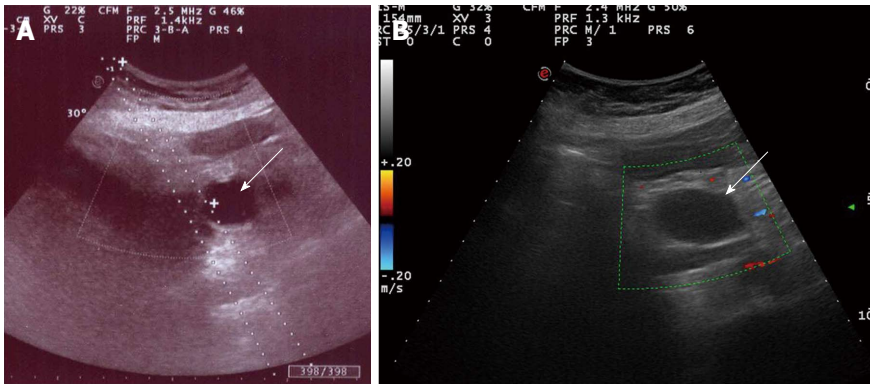

Figure 3 Two-dimensional B-mode ultrasonography (A) and color-Doppler ultrasonography (B) showing pancreatico-duodenal artery pseudoaneurysm (arrows) before and after percutaneous thrombin injection, respectively.

Figure 4 Axial contrast-enhanced computed tomography showing pancreatico-duodenal artery pseudoaneurysm (arrow) 1 wk after the treatment.

the pseudoaneurysm with no endoleak and preserved perfusion of the SMA.

Finally, haemostasis of the puncture site at the right common femoral artery (CFA) was obtained using a vascular closure device (Angioseal 6F, Saint Jude, MN, United States).

Thrombotic or immunologic complications of thrombin were not observed. A 1-wk follow-up abdominal CT scan showed a completely thrombosed PDA pseudoaneurysm with no endoleak or recurrence of bleeding, and preserved flow through the SMA branches (Figure 4). Patient's condition was stable and the blood test normalized. Doppler ultrasound examinations at 2 wk and 3 mo confirmed thrombosis of the pseudoaneurysm, without any echographic signs of blood flow within.

Patient was discharged from the intensive care unit and she is now under careful clinic and imaging follow-up.

DISCUSSION

Natural history of the visceral false aneurysms is potentially the rupture and a lethal abdominal haemorrhage, with a rupture rate of 50% and a mortality rate up to 80%[29].

Causes of SMA aneurysm and pseudoaneurysm formation include chronic pancreatitis, atherosclerosis, trauma, surgery, biopsy, infection, collagen vascular disease, medial necrosis, arthritis and dissection.

Symptoms depend on the location and include abdominal pain, melena, body loss, internal haemorrhage and hypovolemic shock due to pseudoaneurysm rupture.

Our patient did not have history of chronic pancreatitis and was suspected to have an internal haemorrhage because of onset of severe anaemia and lacking a worsening of the brain haemorrhage.

Imaging techniques for the diagnosis of pseudoaneurysms include US, CT, MRI and DSA[4]; this shows precise location, morphology, size of the sac, feeding collateral vessels and efferent arteries if present, and enables immediate endovascular treatment.

PDA or SMA pseudoaneurysms require immediate treatment due to a high mortality, up to 90%, in the case of not treatment[18] and it includes open surgical repair and non surgical procedures.

Surgical treatment, traditionally a first-line therapy option[30], is invasive and is associated with high risk of infection, haemorrhage and long rehabilitation time. Deep retroperitoneal and retroduodenal position of the vessels involved in peri-pancreatic aneurysms is technically challenging for the surgeon and as much as 70% of the PDA aneurysms are not detected at surgery[3].

Non surgical management includes endovascular and percutaneous techniques[31]. At present endovascular treatment is considered the first choice for embolization of PDA and SMA pseudoaneurysm and the technical success ranges from 56% to 100%[10,31-33]. Coils, gelfoam, thrombin, glue (N-butyl-cyanoacrylate), stent-graft and Amplatzer vascular plug (AVP, ev3, Plymouth, Unites States), are different materials for endovascular management and the choice depends on the vascular anatomy of the target lesion and the patient's clinical condition[34].

Recently, 2 new agents have been used for endovascular treatment of aneurysms and pseudoaneurysms: ethylene vinyl alcohol copolymer (Onyx, Micro Therapeutics, Irvine, CA, Unites States)[35] and a multilayer flow modulator stent (Cardiatis, Multilayer, Bruxels, Belgium)[32,36].

When antegrade superselective catheterization of the feeding vessel of the PDA pseudoaneurysm fails owing

Table 1 Literature summary of peripancreatic pseudoaneurysms treated with percutaneous thrombin injection

Ref.	Patient age (yr)	Patient sex	Artery	No	Size (mm)	Technique	Needle	Thrombin	Dose (IU)	Immediate result	Adverse effects	Rebleeding	Retreatment	Follow-up (method)
Sparrow *et al*[18]	50	F	GDA	1	30	US-guided	22 G	Bovine	1000	Success	No	No	No	8 wk (US)
Manazer *et al*[19]	42	M	GDA	1	30 × 30	CT-guided	Not specified	Not specified	4000	Success	No	None	No	10 wk (CT)
Armstrong *et al*[23]	Not available	Not available	SMA	1	Not available	US-guided	Not specified	Human	750	Success	Not available	Yes (two times in 6 mo)	Thrombin injection	6 mo (CT)
Geoghegan *et al*[17]	24	M	GDA	1	40 × 35	CT-guided	22 G	Not specified	Not specified	Success	Mild abdominal pain	No	No	1 wk (CT)
Szopiński *et al*[24]	49	F	SMA	1	60 × 44 × 45	US-guided (after failed TCE)	Spinal needle	Bovine	1600	Success	No	No	No	6 mo (US)
Ghassemi *et al*[26]	77	M	SPDA	1	51 × 46	CT-guided (after failed TCE)	22 G	Not specified	1300	Success	No	No	No	4 mo (CT)
Williams *et al*[25]	55	M	IPDA	1	30 × 15	CT-guided	22 G	Bovine	1000	Success	No	No	No	9 mo (CT)
McErlean *et al*[9]	46	M	GDA/ PDA	1	25 × 20	US-guided	Not specified	Human	Not specified	Success	No	No	No	3 mo (CT)
De Rosa *et al*[13]	Not specified	Not specified	GDA/ SMA	2	Not specified	CT-guided (after failed TCE)	Not specified	Bovine	4500	Success	Not specified	Yes (24 h)	Not known	15 d (death for PE)
De Rosa *et al*[13]	Not specified	Not specified	GDA/ SMA	1	Not specified	US-guided	Not specified	Human	400	Success	Not specified	No	No	Not specified
Nicholson *et al*[15]	Not specified	Not specified	GDA/ SMA	4	Not specified	CT-guided	Not specified	Not specified	Not specified	Success	Not specified	Yes (multiple)	Thrombin injection	6 mo (with CT)
Laganà *et al*[14]	69	M	GDA	1	50	US-guided + coils	22 G	Bovine	2000	Success	No	Yes (1 mo)	Coils	24 mo
Fankhauser *et al*[16]	Not specified	Not specified	PDA	2	Not specified	US + fluoro-guided	Not specified	Not specified	Not specified	Success	Not specified	No	No	Unknown (mean 524 d)
Present Case Report	82	F	PDA	1	20	US-guided	18 G	Human	1000	Success	No	No	No	3 mo (US)

GDA: Gastroduodenal artery; SMA: Superior mesenteric artery; SPDA: Superior pancreaticoduodenal artery; IPDA: Inferior pancreaticoduodenal artery; PDA: Pancreaticoduodenal artery; US: Ultrasound; CT: Computed tomography; TCE: Transcatheter embolization; G: Gauge; PE: Pulmonary embolism; F: Female; M: Male.

to vessel tortuosity, a retrograde catheterization of the PDA by way of collateral vessels from the GDA could potentially be advantageous.

Unfortunately, in our patient a close stenosis at the origin of the CA did not allowed retrograde catheterization of PDA. As Sutton *et al*[6] and Kadir *et al*[7] reported, proximal obstruction of the CA induces consequent compensatory hypertrophy of the PDA and causes hemodynamic alterations that favour the development of PDA aneurysms and pseudoaneurysms[34,37].

An alternative option to endovascular management of the pseudoaneurysms is the percutaneous embolization by thrombin injection under US or CT guidance.

At first, this method was used for the treatment of iatrogenic pseudoaneurysms of the CFA[38,39], but there are few reports of treating visceral artery aneurysms and pseudoaneurysms, usually as second procedure after failed transarterial embolization[9,12-28].

In our case we attempted to identify angiographically the feeding vessel of the pseudoaneurysm, also replacing shape and type of the catheter and changing obliquity of the X-rays beam projection, but superselective catheterization of the feeding branch of the pseudoaneurysm failed.

After exclusion of open surgery approach for high risk-surgery patient, a non-vascular procedure was proposed, by means of percutaneous thrombin injection directly into the pseudoaneurysmal sac.

Thrombin is a clotting factor formed in coagulating form from prothrombin, which hydrolyzes bonds of fibrinogen and allows polymerization of the fibrinogen to form a fibrin clot. The commercially used product is a solution of a sterile protein substance that includes human fibrinogen and artificial aprotinine, which must be mixed with a human thrombin solution in the presence of calcium. After the injection, it acts immediately: the clot is bio-absorbable, and the risk of infection, tissue necrosis or inflammation is minimized.

The first report on the use of thrombin for percutaneous embolization of aneurysms of both peripheral and visceral arteries was in 1986 from Cope *et al*[12].

Afterwards this technique was applied to treat several visceral aneurysms and pseudoaneurysms, and type II and type I endoleak following endovascular repair of abdominal and thoracic aortic aneurysms. Potential complications of thrombin use are distal thrombosis, visceral artery occlusion and immunologic reactions[18]. Given the risk of distal embolization, the use of embolic protection device was suggested[28]. It is advised to evaluate the free flowing component of the total volume of the pseudoaneurysm, and the quantity of thrombin to prevent the leakage of thrombin from the sac[20].

The Table 1 presents an overview of the literature where peri-pancreatic pseudoaneurysms were treated by transabdominal thrombin injection US- or CT-guided, along with volume and type of the used thrombin, results, complications and follow up.

In the majority of cases 1000-1500 IU of thrombin were injected into the pseudoaneurysmal sac and the human thrombin is today preferred to bovine thrombin for a minor risk of anaphylactic reaction. In one case additional use of coils was suggested for the embolisation of the afferent artery, to prevent the possible reperfusion of the pseudoaneurysm[14].

CT usually provides appropriate guide to percutaneous procedure, but US-guide allows real-time evaluation of the amount of thrombin being injected and of the patency of the pseudoaneurysmal sac. Furthermore US-guided injection allows real-time visualization of the needle track, lowing the risk of accidental puncture of bowel, vascular or organs.

Thrombin injection resulted in complete thrombosis and exclusion of the majority of the treated pseudoaneurysmal sacs, even during the follow up imaging control with US or CT scan, although the longest follow-up period was of 24 mo. There were not major complications referred to transabdominal access because of use of small calibre needles, except for our study in which we used an 18 G needle because only an 18 G US-guide was available in emergency. Table 1 shows important risk of early rebleeding of the treated pseudoaneurysm that required at least one additional thrombin injection, reported by some Authors[13-15,23]. These results indicate the importance of a close post-embolization follow-up with US or CT, required to identify high-risk patients, who need further treatment.

In conclusion, transabdominal thrombin injection could be the first line treatment when the incannulation or identification of the feeding vessel of peri-pancreatic pseudoaneurysm failed, especially in patients not candidate for open surgical approach[40]. Moreover, in these patients, this treatment could be considered as "bridge-to-surgery" allowing the stabilisation of the ruptured vessel and the further surgical treatment.

COMMENTS

Case characteristics

An 82-year-old woman with cerebral haemorrhage was admitted in emergency with the suspicion of acute bleeding.

Clinical diagnosis

Severe anaemia (haemoglobin drop to 6.0 g/dL) but haemodynamically stable.

Differential diagnosis

Increasing of the cerebral haemorrhage, thoraco-abdominal source of bleeding.

Laboratory diagnosis

Haemoglobin = 6.0 g/dL; haemodynamically stable.

Imaging diagnosis

Contrast-enhanced thoraco-abdominal computed tomography scan showed an oval, rounded mass of 2-cm on diameter within the pancreatic head with slow centrifugal contrast-enhancement, presumed to be a bleeding pseudoaneurysm with a haematoma and a small haemoperitoneum around the spleen.

Pathological diagnosis

Selective angiography of the superior mesenteric artery confirmed a pancreatico-duodenal artery pseudoaneurysm.

Treatment

The patient was treated with 2 mL (1000 IU) of human thrombin percutaneously injected into the pseudoaneurysmal sac under ultrasonography (US) guide.

Related reports

Few reports described peri-pancreatic pseudoaneurysms treated by percutaneous US-guided thrombin injection after failing of the endovascular treatment.

Term explanation

Pancreatico-duodenal artery pseudoaneurysm, or false aneurysm, is a vessel diameter dilatation without all vessel wall layers and is the consequence of a vessel wall disruption limited only by the adventitia or by the surrounding tissues.

Experiences and lessons

Pancreatico-duodenal artery pseudoaneurysm embolization by percutaneous US-guided thrombin injection is feasible after failing of the endovascular treatment, especially in patients not candidate for open surgical approach.

Peer review

This report describes a successful percutaneous US-guided treatment of the rare pancreatico-duodenal artery pseudoaneurysm after a failed endovascular approach.

REFERENCES

1 **Uher P**, Nyman U, Ivancev K, Lindh M. Aneurysms of the pancreaticoduodenal artery associated with occlusion of the celiac artery. *Abdom Imaging* 1995; **20**: 470-473 [PMID: 7580788]

2 **Iyomasa S**, Matsuzaki Y, Hiei K, Sakaguchi H, Matsunaga H, Yamaguchi Y. Pancreaticoduodenal artery aneurysm: a case report and review of the literature. *J Vasc Surg* 1995; **22**: 161-166 [PMID: 7637116]

3 **Moore E**, Matthews MR, Minion DJ, Quick R, Schwarcz TH, Loh FK, Endean ED. Surgical management of peripancreatic arterial aneurysms. *J Vasc Surg* 2004; **40**: 247-253 [PMID:

15297817 DOI: 10.1016/j.jvs.2004.03.045]
4 **Jesinger RA**, Thoreson AA, Lamba R. Abdominal and pelvic aneurysms and pseudoaneurysms: imaging review with clinical, radiologic, and treatment correlation. *Radio Graphics* 2013; **33**: E71-E96 [DOI: 10.1148/rg.333115036]
5 **Stanley JC**, Wakefield TW, Graham LM, Whitehouse WM, Zelenock GB, Lindenauer SM. Clinical importance and management of splanchnic artery aneurysms. *J Vasc Surg* 1986; **3**: 836-840 [PMID: 3701947 DOI: 10.1067/mva.1986.avs0030836]
6 **Sutton D**, Lawton G. Coeliac stenosis or occlusion with aneurysm of the collateral supply. *Clin Radiol* 1973; **24**: 49-53 [PMID: 4723494]
7 **Kadir S**, Athanasoulis CA, Yune HY, Wilkov H. Aneurysms of the pancreaticoduodenal arteries in association with celiac axis occlusion. *Cardiovasc Radiol* 1978; **1**: 173-177 [PMID: 743713]
8 **Trastek VF**, Pairolero PC, Bernatz PE. Splenic artery aneurysms. *World J Surg* 1985; **9**: 378-383 [PMID: 4013352]
9 **McErlean A**, Looby S, Lee MJ. Percutaneous ultrasound-guided thrombin injection as first-line treatment of pancreatic pseudoaneurysm. *Cardiovasc Intervent Radiol* 2007; **30**: 526-528 [PMID: 17131209 DOI: 10.1007/s00270-006-0174-9]
10 **Spiliopoulos S**, Sabharwal T, Karnabatidis D, Brountzos E, Katsanos K, Krokidis M, Gkoutzios P, Siablis D, Adam A. Endovascular treatment of visceral aneurysms and pseudoaneurysms: long-term outcomes from a multicenter European study. *Cardiovasc Intervent Radiol* 2012; **35**: 1315-1325 [PMID: 22146976 DOI: 10.1007/s00270-011-0312-x]
11 **Sachdev U**, Baril DT, Ellozy SH, Lookstein RA, Silverberg D, Jacobs TS, Carroccio A, Teodorescu VJ, Marin ML. Management of aneurysms involving branches of the celiac and superior mesenteric arteries: a comparison of surgical and endovascular therapy. *J Vasc Surg* 2006; **44**: 718-724 [PMID: 17011997 DOI: 10.1016/j.jvs.2006.06.027]
12 **Cope C**, Zeit R. Coagulation of aneurysms by direct percutaneous thrombin injection. *AJR Am J Roentgenol* 1986; **147**: 383-387 [PMID: 3487958]
13 **De Rosa A**, Gomez D, Pollock JG, Bungay P, De Nunzio M, Hall RI, Thurley P. The radiological management of pseudoaneurysms complicating pancreatitis. *JOP* 2012; **13**: 660-666 [PMID: 23183395 DOI: 10.6092/1590-8577/1193]
14 **Laganà D**, Carrafiello G, Mangini M, Dionigi G, Caronno R, Castelli P, Fugazzola C. Multimodal approach to endovascular treatment of visceral artery aneurysms and pseudoaneurysms. *Eur J Radiol* 2006; **59**: 104-111 [PMID: 16597492 DOI: 10.1016/j.ejrad.2006.02.004]
15 **Nicholson AA**, Patel J, McPherson S, Shaw DR, Kessel D. Endovascular treatment of visceral aneurysms associated with pancreatitis and a suggested classification with therapeutic implications. *J Vasc Interv Radiol* 2006; **17**: 1279-1285 [PMID: 16923974 DOI: 10.1097/01.RVI.0000231948.08617.04]
16 **Fankhauser GT**, Stone WM, Naidu SG, Oderich GS, Ricotta JJ, Bjarnason H, Money SR. The minimally invasive management of visceral artery aneurysms and pseudoaneurysms. *J Vasc Surg* 2011; **53**: 966-970 [PMID: 21216559 DOI: 10.1016/j.jvs.2010.10.071]
17 **Geoghegan T**, Tuite D, McAuley G, O'Keeffe S, Torreggiani WC. Percutaneous thrombin injection for the treatment of a post-pancreatitis pseudoaneurysm of the gastroduodenal artery. *Eur Radiol* 2004; **14**: 2144-2145 [DOI: 10.1007/s00330-004-2399-9]
18 **Sparrow P**, Asquith J, Chalmers N. Ultrasonic-guided percutaneous injection of pancreatic pseudoaneurysm with thrombin. *Cardiovasc Intervent Radiol* 2003; **26**: 312-315 [PMID: 14562987 DOI: 10.1007/s00270-003-0008-y]
19 **Manazer JR**, Monzon JR, Dietz PA, Moglia R, Gold M. Treatment of pancreatic pseudoaneurysm with percutaneous transabdominal thrombin injection. *J Vasc Surg* 2003; **38**: 600-602 [PMID: 12947284 DOI: 10.1016/s0741-5214(03)00454-3]
20 **Puri S**, Nicholson AA, Breen DJ. Percutaneous thrombin injection for the treatment of a post-pancreatitis pseudoaneurysm. *Eur Radiol* 2003; **13** Suppl 4: L79-L82 [PMID: 15018170 DOI: 10.1007/s00330-003-1836-5]
21 **Huang IH**, Zuckerman DA, Matthews JB. Occlusion of a giant splenic artery pseudoaneurysm with percutaneous thrombin-collagen injection. *J Vasc Surg* 2004; **40**: 574-577 [PMID: 15337894 DOI: 10.1016/j.jvs.2004.06.020]
22 **Luchs SG**, Antonacci VP, Reid SK, Pagan-Marin H. Vascular and interventional case of the day. Pancreatic head pseudoaneurysm treated with percutaneous thrombin injection. *AJR Am J Roentgenol* 1999; **173**: 830, 833-834 [PMID: 10470945]
23 **Armstrong EM**, Edwards A, Kingsnorth AN, Freeman S, Roobottom CA. Ultrasound guided thrombin injection to treat a pseudoaneurysm secondary to chronic pancreatitis. *Eur J Vasc Endovasc Surg* 2003; **26**: 448-449 [PMID: 14512011]
24 **Szopiński P**, Ciostek P, Pleban E, Iwanowski J, Serafin-Król M, Marianowska A, Noszczyk W. Percutaneous thrombin injection to complete SMA pseudoaneurysm exclusion after failing of endograft placement. *Cardiovasc Intervent Radiol* 2005; **28**: 509-514 [PMID: 16010511 DOI: 10.1007/s00270-004-0160-z]
25 **Williams M**, Alderson D, Virjee J, Callaway M. CT-guided percutaneous thrombin injection for treatment of an inferior pancreaticoduodenal artery pseudoaneurysm. *Cardiovasc Intervent Radiol* 2006; **29**: 669-671 [PMID: 16604412 DOI: 10.1007/s00270-004-0274-3]
26 **Ghassemi A**, Javit D, Dillon EH. Thrombin injection of a pancreaticoduodenal artery pseudoaneurysm after failed attempts at transcatheter embolization. *J Vasc Surg* 2006; **43**: 618-622 [PMID: 16520183 DOI: 10.1016/j.jvs.2005.11.051]
27 **Wallace MJ**, Choi E, McRae S, Madoff DC, Ahrar K, Pisters P. Superior mesenteric artery pseudoaneurysm following pancreaticoduodenectomy: management by endovascular stent-graft placement and transluminal thrombin injection. *Cardiovasc Intervent Radiol* 2007; **30**: 518-522 [PMID: 17031732 DOI: 10.1007/s00270-006-0109-5]
28 **Juszkat R**, Krasiński Z, Wykrętowicz M, Staniszewski R, Majewski W. Transarterial thrombin injection secured with an embolic protection device as a treatment for a superior mesenteric artery pseudoaneurysm. *Cardiovasc Intervent Radiol* 2011; **34**: 198-201 [PMID: 20058004 DOI: 10.1007/s00270-009-9791-4]
29 **Kaufman JA**, Lee MJ. Vascular and Interventional Radiology: The Requisites, 2nd ed. Philadelphia: Elsevier, 2013: 229-264
30 **Pulli R**, Dorigo W, Troisi N, Pratesi G, Innocenti AA, Pratesi C. Surgical treatment of visceral artery aneurysms: A 25-year experience. *J Vasc Surg* 2008; **48**: 334-342 [PMID: 18644480 DOI: 10.1016/j.jvs.2008.03.043]
31 **Ikeda O**, Tamura Y, Nakasone Y, Iryou Y, Yamashita Y. Nonoperative management of unruptured visceral artery aneurysms: treatment by transcatheter coil embolization. *J Vasc Surg* 2008; **47**: 1212-1219 [PMID: 18440188 DOI: 10.1016/j.jvs.2008.01.032]
32 **Balderi A**, Antonietti A, Ferro L, Peano E, Pedrazzini F, Fonio P, Grosso M. Endovascular treatment of visceral artery aneurysms and pseudoaneurysms: our experience. *Radiol Med* 2012; **117**: 815-830 [PMID: 22228131 DOI: 10.1007/s11547-011-0776-4]
33 **Tulsyan N**, Kashyap VS, Greenberg RK, Sarac TP, Clair DG, Pierce G, Ouriel K. The endovascular management of visceral artery aneurysms and pseudoaneurysms. *J Vasc Surg* 2007; **45**: 276-283; discussion 283 [PMID: 17264002 DOI: 10.1016/j.jvs.2006.10.049]
34 **Flood K**, Nicholson AA. Inferior pancreaticoduodenal artery aneurysms associated with occlusive lesions of the celiac axis: diagnosis, treatment options, outcomes, and review of the literature. *Cardiovasc Intervent Radiol* 2013; **36**: 578-587 [PMID: 23152034 DOI: 10.1007/s00270-012-0473-2]
35 **Jiménez AB**, Herraez JG, Membrives PP, Girelli JH, Haurie G,

Gòmez DD, Berta JE. Transcatheter embolization of a pancreatic pseudoaneurysm using a new liquid embolic agent, ethylene vinyl alcohol copolymer (onyx). *Pancreas* 2009; **38**: 110-112 [DOI: 10.1097/MPA.0b013e318170b666]

36 **Balderi A**, Antonietti A, Pedrazzini F, Ferro L, Leotta L, Peano E, Grosso M. Treatment of a hepatic artery aneurysm by endovascular exclusion using the multilayer cardiatis stent. *Cardiovasc Intervent Radiol* 2010; **33**: 1282-1286 [PMID: 20552194 DOI: 10.1007/s00270-010-9913-z]

37 **Kalva SP**, Athanasoulis CA, Greenfield AJ, Fan CM, Curvelo M, Waltman AC, Wicky S. Inferior pancreaticoduodenal artery aneurysms in association with celiac axis stenosis or occlusion. *Eur J Vasc Endovasc Surg* 2007; **33**: 670-675 [PMID: 17276102 DOI: 10.1016/j.ejvs.2006.12.021]

38 **Kang SS**, Labropoulos N, Mansour MA, Michelini M, Filliung D, Baubly MP, Baker WH. Expanded indications for ultrasound-guided thrombin injection of pseudoaneurysms. *J Vasc Surg* 2000; **31**: 289-298 [PMID: 10664498]

39 **Elford J**, Burrell C, Freeman S, Roobottom C. Human thrombin injection for the percutaneous treatment of iatrogenic pseudoaneurysms. *Cardiovasc Intervent Radiol* 2002; **25**: 115-118 [PMID: 11901428 DOI: 10.1007/s00270-001-0081-z]

40 **Kemmeter P**, Bonnell B, VanderKolk W, Griggs T, VanErp J. Percutaneous thrombin injection of splanchnic artery aneurysms: two case reports. *J Vasc Interv Radiol* 2000; **11**: 469-472 [PMID: 10787206]

P- Reviewer: Lin GM, Yamasaki T **S- Editor**: Ji FF
L- Editor: A **E- Editor**: Liu SQ

World Journal of Radiology

Submit a Manuscript: http://www.wjgnet.com/esps/
Help Desk: http://www.wjgnet.com/esps/helpdesk.aspx
www.wjgnet.com

World J Radiol 2014 August 28; 6(8): I-V
ISSN 1949-8470 (online)

INSTRUCTIONS TO AUTHORS

GENERAL INFORMATION

World Journal of Radiology (*World J Radiol*, *WJR*, online ISSN 1949-8470, DOI: 10.4329) is a peer-reviewed open access (OA) academic journal that aims to guide clinical practice and improve diagnostic and therapeutic skills of clinicians.

Aim and scope

WJR covers topics concerning diagnostic radiology, radiation oncology, radiologic physics, neuroradiology, nuclear radiology, pediatric radiology, vascular/interventional radiology, medical imaging achieved by various modalities and related methods analysis. The current columns of *WJR* include editorial, frontier, diagnostic advances, therapeutics advances, field of vision, mini-reviews, review, topic highlight, medical ethics, original articles, case report, clinical case conference (clinicopathological conference), and autobiography.

We encourage authors to submit their manuscripts to *WJR*. We will give priority to manuscripts that are supported by major national and international foundations and those that are of great basic and clinical significance.

WJR is edited and published by Baishideng Publishing Group (BPG). BPG has a strong professional editorial team composed of science editors, language editors and electronic editors. BPG currently publishes 43 OA clinical medical journals, including 42 in English, has a total of 15471 editorial board members or peer reviewers, and is a world first-class publisher.

Columns

The columns in the issues of *WJR* will include: (1) Editorial: The editorial board members are invited to make comments on an important topic in their field in terms of its current research status and future directions to lead the development of this discipline; (2) Frontier: The editorial board members are invited to select a highly cited cutting-edge original paper of his/her own to summarize major findings, the problems that have been resolved and remain to be resolved, and future research directions to help readers understand his/her important academic point of view and future research directions in the field; (3) Diagnostic Advances: The editorial board members are invited to write high-quality diagnostic advances in their field to improve the diagnostic skills of readers. The topic covers general clinical diagnosis, differential diagnosis, pathological diagnosis, laboratory diagnosis, imaging diagnosis, endoscopic diagnosis, biotechnological diagnosis, functional diagnosis, and physical diagnosis; (4) Therapeutics Advances: The editorial board members are invited to write high-quality therapeutic advances in their field to help improve the therapeutic skills of readers. The topic covers medication therapy, psychotherapy, physical therapy, replacement therapy, interventional therapy, minimally invasive therapy, endoscopic therapy, transplantation therapy, and surgical therapy; (5) Field of Vision: The editorial board members are invited to write commentaries on classic articles, hot topic articles, or latest articles to keep readers at the forefront of research and increase their levels of clinical research. Classic articles refer to papers that are included in Web of Knowledge and have received a large number of citations (ranking in the top 1%) after being published for more than years, reflecting the quality and impact of papers. Hot topic articles refer to papers that are included in Web of Knowledge and have received a large number of citations after being published for no more than 2 years, reflecting cutting-edge trends in scientific research. Latest articles refer to the latest published high-quality papers that are included in PubMed, reflecting the latest research trends. These commentary articles should focus on the status quo of research, the most important research topics, the problems that have now been resolved and remain to be resolved, and future research directions. Basic information about the article to be commented (including authors, article title, journal name, year, volume, and inclusive page numbers); (6) Minireviews: The editorial board members are invited to write short reviews on recent advances and trends in research of molecular biology, genomics, and related cutting-edge technologies to provide readers with the latest knowledge and help improve their diagnostic and therapeutic skills; (7) Review: To make a systematic review to focus on the status quo of research, the most important research topics, the problems that have now been resolved and remain to be resolved, and future research directions; (8) Topic Highlight: The editorial board members are invited to write a series of articles (7-10 articles) to comment and discuss a hot topic to help improve the diagnostic and therapeutic skills of readers; (9) Medical Ethics: The editorial board members are invited to write articles about medical ethics to increase readers' knowledge of medical ethics. The topic covers international ethics guidelines, animal studies, clinical trials, organ transplantation, *etc.*; (10) Clinical Case Conference or Clinicopathological Conference: The editorial board members are invited to contribute high-quality clinical case conference; (11) Original Articles: To report innovative and original findings in radiology; (12) Research Report: To briefly report the novel and innovative findings in radiology; (13) Meta-Analysis: Covers the systematic review, mixedtreatment comparison, meta-regression, and overview of reviews, in order to summarize a given quantitative effect, *e.g.*, the clinical effectiveness and safety of clinical treatments by combining data from two or more randomized controlled trials, thereby providing more precise and externally valid estimates than those which would stem from each individual dataset if analyzed separately from the others; (15) Letters to the Editor: To discuss and make reply to the contributions published in *WJR*, or to introduce and comment on a controversial issue of general interest; (16) Book Reviews: To introduce and comment on quality monographs of radiology; and (17) Autobiography: The editorial board members are invited to write their autobiography to provide readers with stories of success or failure in their scientific research career. The topic covers their basic personal information and information about when they started doing research work, where and how they did research work, what they have achieved, and their lessons from success or failure.

Name of journal

World Journal of Radiology

ISSN

ISSN 1949-8470 (online)

Launch date

December 31, 2009

Frequency

Monthly

Editor-in-Chief

Kai U Juergens, MD, Associate Professor, MRT und PET/CT, Nuklearmedizin Bremen Mitte, ZEMODI - Zentrum für morpholo-

Editorial office
Jin-Lei Wang, Director
Xiu-Xia Song, Vice Director
World Journal of Radiology
Room 903, Building D, Ocean International Center,
No. 62 Dongsihuan Zhonglu, Chaoyang District,
Beijing 100025, China
Telephone: +86-10-85381891
Fax: +86-10-85381893
E-mail: editorialoffice@wjgnet.com
Help Desk: http://www.wjgnet.com/esps/helpdesk.aspx
http://www.wjgnet.com

Publisher
Baishideng Publishing Group Inc
8226 Regency Drive,
Pleasanton, CA 94588, USA
Telephone: +1-925-223-8242
Fax: +1-925-223-8243
E-mail: bpgoffice@wjgnet.com
Help Desk: http://www.wjgnet.com/esps/helpdesk.aspx
http://www.wjgnet.com

Instructions to authors
Full instructions are available online at http://www.wjgnet.com/1948-5204/g_info_20100312180518.htm.

Indexed and Abstracted in
PubMed Central, PubMed, Digital Object Identifier, and Directory of Open Access Journals.

SPECIAL STATEMENT

All articles published in journals owned by the BPG represent the views and opinions of their authors, and not the views, opinions or policies of the BPG, except where otherwise explicitly indicated.

Biostatistical editing
Statisital review is performed after peer review. We invite an expert in Biomedical Statistics to evaluate the statistical method used in the paper, including *t*-test (group or paired comparisons), chi-squared test, Ridit, probit, logit, regression (linear, curvilinear, or stepwise), correlation, analysis of variance, analysis of covariance, *etc*. The reviewing points include: (1) Statistical methods should be described when they are used to verify the results; (2) Whether the statistical techniques are suitable or correct; (3) Only homogeneous data can be averaged. Standard deviations are preferred to standard errors. Give the number of observations and subjects (*n*). Losses in observations, such as drop-outs from the study should be reported; (4) Values such as ED50, LD50, IC50 should have their 95% confidence limits calculated and compared by weighted probit analysis (Bliss and Finney); and (5) The word 'significantly' should be replaced by its synonyms (if it indicates extent) or the *P* value (if it indicates statistical significance).

Conflict-of-interest statement
In the interests of transparency and to help reviewers assess any potential bias, *WJR* requires authors of all papers to declare any competing commercial, personal, political, intellectual, or religious interests in relation to the submitted work. Referees are also asked to indicate any potential conflict they might have reviewing a particular paper. Before submitting, authors are suggested to read "Uniform Requirements for Manuscripts Submitted to Biomedical Journals: Ethical Considerations in the Conduct and Reporting of Research: Conflicts of Interest" from International Committee of Medical Journal Editors (ICMJE), which is available at: http://www.icmje.org/ethical_4conflicts.html.

Sample wording: [Name of individual] has received fees for serving as a speaker, a consultant and an advisory board member for [names of organizations], and has received research funding from [names of organization]. [Name of individual] is an employee of [name of organization]. [Name of individual] owns stocks and shares in [name of organization]. [Name of individual] owns patent [patent identification and brief description].

Statement of informed consent
Manuscripts should contain a statement to the effect that all human studies have been reviewed by the appropriate ethics committee or it should be stated clearly in the text that all persons gave their informed consent prior to their inclusion in the study. Details that might disclose the identity of the subjects under study should be omitted. Authors should also draw attention to the Code of Ethics of the World Medical Association (Declaration of Helsinki, 1964, as revised in 2004).

Statement of human and animal rights
When reporting the results from experiments, authors should follow the highest standards and the trial should conform to Good Clinical Practice (for example, US Food and Drug Administration Good Clinical Practice in FDA-Regulated Clinical Trials; UK Medicines Research Council Guidelines for Good Clinical Practice in Clinical Trials) and/or the World Medical Association Declaration of Helsinki. Generally, we suggest authors follow the lead investigator's national standard. If doubt exists whether the research was conducted in accordance with the above standards, the authors must explain the rationale for their approach and demonstrate that the institutional review body explicitly approved the doubtful aspects of the study.

Before submitting, authors should make their study approved by the relevant research ethics committee or institutional review board. If human participants were involved, manuscripts must be accompanied by a statement that the experiments were undertaken with the understanding and appropriate informed consent of each. Any personal item or information will not be published without explicit consents from the involved patients. If experimental animals were used, the materials and methods (experimental procedures) section must clearly indicate that appropriate measures were taken to minimize pain or discomfort, and details of animal care should be provided.

SUBMISSION OF MANUSCRIPTS

Manuscripts should be typed in 1.5 line spacing and 12 pt. Book Antiqua with ample margins. Number all pages consecutively, and start each of the following sections on a new page: Title Page, Abstract, Introduction, Materials and Methods, Results, Discussion, Acknowledgements, References, Tables, Figures, and Figure Legends. Neither the editors nor the publisher are responsible for the opinions expressed by contributors. Manuscripts formally accepted for publication become the permanent property of BPG, and may not be reproduced by any means, in whole or in part, without the written permission of both the authors and the publisher. We reserve the right to copy-edit and put onto our website accepted manuscripts. Authors should follow the relevant guidelines for the care and use of laboratory animals of their institution or national animal welfare committee. For the sake of transparency in regard to the performance and reporting of clinical trials, we endorse the policy of the ICMJE to refuse to publish papers on clinical trial results if the trial was not recorded in a publicly-accessible registry at its outset. The only register now available, to our knowledge, is http://www.clinicaltrials.gov sponsored by the United States National Library of Medicine and we encourage all potential contributors to register with it. However, in the case that other registers

become available you will be duly notified. A letter of recommendation from each author's organization should be provided with the contributed article to ensure the privacy and secrecy of research is protected.

Authors should retain one copy of the text, tables, photographs and illustrations because rejected manuscripts will not be returned to the author(s) and the editors will not be responsible for loss or damage to photographs and illustrations sustained during mailing.

Online submissions

Manuscripts should be submitted through the Online Submission System at: http://www.wjgnet.com/esps/. Authors are highly recommended to consult the ONLINE INSTRUCTIONS TO AUTHORS (http://www.wjgnet.com/1948-5204/g_info_20100312180518.htm) before attempting to submit online. For assistance, authors encountering problems with the Online Submission System may send an email describing the problem to bpgoffice@wjgnet.com, or by telephone: +86-10-85381891. If you submit your manuscript online, do not make a postal contribution. Repeated online submission for the same manuscript is strictly prohibited.

MANUSCRIPT PREPARATION

All contributions should be written in English. All articles must be submitted using word-processing software. All submissions must be typed in 1.5 line spacing and 12 pt. Book Antiqua with ample margins. Style should conform to our house format. Required information for each of the manuscript sections is as follows:

Title page

Title: Title should be less than 12 words.

Running title: A short running title of less than 6 words should be provided.

Authorship: Authorship credit should be in accordance with the standard proposed by International Committee of Medical Journal Editors, based on (1) substantial contributions to conception and design, acquisition of data, or analysis and interpretation of data; (2) drafting the article or revising it critically for important intellectual content; and (3) final approval of the version to be published. Authors should meet conditions 1, 2, and 3.

Institution: Author names should be given first, then the complete name of institution, city, province and postcode. For example, Xu-Chen Zhang, Li-Xin Mei, Department of Pathology, Chengde Medical College, Chengde 067000, Hebei Province, China. One author may be represented from two institutions, for example, George Sgourakis, Department of General, Visceral, and Transplantation Surgery, Essen 45122, Germany; George Sgourakis, 2nd Surgical Department, Korgialenio-Benakio Red Cross Hospital, Athens 15451, Greece

Author contributions: The format of this section should be: Author contributions: Wang CL and Liang L contributed equally to this work; Wang CL, Liang L, Fu JF, Zou CC, Hong F and Wu XM designed the research; Wang CL, Zou CC, Hong F and Wu XM performed the research; Xue JZ and Lu JR contributed new reagents/analytic tools; Wang CL, Liang L and Fu JF analyzed the data; and Wang CL, Liang L and Fu JF wrote the paper.

Supportive foundations: The complete name and number of supportive foundations should be provided, e.g. Supported by National Natural Science Foundation of China, No. 30224801

Correspondence to: Only one corresponding address should be provided. Author names should be given first, then author title, affiliation, the complete name of institution, city, postcode, province, country, and email. All the letters in the email should be in lower case. A space interval should be inserted between country name and email address. For example, Montgomery Bissell, MD, Professor of Medicine, Chief, Liver Center, Gastroenterology Division, University of California, Box 0538, San Francisco, CA 94143, United States. montgomery.bissell@ucsf.edu

Telephone and fax: Telephone and fax should consist of +, country number, district number and telephone or fax number, e.g. Telephone: +86-10-85381891 Fax: +86-10-85381893

Peer reviewers: All articles received are subject to peer review. Normally, three experts are invited for each article. Decision on acceptance is made only when at least two experts recommend publication of an article. All peer-reviewers are acknowledged on Express Submission and Peer-review System website.

Abstract

There are unstructured abstracts (no less than 200 words) and structured abstracts. The specific requirements for structured abstracts are as follows:

An informative, structured abstract should accompany each manuscript. Abstracts of original contributions should be structured into the following sections: AIM (no more than 20 words; Only the purpose of the study should be included. Please write the Aim in the form of "To investigate/study/…"), METHODS (no less than 140 words for Original Articles; and no less than 80 words for Brief Articles), RESULTS (no less than 150 words for Original Articles and no less than 120 words for Brief Articles; You should present *P* values where appropriate and must provide relevant data to illustrate how they were obtained, e.g. 6.92 ± 3.86 *vs* 3.61 ± 1.67, $P < 0.001$), and CONCLUSION (no more than 26 words).

Key words

Please list 5-10 key words, selected mainly from *Index Medicus*, which reflect the content of the study.

Core tip

Please write a summary of less than 100 words to outline the most innovative and important arguments and core contents in your paper to attract readers.

Text

For articles of these sections, original articles and brief articles, the main text should be structured into the following sections: INTRODUCTION, MATERIALS AND METHODS, RESULTS and DISCUSSION, and should include appropriate Figures and Tables. Data should be presented in the main text or in Figures and Tables, but not in both. The main text format of these sections, editorial, topic highlight, case report, letters to the editors, can be found at: http://www.wjgnet.com/1948-5204/g_info_list.htm.

Illustrations

Figures should be numbered as 1, 2, 3, *etc*., and mentioned clearly in the main text. Provide a brief title for each figure on a separate page. Detailed legends should not be provided under the figures. This part should be added into the text where the figures are applicable. Keeping all elements compiled is necessary in line-art image. Scale bars should be used rather than magnification factors, with the length of the bar defined in the legend rather than on the bar itself. File names should identify the figure and panel. Avoid layering type directly over shaded or textured areas. Please use uniform legends for the same subjects. For example: Figure 1 Pathological changes in atrophic gastritis after treatment. A: ...; B: ...; C: ...; D: ...; E: ...; F: ...; G: …*etc*. It is our principle to publish high resolution-figures for the E-versions.

Tables

Three-line tables should be numbered 1, 2, 3, *etc*., and mentioned clearly in the main text. Provide a brief title for each table. Detailed legends should not be included under tables, but rather added into the text where applicable. The information should complement, but not duplicate the text. Use one horizontal line under the title, a second under column heads, and a third below the Table, above any footnotes. Vertical and italic lines should be omitted.

Notes in tables and illustrations

Data that are not statistically significant should not be noted. $^{a}P < 0.05$, $^{b}P < 0.01$ should be noted ($P > 0.05$ should not be noted). If there are other series of P values, $^{c}P < 0.05$ and $^{d}P < 0.01$ are used. A third series of P values can be expressed as $^{e}P < 0.05$ and $^{f}P < 0.01$. Other notes in tables or under illustrations should be expressed as ^{1}F, ^{2}F, ^{3}F; or sometimes as other symbols with a superscript (Arabic numerals) in the upper left corner. In a multi-curve illustration, each curve should be labeled with ●, ○, ■, □, ▲, △, *etc*., in a certain sequence.

Acknowledgments

Brief acknowledgments of persons who have made genuine contributions to the manuscript and who endorse the data and conclusions should be included. Authors are responsible for obtaining written permission to use any copyrighted text and/or illustrations.

REFERENCES

Coding system

The author should number the references in Arabic numerals according to the citation order in the text. Put reference numbers in square brackets in superscript at the end of citation content or after the cited author's name. For citation content which is part of the narration, the coding number and square brackets should be typeset normally. For example, "Crohn's disease (CD) is associated with increased intestinal permeability[1,2]". If references are cited directly in the text, they should be put together within the text, for example, "From references[19,22-24], we know that..."

When the authors write the references, please ensure that the order in text is the same as in the references section, and also ensure the spelling accuracy of the first author's name. Do not list the same citation twice.

PMID and DOI

Pleased provide PubMed citation numbers to the reference list, e.g. PMID and DOI, which can be found at http://www.ncbi.nlm.nih.gov/sites/entrez?db=pubmed and http://www.crossref.org/SimpleTextQuery/, respectively. The numbers will be used in E-version of this journal.

Style for journal references

Authors: the name of the first author should be typed in bold-faced letters. The family name of all authors should be typed with the initial letter capitalized, followed by their abbreviated first and middle initials. (For example, Lian-Sheng Ma is abbreviated as Ma LS, Bo-Rong Pan as Pan BR). The title of the cited article and italicized journal title (journal title should be in its abbreviated form as shown in PubMed), publication date, volume number (in black), start page, and end page [PMID: 11819634 DOI: 10.3748/wjg.13.5396].

Style for book references

Authors: the name of the first author should be typed in bold-faced letters. The surname of all authors should be typed with the initial letter capitalized, followed by their abbreviated middle and first initials. (For example, Lian-Sheng Ma is abbreviated as Ma LS, Bo-Rong Pan as Pan BR) Book title. Publication number. Publication place: Publication press, Year: start page and end page.

Format

Journals

English journal article (list all authors and include the PMID where applicable)

1 **Jung EM**, Clevert DA, Schreyer AG, Schmitt S, Rennert J, Kubale R, Feuerbach S, Jung F. Evaluation of quantitative contrast harmonic imaging to assess malignancy of liver tumors: A prospective controlled two-center study. *World J Gastroenterol* 2007; **13**: 6356-6364 [PMID: 18081224 DOI: 10.3748/wjg.13.6356]

Chinese journal article (list all authors and include the PMID where applicable)

2 **Lin GZ**, Wang XZ, Wang P, Lin J, Yang FD. Immunologic effect of Jianpi Yishen decoction in treatment of Pixu-diarrhoea. *Shijie Huaren Xiaohua Zazhi* 1999; **7**: 285-287

In press

3 **Tian D**, Araki H, Stahl E, Bergelson J, Kreitman M. Signature of balancing selection in Arabidopsis. *Proc Natl Acad Sci USA* 2006; In press

Organization as author

4 **Diabetes Prevention Program Research Group**. Hypertension, insulin, and proinsulin in participants with impaired glucose tolerance. *Hypertension* 2002; **40**: 679-686 [PMID: 12411462 DOI:10.1161/01.HYP.0000035706.28494.09]

Both personal authors and an organization as author

5 **Vallancien G**, Emberton M, Harving N, van Moorselaar RJ; Alf-One Study Group. Sexual dysfunction in 1, 274 European men suffering from lower urinary tract symptoms. *J Urol* 2003; **169**: 2257-2261 [PMID: 12771764 DOI:10.1097/01.ju.0000067940.76090.73]

No author given

6 21st century heart solution may have a sting in the tail. *BMJ* 2002; **325**: 184 [PMID: 12142303 DOI:10.1136/bmj.325.7357.184]

Volume with supplement

7 **Geraud G**, Spierings EL, Keywood C. Tolerability and safety of frovatriptan with short- and long-term use for treatment of migraine and in comparison with sumatriptan. *Headache* 2002; **42** Suppl 2: S93-99 [PMID: 12028325 DOI:10.1046/j.1526-4610.42.s2.7.x]

Issue with no volume

8 **Banit DM**, Kaufer H, Hartford JM. Intraoperative frozen section analysis in revision total joint arthroplasty. *Clin Orthop Relat Res* 2002; (**401**): 230-238 [PMID: 12151900 DOI:10.1097/00003086-200208000-00026]

No volume or issue

9 Outreach: Bringing HIV-positive individuals into care. *HRSA Careaction* 2002; 1-6 [PMID: 12154804]

Books

Personal author(s)

10 **Sherlock S**, Dooley J. Diseases of the liver and billiary system. 9th ed. Oxford: Blackwell Sci Pub, 1993: 258-296

Chapter in a book (list all authors)

11 **Lam SK**. Academic investigator's perspectives of medical treatment for peptic ulcer. In: Swabb EA, Azabo S. Ulcer disease: investigation and basis for therapy. New York: Marcel Dekker, 1991: 431-450

Author(s) and editor(s)

12 **Breedlove GK**, Schorfheide AM. Adolescent pregnancy. 2nd ed. Wieczorek RR, editor. White Plains (NY): March of Dimes Education Services, 2001: 20-34

Conference proceedings

13 **Harnden P**, Joffe JK, Jones WG, editors. Germ cell tumours V. Proceedings of the 5th Germ cell tumours Conference; 2001 Sep 13-15; Leeds, UK. New York: Springer, 2002: 30-56

Conference paper

14 **Christensen S**, Oppacher F. An analysis of Koza's computational effort statistic for genetic programming. In: Foster JA, Lutton E, Miller J, Ryan C, Tettamanzi AG, editors. Genetic programming. EuroGP 2002: Proceedings of the 5th European Conference on Genetic Programming; 2002 Apr 3-5; Kinsdale, Ireland. Berlin: Springer, 2002: 182-191

Electronic journal (list all authors)

15 Morse SS. Factors in the emergence of infectious diseases. Emerg Infect Dis serial online, 1995-01-03, cited 1996-06-05; 1(1): 24 screens. Available from: URL: http://www.cdc.gov/ncidod/eid/index.htm

Patent (list all authors)

16 **Pagedas AC**, inventor; Ancel Surgical R&D Inc., assignee. Flexible endoscopic grasping and cutting device and positioning tool assembly. United States patent US 20020103498. 2002 Aug 1

Statistical data
Write as mean ± SD or mean ± SE.

Statistical expression
Express *t* test as *t* (in italics), *F* test as *F* (in italics), chi square test as χ^2 (in Greek), related coefficient as *r* (in italics), degree of freedom as υ (in Greek), sample number as *n* (in italics), and probability as *P* (in italics).

Units
Use SI units. For example: body mass, m (B) = 78 kg; blood pressure, p (B) = 16.2/12.3 kPa; incubation time, t (incubation) = 96 h, blood glucose concentration, c (glucose) 6.4 ± 2.1 mmol/L; blood CEA mass concentration, p (CEA) = 8.6 24.5 μg/L; CO_2 volume fraction, 50 mL/L CO_2, not 5% CO_2; likewise for 40 g/L formaldehyde, not 10% formalin; and mass fraction, 8 ng/g, *etc.* Arabic numerals such as 23, 243, 641 should be read 23243641.

The format for how to accurately write common units and quantums can be found at: http://www.wjgnet.com/1948-5204/g_info_20100312183048.htm.

Abbreviations
Standard abbreviations should be defined in the abstract and on first mention in the text. In general, terms should not be abbreviated unless they are used repeatedly and the abbreviation is helpful to the reader. Permissible abbreviations are listed in Units, Symbols and Abbreviations: A Guide for Biological and Medical Editors and Authors (Ed. Baron DN, 1988) published by The Royal Society of Medicine, London. Certain commonly used abbreviations, such as DNA, RNA, HIV, LD50, PCR, HBV, ECG, WBC, RBC, CT, ESR, CSF, IgG, ELISA, PBS, ATP, EDTA, mAb, can be used directly without further explanation.

Italics
Quantities: *t* time or temperature, *c* concentration, *A* area, *l* length, *m* mass, *V* volume.
Genotypes: *gyrA*, *arg* 1, *c myc*, *c fos*, *etc.*
Restriction enzymes: *Eco*RI, *Hin*dI, *Bam*HI, *Kbo* I, *Kpn* I, *etc.*
Biology: *H. pylori*, *E coli*, *etc.*

Examples for paper writing
All types of articles' writing style and requirement will be found in the link: http://www.wjgnet.com/esps/NavigationInfo.aspx?id=15

SUBMISSION OF THE REVISED MANUSCRIPTS AFTER ACCEPTED

Authors must revise their manuscript carefully according to the revision policies of BPG. The revised version, along with the signed copyright transfer agreement, responses to the reviewers, and English language Grade B certificate (for non-native speakers of English), should be submitted to the online system via the link contained in the e-mail sent by the editor. If you have any questions about the revision, please send e-mail to esps@wjgnet.com.

Language evaluation
The language of a manuscript will be graded before it is sent for revision. (1) Grade A: priority publishing; (2) Grade B: minor language polishing; (3) Grade C: a great deal of language polishing needed; and (4) Grade D: rejected. Revised articles should reach Grade A or B.

Copyright assignment form
Please download a Copyright assignment form from http://www.wjgnet.com/1948-5204/g_info_20100312182928.htm.

Responses to reviewers
Please revise your article according to the comments/suggestions provided by the reviewers. The format for responses to the reviewers' comments can be found at: http://www.wjgnet.com/1948-5204/g_info_20100312182841.htm.

Proof of financial support
For papers supported by a foundation, authors should provide a copy of the approval document and serial number of the foundation.

STATEMENT ABOUT ANONYMOUS PUBLICATION OF THE PEER REVIEWERS' COMMENTS

In order to increase the quality of peer review, push authors to carefully revise their manuscripts based on the peer reviewers' comments, and promote academic interactions among peer reviewers, authors and readers, we decide to anonymously publish the reviewers' comments and author's responses at the same time the manuscript is published online.

PUBLICATION FEE

WJR is an international, peer-reviewed, OA online journal. Articles published by this journal are distributed under the terms of the Creative Commons Attribution Non-commercial License, which permits use, distribution, and reproduction in any medium and format, provided the original work is properly cited. The use is non-commercial and is otherwise in compliance with the license. Authors of accepted articles must pay a publication fee. Publication fee: 698 USD per article. All invited articles are published free of charge.

Published by **Baishideng Publishing Group Inc**
8226 Regency Drive, Pleasanton, CA 94588, USA
Telephone: +1-925-223-8242
Fax: +1-925-223-8243
E-mail: bpgoffice@wjgnet.com
Help Desk: http://www.wjgnet.com/esps/helpdesk.aspx
http://www.wjgnet.com